CRANFIELD UNIVERSITY

ANTONIO LIGGIERI

REFUELLING TANKER AERODYNAMICS AND HOSE CHARACTERISTICS

SCHOOL OF ENGINEERING

MSc. (by Research)
Academic Year: 2011 - 2012

Supervisor: Dr. David Macmanus
December 2012

CRANFIELD UNIVERSITY

SCHOOL OF ENGINEERING

MSc. (by Research)

Academic Year 2011 - 2012

ANTONIO LIGGIERI

REFUELLING TANKER AERODYNAMICS AND HOSE CHARACTERISTICS

Supervisor: Dr. David Macmanus

December 2012

This thesis is submitted in partial fulfilment of the requirements for the degree of MSc. (by Research)

ABSTRACT

The present work is conducted within the context of air to air refuelling technologies and aims at the development of an understanding of a typical refuelling tanker wake like that of an A330 [54] and the A400M [54]. The wake is particularly investigated within the near field and extended near field wake regions in close vicinity to the rear fuselage. Moreover, the interaction between the wake and the refuelling hose is studied including the resulting hose characteristics. A number of refuelling conditions and aircraft models are considered for the investigation of the wake. Moreover, an arbitrary hose fairing model is considered to study the effect of the fairing on the flow field and the refuelling hose. Different refuelling configurations are taken into account for the investigation of the hose characteristics. Various hose exit positions were studied within the near field wake to assess the impact on the hose characteristics.

The probe hose engagement with the associated hose whip phenomenon is a major topic within this work. The hose whip is a highly undesired phenomenon and is amplified by a specific hose shape which is characterised through an inflection point along the hose. The present research reveals that the rear fuselage wake has a crucial impact on the hose characteristics. In particular, the rear fuselage upwash is the primary cause for formation of the undesired hose inflection point. The findings obtained from the present research are used for the suggestion of palliatives to avoid undesirable hose characteristics. In particular, there is one approach recommended which aims at the avoidance of a hose-upwash interaction. It leads to the suggestion of a circumferentially shifted and radially displaced hose exit and deployment of the refuelling hose.

ACKNOWLEDGEMENTS

I wish to express my appreciation to my supervisor Dr. David Macmanus for guiding me throughout my work and above all for giving me the chance to conduct this rewarding degree programme at Cranfield University. His mentoring has always been inspiring and important for the development of my mindset and his experience as well as his knowledge has been an invaluable asset to me.

Moreover, I wish to extend my appreciation to Cobham and the ASTRAEA programme partners for their general support, in particular to Andrew Truran and Tom Rendall for their close cooperation.

Lastly I wish to thank to all my friends and fellow students I met throughout this year for being enriching company at any time, in particular to Alice Miranda for her proactive support at the start of my degree programme and for introducing me to the administrative aspects.

This work is funded by Cobham Mission Equipment as part of the ASTRAEA Programme. The ASTRAEA programme is co-funded by AOS, BAE Systems, Cobham, EADS Cassidian, QinetiQ, Rolls-Royce,

Thales, the Technology Strategy Board, the Welsh Assembly Government and Scottish Enterprise. Website:

http://www.astraea.aero/

TABLE OF CONTENTS

FIGURES

TABLES

NOTATIONS

A_d	Drogue reference area	[m^2]
A_{ref}	Generic reference area	[m^2]
C_l	Lift coefficient	[-]
C_d	Drag coefficient	[-]
C_{ref}	Reference chord	[m]
c	Speed of sound	[m/s]
D_d	Drogue diameter	[m]
D_f	Fuselage diameter	[m]
D_b	Beam diameter	[m]
d	Diameter	[m]
F_{lift}	Lift force	[N]
H	Height	[m]
H_{hef}	Hose exit fairing height	[m]
L	Length	[m]
L_b	Beam length	[m]
L_f	Fuselage length	[m]
L_h	Hose length	[m]
L_{rf}	Rear fuselage length	[m]
L_{hef}	Hose exit fairing length	[m]
Ma	Mach number	[-]
M_b	Bending moment	[Nm]
N_b	Number of beams	[-]

P	Pressure	[Pa]
P_{ref}	Reference pressure	[Pa]
P_{dyn}	Dynamic pressure	[Pa]
Re	Reynolds number	[-]
r	Radius	[m]
T	Temperature	[K]
T_{ref}	Reference temperature	[K]
V	Velocity	[m/s]
V_{wave}	Velocity component in x direction	[m/s]
V_x	Velocity component in x direction	[m]
V_y	Velocity component in y direction	[m]
V_z	Velocity component in z direction	[m]
V_∞	Free stream velocity	[m/s]
W	Width	[m]
W_s	Wingspan	[m]
W_{hef}	Hose exit fairing width	[m]
x	Spatial direction x	[m]
y	Spatial direction y	[m]
y^+	Dimensionless wall distance	[-]
z	Spatial direction z	[m]

α	Angle of attack	[°]
β	Upsweep angle	[°]
Δ	Difference related to context	[-]
ε	Upwash angle	[°]
φ	Circumferential variation hose exi t	[°]
θ	Ventilation angle	[°]
γ	Rear fuselage angle	[°]
χ	Shear strain rate	[1/s]
ω	Vorticity	[1/s]

ABBREVIATIONS

CU	Cranfield University
UAV	Unmanned aerial vehicles
ASTRAEA	Autonomous Systems Technology Related Airborne Evaluation & Assessment
UAS	Unmanned aerial systems
NASA	National Aeronautics and Space Administration
CFD	Computational Fluid Dynamics
DPW-2	2nd Drag Prediction Workshop
DLR	German Aerospace Centre
DPW-4	4th Drag Prediction Workshop
CRM	Common Research Model
AIR	Automated In-flight Refuelling
IMRAD	Introduction, Methods, Results and Discussion
HEF	Hose Exit Fairing
SDR_x	Spatial Drogue Range with indices for spatial direction

1 INTRODUCTION

In aviation the application of unmanned aircraft systems (UAS) is becoming more important, both in the defence and civil domain. Even though these technologies are still relatively new some of them already contribute substantially to safety and reliability. The UAS industry is a growing market with a high potential for research. In the UK the relevance of these technologies is reflected in the £62 million ASTRAEA program [1]. The ASTRAEA program is a consortium of several universities and industrial partners, with the aim to enable the routine use of UAS in all classes of airspace [1]. In particular it is planned that this is achieved without the need for restrictive or specialised conditions of operation [1].

The need for UAS arises due to various reasons. Figure 1-1 shows two drones during automated refuelling in formation and close proximity. In this case the automated refuelling system can be regarded as an UAS and enables the drones to travel greater distances and over longer continuous time spans for intelligence or reconnaissance of targets.

Figure 1-1 Two unmanned drones during in-flight refuelling with a drogue and probe system [60]

Figure 1-2 shows an A330 [54] refuelling tanker with an A400M [54] transport aircraft during in-flight refuelling. In the case of a transport aircraft, in-flight refuelling enables more goods to be loaded since the aircraft can be refuelled in the air after take-off.

Figure 1-2 An A330 [54] refuelling tanker with an A400M [54] receiver aircraft during in-flight refuelling with a drogue and probe system [64]

However, manually operated in-flight refuelling is hazardous and requires a lot of exercise by pilots and has led to accidents in the past [2]. It is reported that refuelling manoeuvres with a hose and drogue system suffered a 2.5% failure rate [2]. This is a typical example where a properly applied UAS can contribute to increased safety. Up to now the routine use of these technologies has not yet been achieved. In fact, automated in-flight refuelling capabilities are a great limitation of current UAVs [20] and are therefore a subject of research.

The overall aim of the ASTRAEA programme [1] is to enable the wider use of UAVs in all airspaces. Part of this is to look at the technologies required for air to air refuelling using autonomous air systems. Within this context the research reported here focuses on the investigation of the tanker wake and the refuelling hose characteristics.

The principle of in-flight refuelling technology for a UAV is the same as today's conventional probe and drogue systems, where a hose and drogue is deployed from the wings or from the rear part of the fuselage. Figure 1-3 shows schematically a typical assembly.

a)

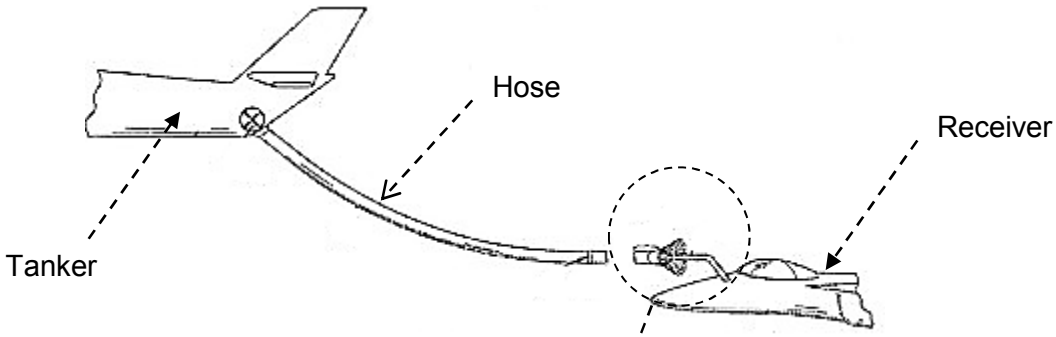

b)

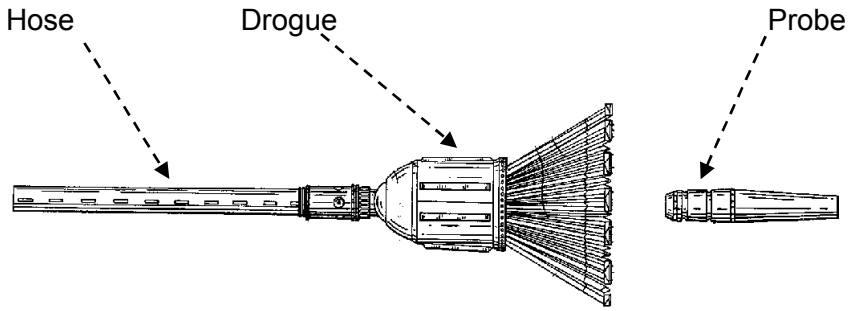

Figure 1-3 a) Hose and drogue system schematic refuelling configuration [55] b) Zoomed hose-drogue-probe configuration [56]

The hose simply delivers fuel from the tanker to the receiver aircraft. The drogue is mounted at the end of the hose and has two main functions. It acts as an aerodynamic device which stabilises the hose during flight and provides a funnel to aid insertion of the approaching receiver aircraft probe into the hose [3].

Unlike the flying boom which is shown in Figure 1-4 where an operator in the tanker aircraft adopts the insertion of the tube into the receptacle of the receiver aircraft, the hook-up with the hose and drogue system is completely dependent

on the pilot of the receiver aircraft. The position of the hose and drogue is determined by the physical circumstances and cannot be manipulated in any way.

a)

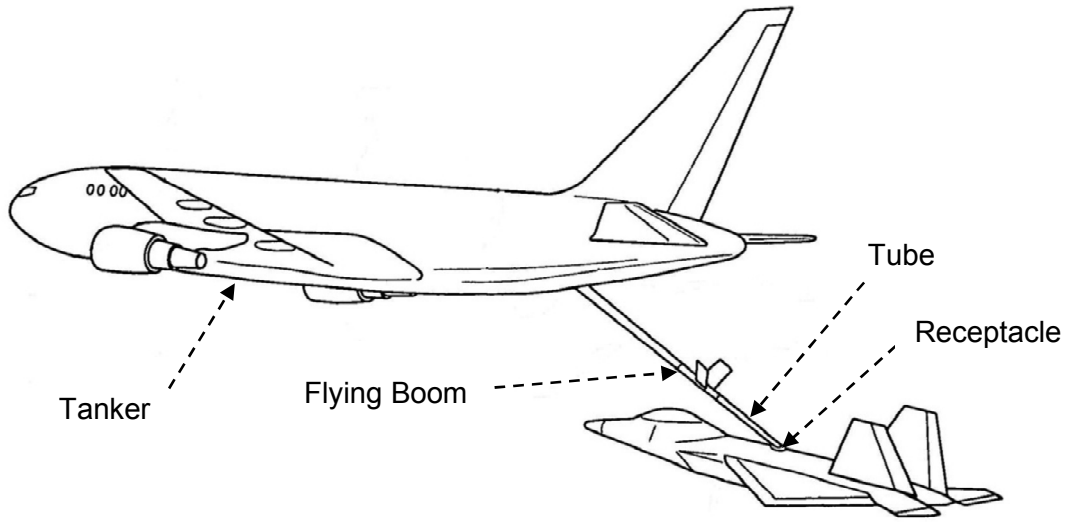

b)

Figure 1-4 a) Flying boom system schematic refuelling configuration [57] b) Photograph of an F16 during in-flight refuelling with a flying boom system [58]

This is illustrated in Figure 1-5 where the approach of the receiver to the tanker with the trailed hose is shown.

Figure 1-5 Approaching receiver aircraft for hose probe engagement [59]

The only feedback the pilot has is his optical perception. The pilot leads the probe close to the drogue and tries to hook-up with a short acceleration of the aircraft. The procedure must be conducted as smooth and skilfully as possible. A too strong collision of probe and hose induces a wave which can lead to a dramatic whipping of the drogue. This is an unwanted phenomenon as it can cause severe damage like a hose-drogue separation [19] or supporting structure damage of the receiver aircraft [21]. This delicate procedure is envisaged to be supported by an autonomous system which will be realized through the use of control and feedback technology. Since the position of the drogue must be by definition within a certain spatial range, the reliable prediction of the static hose shape and drogue position is a crucial factor for the development of the system. Furthermore, the hose can assume different static shapes, which affects the dynamic response to perturbations associated with the hook-up [74]. Both parameters, position and shape, are notably influenced by the local flow field of the tanker. The rear fuselage shape of the tanker in turn, is one major parameter which forms the characteristic of the wake within which the refuelling hose is exposed. Therefore, the determination of representative tanker aircraft is a vital step for the validity of the conclusions regarding the hose characteristics. The present study considers two tanker

types. A conventional civil aircraft like the A330 [54] modified for military purposes and a typical transport aircraft like the A400M [54]. Both fuselages are of different type and will generate wakes of different nature. For the investigation of the wake-hose interaction mainly the A330 [54] is considered. The A400M [54] wake is also predicted, but is investigated qualitatively and without the hose. There are no previous studies available of the wake-hose interaction for different fuselages under multiple conditions. The present work explores this research topic intensively. It generates valuable information for further research, and could lead to novel in-flight refuelling designs for the future.

1.1 Aims and objectives

The overall aim of the study is to develop an understanding of the rear fuselage wake through the use of computational fluid dynamics (CFD), as well as an understanding of the wake-hose interaction and the resulting hose characteristics. To achieve this, the following research and modelling strategy has been defined.

1.1.1 Research and modelling strategy

Setting up the research and modelling strategy involves

1. Review on rear fuselage flows and assessment of different tanker fuselage types
2. Clear definition of the research object which is represented by the wake and the wake-hose interaction
3. Data and information collection for inflight-refuelling cases
4. Assessment and selection of tools and methods suitable to model and simulate the inflight-refuelling cases
5. Build-up, simulation and validation of the inflight-refuelling cases for different simulation scenarios
6. Analysis of the calculation results
7. Derivation of conclusions

1.1.2 Outcome

1) A clear understanding of the wake aerodynamics, in particular close to the rear part of the fuselage
2) A correlation between the wake aerodynamics and the hose characteristics
3) Formulation of generic rules for hose deployment
4) Suggestion of palliatives
5) Suggestions for further research

2 LITERATURE REVIEW

The literature review comprises an assessment of the currently available literature on the subject as well as the identification of suitable experimental data for the CFD validation. Relevant fields include experimental and CFD studies about aircraft wakes, in particular near field wakes, as well as studies about upswept rear fuselages. Furthermore there is an interest in suitable full aircraft models and wind tunnel experiments as well as CFD methods in the present area of research. In addition to the CFD part, literature about the current state of research associated with autonomous in-flight refuelling is of interest. Particular attention is given to key difficulties of autonomous in-flight refuelling (AIR), how these were previously addressed as well as corresponding hose and drogue modelling approaches. The current work enables insights into a real world problem through the research with models and simulations. There are different approaches for research of this type. A sub chapter in Appendix A.1 discusses different research philosophies and introduces the philosophy and structure of the current study.

2.1 Validation cases

This section gives an overview of the aircraft types considered and the corresponding geometries used for the wake and hose predictions. The availability of original aircraft geometries is often restricted even for research purposes. For the present study no original geometries are available, neither for the A330 [54] nor for the A400M [54]. However, the AIAA provides public domain information from their drag prediction workshops (DPW) [4] [5]. These are wind tunnel experiments conducted with full aircraft configurations at model scale, which can be used as substitute geometries.

2.1.1 A330 substitute

The second drag prediction workshop DPW-2 [4] used the DLR-F6 full aircraft model while for the DPW-4 [5] the NASA common research full aircraft model (CRM) was used (Figure 2-2 and Figure 2-3). Both experimental series focus on the prediction of drag. Experimental outputs are the main aircraft forces and moments. Both models are similar to a typical civil aircraft like the A330 [54] shown in Figure 2-1. For this current work they are considered as potential substitute configurations. The experiments along with the aircraft models have advantages and disadvantages. These will be discussed later in Section 3.1.1 where the discussion on geometric modelling is conducted.

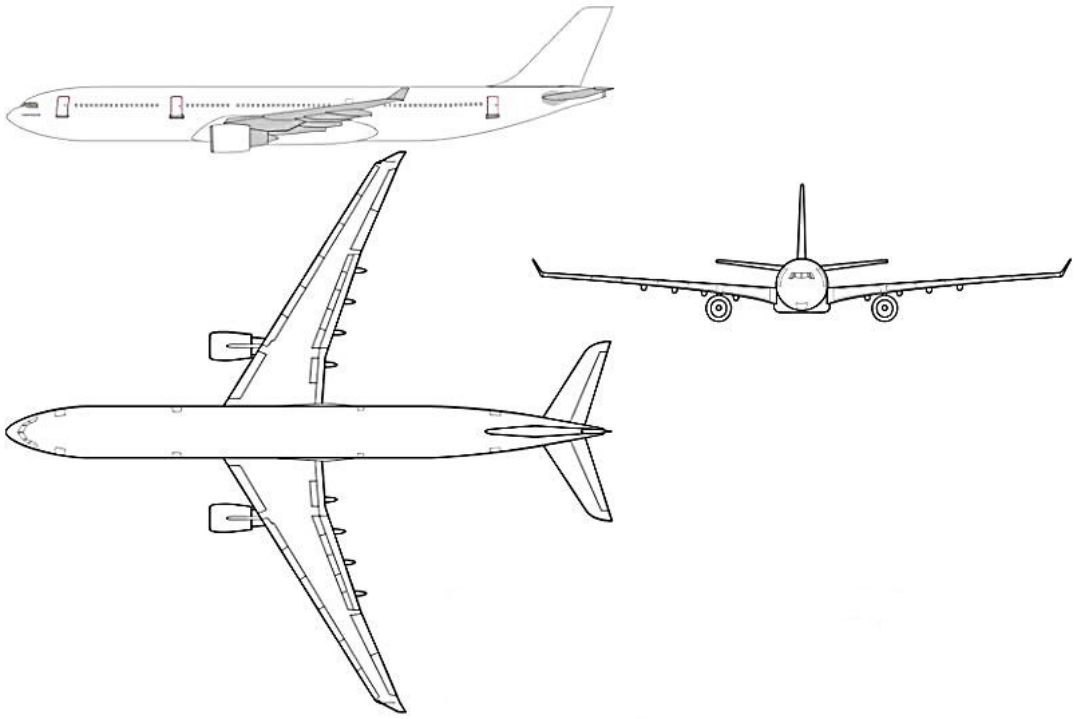

Figure 2-1 General arrangement of an A330 shown in side, front and top view and quantities in full scale [50]

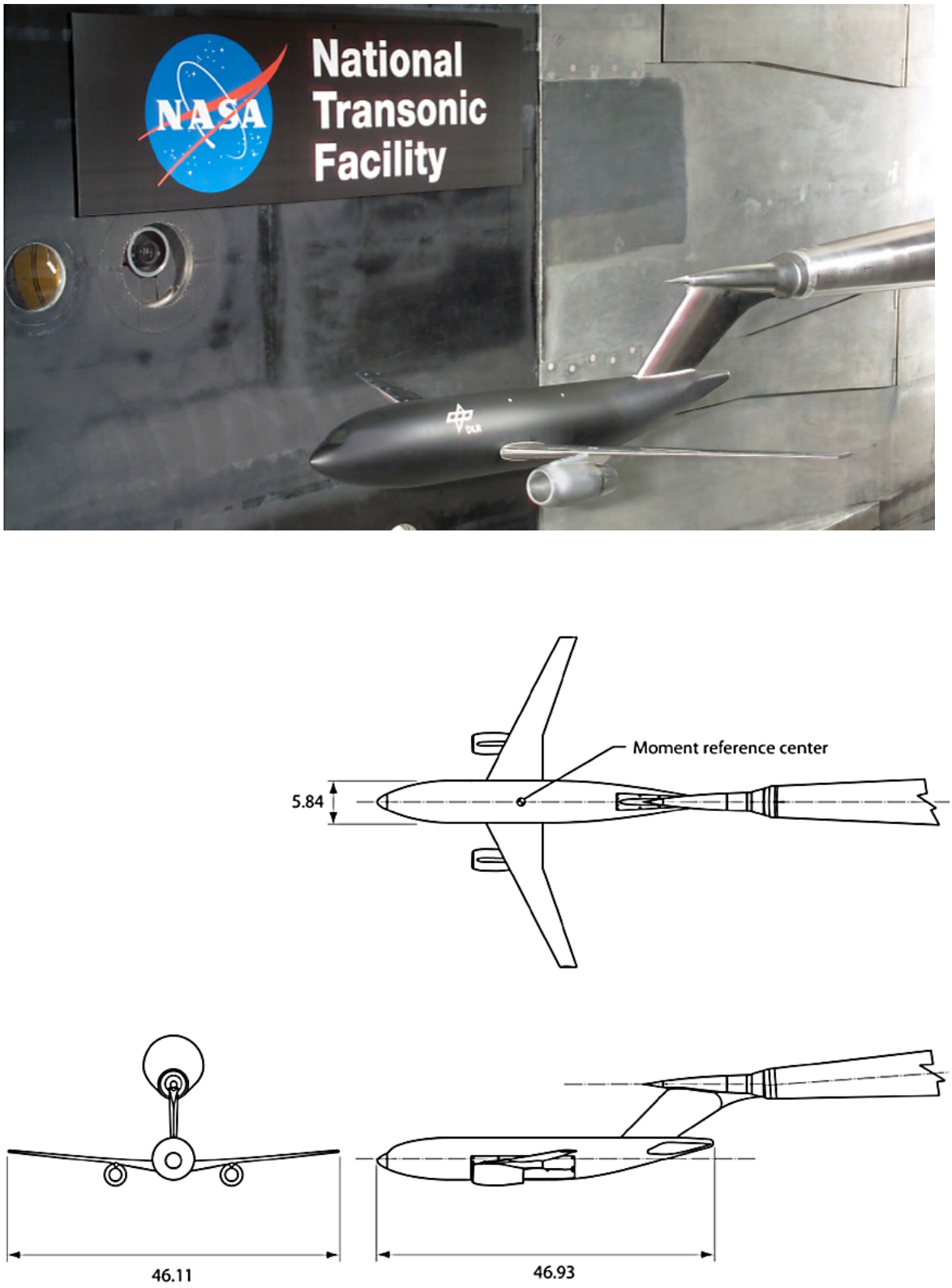

Figure 2-2 DLR-F6 wing body nacelle configuration in wind tunnel (top) [4] and top, front, side view sketch [4] (bottom) with dimensions in inch.

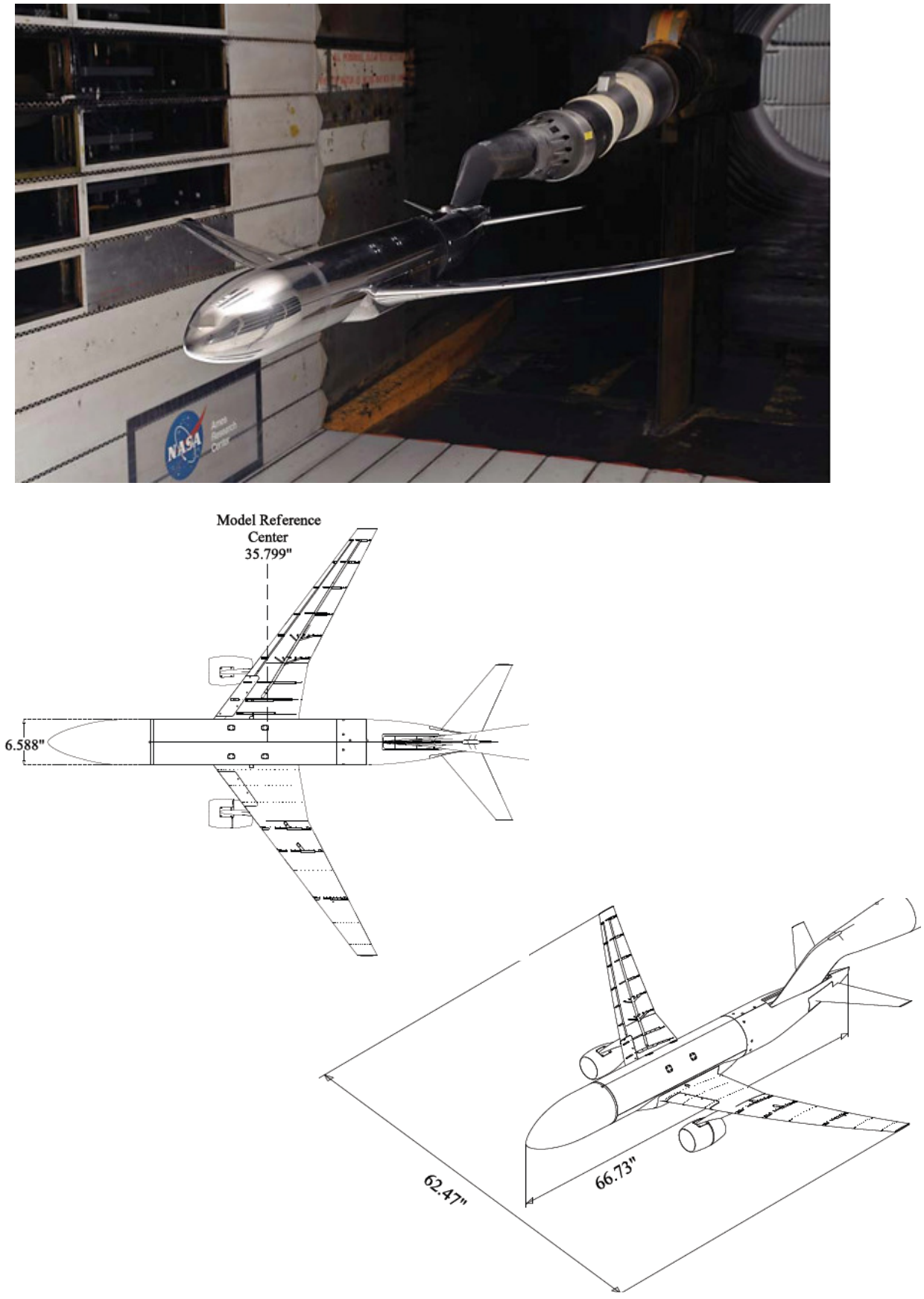

Figure 2-3 CRM wing body tail nacelle configuration in wind tunnel (top) [5] and top, isometric view sketch [5] (bottom) with dimensions in inch.

2.1.2 A400M substitute

A suitable full aircraft substitute for a typical transport aircraft like the A400M [54] (Figure 2-5) could not be found. Since the investigations focus on the characteristics of the rear fuselage aerodynamics, a fuselage only configuration also suits the requirement of the study. Peake investigated the flow about upswept rear fuselages of typical transport aircraft [14] both experimentally and computationally. Figure 2-4 shows schematically the geometry used by Peake [14]. A photograph of the wind tunnel model can be observed in Figure 2-6. It is simply a cylinder with a semi-sphere at one end and a flattened cone at the other end.

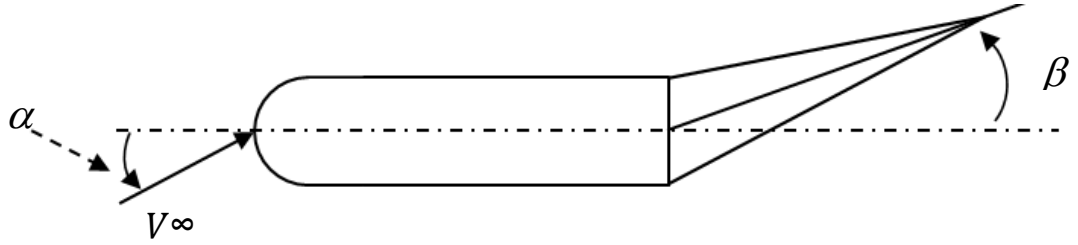

Figure 2-4 Symbolic sketch of the transport aircraft geometry used by Peake [14] with definitions for angle of attack α and upsweep angle β

Three different experimental methods were conducted on this geometry – oil dot for the visualisation of surface streamlines and thus possible separation lines, forces and moments related to the rear part of the geometry as well as circumferential surface pressure distribution measurements. The pressure distributions are available for two angles of attack α and for one upsweep angle β of 5°. These are suitable for the validation of the CFD model at corresponding wind tunnel operating conditions. Therefore, this model has been considered for possible further research on hose characteristics in conjunction with the A400M [54] aircraft and may be regarded as an assessment of a suitable validation case. Hence, the CFD validation with the experimental data available is performed and the wake characteristics are qualitatively investigated, but hose simulations with this geometry are not conducted.

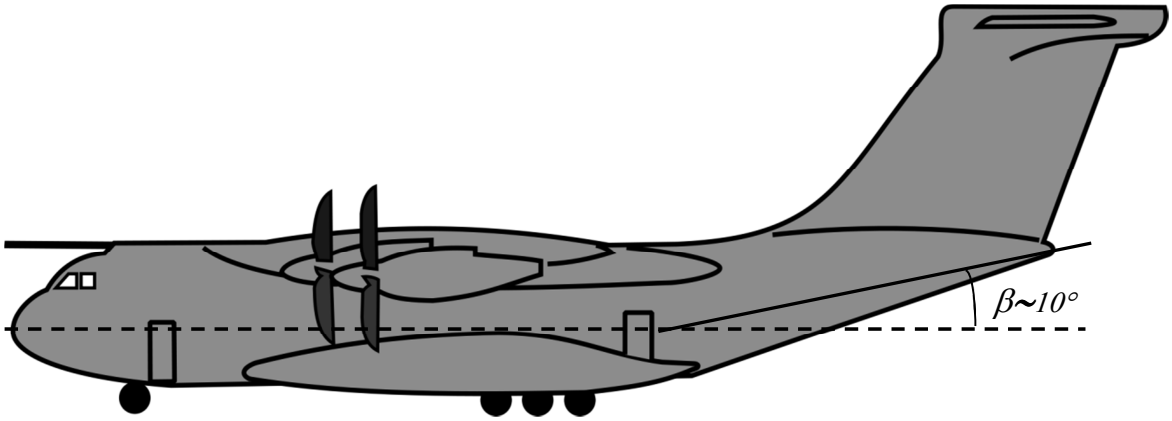

Figure 2-5 A400M [54] side view sketch with indicated upsweep angle β [51]

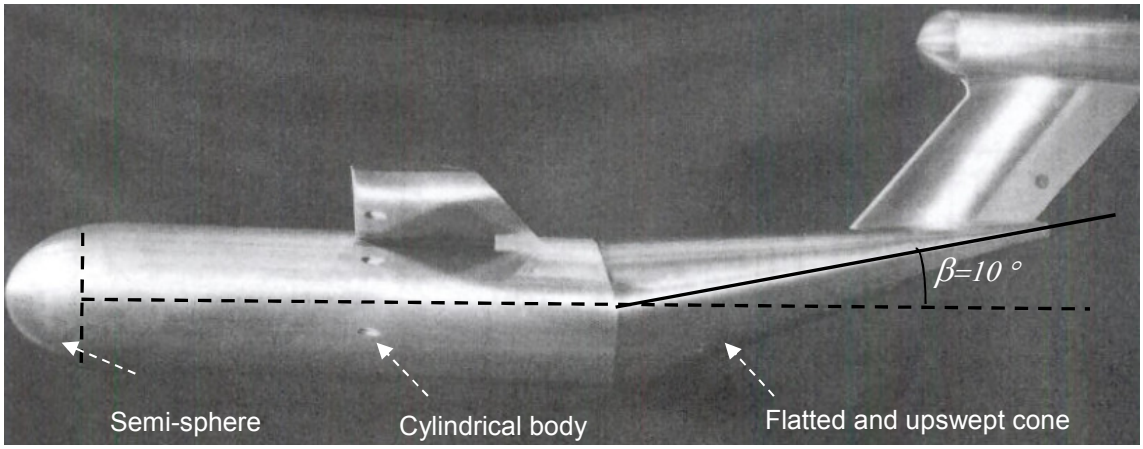

Figure 2-6 Transport aircraft wing body configuration with indicated upsweep angle β [14]

2.2 Wake studies

The review has shown that the investigation of an aircraft wake is a well-developed research area. This is especially true for the investigation of the extended near field, mid- and far field wake shown in Figure 2-7, where plenty of information is available in the public domain [7] [8] [23] [43] [44] [45] [46] [47] [48] [49]. In contrast there are relatively few studies for the near field wake. Even less public domain information is available on the CFD based wake prediction in the immediate vicinity of the rear fuselage [8] [62]. However, the refuelling hose deployment from a tanker takes place in immediate vicinity to the aircraft, and therefore the wake region of interest is the near field and the

extended near field region. Parts of both regions associated with hose deployment are investigated in the present work and are discussed in Section 4.2.

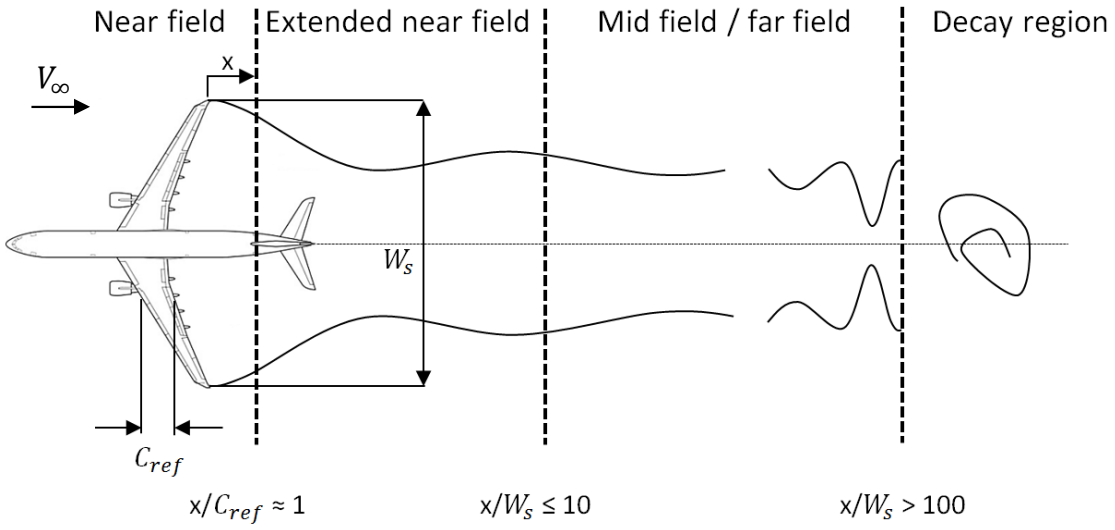

Figure 2-7 Definition of different aircraft wake regions from near field (left) to mid and far field, up to the region where the wake structure decays [50] [23]

2.3 Rear fuselage studies

Most of the public domain rear fuselage studies are either limited to experimental investigations or compared to results of a potential flow calculation [13]. Interestingly, most of the rear fuselage investigations that were found address the effect of the rear fuselage upsweep, also termed afterbody upsweep. Some of them correlate with the body characteristics of the A330 [54] aircraft, while others focus specifically on military transport aircraft [13] [14] like the A400M [54]. For this study the relevant geometrical differences are given through the afterbody shape. The afterbody cross sections of a transport aircraft tend to have high aspect ratio elliptical geometries, with a flattened lower surface. The afterbody cross sections of a typical modern civil aircraft are mostly circular.

2.3.1 Separation

For the wake characteristics of a rear fuselage flow the geometry plays an important role. The geometry has a critical impact on whether separation occurs or not. There are several methods how separation can be visualised. Figure 2-8 shows the oil dot method. It allows the visualisation of surface streamlines.

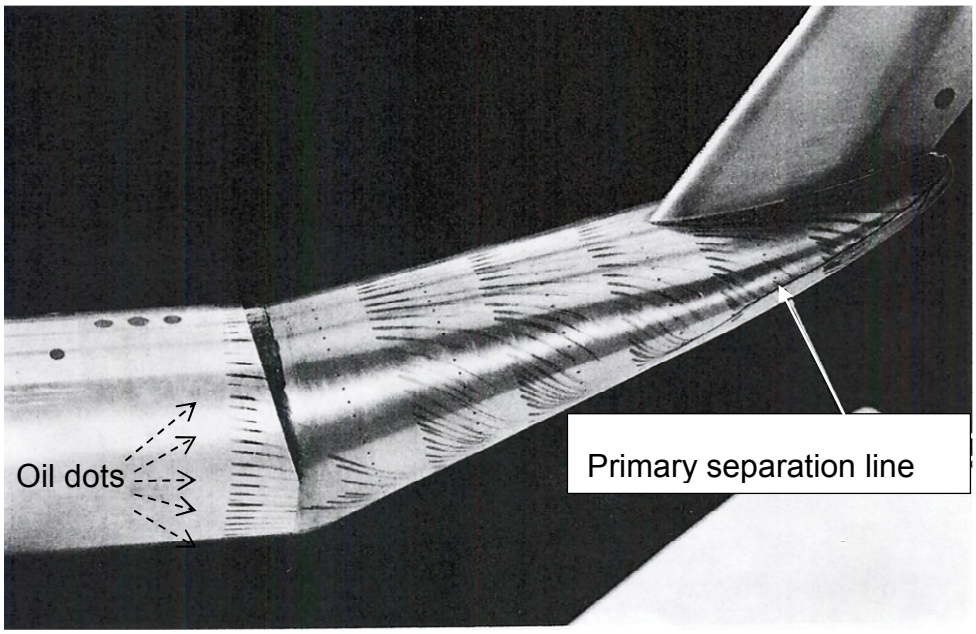

Figure 2-8 Visualisation of surface streamlines on the beaver tail rear fuselage through the use of oil dots [14]

The surface streamline path indicates the presence of separation. The streamlines converge towards the position where separation takes place and form a straight line – this is the separation line. The determination of separation and therefore the visualisation of separation lines and associated vortex formation is part of the wake analysis through the use of CFD. The CFD results will be compared graphically to oil dot visualisations from experiments.

2.4 Rear fuselage wake characteristics

This section discusses generically the wake characteristics of the two fuselage types of interest, which are that of a transport and a civil aircraft. Although both fuselage types show similar aerodynamic behaviour there are distinct differences that are particularly of interest for the calculation of the hose characteristics.

2.4.1 Transport aircraft

Figure 2-9 a) shows schematically the separated flow of a fuselage only configuration where the wake beneath the rear fuselage is typically characterised through two vortices which originate from the underside of the afterbody [14]. This is especially true for afterbody shapes similar to those of a transport aircraft like the A400M [54]. This can be observed in Figure 2-9 b) where the vortices are shown in a photograph taken during an experiment.

a)

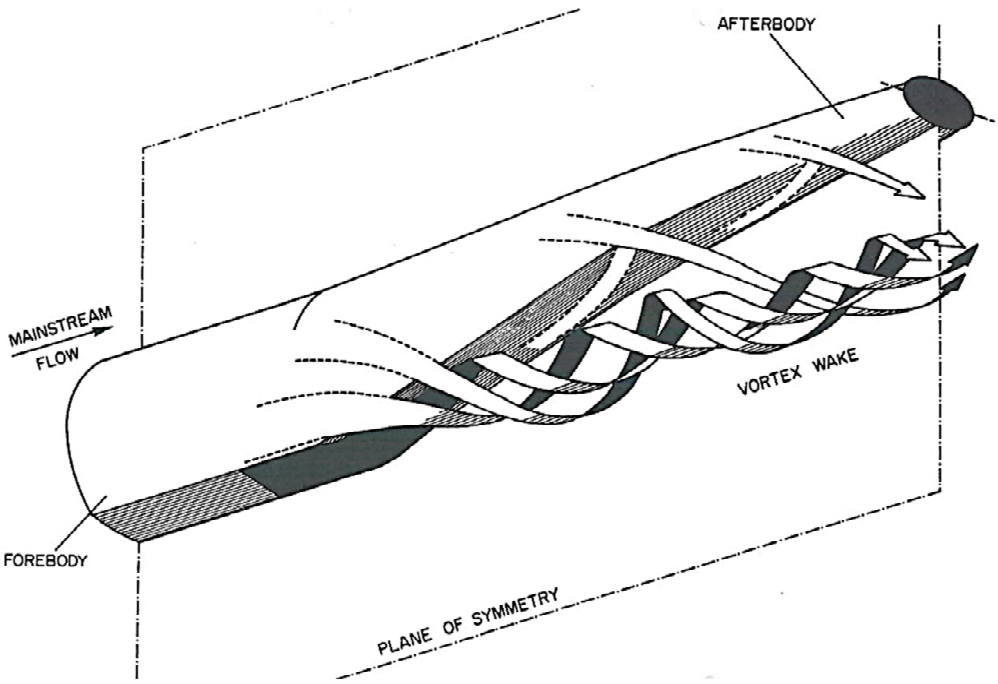

b)

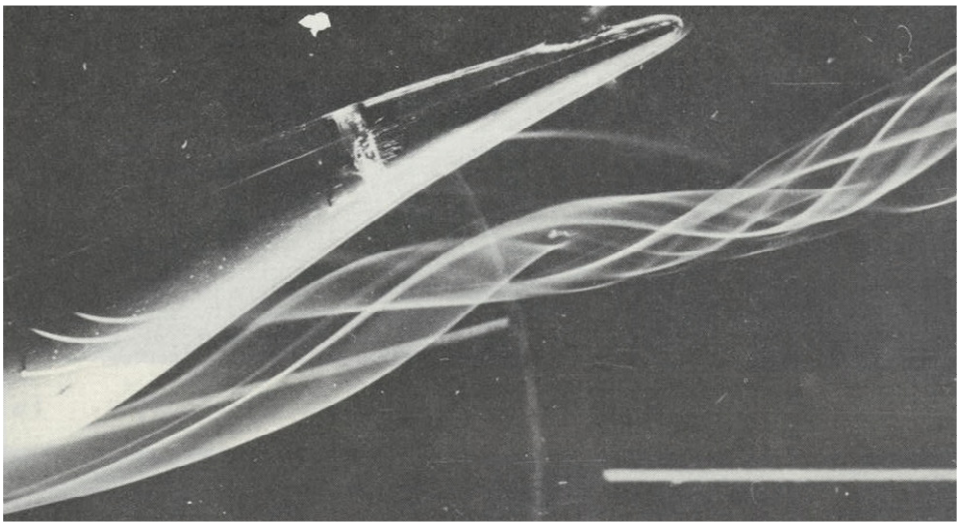

Figure 2-9 a) Schematic rear fuselage sliced at symmetry plane, with separated flow forming a vortex from underneath the body [14], b) Vortex visualised through addition of fluorescence to the flow [9]

The vortices are typically of small scale; the vortex wake is steady and has low frequency time variations in the flow [14]. Moreover, the overall flow characteristics remain unchanged with increasing Reynolds number as well as the vortex strength [14]. The appearance of these vortices in the cross flow plane just downstream of the fuselage is similar in many respects to separations which usually occur on slender delta and rectangular wings [9]. Figure 2-10 a) shows, that for zero yaw there is also complete flow symmetry. This fact may be of interest for the determination of the hose exit position. For instance, from this point of view it appears favourable to choose the hose exit along the centreline of the fuselage due to existence of symmetrical conditions. A circumferential deployment of the hose may cause excitations on the hose due to vortex-hose interaction. Hose studies have investigated similar phenomena [36]. These are discussed later in this report in Section 2.5.4.2

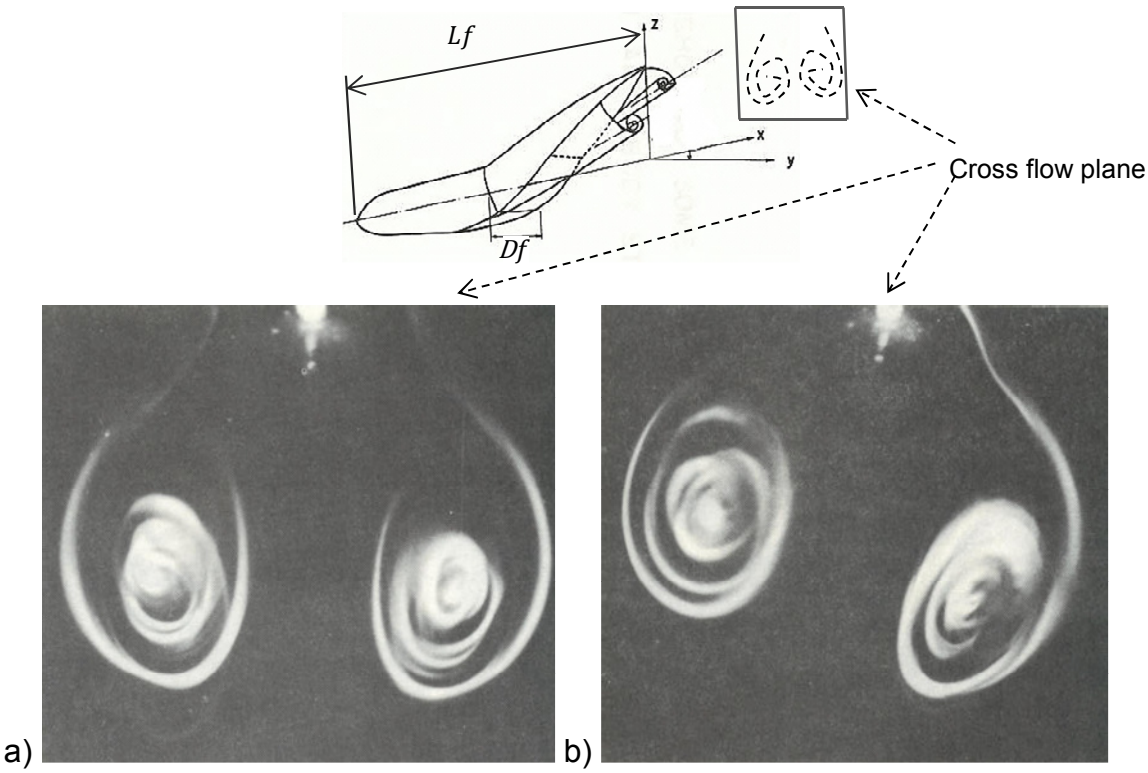

Figure 2-10 Visualised pair of vortices on cross flow plane x= Lf downstream the fuselage, a) with zero yaw and b) with non-zero yaw [9]

2.4.2 Modern civil aircraft

The purpose of a civil aircraft differs from that of a transport aircraft. The lower part of a transport aircraft rear fuselage tends to be flat and provides the prerequisites for a functional requirement - the loading ramp installation. The rear fuselage of a civil aircraft is designed differently. There is no special functional requirement and therefore there is the freedom for aerodynamically favourable design. Figure 2-11 shows the rear fuselage wake characteristics of a typical civil aircraft with wing box indicated as a red surface. At 7° angle of attack it can be observed that separation occurs on the upper side of the rear fuselage [62]. The separation causes the formation of a vortex pair. The number of generated vortex pairs depends on the amount of vortex generation sources. The wing box acts also as a vortex generator and produces a pair of vortices which are shed into the rear fuselage wake [62]. This is illustrated in Figure 2-11.

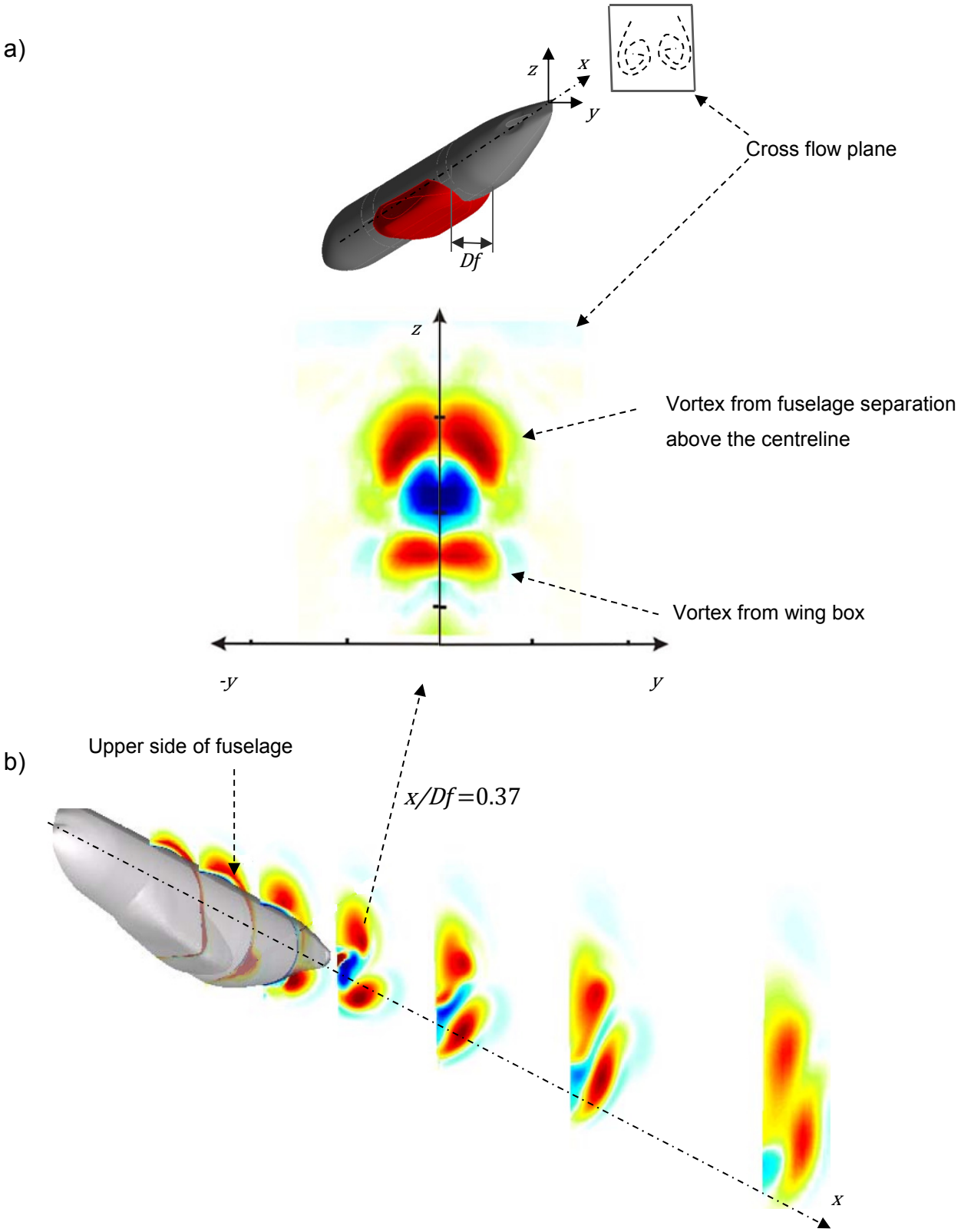

Figure 2-11 a) Two pairs of vortices at cross flow plane x/Df=0.37 which is right behind the fuselage in figure b) along with the further downstream development [62].

2.4.3 Summary

The review on rear fuselage flows has shown, that the geometrical design of a civil aircraft like the A330 [54] is aerodynamically more favourable than that of a transport aircraft like the A400M [54]. For a typical civil aircraft the rear fuselage flow tends to stay attached at angles of attack close to the optimum design point, whereas for a typical transport aircraft the flow tends to separate [14] [9]. If separation occurs, the wake of a transport aircraft is characterised through a pair of vortices which shed into the flow underneath the rear fuselage. For the rear fuselage of a civil aircraft the flow tends to separate only as the angle of attack increases. Therefore, if separation occurs on the rear fuselage wake of a civil aircraft the wake is characterised through a pair of vortices above the rear fuselage which shed into the flow. Consequently, perturbations on the refuelling hose due to vortical flow are more likely, for a transport aircraft than for civil aircraft. The real fuselage flow of a civil aircraft however is expected to be benign. Computationally, both cases need to be treated differently. The gridding for the transport aircraft model needs special attention and effort in the near field wake region as well as in the extended near field wake region for the strong vortical structures to be resolved. Also special attention will probably be given to convergence strategies, as velocity and pressure gradients are high, especially radially from the vortex cores outward. Hence, the volume grid for a transport aircraft model needs to be much finer than that of a civil aircraft. Due to the benign nature of the near wake field underneath the fuselage of a civil aircraft, the grid can be coarser to obtain sufficiently valid results. In the present study this fact has been considered through the use of static meshes for the civil aircraft substitutes and adaptive meshes for the transport aircraft substitutes. The difference of both approaches is discussed later in the methods section.

2.5 Refuelling hose studies

Several refuelling hose studies have been carried out in the last decade [19] [21] [26] [31] [37] [71] [72] [78]. Most of them were conducted recently which indicates that the topic is becoming more important. Most of the reviewed studies focus on the dynamic response of the hose after the probe-hose engagement and the associated hose whip effect [19] [21] [26] [31] [37] [71], or on the response on other excitation sources like wake vortices [36]. Interestingly, even though the initial static hose characteristic is expected to essentially affect the dynamic response [19] [78], all the studies that were found considered either one single hose shape [71] [78] or different hose positions derived from different flight conditions but all with the same characteristics [72]. Also, most of the hose characteristics considered have a benign effect on the hose whip phenomenon. The relation between hose characteristic and hose whip amplification is explained later in Section 3.5.3. Hence, no shape characteristic variations were made to study the impact of the initial curvature on the dynamic response of the hose. However, in real applications the hose may assume different static shapes for different refuelling conditions and different aircraft. Thus, the study of the dynamic response with one single initial shape is possibly only valid for one specific case. Since the hose whip effect is a significant load case during the aerial refuelling design and operation, a detailed dynamic load analysis accounting for hose whip for every particular system configuration is strongly recommended [21]. The present work focusses on the aspect of the initial static curvature and hose characteristics in dependence of different refuelling conditions and aircraft geometries. Thus, the results of the hose characteristics may enhance the investigation range for future studies on the dynamic response, since a number of different static hose characteristics for different system configurations are calculated.

2.5.1 Influential parameters on hose

As the static hose shape is determined all calculations are conducted using steady state models. Hence, only the steady tanker wake is considered and all transient effects like atmospheric turbulence and wind are neglected. This is a

valid assumption insofar as it is expected that the tanker wake has the most impact on the static hose shape and the final drogue position. Even though, for the present work, transient effects are not directly relevant, the context is of automated in-flight refuelling and is therefore considered within the literature review. It also enables the present work to be placed into the bigger context and to link it to previous studies as well as to possible future work.

2.5.2 Unstable drogue position

For the automated probe-hose engagement the behaviour of the drogue is of interest. This spawned a number of research topics like the prediction of the drag upon the drogue and drogue's position, as well as the effects of turbulence and wind upon the drogue [26] [27] [28] [29] [30]. Studies on these aspects were carried out both experimentally [29] and computationally [30]. One finding is that the drogue is unable to maintain a steady-state position relative to the tanker in the presence of wind and atmospheric turbulence [26] which can be observed in Figure 2-12. A similar result was reported by a NASA flight test in which the motion was found to make it difficult for the receiver aircraft to engage with the refuelling system [26].

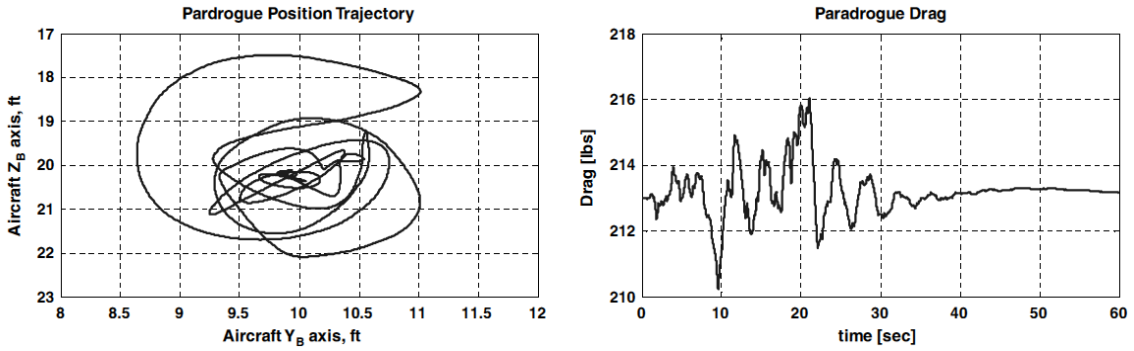

Figure 2-12 The described trajectory of the drogue with view towards hose exit (left) due to atmospheric turbulence and the corresponding drag over 60 seconds [26]

One of the reviewed studies included the approaching aircraft in the model and considered the flow field in front of the receiver aircraft [31] (Figure 2-13). It

revealed an additional source of disturbance regarding the stable drogue position.

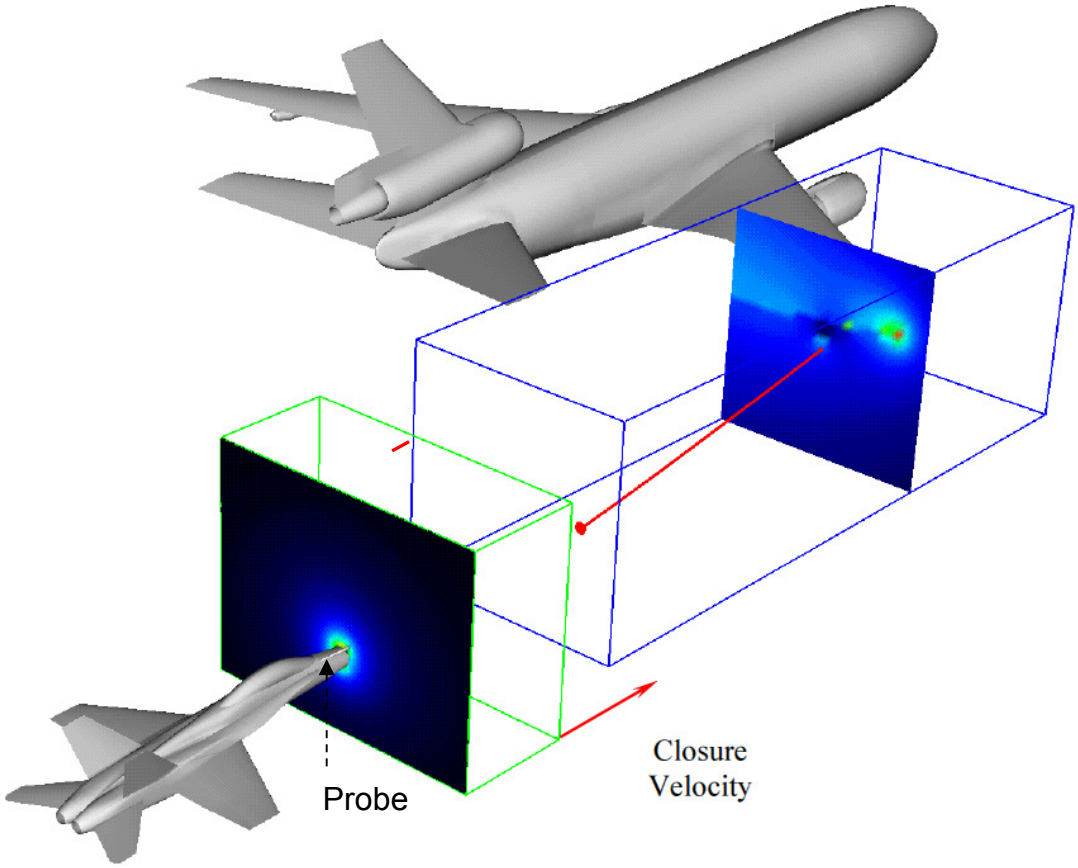

Figure 2-13 Computational model of two coupled flow fields, one from the approaching receiver aircraft (green box) and the wake field of the tanker (blue box) [31]

An F/A-18D receiver aircraft is considered. As the receiver aircraft approaches the drogue, the drogue tends to move away from its forebody. Figure 2-13 shows that the probe on the F/A-18D is located near the side of the canopy on the upper-starboard side. Hence, the drogue swings outward and upward during a coupling [31]. Depending on the canopy geometry and probe position the drogue behaviour is very likely to be influenced in different ways. These facts initiated studies about possible control of the drogue position in flight. In particular this was tried through the use of an active feedback control system [28].

2.5.3 Hose model concept

All reviewed refuelling hose studies used the same conceptual approach for the hose modelling. Figure 2-14 shows the model concept, which consists of a towed mass connected through a cable to a travelling tow point. For the case of in-flight refuelling the tow point is represented by the nominal hose exit, the cable by the hose and the mass by the drogue.

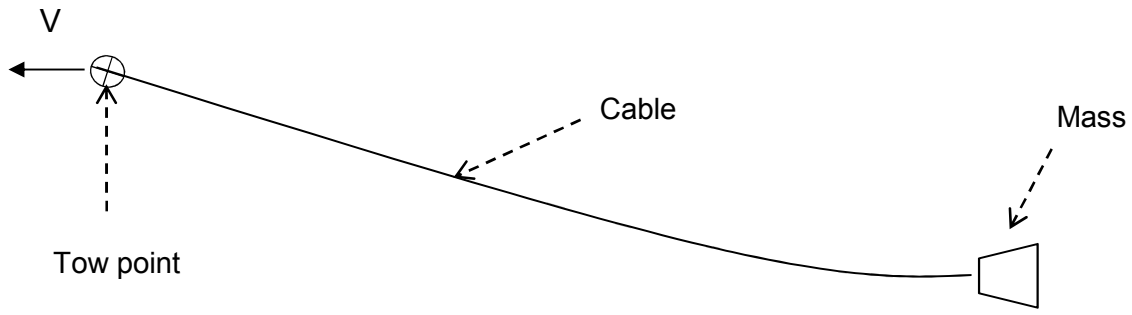

Figure 2-14 Towed cable and mass system with travelling tow point

A general cable system may be divided into two main groups: the low tension cable systems and the high tension cable systems depending on whether the cable is used for load bearing or not. The in-flight refuelling system uses the hose to transfer fuel from one aircraft to another and can be classified as a low tension cable system [36]. In the context of in-flight refuelling such a low tension cable system suffers complex dynamic instabilities [73] from different sources. For investigations on the dynamic response to excitations of such a cable system the initial shape of the cable is of fundamental interest [19] [78]. Amongst others, one major source of dynamic instability is the perturbation which is associated to the engagement of the hose with the receiver aircraft probe. The perturbation occurs longitudinally since the drogue is pushed upstream by the probe. The longitudinal drogue displacement causes a hose slack and induces a wave onto the slacked hose as illustrated in Figure 2-15. The response of the hose is non-linear. Therefore, even for moderate closure rates below 3 m/s [73] [74] and small displacements the dynamic response can result into a dramatic hose whip. This is particularly the case for fuselage

centreline deployed hoses which are affected by the afterbody upwash [74]. Close to the hose exit the hose is lifted by the upwash which causes an inflection point in the hose. This mechanism will be discussed later in the results section 4.2.1.1. As the hose is longitudinally perturbed the formation of a 'sine' wave is initiated [74] (Figure 2-18). Therefore, any static hose characteristic that favours the formation and propagation of a wave needs to be avoided.

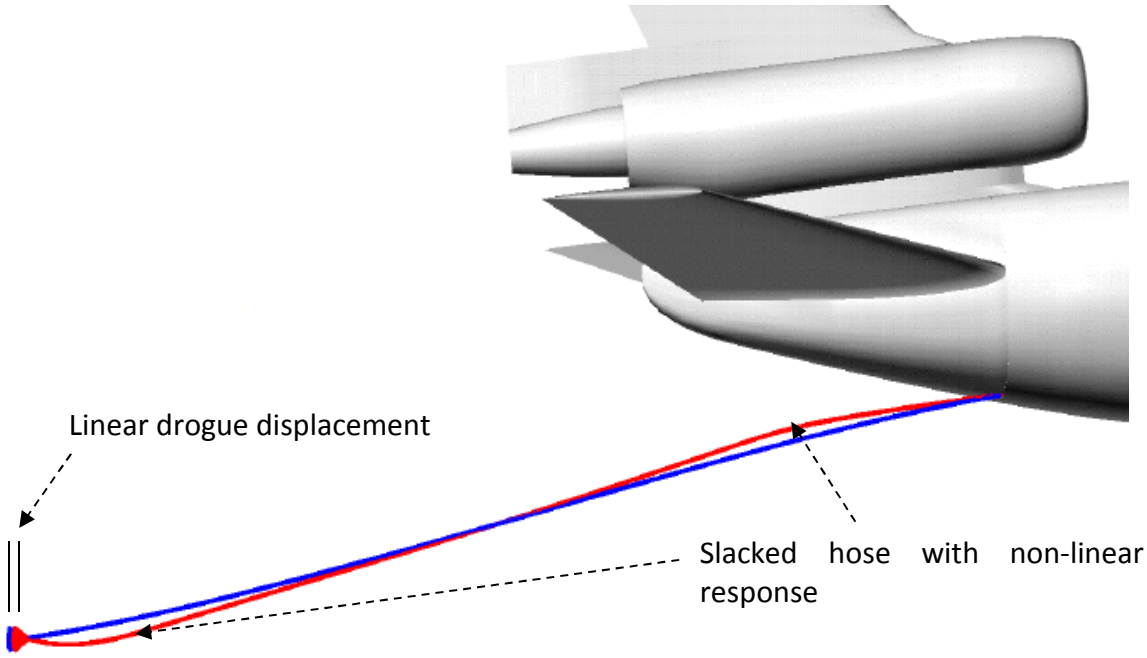

Figure 2-15 Result of a dynamic response calculation where an undisturbed hose under full tension (blue) is compared to a slacked hose due to drogue displacement (red) [78]. The slacked hose assumes the red shape after 0.5 s

Figure 2-16 shows the first three modes on a string. The string can be substituted through the cable and represents the hose. Depending on the initial modal shape of the hose the dynamic response is different. The worst possible shape is the 3rd mode which corresponds to the vibration mode [78]. It favours the hose whip amplification because of two mechanisms. Firstly, this characteristic favours the formation of a wave as it describes a curvature similar to a sine wave. This shape is characterised through the inflection point, also indicated in Figure 2-16, and is an advantageous initial condition for a wave formation [74]. Secondly, it favours an amplification of the propagating wave due to interaction with the rear fuselage upwash as shown in Figure 2-17,

because the part of the hose between hose exit at the tanker and the inflection point tends to be move in the amplification direction by the afterbody upwash.

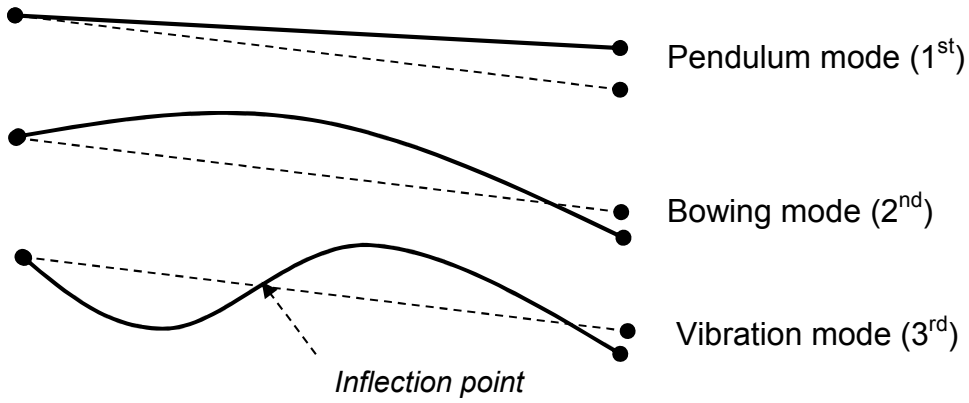

Figure 2-16 First three modal shapes [26]

However, the wave propagation is influenced by the surrounding flow in different respects. Depending on propagation velocity and propagation direction the wave is either damped or amplified. As shown in Figure 2-17 a) the upstream travelling wave is always damped, due to the resetting effect of the aerodynamic forces [26] [37]. Figure 2-17 b) shows that the amplitude increases if the airflow speed $V\infty$ is higher than the wave propagation speed V_{wave} but is slightly damped if the airflow speed is slower [36] [37]. The amplification effect can be observed in Figure 2-18, where the result of a dynamic response calculation is shown. The calculation has been made with a KC-10 full scale configuration for the Mach number of 0.63 at an altitude of 25000 ft, a lift coefficient of 0.52 with a required angle of attack of 2.73° [74].

a)

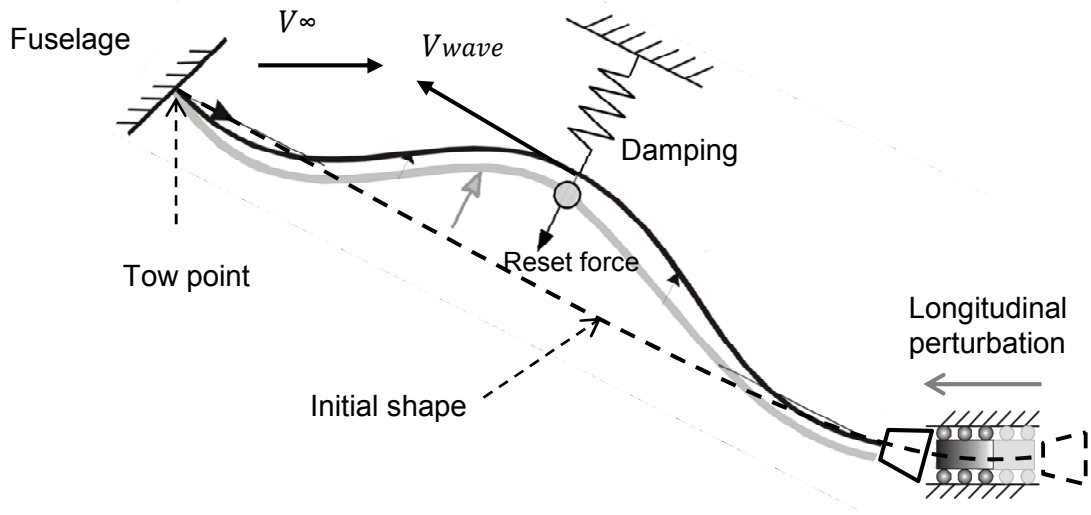

b)

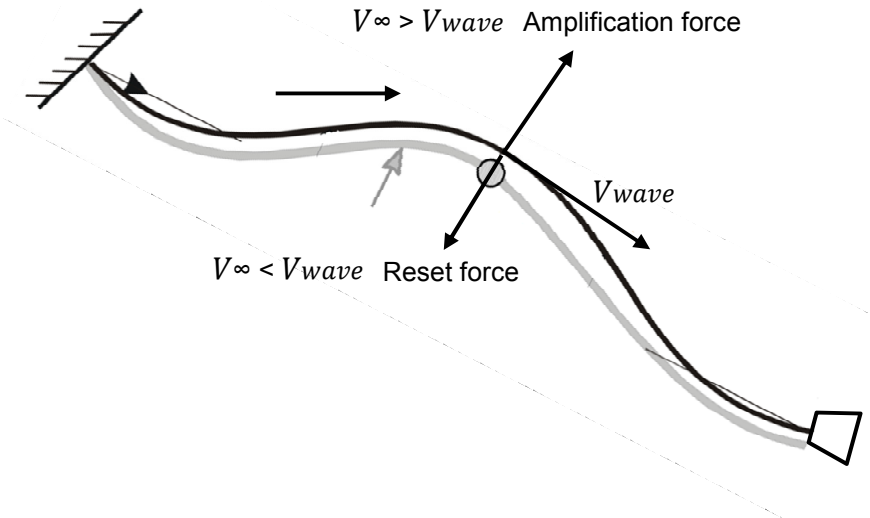

Figure 2-17 Schematic hose deformation due to a longitudinal perturbation at the hose end, a) always damped upstream travelling wave b) amplified downstream travelling wave if $V\infty > Vwave$ *and slightly damped if* $V\infty < Vwave$

Figure 2-18 shows, that the hose is longitudinally perturbed at t=0. At t=0.5s a hose slack with an initiated, upstream travelling wave can be observed. At t=0.75s the wake still travels upstream. Between t=0.75 and t=1s the wave is reflected at the tanker, travels downstream and is amplified through the surrounding flow. The amplitude at t=0.75 is notably lower than at t=1s. The amplitude increases even more from t=1s to t=1.25s. After t=1.3s the high wave energy results into a dramatic hose whip. An inflected hose favours the negative effect of a hose whip and needs to be avoided [74].

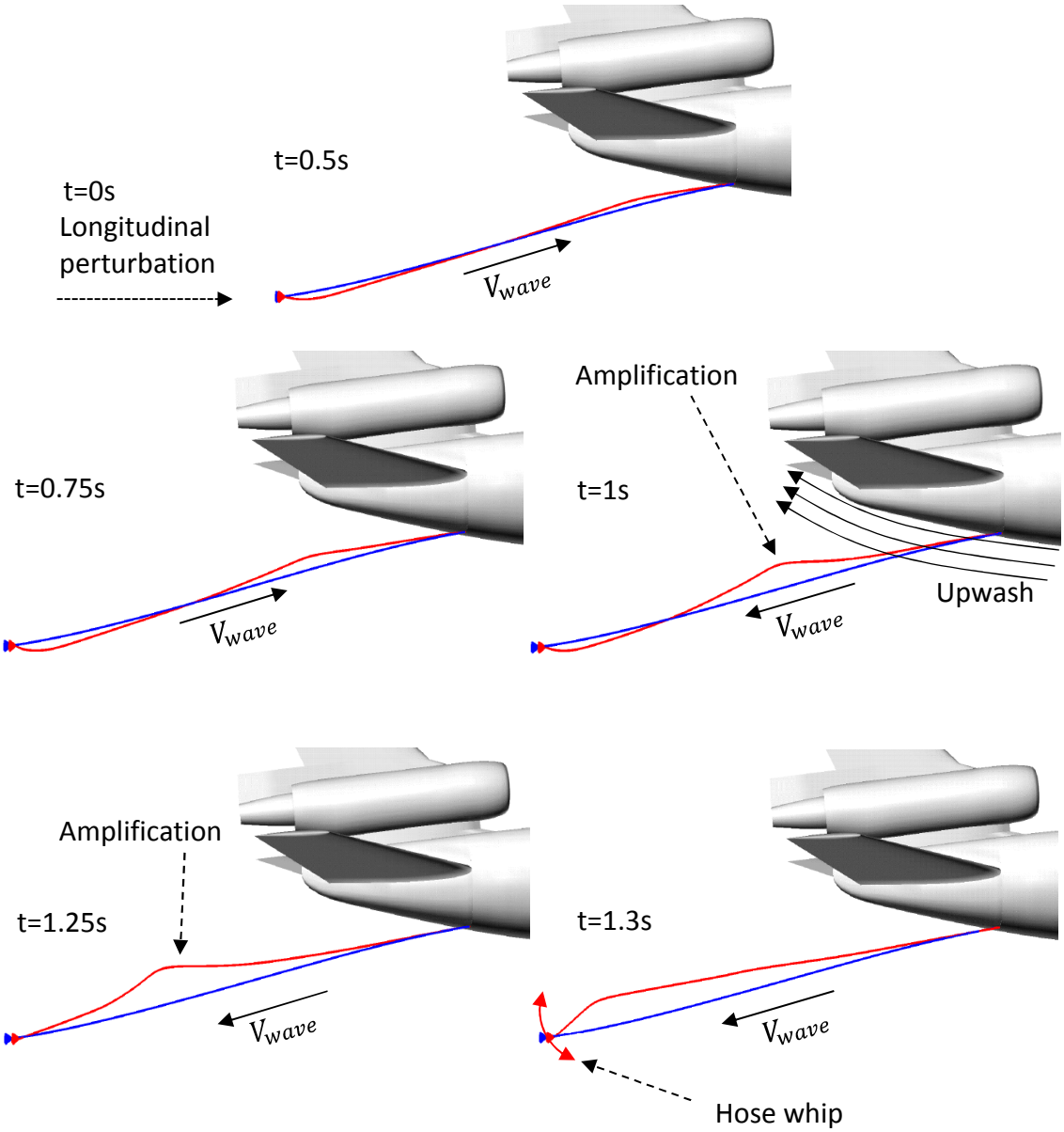

Figure 2-18 Calculated wake propagation along the hose (red) shown for different time steps with indicated travelling direction by the arrows, where the blue hose is the initial reference hose [74]

2.5.4 Modelling approach

Three approaches have been identified for the hose to be modelled – analytical [37], finite element method (FEM) [21] [36] and finite segment [26].

2.5.4.1 Analytical approach

The analytical approach is a classical derivation of ordinary differential equations (ODE). The derived function describes the propagation of a perturbation induced wave along the hose. The application is limited due to assumptions made to derive the ODE`s. To keep the differential equations as ordinary it is assumed that the wave propagates into two spatial dimensions. Figure 2-19 shows schematically a 2D wave with vertical amplitudes in Z and no horizontal amplitudes in Y.

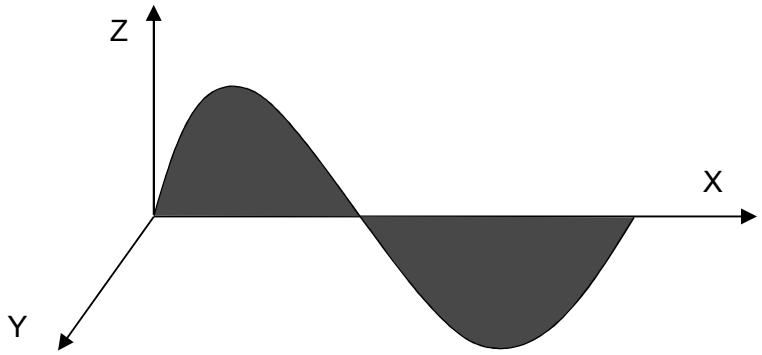

Figure 2-19 Sketch of a 2D wave with propagation direction in X, amplitudes in Z and no amplitudes in Y

The 2D approach is sufficient if the lateral forces on the hose neutralize each other, which is the case when the hose is deployed at the centreline of the fuselage and the aircraft flies at zero yaw. Furthermore transient effects like atmospheric turbulence and wind have to be neglected [37]. However, for the analytical solution the initial cable shape is predefined as straight, and as stated previously, the initial shape is fundamental to the wave propagation [78]. Furthermore, in the analytical study the flow is assumed to be uniform [37]. To consider a non-uniform line as the initial condition, an analytical approach can be applied if the cable is subdivided into straight lines which approximate the curved parts of the cable. The result of each solution is then considered as the

initial condition for the next straight line and so on. This approach could be of interest for fundamental studies on the dynamics of the hose, where a uniform flow can be sufficient as a boundary condition.

2.5.4.2 Finite element approach

The finite element approach has been used for the whip phenomenon investigation which occurs in association with the probe-drogue engagement [21] and the excitation of the hose through vortices [36]. The dynamic FEM stability analysis was carried out by Zhu [36] with the approach of a conventional modal and spectrum analysis. Figure 2-20 shows that Zhu [36] investigated the system imposing an excitation at the tow point.

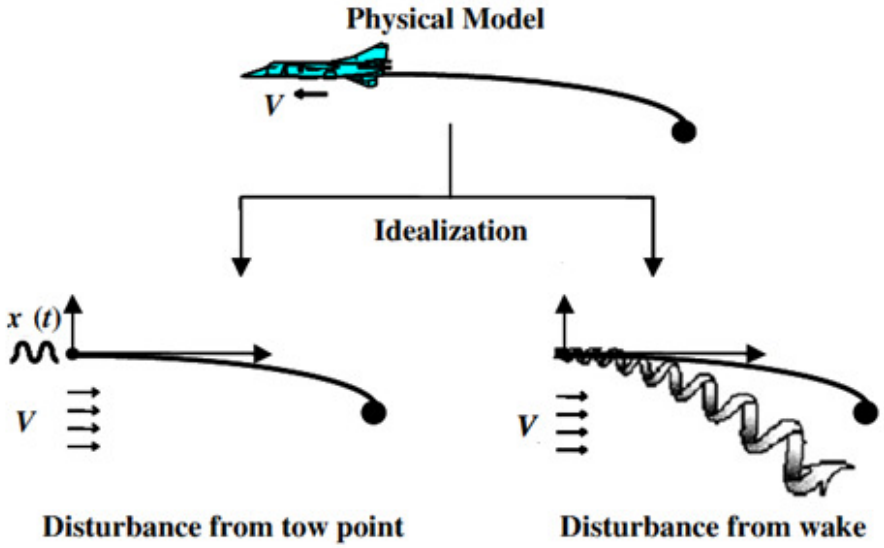

Figure 2-20 Modelling approach by Zhu [36] and its idealisations for the disturbances, left mechanically from tow point and right aerodynamic excitation through a vortex

In the case of in-flight refuelling the first disturbance originates from the drogue due to the engagement with the receiver aircraft. The generated wave first travels upstream and is then reflected at the tanker fuselage. The conditions under which the FEM studies were made correspond to the wake propagation phase after reflexion at the rear body and could therefore be relevant to future research of the present study. It was found that this approach is inappropriate for towed cable systems [36]. The cause of instability is not the resonance of

the system but the excitation through the absorption of energy from the surrounding flow [36] [37].

2.5.4.3 Finite segment model

The finite segment method models the hose by a series of joint connected rigid cylindrical bars (Figure 2-21).

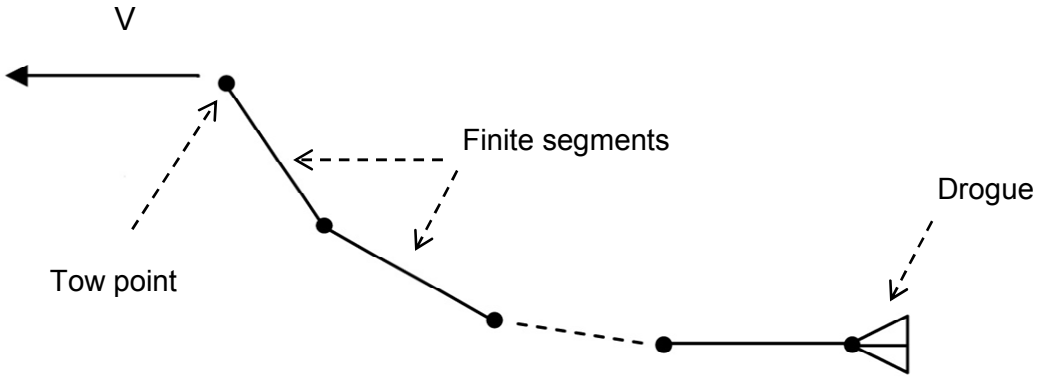

Figure 2-21 Connected single rigid cylindrical beams as a finite segment approximation for a cable [26]

This approach allows the gravitational forces to be taken into account, as well as aerodynamic forces for the impact of the tanker wake on the hose. This leads to a set of differential equations of motion with six degrees of freedom. The present study makes use of this model. As extension to the forces which originate from the tanker wake flow field, atmospheric turbulence and wind effects may be considered as well through the use of appropriate models. The present studies consider the wake forces, turbulence intensity and surface roughness of the hose, which have a notable impact on the drag coefficient of the hose [6]. Wind and atmospheric turbulence are neglected.

2.6 Summary

Autonomous in-flight refuelling typically means a manoeuvre where a receiver aircraft automatically finds a tanker aircraft with a following engagement of drogue and probe in order to transfer fuel from the tanker to the receiver. The behaviour of hose and drogue plays an important role for the success of the manoeuvre. In terms of wake propagation along the hose the ideal scenario of a drogue-probe engagement is that the introduced collision energy is lower than the dissipated energy of the upstream travelling wave. If this is the case no reflection at the tanker will occur and thus no amplification of the wave will take place. However, as this is an ideal scenario the wave propagation effect has been investigated extensively. For these studies the initial static shape of the hose before coupling is of fundamental interest, as it has a crucial impact on the dynamic response of the hose [78]. The initial shape in turn is notably affected by the local flow field of the tanker. No studies were found which focussed on the particular correlation of tanker wake and initial hose shape. In most cases the studies considered one shape as initial condition for the hose response. The present work particularly addresses the impact of the tanker wake on the hose. The wake is predicted with CFD methods and representative tanker geometries at representative refuelling conditions. This enables the development of a generic understanding of the tanker wake, but also the derivation of hose characteristics related to the refuelling conditions. The results of the study will provide a base for a broader investigation of the hose response effect since more than one initial shape can be considered. Furthermore the initial shape can be tracked back to specific in-flight refuelling conditions. This in turn can lead to rules for design purposes for in-flight refuelling systems.

3 METHODS

This chapter introduces the methods and methodologies used to address the problem and to achieve the objectives. This comprises an explanation of the simulation tools used and how the tools are interrelated, in particular the CFD predicted wake with the hose modelling.

3.1 Aircraft geometry modelling

3.1.1 A330 Substitute

In the present case the A330 [54] and A400M [54] are the main aircraft of reference. The in-flight refuelling simulations are carried out by consideration of substitution geometries similar to the A330 [54]. Through the use of surrogate geometries the fidelity of the geometrical modelling becomes limited. However, the present work focusses on the general behaviour of a refuelling hose exposed to the tanker wake. For this purpose the use of a similar geometry is still acceptable, because it still allows generic conclusions to be drawn about the behaviour of the hose. Nevertheless, it is desirable to keep the highest possible fidelity as this strengthens the validity of the conclusions. Therefore, special attention is given to the selection of the A330 [54] substitute. For the selection process pertinent comparison parameters have been defined. As the present study focusses on the rear fuselage part of the aircraft, most of the parameters are related to that region and are defined as follows. Figure 3-1 shows the outline of the DLR-F6 [4] fuselage on the symmetry plane with the definition of the fuselage length L_f and the fuselage diameter D_f.

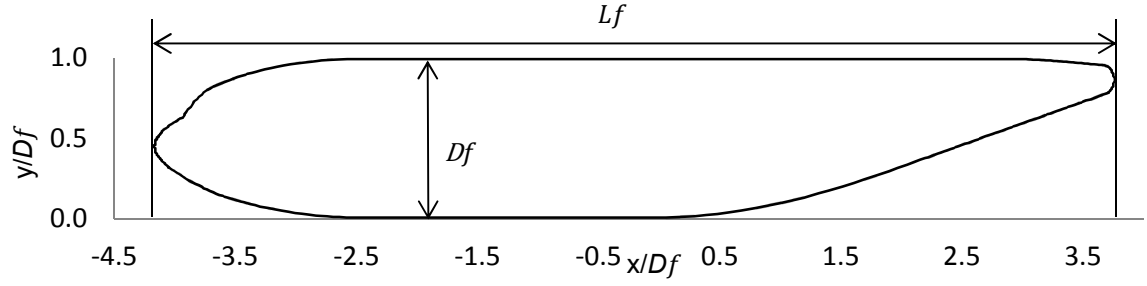

Figure 3-1 DLR-F6 [4] fuselage outline normalised by the fuselage diameter $\boldsymbol{D_f}$ and indicated fuselage length $\boldsymbol{L_f}$

Figure 3-2 shows the outline of the rear fuselage part with the definition of all other geometrical parameters. The chart dimensions are normalised by the fuselage diameter D_f. The coordinate system origin lies at the intersection point of the ordinate with the horizontal tangent on the lower part of the outline. γ is the positive angle between abscissa and the extension of the longest straight distance along the lower part of the fuselage symmetry outline. β is the positive angle between a straight line which intersects the ordinate at 0.5 and goes through the maximum X-value of the fuselage outline.

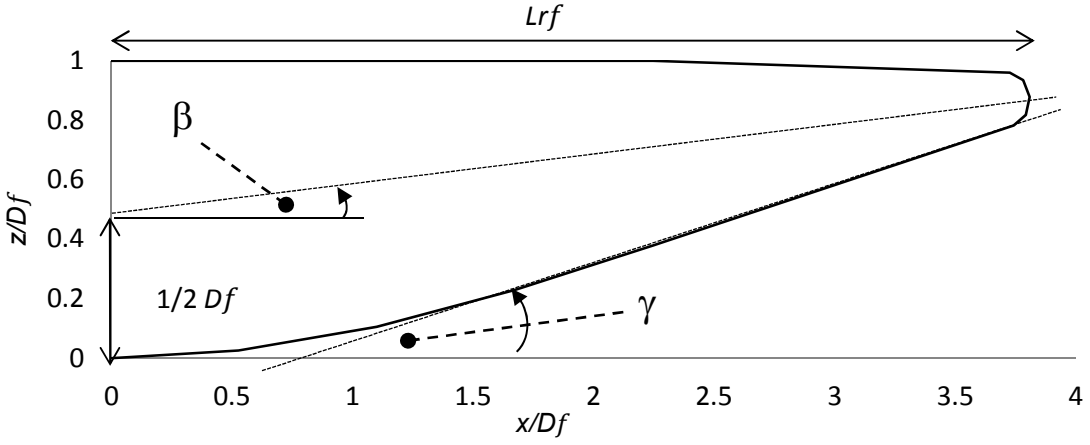

Figure 3-2 Definition of upsweep angle β and rear fuselage angle γ along with definition of fuselage diameter $\boldsymbol{D_f}$ and rear fuselage length $\boldsymbol{L_{rf}}$.

Table 3-1 presents the geometric parameters for the DLR-F6 [4] and the CRM [5] models in comparison with the A330 [54] geometry [39].

	Parameter	*A330*	*CRM*	*DLR*	$\frac{CRM}{A330}$	$\frac{DLR}{A330}$	$1-\frac{CRM}{A330}$	$1-\frac{DLR}{A330}$
1	D_f/L_f *[-]*	0.10	0.12	0.10	1.11	1.33	0.11	0.33
2	L_{rf}/D_f *[-]*	3.27	3.60	3.54	1.08	1.10	0.08	0.10
3	β *[°]*	7.00	3.20	5.70	0.46	0.81	0.54	0.19
4	γ *[°]*	18.00	13.00	15.0	0.72	0.83	0.28	0.17

Table 3-1 CRM [5] and DLR-F6 [4] geometric parameters in direct comparison to the A330 geometry [39] in model scale with ratios and differences Δ in absolute values

Row five and six contain non-dimensional values for the corresponding aircraft model relative to the absolute value of the A330 [54]. Row seven and eight contain the differences of the non-dimensional values relative to the A330 [54]. The data from row five and six is plotted in Figure 3-3.

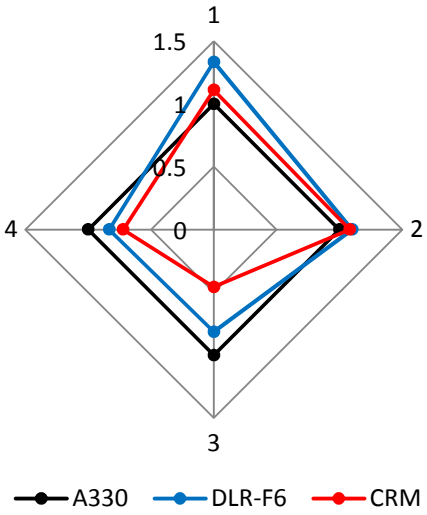

Figure 3-3 Polar plots for the ratios related to the A330 with circumferentially indicated parameter index 1 -4 from Table 3-1

The non-dimensional values CRM/A330 and DLR-F6/A330 in column five and six are plotted radially in comparison to the non-dimensional value of 1 for the A330 [54], while the parameter index 1 - 4 in row one is indicated circumferentially. It can be observed, that the blue line for the DLR-F6 [4] indicates good agreement with those of the A330 [54] except to parameter D_f/L_f, where the CRM is in better agreement. This parameter is related to the overall length of the fuselage. However, as the study focusses on the rear part of the fuselage the other parameters related to that part are considered as more important. In good agreement are the upsweep angle β and above all the rear fuselage angle γ. This angle is considered as the most important shape parameter, as it has the highest geometrical impact on the rear fuselage upwash, and therefore on a flow region where the hose is exposed. Figure 3-4 shows the differences relative to the A330 [54] in direct comparison. The differences for all parameters are higher for the CRM apart from parameter

$D_f/L_f$and L_{rf}/D_f, where the difference of L_{rf}/D_f(2) is 20%. Hence, the parameters indicating similarity to the A330 [54] outnumber those for the DLR-F6 [54]

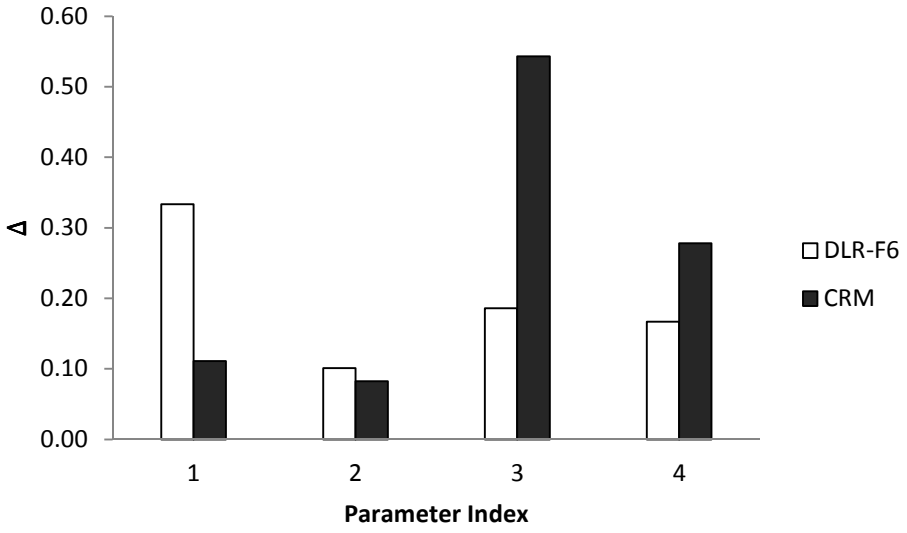

Figure 3-4 Differences in percentage of CRM and DLR-F6 relative to A330, data from Table 3-1 row seven and eight

A further distinction point is on the experimental conditions. The configurations and experimental range differ between the aircraft models. The experiments for the DLR-F6 [4] were carried out with a wing body (WB) configuration whereas for the CRM [5] there was both a WB and wing body tail (WBT) configuration (Figure 3-5). The operation conditions for the DLR-F6 range from a lift coefficient (Cl) of 0 to 0.68 and a maximum Mach number of 0.75 whereas for the CRM from 0 to 0.95 and a Mach number up to 0.87.

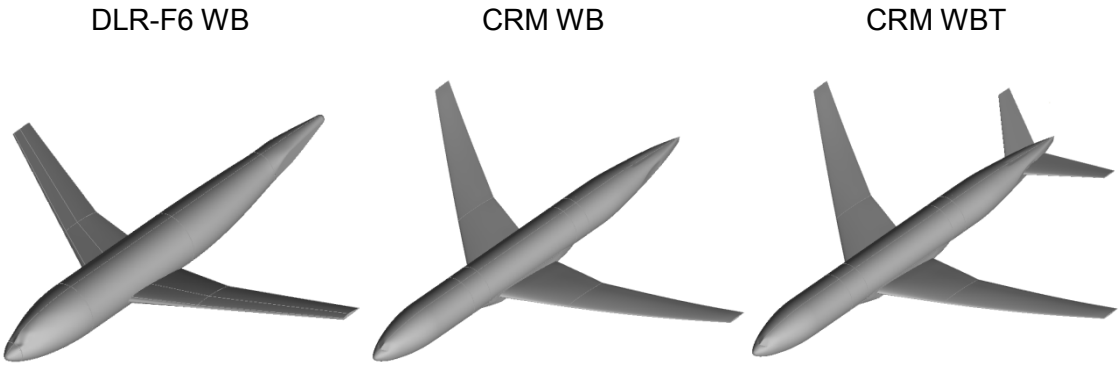

Figure 3-5 WB configuration of the DLR-F6, WB configuration of CRM and WBT configuration of CRM, from left to right

For the CFD approach evaluation both models are considered. In particular this means that for both models a CFD validation is performed. For the hose calculations also both models are considered. The influence of hose exit fairing (HEF) is also investigated in this work, but in conjunction with one aircraft geometry. For this purpose the DLR-F6 is taken into account, due to the rear fuselage similarity to the A330 [54].

3.1.2 Hose fairing modelling

The location on the fuselage where the hose is deployed is usually equipped with a fairing. The fairing is a cover for the hose trailing mechanism and slot for the drogue. Figure 3-6 shows a hose exit fairing (HEF) on an A330MRT [54].

Figure 3-6 Rear fuselage of A330 with mounted hose exit fairing [53]

The fairing is fitted onto the fuselage and projects into the airflow around the fuselage. Hence, the fairing is expected to have an influence on the wake field. The effects on the wake as well as on the hose are therefore of interest. In the present work this is investigated through the use of an arbitrary hose exit fairing in conjunction with the DLR-F6 [4]. Figure 3-7 shows the surface model of the designed HEF with indicated quantities length L_{hef}, width W_{hef} and height H_{hef}. In Table 3-2 the quantities are shown normalised by the DLR-F6 [4] fuselage diameter D_f. Figure 3-8 shows the attached hose fairing model onto the DLR-F6 [4] geometry.

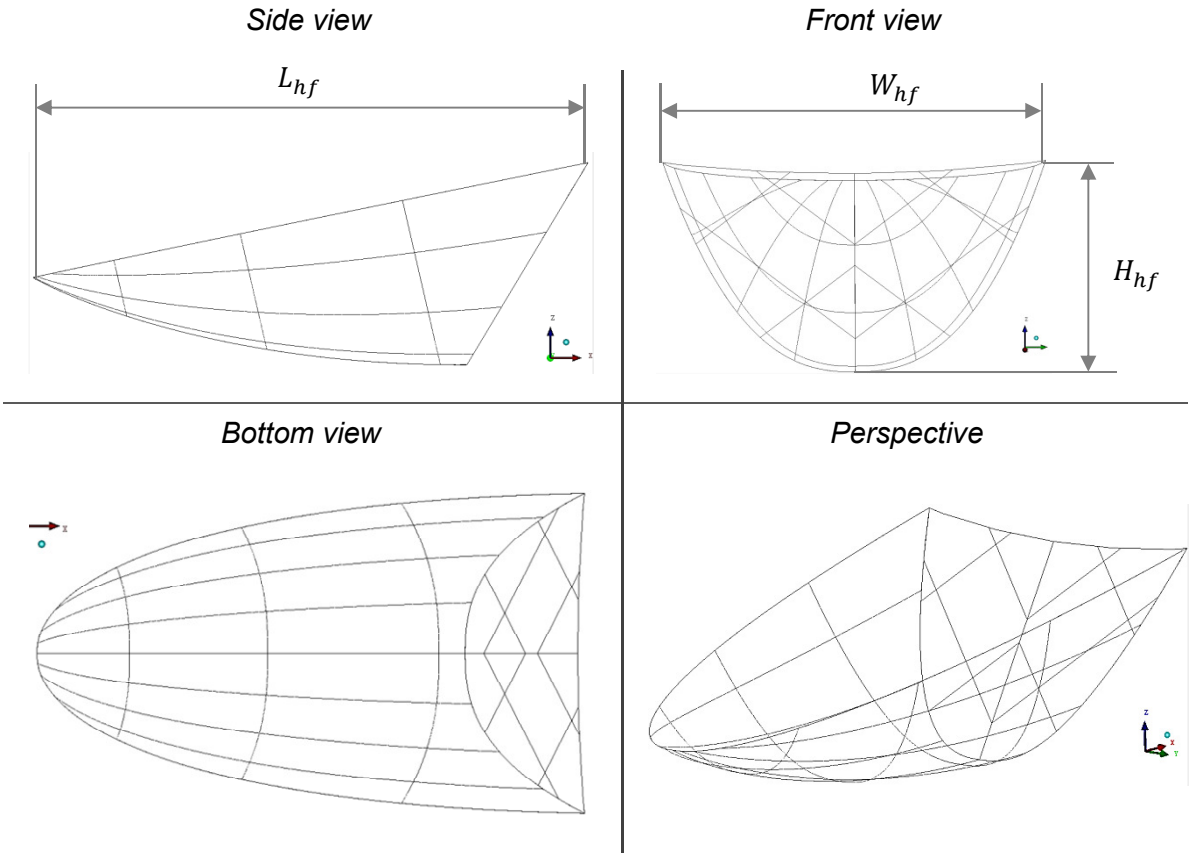

Figure 3-7 Surface model of an arbitrary hose exit faring

Parameter	Unit	Value
D_f	m	7.5
$\frac{L_{hf}}{D_f}$	-	0.18
$\frac{W_{hf}}{D_f}$	-	0.1
$\frac{W_{hf}}{D_f}$	-	0.06

Table 3-2 Hose exit fairing quantities normalised by DLR-F6 [4] fuselage diameter $\boldsymbol{D_f}$

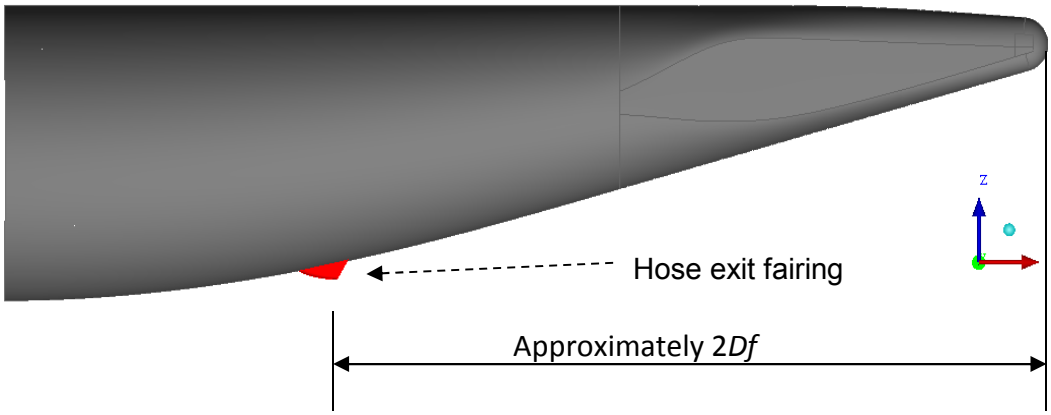

Figure 3-8 Side view of the DLR-F6 [4] CAD model with attached hose exit fairing

3.1.3 A400M substitute

A digital model for the transport aircraft body was not available; therefore, for the CFD simulations a new model has been built. The geometric information has been taken from Peake's report on his studies about upswept rear fuselages [14]. The drawings from the report are presented in Appendix B1. For the rear fuselage wake studies of the transport aircraft model five different upsweep angles are considered. Figure 3-9 shows all five models from lateral view with upsweep angle β from 0° to 20° in steps of 5°, as well as the fuselage diameter D_f and fuselage length L_f as a function of D_f.

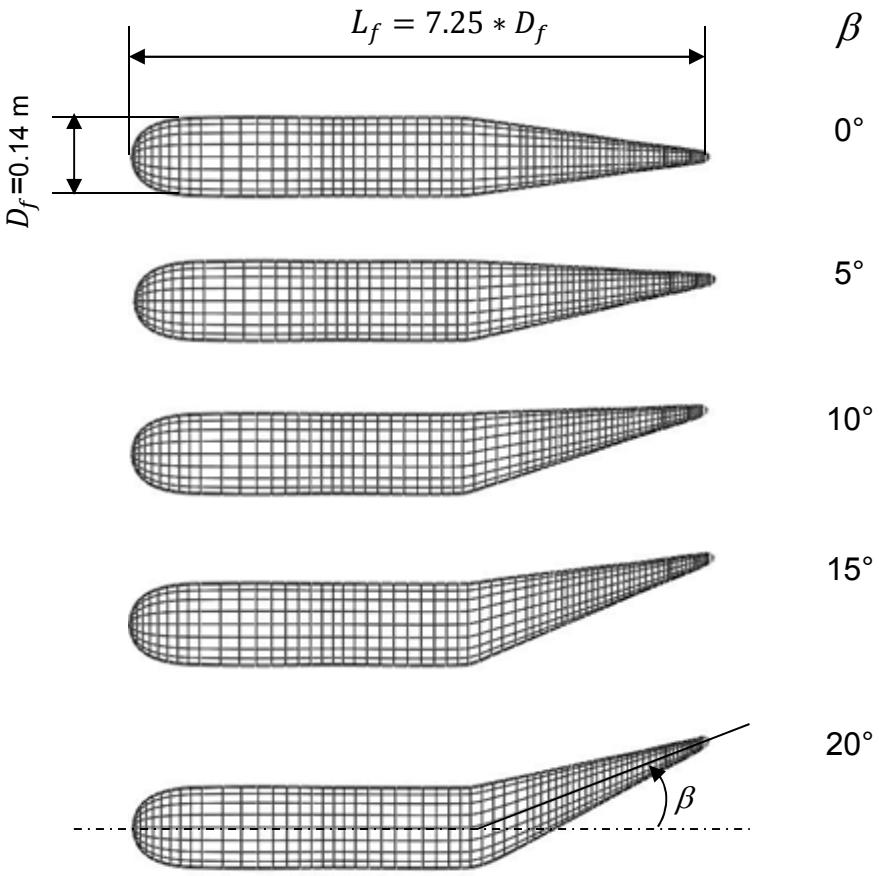

Figure 3-9 Transport aircraft model with upswept rear fuselage in 5° steps from 0° to 20°

3.2 Wake prediction

This chapter comprises a general introduction to computational fluid dynamics (CFD) as well as an overview on how the method was particularly used in this work. Furthermore it explains how the wake field is linked to the actual hose modelling.

3.2.1 CFD introduction

Computational fluid dynamics (CFD) means the calculation based modelling of fluid flow. Fluid flow is a highly complex physical process, which is fully described through the Navier Stokes equations. However, there are many approaches for fluid flow to be predicted. Some approaches deal with simplifications, which allow shorter calculation times but still provide sufficient validity for a specific application. The direct numerical simulation (DNS) solves the full Navier Stokes equations without any simplifications. However, this method is not suitable for industrially relevant engineering problems, as the computational costs are too high [61]. Instead the turbulence is simplified though the use of turbulence models. The need for turbulence models arises through the use of the Reynolds Averaged Navier Stokes method (RANS), which is a statistical approximation of the full Navier Stokes equation. The governing equations are time averaged and describe a mean flow. The approximation introduces a mathematical closure problem, associated with the Reynolds stress terms, which have to be determined. This is solved through the application of turbulence models.

3.2.1.1 Turbulence

There are different approaches to model turbulence. The classes of turbulence models are typically determined by the number of equations which describe the turbulence. For instance, there are one- and two equation models. A common model used in aerospace is the Spalart Almaras (SA) model which was specifically developed for aerodynamics applications [40]. The turbulence is modelled through the determination of turbulent viscosity. Two further commonly used models are the k-epsilon or the k-omega model [40] [41]. Both

are two equation models and describe turbulence through the consideration of turbulent energy and scale. Both have advantages and disadvantages. In particular the k-epsilon model works better in the free stream region whereas the k-omega is better close to the boundary. The Shear Stress Transport model (SST) combines k-epsilon and k-omega in order to benefit from the advantages they offer [40] [41]. For flows similar to those of the present study, both turbulence models, SST and SA, show good agreement with experimental results [62]. Hence, for the present study the SA model and the SST model have been applied.

3.2.2 CFD validation and approach

The credibility of any CFD result can be strengthened through an appropriate validation. Validation is defined as the process of determining the degree to which a model is an accurate representation of the real world from the perspective of the intended uses of the model [66]. This chapter introduces the process approach and the tools used for the CFD simulation.

3.2.2.1 Software

The CFD simulations are carried out with ANSYS CFX v12.1 [42], which is a well-established computational code in industry. CFX [42] originates from and was developed for turbo machinery applications. Today CFX [42] is also applied in many other industries like automotive and aerospace. CFX [42] uses the Reynolds Averaged Navier Stokes (RANS) equations for the flow solver. The software is very comprehensive as it offers a number of turbulent models, for compressible and incompressible turbulent flows as well as heat transfer.

3.2.2.2 Solver settings

The following solver settings were used for the CFD simulations

- Solver type: Segregated (SIMPLE algorithm)
- Linear system solver: ILU
- Ideal gas model for compressible flow as free stream Mach number > 0.3
- Discretisation order for p-mass and momentum: High resolution which corresponds to 2^{nd} Order (CFX [42] specific algorithm)
- Order turbulence: High resolution which corresponds to 2^{nd} Order (CFX [42] specific algorithm)

3.2.2.3 Convergence strategies and criterion

In numerical calculations convergence means the approach of the residual values to the value of 0. A numerical residual in turn represents the error which originates from the discretisation of the continuous equations. Thus, the smaller the residuals are the smaller is the error. The target of any convergence strategy is to obtain the smallest possible residual value. Residuals are closely

related to discretisation. For instance, one approach to get better convergence is to first solve the flow field with a 1^{st} order scheme discretisation. The solution for a 1^{st} order scheme is obtained linearly since the discretisation is only made up to 1^{st} order. Therefore, the solution converges much better. As a second step, the calculated flow field can be used as initial condition for the 2^{nd} order scheme which is non-linear and more valid results are obtained. It is also a suitable strategy to calculate the flow field first with a transient solver. A high resolution time stepping allows high pressure or velocity gradients within the flow domain to be solved. The obtained flow field can also be used as an initial condition for a further steady state calculation. The target residuals for 3D CFD applications are typically in the order of 10^{-4} and 10^{-5} depending on the complexity of the flow. Convergence strongly depends on the gradients within the domain. The higher the gradients the more difficult it is to obtain a converged solution. An illustrative example is the variation of the angle of attack (AOA) for an aircraft. With the same mesh at very high AOA, which can be regarded as off design points, the flow field is more complex compared to the flow obtained from lower AOA. Off design flow fields show higher pressure and velocity gradients than near design optimum flow fields. Hence, it is always more difficult to obtain convergence for off design flow fields, which in the case of an aircraft are caused through higher angles of attack.

The code development of commercial codes like Ansys CFX [42] involves major effort on convergence strategies. Therefore, one of the most outstanding features of CFX [42] is the convergence ability. For most cases in the current study the solution converged very quickly up to the order of 10^{-5}, which is the defined convergence criterion for mass and momentum. This was typically the case for AOA close to the design point of the aircraft. For AOA far away from the design point a criterion in the order of 10^{-4} has been accepted. Figure 3-10 illustrates the convergence history for a case with high angle of attack and it shows that convergence is obtained in the order of 10^{-4} after only 50 iterations. Hence, due to the convergence strategies implemented in CFX [42], the application of manual convergence strategies was not necessary. In addition to convergence of mass and momentum, both lift coefficient Cl and drag

coefficient Cd were considered as convergence criteria. Both are integral comparison parameters to the wind tunnel experiments and therefore relevant. For all calculations Cl and Cd have reached a consistent level of convergence.

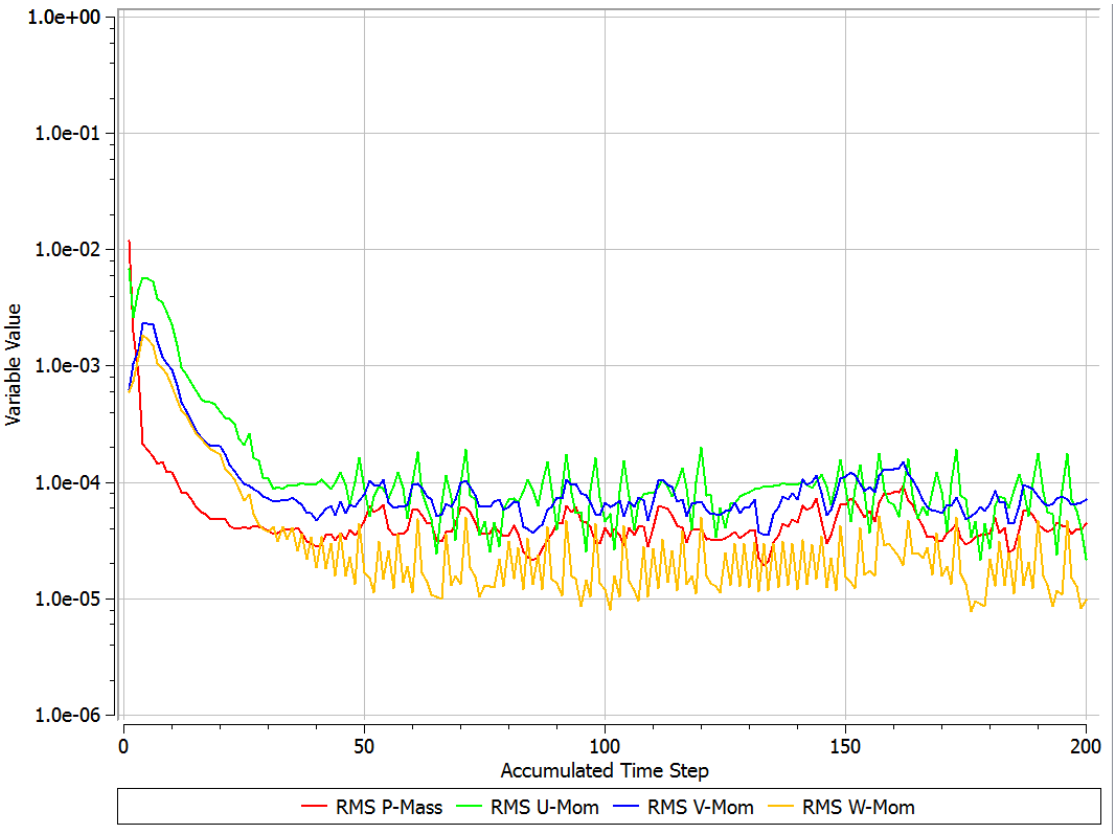

Figure 3-10 Mass and momentum residuals as a function of iterations for a solution in CFX [42]

3.2.2.4 Comparison parameters

The experimental data provided from DPW-2 [4] and DPW-4 [5] is forces and moments for the main aircraft. Hence, comparison parameters to the experiments are lift coefficient Cl and drag coefficient Cd, which are both a function of the angle of attack α (AOA). To obtain a target Cl, in a calculation α is varied until a nominal Cl value is met. The final AOA can be regarded as a calculation result. Thus, the computed correlation between α and Cl is also a comparison parameter to the experiments.

3.2.2.5 Mesh dependency study

Ideally, the target of any mesh dependency study is to find the coarsest possible mesh with the minimal induced numerical error due to insufficient mesh resolution. Therefore a number of meshes with different resolutions are made. A parameter which has to be a result of the calculation is plotted as a function of a mesh convergence index (GCI). The parameter value converges asymptotically to a constant value with increasing mesh resolution. The coarsest mesh which shows a convergence value very close to the asymptotic value would typically be chosen.

For the present work a mesh convergence study has been carried out for both the DLR-F6 [4] and CRM [5] model. As shown in Figure 3-11 three meshes with three different densities were considered for each model at model scale. The following approach proposed by Roache has been used [38]

$$C = \frac{E}{N^P} \qquad \text{Eq. (3-1)}$$

Where

- C is a convergence parameter (result of the calculation)
- E is the error
- N is the amount if mesh points
- P is an exponent which can be obtained considering the grid refinement ratio

C can be any result of the calculation. The experimental data provide Cd and Cl. Hence, the convergence study is made for Cd as the converging parameter at a constant Cl for a coarse, medium and fine mesh [38] as shown in Figure 3-11.

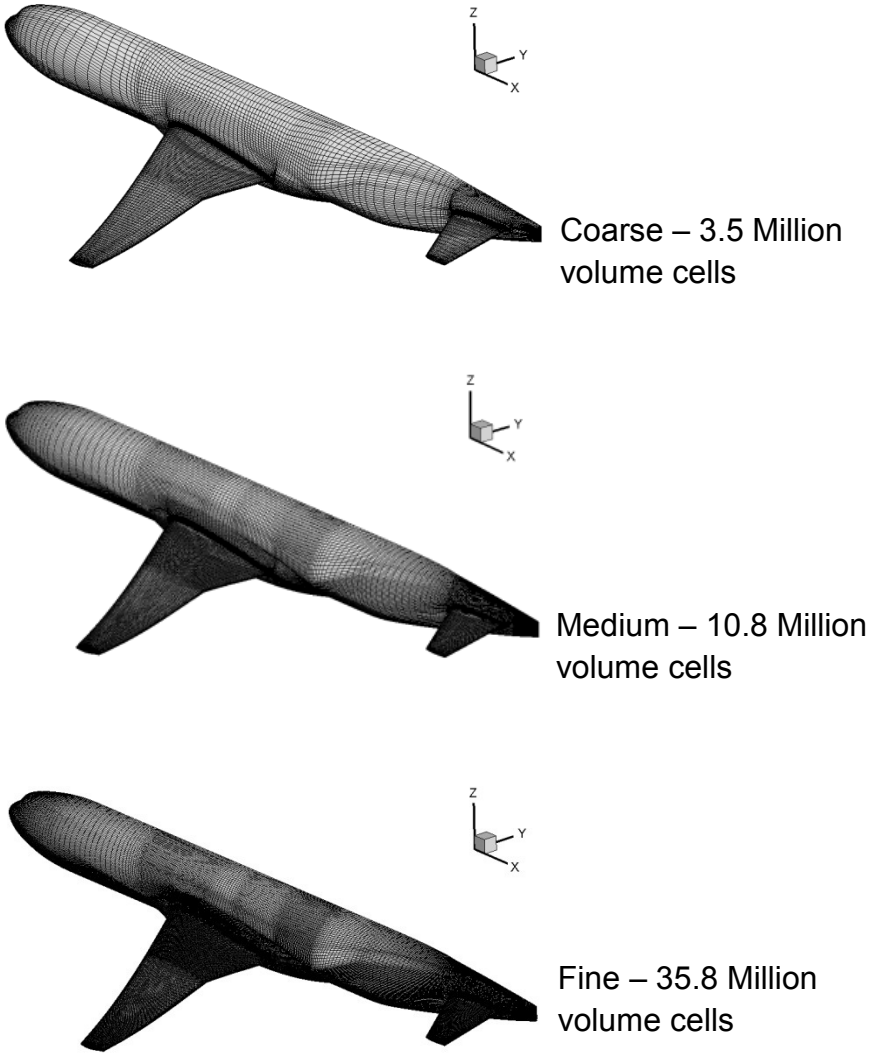

Figure 3-11 Surface meshes of CRM WBT with different mesh resolutions

3.2.2.6 Adaptive mesh refinement

For the transport aircraft body geometry (TAB) high gradients due to separation on the rear part of the fuselage are expected. Therefore, to keep the numerical error as low as possible, an adaptive mesh refinement (AMR) approach has been chosen. The principle of this approach is a local refinement of the initial mesh in dependence of an adaption criterion specified. The initial mesh is an unstructured tetra mesh, which has the advantage that no hanging nodes are produced. Figure 3-12 shows the principle of the AMR technology in CFX [42]. The mesh is not adapted to the geometry but in the free stream. This requires a good resolution of the initial surface mesh. To avoid a too high resolution of the free stream mesh a minimum cell edge length must be specified. This depends on the scale of the flow features that are expected and on the wanted resolution of the flow features.

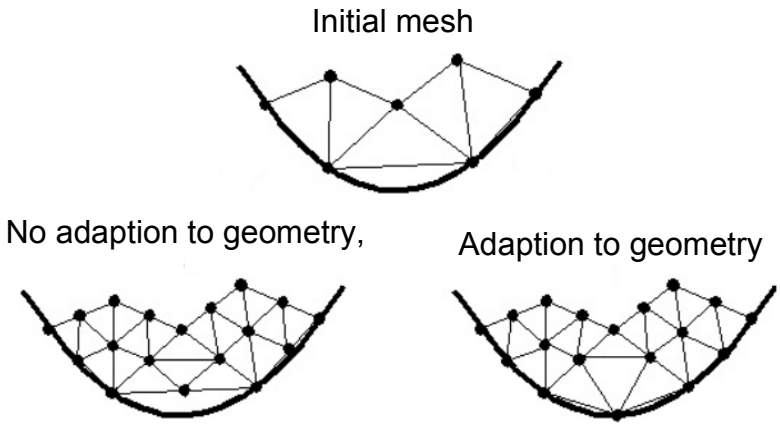

Figure 3-12 Initial mesh on the top and result after adaption on lower left side, which shows that only the volume mesh is considered for adaption.

Figure 3-13 shows the residual response on the adaption. A rapid increase of two orders of magnitude for the residuals can be observed after the adaption. A residual is basically a solution comparison between the latest two solutions. Therefore, the rapid increase originates from the difference between the solution on the old coarse mesh and the solution on the new fine mesh. The refinement result is illustrated in Figure 3-14 b), where the density for the refined mesh is much higher around the body as well as in the wake region where separation vortices are expected to develop. The illustrated density is

achieved after 3 refinement steps with vorticity as refinement criterion, through which the strength and direction of a vortex can be described. The mesh density in the wake region is not fine enough for an adequate resolution of the vortices. A finer initial volume mesh and more refinement steps were required for proper resolution. However, as the wake of the model shown is investigated qualitatively rather than quantitatively, the resulting mesh resolution is considered as a proper compromise between computational cost and numerical uncertainty.

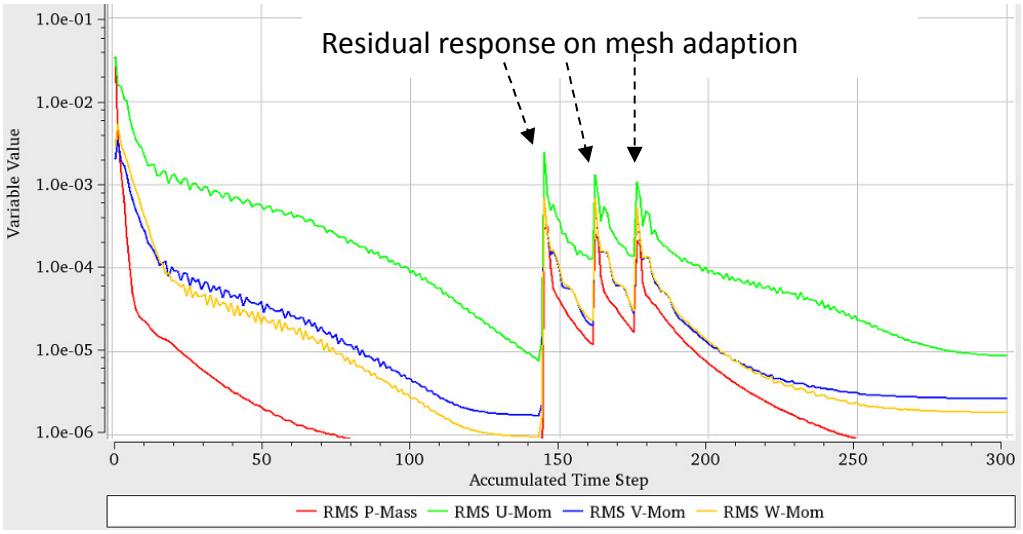

Figure 3-13 Residual peaks due to mesh adaption

a)

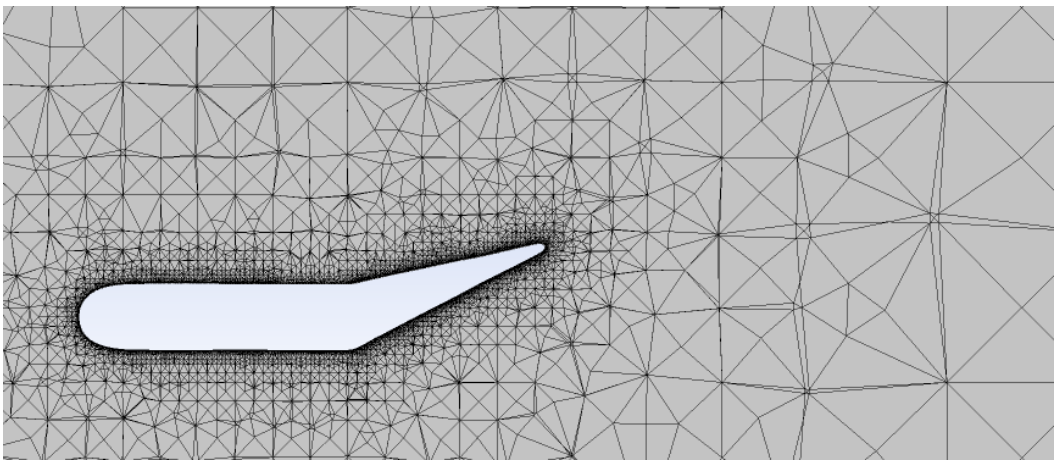

b)

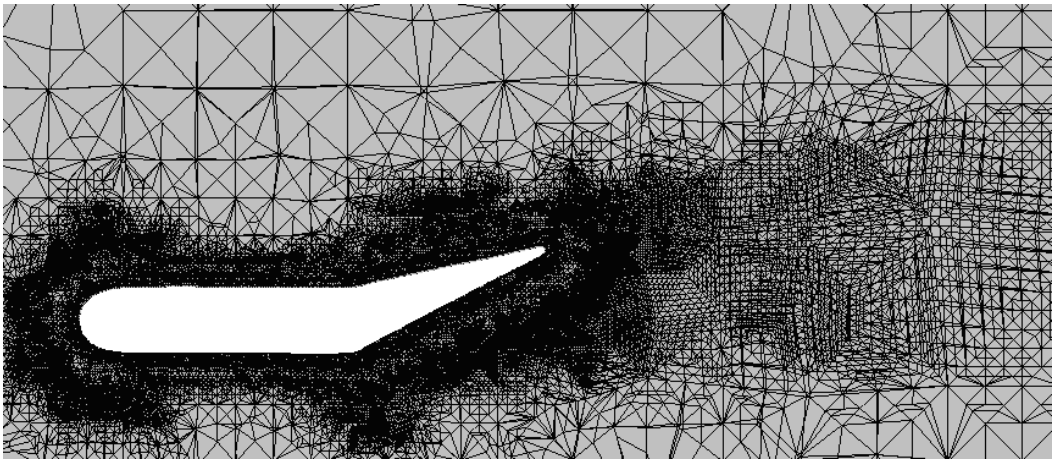

Figure 3-14 a) Initial unstructured mesh for the transport aircraft model [14] 20° upsweep configuration and b) the refined mesh after adaptive mesh refinement

3.2.2.7 Transition to full scale inflight refuelling conditions

The experiments were carried out at model scale, which means that the validation is made at model scale. However, the hose predictions are made at geometrical full scale as well as at full scale Reynolds number. Hence, a wake from a full scale model with full scale Reynolds number is required. The validation for the full scale inflight refuelling simulations has been made in three steps.

Step 1: CFD Validation at model scale at wind tunnel conditions → model scale Reynolds number

The Reynolds number (Re) as a dimensionless quantity is the determining magnitude for a fluid flow as it describes the ratio between inertial and viscous forces. The definition is

$$Re = \frac{\rho \cdot V_{\infty} . C_{ref}}{\mu} \qquad \text{Eq. (3-2)}$$

Where

- Re is the Reynolds Number [-]
- ρ is the density [kg/m^3]
- V is the velocity [m/s]
- C_{ref} is the chord [m] (reference length)
- μ is the dynamic viscosity [Pa*s]

The Reynolds number can be used to compare the flow similarity of different experimental cases. For example the difference between the cases can be the geometrical scale.

Step 2: CFD Validation at geometrical full scale at wind tunnel conditions by keeping the Reynolds number constant → still model scale Reynolds number

In the present case, the determining up-scaling parameter is given through the chord which is the reference length. To keep Re constant, the increased chord is compensated through a smaller density and therefore a higher operation pressure. To obtain the desired density, the pressure has to be changed accordingly.

$$\rho_{new} = \frac{Re \cdot \mu}{V \cdot C_{ref} \cdot scaling\ factor}$$

$$P_{new} = \left(\frac{Re \cdot \mu}{V \cdot C_{ref} \cdot scaling\ factor} \right) \cdot R \cdot T$$

Where

- P is the pressure
- R is the universal gas constant in J/kg*K
- T is the temperature in K

The density results according to the new operation pressure of the simulation. The decision to choose the density rather than the viscosity is based on the fact that both drag prediction workshop (DPW) experiments [4] [5] provide information about the temperature but not about the pressure. Viscosity is mainly affected by the temperature. Therefore, the clearly defined parameters are conserved. If the comparison parameters, Cd and the correlation between Cl and α in step 2 correlate with those from step 1, the validation of the geometrical full scale model can be considered as successful. This is the basis for the in-flight refuelling simulations at full scale because it shows that the results are reproducible also at full scale. This is crucial since the Reynolds number for the inflight refuelling simulations are much higher.

Step 3: CFD Validation at geometrical full scale at real inflight refuelling conditions → full scale Reynolds number

In case of a resultant deviation of the dimensionless comparison parameters Cl, Cd the scaling method of the model can be excluded as a cause. This would then typically lead to the assumption that the deviation of the dimensionless comparison parameters Cl, Cd is caused by Reynolds number effects.

3.2.3 Data extraction

In the present study the tow point of the towed cable system corresponds to the nominal hose exit (NHE), which is a predefined spatial position within the CFD computational domain (Figure 3-11). However, the hose modelling and prediction is not directly performed in real time with the CFD calculation. Instead there is a separate modelling for which the wake data of the CFD simulation is required. For the hose predictions a 3D section of the entire CFD domain is needed which can be regarded as a CFD sub-domain. The extents of the 3D sub-domain are defined as spatial distances relative to the nominal hose exit.

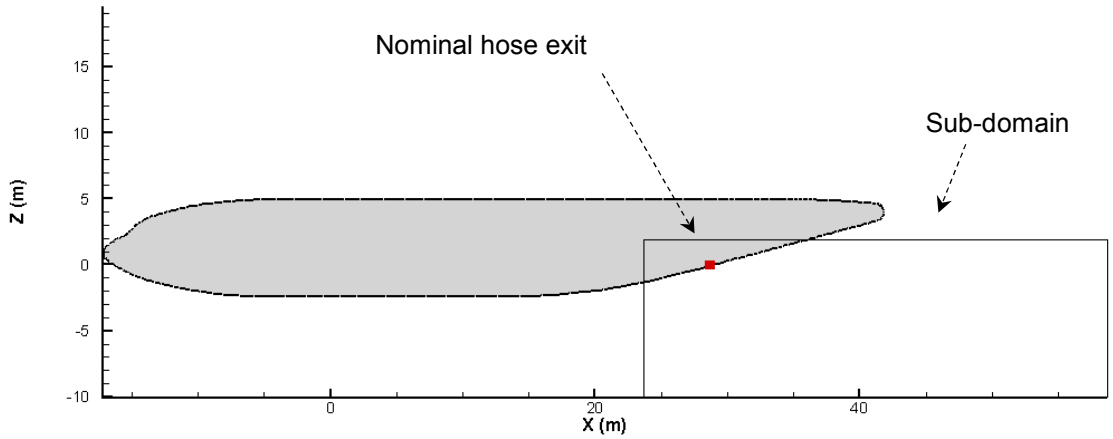

Figure 3-15 DLR-F6 [4] geometry within CFD domain with nominal hose exit and defined sub-domain

The wake data for the hose prediction consists of the velocity components V_x, V_y and V_z. Furthermore, the velocity components have to be addressed to the coordinates of an equidistant mesh. Therefore a 3D interpolation from the original CFD domain on an equidistant mesh is performed.

3.2.3.1 Procedure

1. Conversion of any CFD results file to CGNS format
2. Import the CGNS file to Tecplot [77]
3. Define a rectangular subdomain and generate an equidistant mesh within the subdomain
4. Perform a 3D interpolation from CGNS data set onto equidistant mesh
5. Write file with XYZ and V_x, V_y, V_z. values in ASCII format

3.3 Hose modelling

The theoretical basics for the hose model are derived from the Engineering Sciences Data Unit (ESDU), document number 80025 [6]. The document suggests a method for the estimation of mean forces induced by flow on cylindrical structures of circular cross sections [6]. This accounts to the aerodynamic forces. Along with gravitation these are the externally acting forces. The inner forces which originate from the hose elasticity are considered through the application of a bending moment Mb between the single beams. The beams in contrast are assumed to be rigid.

3.3.1 Applicability and limitations

The approach applies the laws which describe a uniform 2D flow around a circle (Figure 3-16).

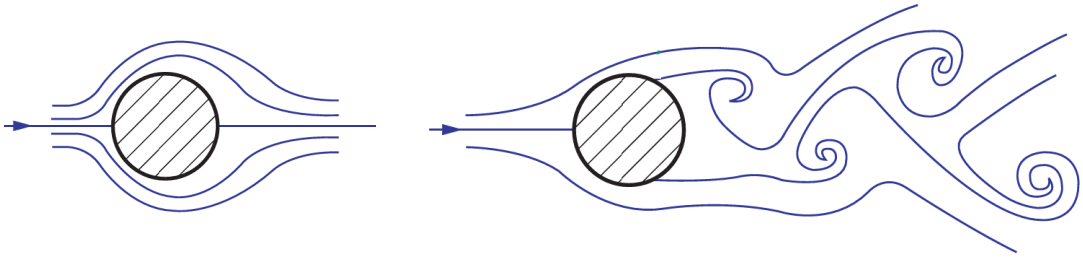

Figure 3-16 Attached flow around a circle left and laminar separation with Karman vortex street right [6]

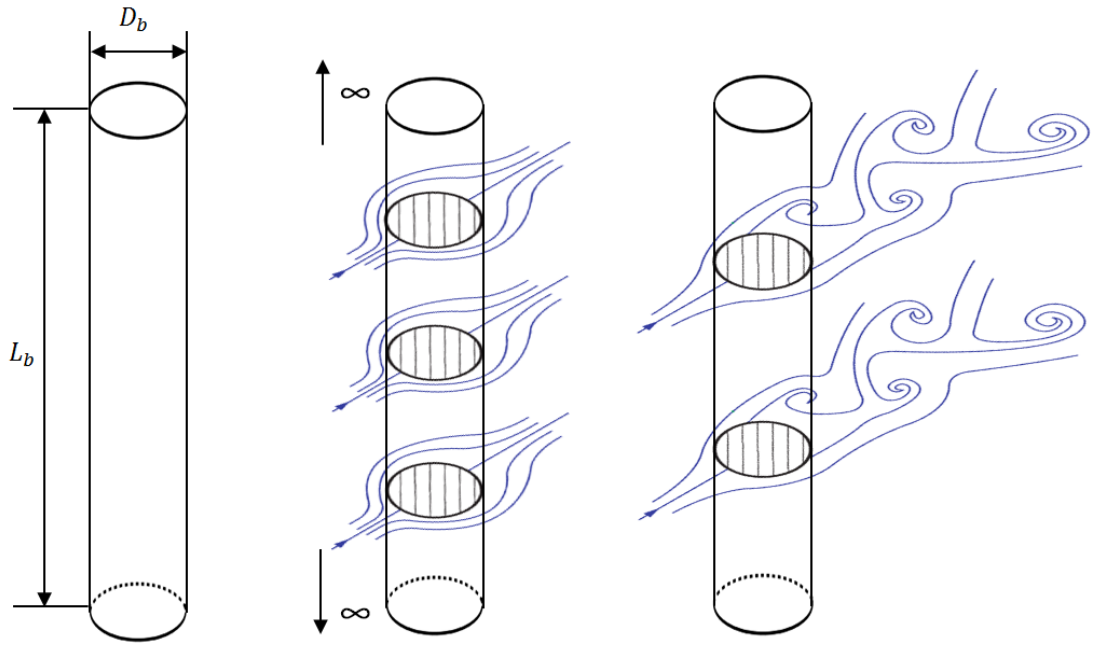

Figure 3-17 Beam with finite dimensions (left), attached 2D flow around a cylindrical beam of infinite length (middle) and laminar 2D separation with Karman vortex street around a cylindrical beam of infinite length (right) [6]

For an extruded circle (Figure 3-17), which represents a cylindrical beam and thus a 3D body, these conditions only apply if the beam length is long enough that the three dimensional flow around the ends of the beam can be neglected. This would typically be the case for an infinitely long beam where the impact of the tip flow on the resulting forces is much lower than the impact of the flow over the entire beam length. Furthermore it is stated that for finite beams the approach is still applicable in the presence of endplates at the ends of the beam if the beam length and diameter ratio L_b/D_b is greater than 6 [6]. As shown in Figure 3-18 the approach for the present work is the use of a joint connected beams array. Therefore, the tip flow problem disappears as the single bars are connected.

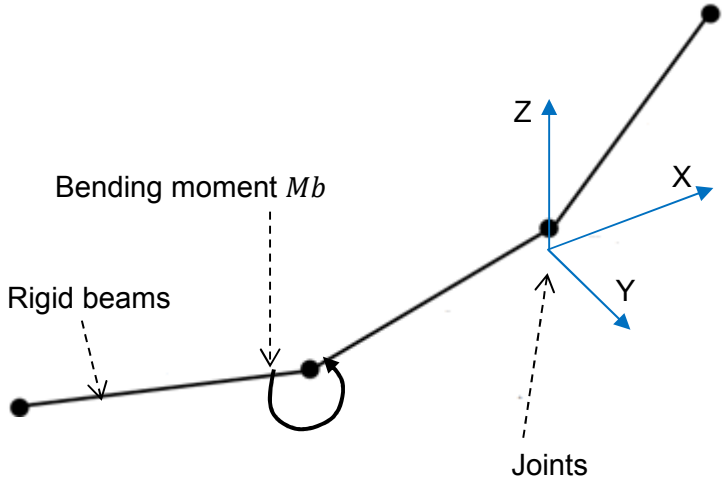

Figure 3-18 Joint connected rigid beams and imposed bending moment which accounts to the elasticity of the hose [26]

The outer forces on the hose which are the aerodynamic as well as the gravitational forces are calculated separately for every beam. Every single beam must satisfy the ratio restriction between the beam length L_b and the beam diameter D_b. The outer hose diameter corresponds to D_b and is given through the employed hose, as well as the overall length of the hose L_h. The number N_b of beams in which the overall hose length is subdivided determines the beam length L_b. Hence, with an appropriate segmentation of the entire hose it can be accounted to the ratio and therefore the 2D approach is applicable for the present work.

3.3.2 Drag modelling

The drag coefficient of a bluff body like a circular cylinder is primarily determined by the flow pattern around the body. In the present case the separation points determine the wake region behind the cylinder which in turn accounts for the drag. As shown in Figure 3-19 the location of the separation points is predominantly determined by the Reynolds number (Re), where the Re reference length is the cylinder diameter. However, the turbulence characteristics of the approaching flow and the cylinder surface roughness also have a significant impact on the separation point locations, as they affect the boundary layer [6].

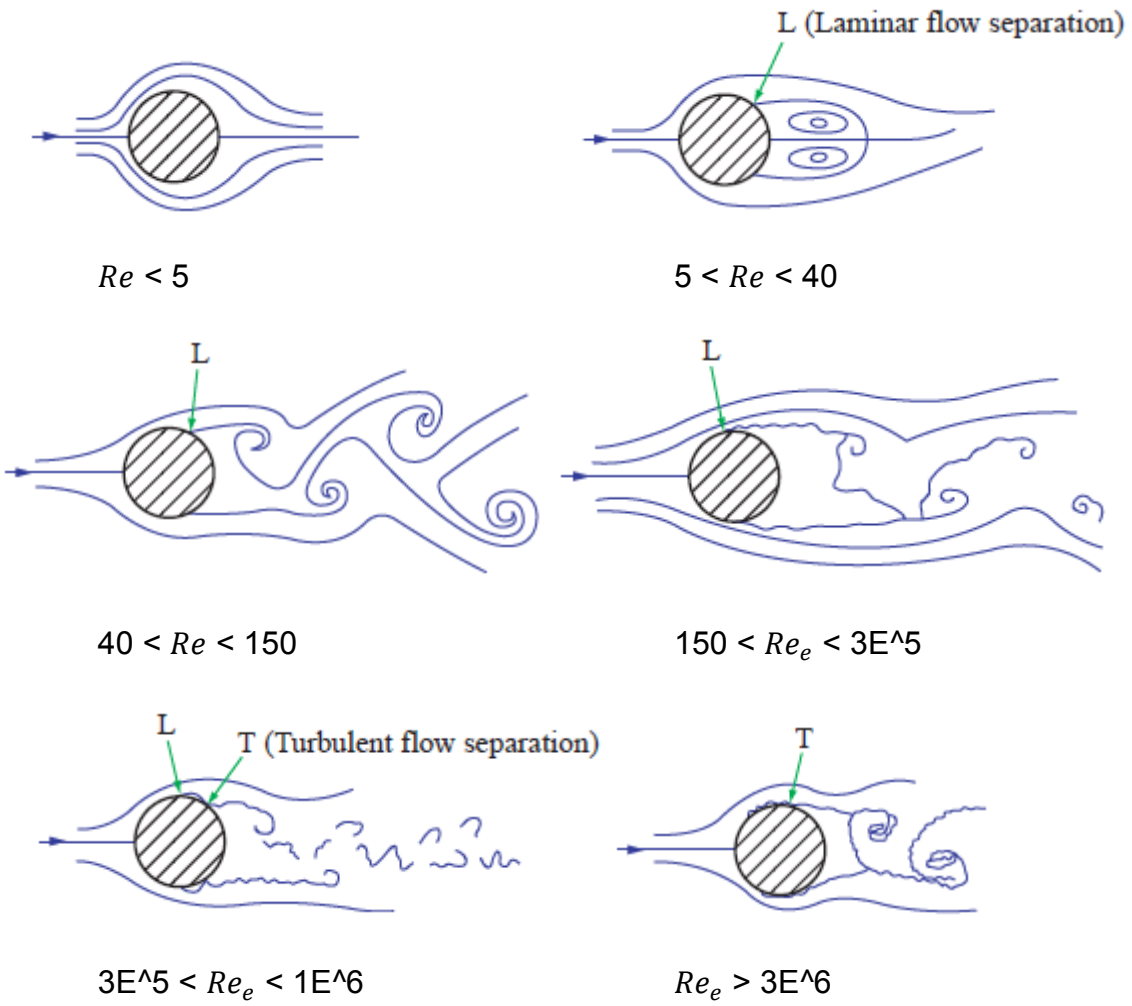

Figure 3-19 2D flow separation point locations on a circular geometry for different Revnolds numbers [6]

3.3.2.1 Surface roughness and approaching turbulence

The hose model takes into account the boundary layer effects on the drag coefficient. The higher the kinetic energy in the boundary layer, the more downstream the separation takes place. A turbulent boundary layer (BL) has more kinetic energy than a laminar BL. Hence, if the boundary layer is turbulent the separation point is shifted downstream and the drag decreases. At a critical Reynolds number Re_e the BL transitions from laminar to turbulent. This can be observed in Figure 3-19 bottom left, where the turbulent flow separation point indicated by a ”T” is more downstream than the laminar one indicated by an “L”. The transition can be initiated through small disturbances in the flow, for instance through irregularities on the surface as well as high turbulence intensity in the approaching flow. Hence, the critical Reynolds number is a function of the surface roughness and the free stream turbulence intensity [6]. Figure 3-20 shows how the drag force acts on a cylinder normal to the flow.

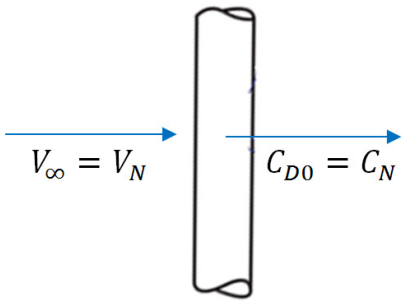

Figure 3-20 Cylinder normal to the flow with drag force coefficient [6]

Where

- V_∞ is the free stream velocity
- V_N is the velocity normal to the flow
- C_{D0} is the cylinder drag coefficient normal to the flow
- C_N is the cylinder drag coefficient normal to the cylinder

$$C_{D0} = f[Re_e, \frac{\varepsilon}{D_b}] \quad \text{Eq. (3-3)}$$

$$Re_e = \lambda_T \cdot \lambda_R \cdot Re \quad \text{Eq. (3-4)}$$

Where

- C_{D0} is the cylinder drag coefficient normal to the flow
- Re_e is the effective Reynolds number considering turbulence intensity and surface roughness
- λ_T the surface roughness parameter
- λ_R the turbulence intensity parameter
- ε is the effective roughness height of surface
- D_b is the cylinder diameter

Figure 3-21 shows C_{D0} dependent on the Reynolds number. It can be observed that the notable drop of C_{D0} for the rough surface takes place at a much lower Reynolds number (curve 2) than for the smooth surface. This is because the BL becomes turbulent earlier due to the rough surface. In the calculation this is considered by λ_R which is the ratio between $Re1/\ Re2$

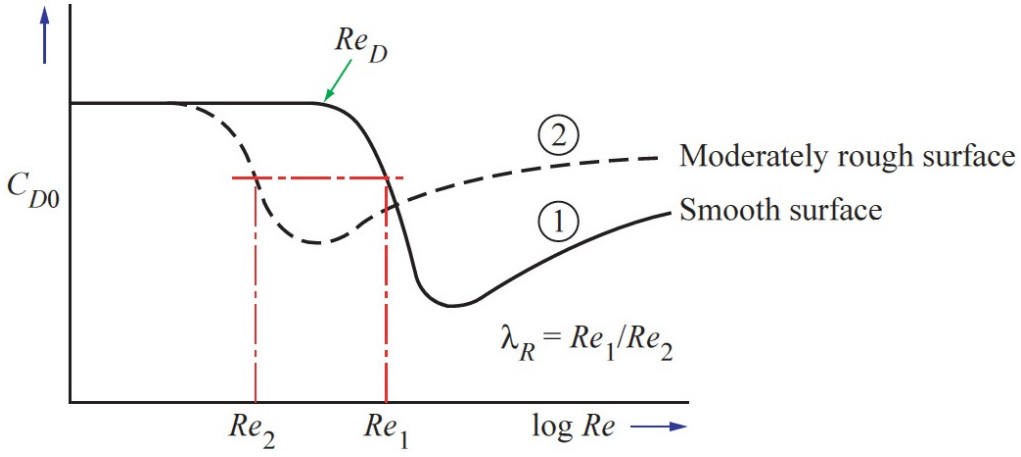

Figure 3-21 Drag coefficient as a function of Reynolds number for a cylinder normal to the flow and the influence of the surface roughness (dashed curve) on the drag coefficient [6]

The approaching turbulence has the same effect on the drag. Higher free stream turbulence intensity provokes a notably earlier transition of the laminar BL to a turbulent one. This can be seen in Fig 3-22 where the drop in C_{D0} takes place at a lower Reynolds number for a turbulent free stream (curve 2) compared to the free stream with lower turbulence.

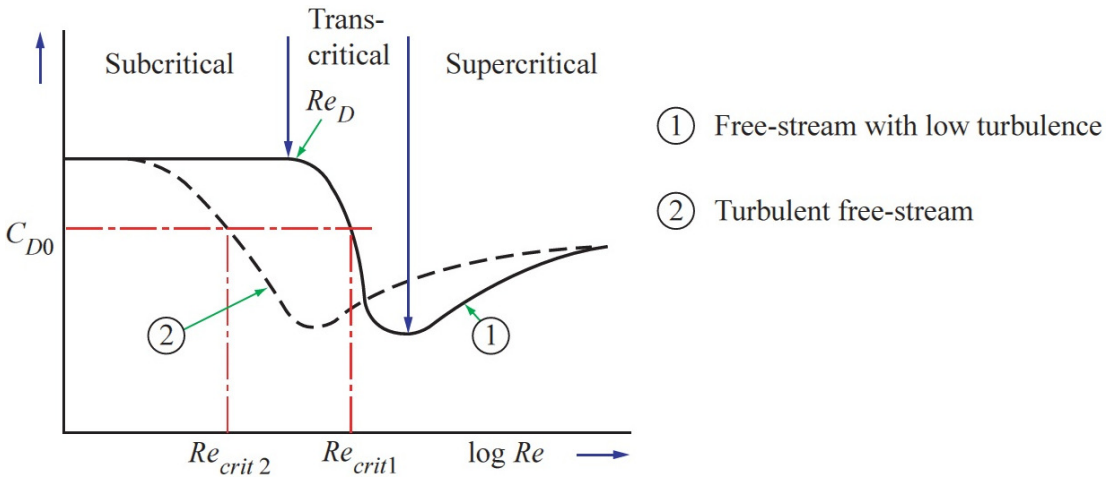

Figure 3-22 Drag coefficient C_{D0} as a function of Reynolds number for a cylinder normal to the flow and the influence of higher turbulence intensity (dashed curve) on C_{D0} [6]

The implemented model takes both effects into account. The critical Reynolds number Re_e is calculated based on both the given roughness as well as the estimated free stream turbulence which is computed. The value is compared to the free stream Reynolds number (Re). If the free stream Re number is equal or higher than Re_e the boundary layer is considered as turbulent and C_{D0} is lower. If the free stream Re number is smaller than Re_e the boundary layer is considered as laminar and C_{D0} is higher. In the calculation this is considered by λ_T which is the ratio between Re_e1/Re_e2.

3.3.2.2 Cylinder inclination

C_{D0} is the drag coefficient for a cylinder normal to the flow. The drag coefficient changes with the inclination of the cylinder. A distinction is made between sub- and supercritical Reynolds numbers [6].

Subcritical (Re_e< 3x10^5)

For subcritical Reynolds numbers experimental data show that the force coefficients are dependent on the component of free-stream velocity normal to the cylinder axis, *i.e.* on $V_N = V_\infty cos\phi$ and on the stream wise component of Reynolds number [6]. Thus, as shown in Figure 3-23 for inclined cylinders the normal force is given by

$$C_N = C_{D0} \cdot cos^2 \Phi \qquad \text{Eq. (3-5)}$$

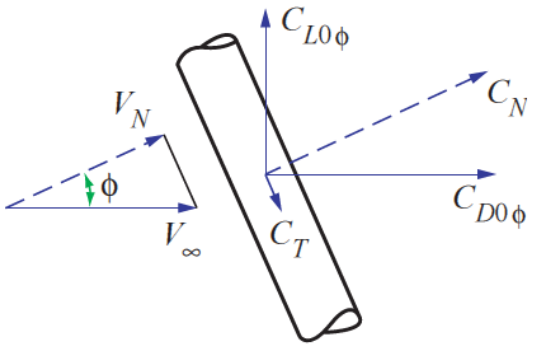

Figure 3-23 Inclined cylinder with acting force coefficients [6]

Where

- C_N is the drag force coefficient normal to the cylinder
- C_{D0} is the cylinder drag coefficient normal to the flow
- $C_{D0\Phi}$ is drag force coefficient in free stream direction and a function of the inclination angle Φ.
- $C_{L0\Phi}$ is lift force coefficient normal to free stream direction and a function of the inclination angle Φ.
- Φ is the inclination angle between the free stream velocity V_∞ and the velocity component normal to the cylinder V_N

Supercritical (Re_e> 3x10^5)

With the use of the simple cross-flow theory for supercritical Reynolds numbers C_N tends to be underestimated [6]. The reason for this is that while the laminar boundary layer (and the associated pressure distribution) tends to depend only on the cross-flow velocity, when the transition to turbulent flow in the boundary layer has occurred the subsequent development and separation of the boundary layer are adversely affected by the three dimensional nature of the turbulent wake flow. This exerts a considerable influence on the pressure distribution and increases the flow-induced forces over those predicted using simple cross-flow theory [6]. Hence, the tangential force can be ignored.

The force coefficients are estimated as follows

$$C_N = C_{D0} \cdot f_\Phi \qquad \text{Eq. (3-6)}$$

$$C_{D0\Phi} = C_N \cdot cos\Phi \qquad \text{Eq. (3-7)}$$

$$C_{L0\Phi} = C_N \cdot sin\Phi \qquad \text{Eq. (3-8)}$$

Where f_Φ is given by a function like that shown in Figure 3-24.

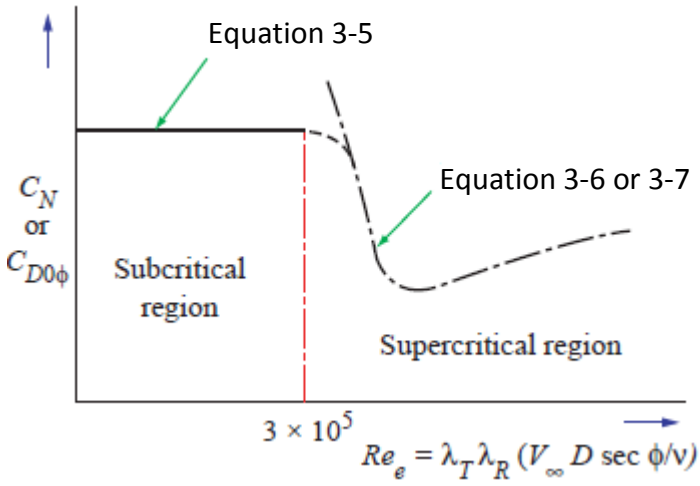

Figure 3-24 Drag coefficients C_N or $C_{D0\Phi}$ as a function of Reynolds number for a cylinder normal or inclined to the flow [6]

3.4 Drogue modelling

The drogue is modelled as a conical body with a specified cone length L_d and cone diameter D_d. Figure 3-25 shows the cone normal to the free stream flow V_∞ and the resulting direction of the cone drag force coefficient C_{D0d}.

a)

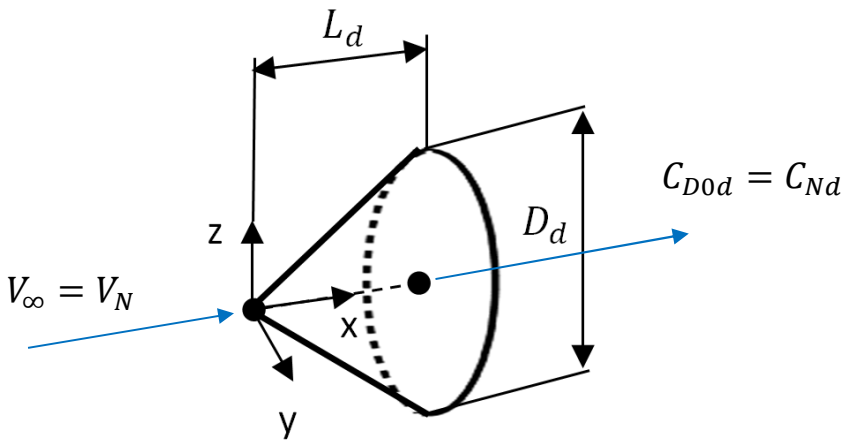

b)

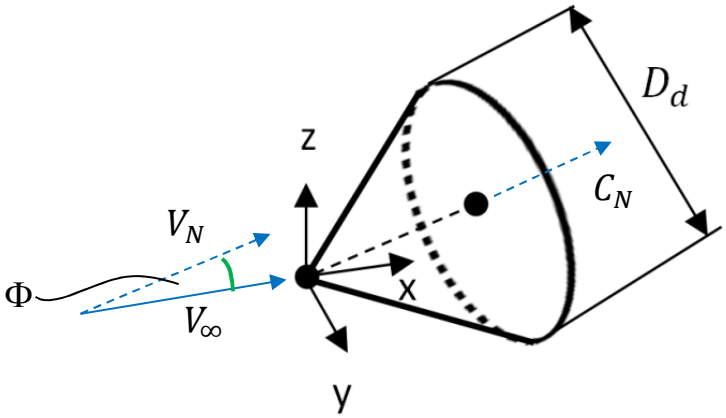

Figure 3-25 a) Cone normal to flow and b) cone inclined to flow

The magnitude of the drag force coefficient C_{D0d} is assumed to be constant both for the cone normal to the flow and for the inclined cone. The drag force F_d is calculated as follows

$$F_d = C_{Nd} \cdot \frac{1}{2} \cdot \rho \cdot {V_N}^2 \cdot A_d \quad \text{Eq. (3-9)}$$

$$A_d = \frac{{D_d}^2 \pi}{4} \quad \text{Eq. (3-10)}$$

Where

- C_{Nd} is the normal drag force coefficient of the drogue
- ρ is the density, which is assumed to be constant
- V_N is the velocity normal to the cone and a function of free stream velocity V_∞ and cone inclination angle Φ
- Φ is the inclination angle between the free stream velocity V_∞ and the velocity component normal to the cone V_N
- A_d is the reference area for the calculation of F_d

3.5 Hose model implementation in MATLAB

The basic code was inherited from Bristol University and written with the high-level programming language of MATLAB [75]. The capability of the code was limited to the static hose shape simulation based on a 3D Rankine body flow pattern. The flow field is generated within the code and in real time with the calculation of the static hose shape. However, the current work requires the static hose shape to be calculated based on the near field wake of two different aircraft models and not in real time. Hence, the code's capabilities were required to be extended for static hose shape simulations based on a generic external flow field. An interface between the aircraft wake data and the hose model has been implemented which allows the generic wake data to be processed.

3.5.1 Flow field interface

The wake flow field extracted from the CFD domain is available for the program as an ASCII file which contains the X Y Z space coordinates with index i j k and the corresponding velocity components V_x, V_y, V_z. Hence the file consists of six rows and n columns where n is the product of i j k and thus the number of cells of the equidistant mesh. For a faster processing the ASCII file is converted into

a binary file with the extension .mat. The local flow field velocities are determined through a 3D interpolation. The interpolation is performed by a function implemented in MATLAB termed `interp3`. The hose predictions have been carried out with MATLAB version R2012a [67].

3.5.2 Convergence strategies

The dependent variables for the spatial position prediction of the hose are solved explicitly. The hose predictions are all carried out steady state. Therefore, a pseudo time stepping with an artificial time step is required. However, the time step does not represent the real behaviour of the physical problem. Hence, the determination of the required time step is not based on the expected motion of the hose over time. Instead the time stepping has to be chosen in dependence of nodal points along the hose, which corresponds to a discretisation in space. The relationship between the number of nodal points and the required time step is inversely proportional - the more nodal points along the hose the smaller the required time step. Figure 3-26 shows on the left side the initial condition for the hose position as a horizontally arranged array. On the right side the final solution is shown where all attacking forces are in equilibrium.

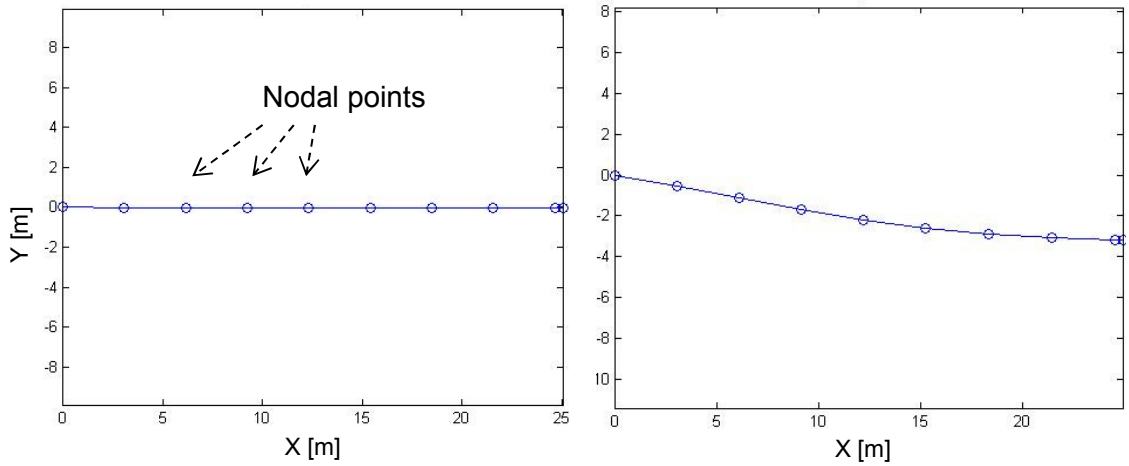

Figure 3-26 Arbitrary example of an initial condition for hose position with 10 nodal points (left) and final static hose position on the right

The new position of every nodal point is calculated iteratively until equilibrium is obtained between the acting aerodynamic and gravitational forces. This is the equilibrium of forces and moments and thus the steady state hose shape as shown in Figure 3-26 on the right.

3.6 Determination of hose characteristics

The hose characteristics are defined through the static hose shape and the spatial drogue position. The static hose shape is important for the dynamic response to perturbations associated to the hose-probe engagement [73] [74]. The spatial drogue position is important for design purposes, as the drogue must fulfil a specific catenary requirement.

3.6.1 Definition of hose shape

The result of a hose calculation is the spatial position of 10 nodal points in X, Y and Z. The number of nodes is inversely proportional to the artificial time step used in the calculation. Hence, the more nodal points used the smaller the required time step becomes and the solution takes longer to converge. A sensitivity study on how the number of nodal points affects the result of the static hose characteristics has been conducted, as well as the effect of the subdomain discretisation and the associated 3D interpolation from the CFD domain onto the subdomain. For the current hose length of approximately 30 m the amount of 10 nodal points with equidistant subdomain spacing of 0.25m has been assessed as a reasonable compromise between calculation effort and discretisation error. However, for an accurate analysis of a possible inflection point the hose is approximated by a polynomial function. Although the hose results are available for a 3D Cartesian coordinate system, as shown in Figure 3-27, the post processing is always made in a 2D Cartesian coordinate system on the XZ and the XY planes.

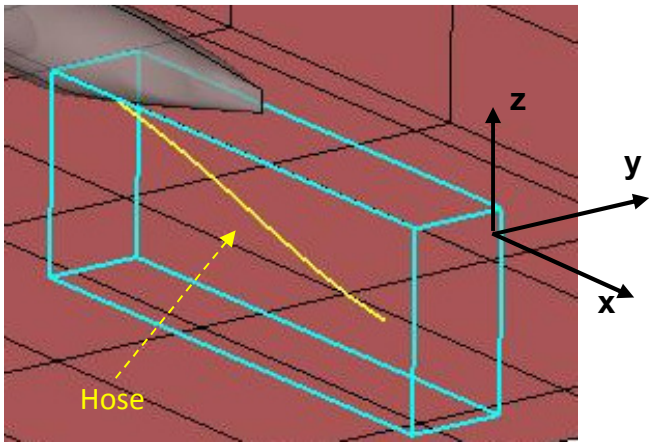

Figure 3-27 Hose result with definition of coordinate system

The polynomial function is of degree 4 and satisfies the course of the 10 nodal points in the 2D planes with a minimum least square error of R^2=0.997. The inflection point is then determined through the evaluation of the 2nd derivation. The derivation is set to zero through which the value of the abscissa can be obtained where the inflection point takes place. The inflection point position along the ordinate is the function value of the original curve evaluated with the ordinate value for the inflection point. An example of the procedure is explained as follows:

1. Determine a polynomial function f(x) of degree 4 to approximate the hose shape as shown in Figure 3-28 the red line
2. Perform two derivations f'(x), f''(x) for f(x)
3. Evaluate x for f''(x)=0 and obtain x1 and x2
4. Evaluate y1 for f(x1) and y2 for f(x2)

The value pairs x1,y1 and x2,y2 obtained from this procedure are the positions of the inflection points along the hose, which is illustrated in Figure 3-28 with the black circle.

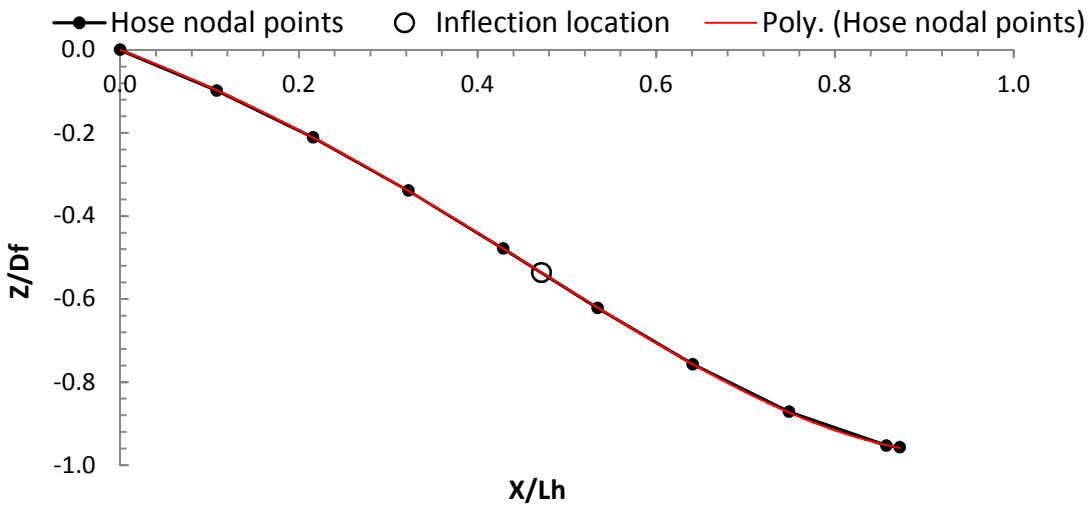

Figure 3-28 Arbitrary example of a calculated hose shape defined by 10 nodal points (black dots) approximated through a polynomial function of degree 4 (red line) and the calculated inflection point position (black circle)

3.6.2 Definition of spatial drogue position

The second evaluation parameter for the hose characteristics is whether the final static drogue position satisfies Cobham's refuelling systems catenary requirement. The catenary requirement is defined as the vertical spatial range within which the drogue must be positioned at fully trailed hose as listed in Table 3-3.

Parameter	Unit	Value
Upper limit relative to hose exit	feet	5
Lower limit relative to hose exit	feet	25

Table 3-3 Catenary requirement defined through an upper and lower vertical spatial limit

The requirement is graphically considered through two horizontal dashed lines which indicate the upper and the lower limit of the vertical spatial hose range SDR_z as can be observed in Figure 3-29. The values are normalised by the the fuselage diameter D_f.

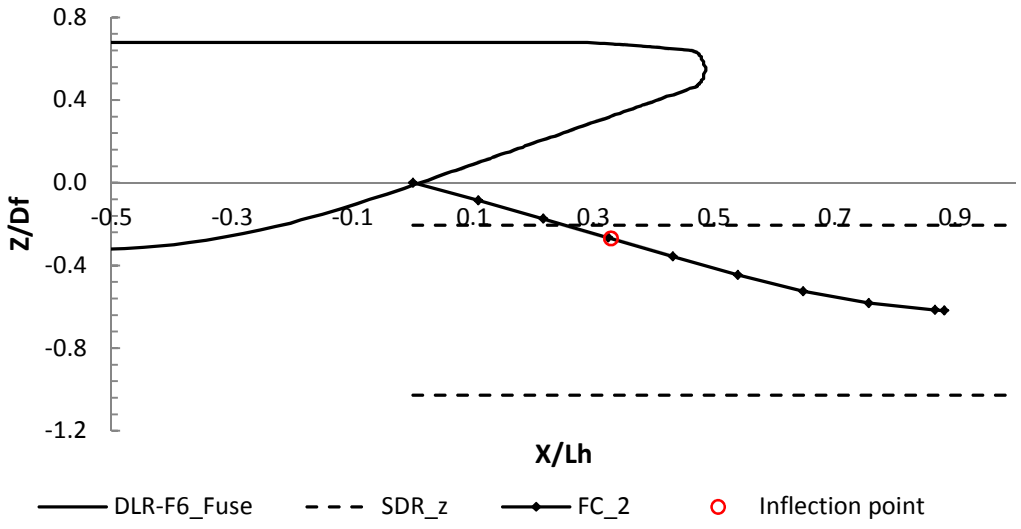

Figure 3-29 Arbitrary example of a calculated hose shape (black dots) and the dashed lines which indicate the upper and lower limit of the vertical spatial drogue range SDR_z

3.6.3 Summary

The methods used for the in-flight refuelling simulations are computational fluid dynamics (CFD) for the wake prediction and a finite segment model for the hose calculations. The wake and hose prediction are not made in real time. Hence, the wake is first computed and is then used as an input for the hose calculations. The post processed result of a hose calculation within the CFD domain is presented in Figure 3-30 as a yellow line along with the blue lined subdomain.

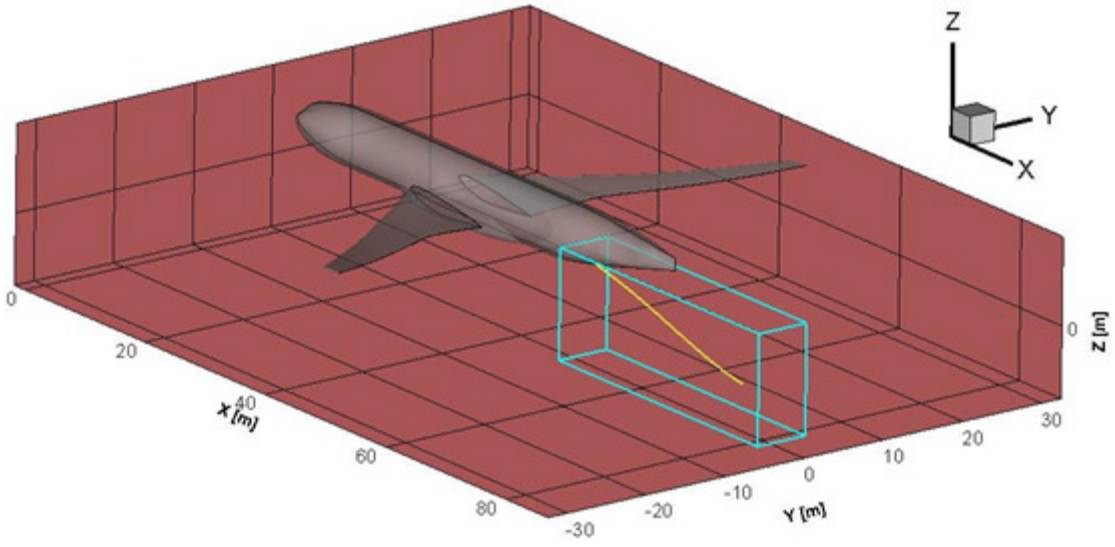

Figure 3-30 Calculated hose shape (yellow curve) included into the CFD domain of the CRM [5] WB configuration and the CFD sub-domain indicated in bright blue

Two different full aircraft models similar to modern civil aircraft were used as A330 [54] substitutes. These are the common research model (CRM) wing body and wing body tail configuration from drag prediction workshop 4 (DPW-4) [5] and the DLR-F6 wing body configuration from DPW-2 [4]. Experimental data from the public domain is available for both aircraft models. The data is used for the CFD validation. To study the impact of the hose exit fairing on the flow field and on the hose the DLR-F6 aircraft has been equipped with an arbitrary hose exit fairing. Furthermore, a fuselage only geometric model has been built up for the wake prediction of a typical transport aircraft with different upsweep angles. These simulations are validated with wind tunnel experiments, where forces and moments as well as circumferential pressure distributions are available. The

wake characteristics are analysed qualitatively. Hose characteristics with this geometry were not determined.

4 NUMERICAL RESULTS

This chapter contains numerical results obtained both from the CFD simulations and the hose characteristics calculations. This comprises the validation of the CFD model at model scale and at full scale, the analysis of the wake characteristics of the A330 [54] and A400M substitutes, as well as the in-flight refuelling simulations with hose predictions.

4.1 CFD validation

The results of the CFD validation for all aircraft models used are presented. These are both full aircraft models - the DLR-F6 [4] and the CRM [5] as well as the fuselage only transport aircraft model TAB [14]. For the full aircraft models the results of the mesh convergence study is presented as well as the results of a turbulence model study.

4.1.1 DLR-F6 aircraft geometry

The DLR-F6 aircraft model was used for the 2nd drag prediction workshop DPW-2 [4]. The experiments were carried out in a transonic wind tunnel at model scale. The model reference quantities and a sketch of the wind tunnel circuit are presented in chapter 2.1.1.

Parameter	Unit	Input	Calculated	Calculation method
Re	-	3e^06		
Ma	-	0.75		
T_{ref}	K	305		
C_{ref}	in	5.56		
C_{ref}	m		0.1412	Conversion
P_{ref}	Pa		134`238	Ideal Gas Law
η	kg/m*s		1.8951e-05	Sutherland
ρ	kg/m^3		1.5335	
c	m/s		350.1	
V_∞	m/s		262.6	

Table 4-1 Wind tunnel experimental conditions with original input data and calculated data, including the calculation method for the DLR-F6 aircraft model [4]

Table 4-1 contains the wind tunnel experimental parameters. The values termed input in row three stem from the AIAA DPW-2 internet site [4] and provide the basis for the CFD simulations at wind tunnel conditions. The calculated values in row four derive from the input values through a specific method, which is listed in row five - the calculation method. The simulations for the DLR-F6 [4] were carried out in a rectangular CFD domain as shown in Figure 4-1. The extents specified through height H width W and length L are normalised by the wingspan W_S. For the simulation of infinite free stream conditions the boundaries must be placed far enough from the aircraft. This requirement is considered through the extent of 17 times the wingspan in Z and Y direction and 40 times in X direction.

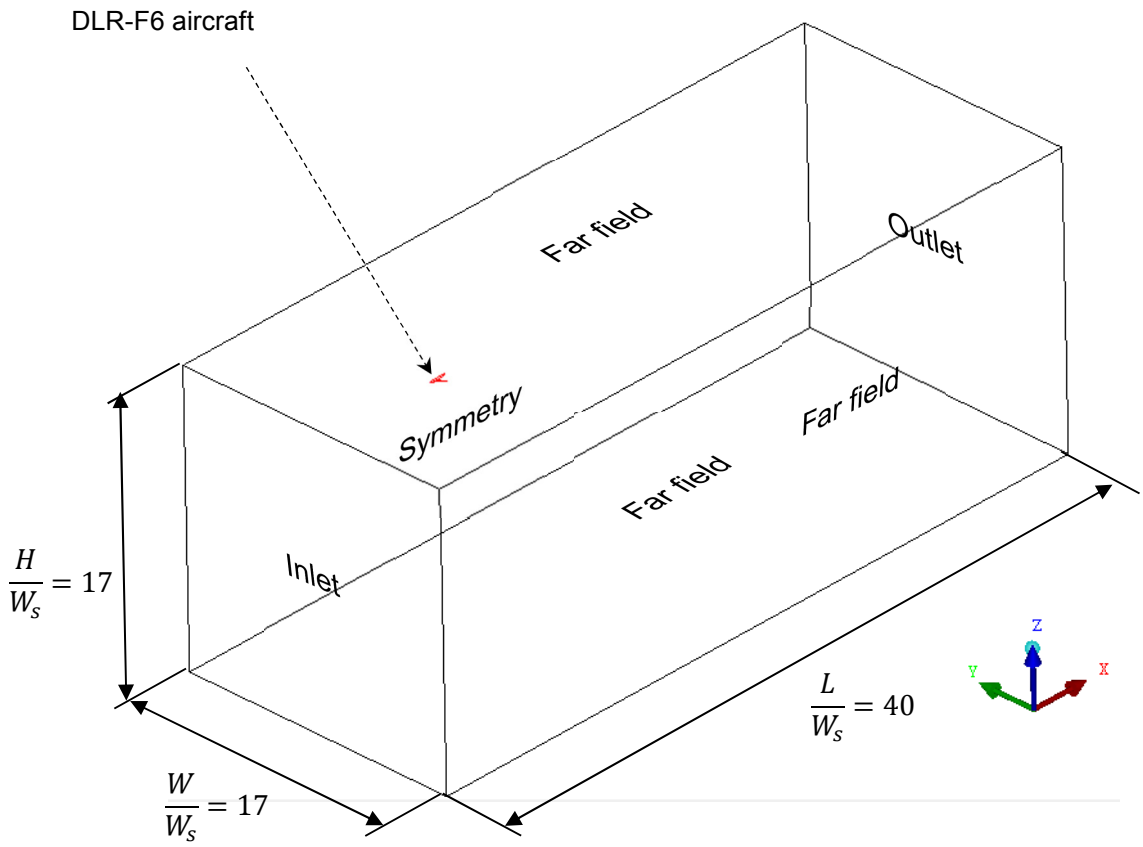

Figure 4-1 Rectangular CFD domain with DLR-F6 geometry and extensions normalised by wingspan $\boldsymbol{W_s}$

		Inlet	Outlet	Far Field	Symmetry	Aircraft
CFX-Term		Inlet	Outlet	Opening	Symmetry	Wall
Type		1st Type	1st Type	Mixed	2nd Type	1st Type
Type-Name		Dirichlet	Dirichlet		Neumann	Dirichlet
V_∞	m/s	262.6	calculated	calculated	calculated	0
P_{stat}	Pa	calculated	134`238	134`238	calculated	calculated
T_{stat}	K	305	305	calculated	calculated	305

Table 4-2 Boundary names, conditions and types DPW-2 experiments with DLR-F6 WB geometry [4]

The CFD domain has seven boundary patches from which one is specified as the inlet, one is specified as the outlet, three as far field, one as symmetry and one as aircraft. The corresponding boundary types along with magnitudes are specified in Table 4-2. The inlet is a boundary of type Dirichlet. Fixed magnitudes are velocity and temperature. The direction of the velocity vector corresponds to the angle of attack. The outlet is also a Dirichlet boundary type. The pressure is set to a relative value of zero. At the far field boundary condition velocity and pressure is calculated according to the internal flow field. It allows infinite free stream conditions to be simulated. The symmetry boundary condition allows a half domain calculation. There is no yaw applied at the inlet. Hence, it is feasible to use a symmetrical approach which decreases the computational cost. The aircraft is also a Dirichlet with a no slip condition that means a fixed velocity of zero in all three spatial directions.

4.1.2 CRM aircraft geometry

For the DPW-4 [5] the common research model CRM was used. The experiments were also carried out in a transonic wind tunnel at model scale. The model reference quantities and a sketch of the wind tunnel circuit are presented in chapter 2.1.1.

Parameter	Unit	Input	Calculated	Calculation method
Re	-	5e^06		
Ma	-	0.85		
T_{ref}	K	311		
C_{ref}	in	7.45		
C_{ref}	m		0.1892	Conversion
P_{ref}	Pa		150`985	Ideal Gas Law
η	kg/m*s		1.924e-05	Sutherland
ρ	kg/m^3		1.692	
c	m/s		353.5	
V_∞	m/s		300.4	

Table 4-3 Wind tunnel experimental conditions with original input data and calculated data, including the calculation method for the common research model [5]

The wind tunnel experimental parameters are listed in Table 4-3, where the values termed input in row three originate from the AIAA DPW-4 internet site [5] and provide the basis for the CFD simulations at wind tunnel conditions. Derivation and conversion methods are identical to those from the DLR-F6 [4]. For this simulations however, a semi-sphere domain has been used as shown in Figure 4-2. The extents specified through the diameter d are normalised by the wingspan W_s. The infinite free stream condition requirement is considered through the extent of 20 times the wingspan for d.

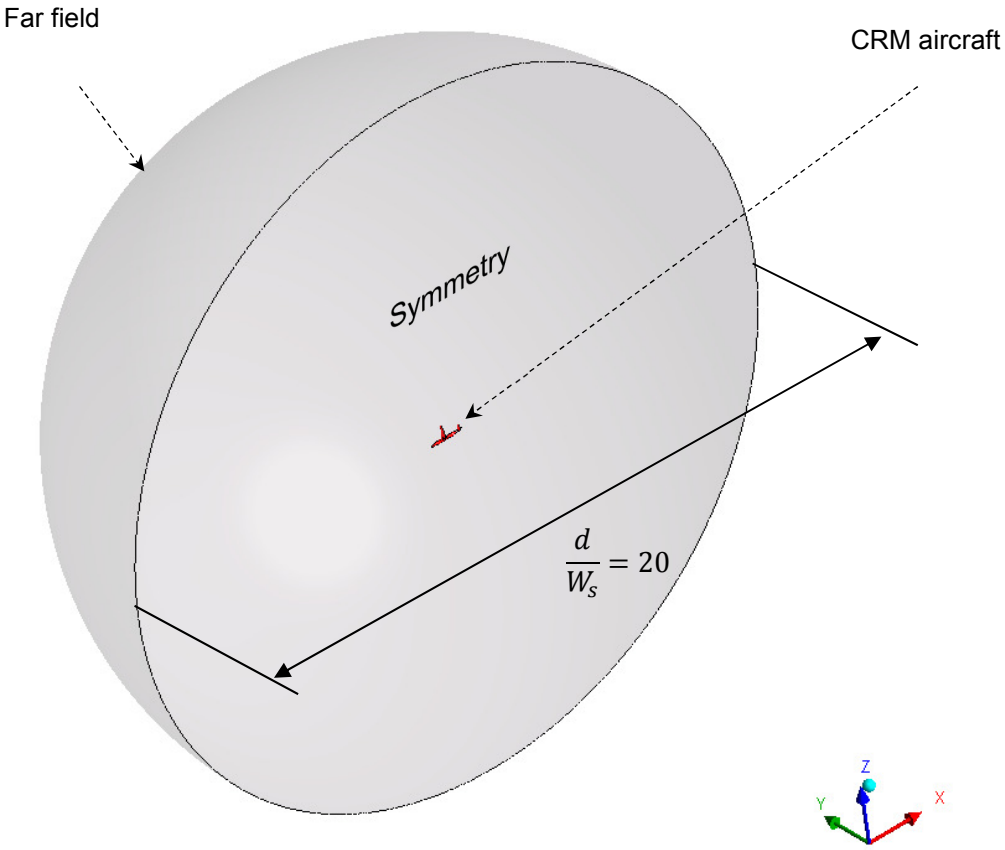

Figure 4-2 Spherical CFD domain with CRM geometry and extensions defined through diameter $\boldsymbol{d}$ *and normalised by wingspan* $\boldsymbol{W_s}$

		Far Field	Symmetry	Aircraft
CFX-Term		Opening	Symmetry	Wall
Type		Mixed	2nd Type	1st Type
Type-Name			Neumann	Dirichlet
V_∞	m/s	300.4	calculated	0
P_{stat}	Pa	134`238	calculated	calculated
T_{stat}	K	311	calculated	311

Table 4-4 Boundary names, conditions and types, DPW-4 experiments with CRM WB and WBT geometry [4]

In this case inlet and outlet boundary conditions are handled differently. There are no distinct inlets and outlets where the velocity, temperature and pressure are given at geometrically independent patches. There is one patch termed far field, on which the boundary conditions for inlet and outlet are applied. The symmetry boundary condition allows a half domain calculation. There is no yaw

applied at the inlet. Hence, it is feasible to use a symmetrical approach which decreases the computational cost. The aircraft surface is also a Dirichlet with a no slip condition that means a fixed velocity of zero in all three spatial directions.

4.1.3 TAB aircraft geometry

The experimental data for the validation of the transport aircraft body only geometry TAB [14] stem from Peak's experimental investigations on upswept rear fuselages of transport aircraft like geometries [14]. The forces and moments on the afterbody are provided as validation data over the entire upsweep angle range of β=0° to β=20°. For some configurations photographs of oil dot visualisations are available, which can be visually compared to surface streamlines plots of the CFD results. Also pressure distributions for one upsweep angle of β=5° is available. However, the validation has been made through comparison of the experimental forces and streamlines photographs. The experimental operation conditions are listed in Table 4-5, and the rectangular CFD domain is illustrated in Figure 4-3.

Parameter	Unit	Input	Calculated	Calculation method
Re	-	3e^06		
Ma	-	0.73		
T_{ref}	K	315		
L_{ref}	in	40		
L_{ref}	m		1.016	Conversion
P_{ref}	Pa		199`948	Ideal Gas Law
η	kg/m*s		1.9433e-05	Sutherland
ρ	kg/m^3		2.21	
c	m/s		356	
V_∞	m/s		260	

Table 4-5 Wind tunnel experimental conditions with original input data and calculated data, including the calculation method for the transport aircraft model [14]

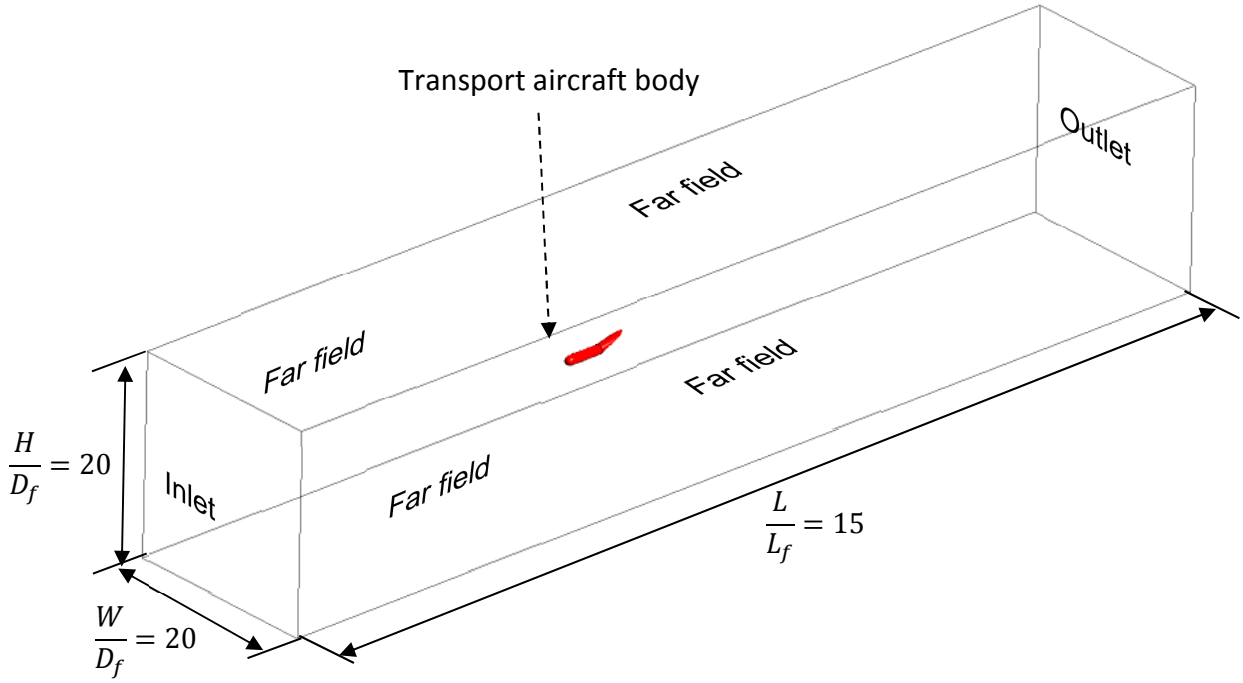

Figure 4-3 Rectangular CFD domain with transport aircraft geometry and domain extensions normalised by fuselage diameter $\boldsymbol{D_f}$ in Z and Y direction, and to fuselage length $\boldsymbol{L_f}$ in X direction for the transport aircraft model [14]

The simulations of the TAB [14] model were initially envisaged to be carried out with wind tunnel walls. Hence, the extensions correspond to the wind tunnel dimensions. However, the CFD results were of poor quality. The deviation from the experimental results of C_d and C_l was too high. Therefore, the patches which were initially specified as walls were then specified as a far field patch which can be seen in Table 4-6. The free stream boundary condition requirement seems to be fulfilled and the CFD and the experimental results have been shown to accord with each other. The remaining boundaries are applied in the same manner as for the rectangular domain of the DLR-F6 [4] with the exception of the symmetry boundary condition. The wake of this aircraft model was to be analysed by considering the application of yaw. Due to time constraints the yaw simulations have been deferred. Hence, no symmetry boundary condition has been applied.

		Inlet	Outlet	Far Field	Body
CFX-Term		Inlet	Outlet	Opening	Wall
Type		1st Type	1st Type	Mixed	1st Type
Type-Name		Dirichlet	Dirichlet		Dirichlet
V_∞	m/s	260	calculated	calculated	0
P_{stat}	Pa	calculated	199`948	199`948	calculated
T_{stat}	K	315	315	calculated	315

Table 4-6 Boundary names, conditions and types for the CFD simulations at experimental operation conditions with the transport aircraft geometry [14]

4.1.4 Mesh convergence

A mesh sensitivity analysis has been performed both for the DLR-F6 [4] and the CRM [5]. The meshes used for the study originate from the second drag prediction workshop for the DLR-F6 [4] and from the fourth drag prediction workshop for the common research model [5]. All meshes are presented below in Table 4-7 as well as the result of the study in Figure 4-4. The detailed procedure of a mesh sensitivity analysis is outlined in reference “Procedure for Estimation and Reporting of Uncertainty Due to Discretization in CFD Applications” [64].

4.1.4.1 DLR-F6 and CRM

Table 4-2 shows a summary of all DLR-F6 [4] and CRM [5] meshes with volume and surface densities for every wing body (WB) and wing body tail (WBT) configuration. The sensitivity analysis is performed based on coarse, medium and fine meshes. The meshes which were used for the sensitivity analysis are listed in Table 4-7 for all full aircraft configurations and the results are shown in Figure 4-4.

Configuration	Mesh density	Number of nodes (Volume mesh)	Number of nodes (Surface mesh)
DLR – F6 WB	Coarse	2 million	50`000
	Medium	5.2 million	57`000
	Fine	14 million	128`000
CRM WB	Coarse	2 million	48`000
	Medium	5.2 million	55`000
	Fine	14 million	122`000
CRM WBT	Coarse	3.5 million	32`000
	Medium	11 million	58`000
	Fine	36 million	152`000

Table 4-7 Meshes for all DLR-F6 [4] and CRM [5] configurations with volume and surface densities

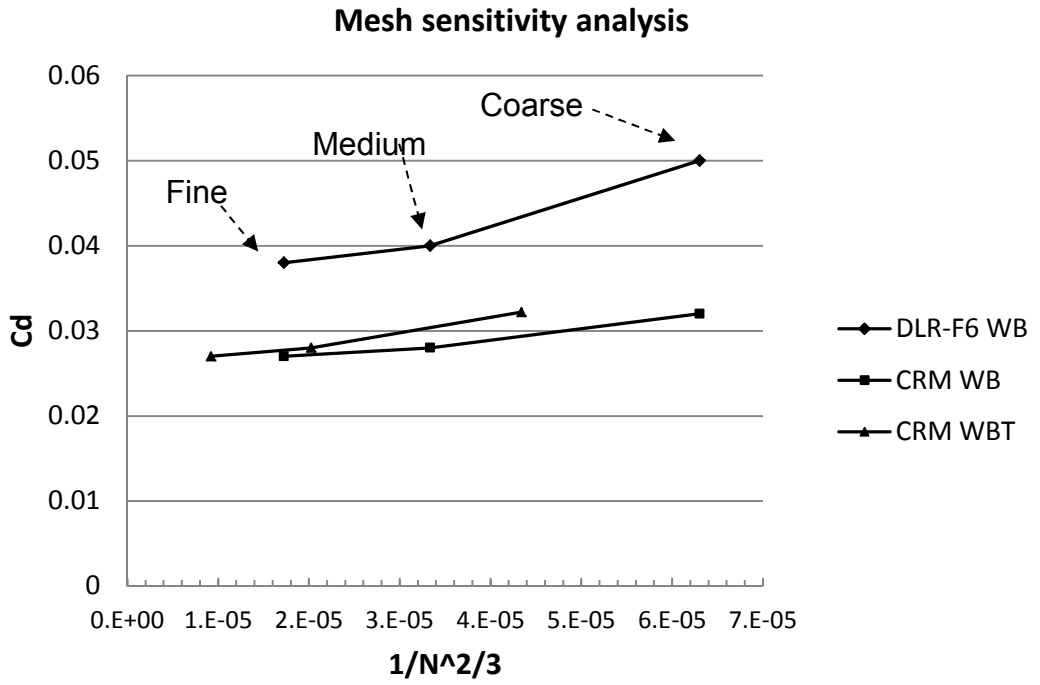

Figure 4-4 Convergence of representative parameter Cd as a function of GCI 1/N^p for all full aircraft configurations of A330 [54] substitutes DLR-F6 [4] and CRM [5]

The results of the mesh sensitivity study in Figure 4-4 show that for all aircraft configurations the difference of the dependent parameter C_d notably decreases from medium to fine compared to the difference from coarse to medium. For the DLR-F6 [4] $\Delta\ C_d$ coarse to medium is 0.01 whereas $\Delta\, C_d$ medium to fine is 0.002. Hence, the differences of the numerical error from medium to fine is 5% relative to the medium mesh and much lower than that one from coarse to medium where the difference is 20% relative to the coarse mesh. For both CRM [4] configurations the WB and WBT $\Delta\ C_d$ coarse to medium is 0.004 whereas $\Delta\, C_d$ medium to fine is 0.00. Hence, the differences of the numerical error from medium to fine is 3.7% relative to the medium mesh and much lower than the one from coarse to medium where the difference is 12.5% relative to the coarse mesh. All simulations for the CRM [5] are carried out with the medium mesh, since the error difference from medium to fine is 3.7% as well as all simulations for the DLR-F6 [4] with an error of 5% from medium to fine. Using the medium mesh was considered to be a good compromise between the available computational and time resources respectively and the numerical error. Using

the fine mesh for all configurations would have placed a too large risk on the project.

4.1.4.2 Transport aircraft body

For the transport aircraft body (TAB) an adaptive mesh refinement approach has been adopted. A high density initial surface mesh was used in conjunction with the adaptive mesh refinement for the volume mesh. Table 4-8 contains a summary of all TAB [14] meshes with volume and surface densities for every upsweep angle configurations with densities for the initial meshes and those after adaption. As notable vortical flows were expected due to large separation regions on the rear body, vorticity has been chosen as the adaption criterion in conjunction with a minimal cell edge length to avoid volume mesh density which is too high. All present initial meshes fulfil the y^+ requirement for an adequate resolution of the boundary layer, which is a y^+ value not higher than 1 [40] [41].

Configuration	Mesh density	Number of nodes (Volume mesh)	Number of nodes (Surface mesh)
TAB			
0°	Medium	3 million	20`000
	Fine	5.2 million	45`000
	AMR	7.2 million	75'000
5°	Medium	3 million	20`000
	Fine	5.2 million	45`000
	AMR	7.5 million	75'000
10°	Medium	3 million	20`000
	Fine	5.2 million	45`000
	AMR	8 million	73'000
15°	Medium	3 million	20`000
	Fine	5.2 million	45`000
	AMR	8 million	75'000
20°	Medium	3 million	20`000
	Fine	5.2 million	45`000
	AMR	11 million	80`000

Table 4-8 Meshes for all TAB [14] configurations with volume and surface densities, where coarse and medium are manually generated meshes and AMR the mesh after adaptive mesh refinement

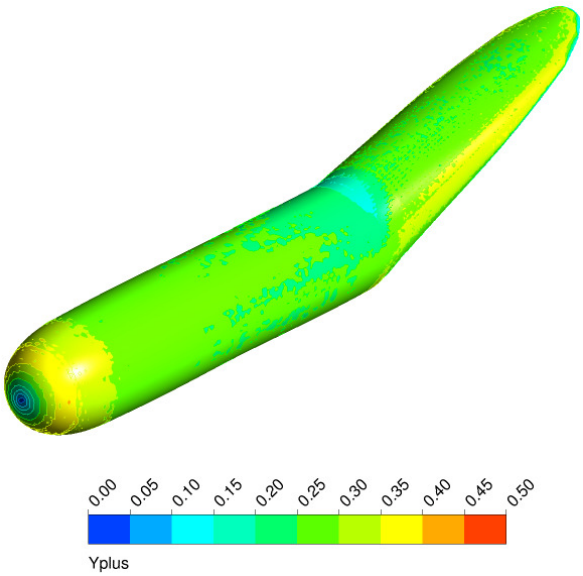

Figure 4-5 Transport aircraft body only geometry with y^+ contours on the surface and a legend with a range from 0 to 0.5

The separation mechanism occurs in the boundary layer of a flow. Hence, to predict a separation as accurate as possible, which means within the capability and limitation of the used turbulence model, the boundary layer must be resolved accordingly. The measure for an adequate resolution of the boundary layer is the dimensionless wall distance

$$y^+ = \frac{u_* \cdot y}{\nu} \qquad \text{Eq. (4-1)}$$

which describes the nominal distance of the first cell from the wall according to the absolute cell distance y, the local friction velocity u_* and viscosity ν. For the present simulations the viscosity can be assumed as constant over the whole body since the calculation is carried out isothermally. Hence, for constant first cell spacing over the entire model, y^+ changes with the variation of the local friction velocity. For the Spalart Allmaras turbulence model used [40] y^+ needs to be approximately equal to 1 [70], which ensures that the first cell lies within the laminar sub layer. This requirement has been entirely fulfilled for the transport aircraft model as shown in Figure 4-5, since y^+ is well below 0.5 on the whole body.

4.1.5 Validation results

The CFD validation for the wing body WB configuration both for the DLR-F6 [4] and the CRM [5] have been carried out at wind tunnel operation conditions and at a target lift coefficient Cl of 0.5. The wing body tail WBT configuration of the CRM has been validated for a broader range and therefore, a Cl versus Cd polar diagram is available. The body only transport aircraft model TAB [14] has been validated for upsweep configurations 0° to 20° and through consideration of two angles of attack, 0° and 5°. For both experiments the comparison parameters are Cl and Cd. The validation results are summarized below.

4.1.5.1 A330 substitutes

Table 4-9 shows the validation results for the DLR-F6 [4] where two different turbulence models, the SST and SA turbulence model, were considered. It can be observed that for a constant target Cl of 0.5 the resultant drag coefficient is over predicted by a value of 0.0105 for both turbulence models and that the resultant angle of attack α is over predicted by the SST turbulence model and under predicted by the SA turbulence model. In both cases the absolute difference value is the same, but with different polarity due to under and over prediction.

DLR-F6 WB		Experiment	SST	SA
Cl	-	0.5	0.5	0.5
Cd	-	0.0295	0.04	0.04
α	°	0.25	0.31	0.2

Table 4-9 Experimental lift, drag coefficient Cl, Cd and angle of attack α of DLR-F6 WB configuration compared to those from CFD calculation with SST and SA turbulence model

Table 4-10 shows validation results for the CRM WB configuration [4] where the SST turbulence model was used. It can be observed that for a constant target Cl of 0.5 the resultant drag coefficient is over predicted by a value of 0.0032 and that the resultant angle of attack α is under predicted by 0.69°.

CRM WB		Experiment	SST
Cl	-	0.5	0.5
Cd	-	0.0248	0.028
α	°	2.79	2.1

Table 4-10 Experimental lift, drag coefficient Cl, Cd and angle of attack α of CRM [5] WB configuration for one operation point compared to those from CFD calculation with SST turbulence model

Figure 4-6 shows a polar diagram with the validation results for the CRM WBT configuration [4] where the SST turbulence model was used. The validation has been carried out for a lift coefficient Cl of 0 to 0.8. It can be observed that the resultant drag coefficient Cd for the entire range of Cl is either in excellent agreement (black arrows) or over predicted but never under predicted.

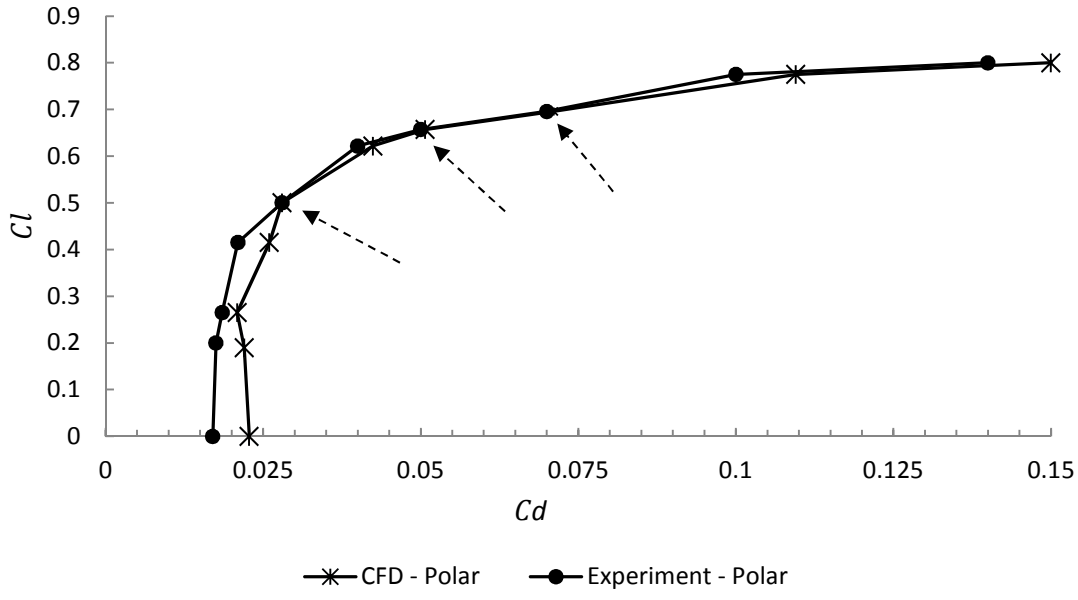

Figure 4-6 Experimental lift coefficient Cl as a function of drag coefficient Cd of CRM WBT configuration compared to those from the CFD calculation with SST turbulence model, at Re=5E^6 and Ma=0.85

4.1.5.2 Transport aircraft body

Figure 4-7 and 4-18 shows the validation results for the transport aircraft model body only configuration TAB [4] where the SA turbulence model was used. The lift and drag coefficients refer to the rear body section. The validation has been carried out for upsweep angles β of 0° to 20° at steps of 5° and for two different angles of attack α which are 0° in Figure 4-7 a) b) and 5° in Figure 4-8. For this model an adaptive mesh refinement approach has been used. The mesh was adaptively refined three times throughout the convergence history based on the refinement criterion specified, which is the vorticity in conjunction with a minimal cell edge size to avoid too much refinement. Figure 4-7 a) shows the results with the initial mesh and b) the results obtained with the adaptive mesh refinement approach.

a)

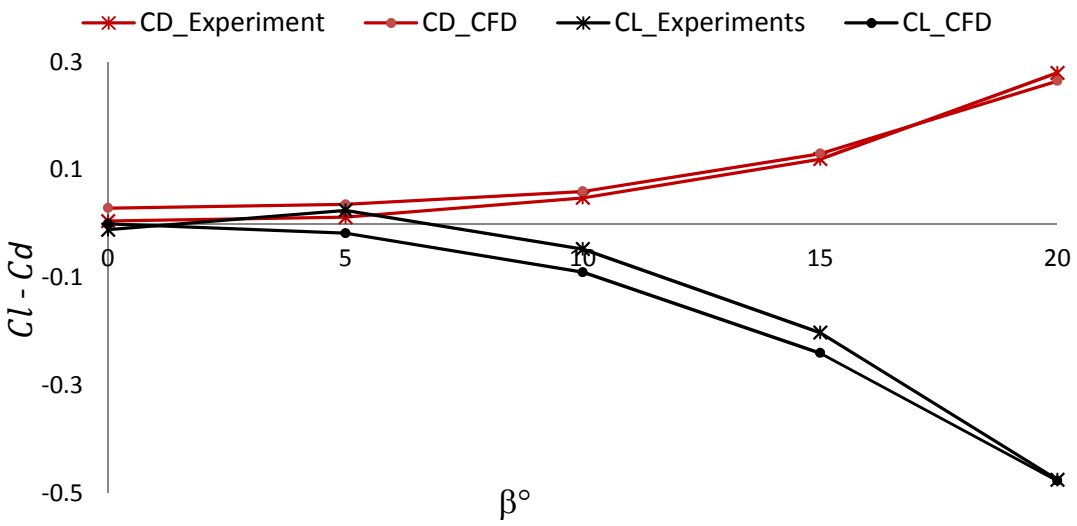

b)

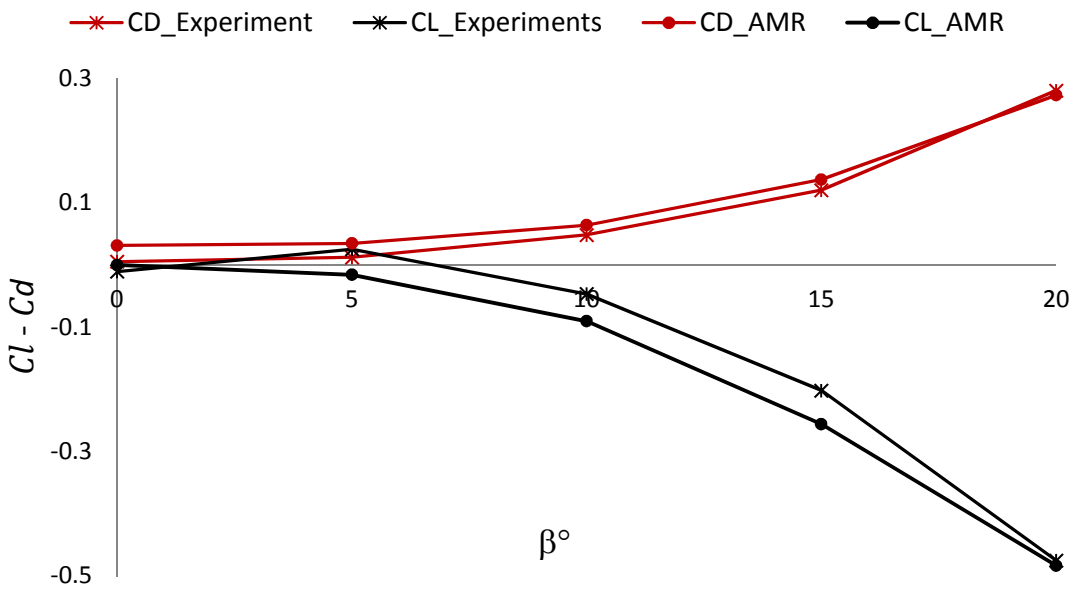

Figure 4-7 Rear fuselage only lift coefficient Cl and drag coefficient Cd as a function of upsweep angle β from 0 to 20° at an angle of attack α of 0°, a) fine initial mesh b) after adaptive mesh refinement, Re=3E^6 Ma=0.73

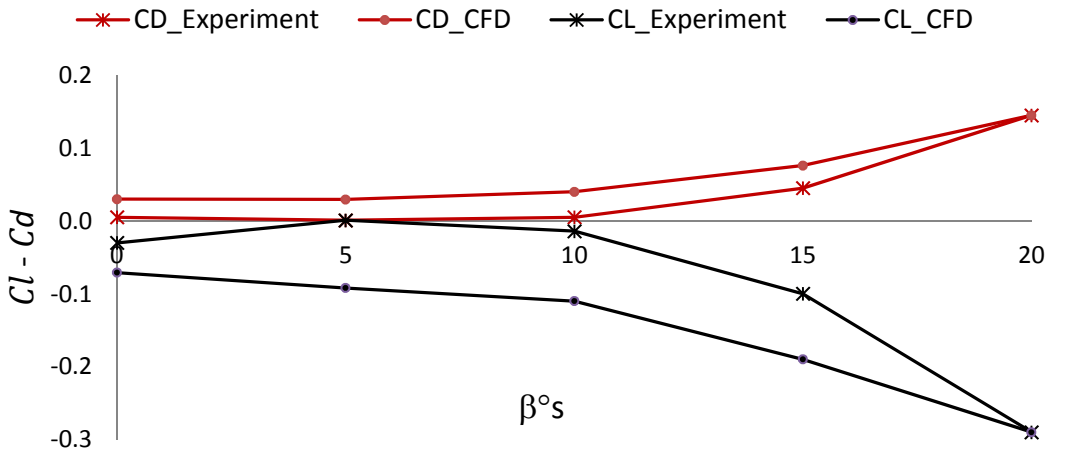

Figure 4-8 Lift and drag coefficient Cl – Cd as a function of upsweep angle β from 0 to 20° at an angle of attack α of 5°.

Figure 4-7 a) and b) shows a maximum deviation of drag coefficient Cd with the experiments at an α of 0° of 0.011 for upsweep angle β=5° which corresponds to a deviation of 44% relative to the experimental value of 0.025. The maximum deviation for lift coefficient over the entire range of β is -0.043 for an upsweep angle of β=5° which corresponds to a deviation of 93% relative to the experimental value of -0.045. For both the fine mesh and the mesh after adaption the difference between the experiments and the calculation is in the same order. However, for an α of 5° in Figure 4-8 only Cd is in the order of the previous explained differences. Cl is except to a β of 0 and 20° over the entire range of β strongly deviated from the experimental values. However, for both angles of attack α the deviation has the same polarity for both Cl and Cd. Cd is always either in agreement or is over predicted and Cl is either in agreement or is under predicted. The tendency for Cd to be over predicted is consistent with the validation results from the full aircraft models DLR-F6 [4] and CRM [5]. Although the CFD results with 5° angle of attack deviate from those of the experiments, they cannot be considered a priori as wrong. This would imply that the experiments were carried out methodically right and there is no evidence for it. Furthermore, no information is provided about the measurement uncertainty. Nevertheless, due to time constraints, only one angle of attack could be considered. The transport aircraft wake analysis is carried out at the angle of attack of 0°, where the agreement between CFD and experiments is considerably better. For some of the experimental configurations there are photographs of the oil dot visualisations available. Figure 4-9 a) shows one of those photographs in comparison with surface streamlines from the CFD calculation in Figure 4-9 b) and illustrates the close similarities of the surface flow characteristics between the experiment and CFD as well as the agreement of the separation line position.

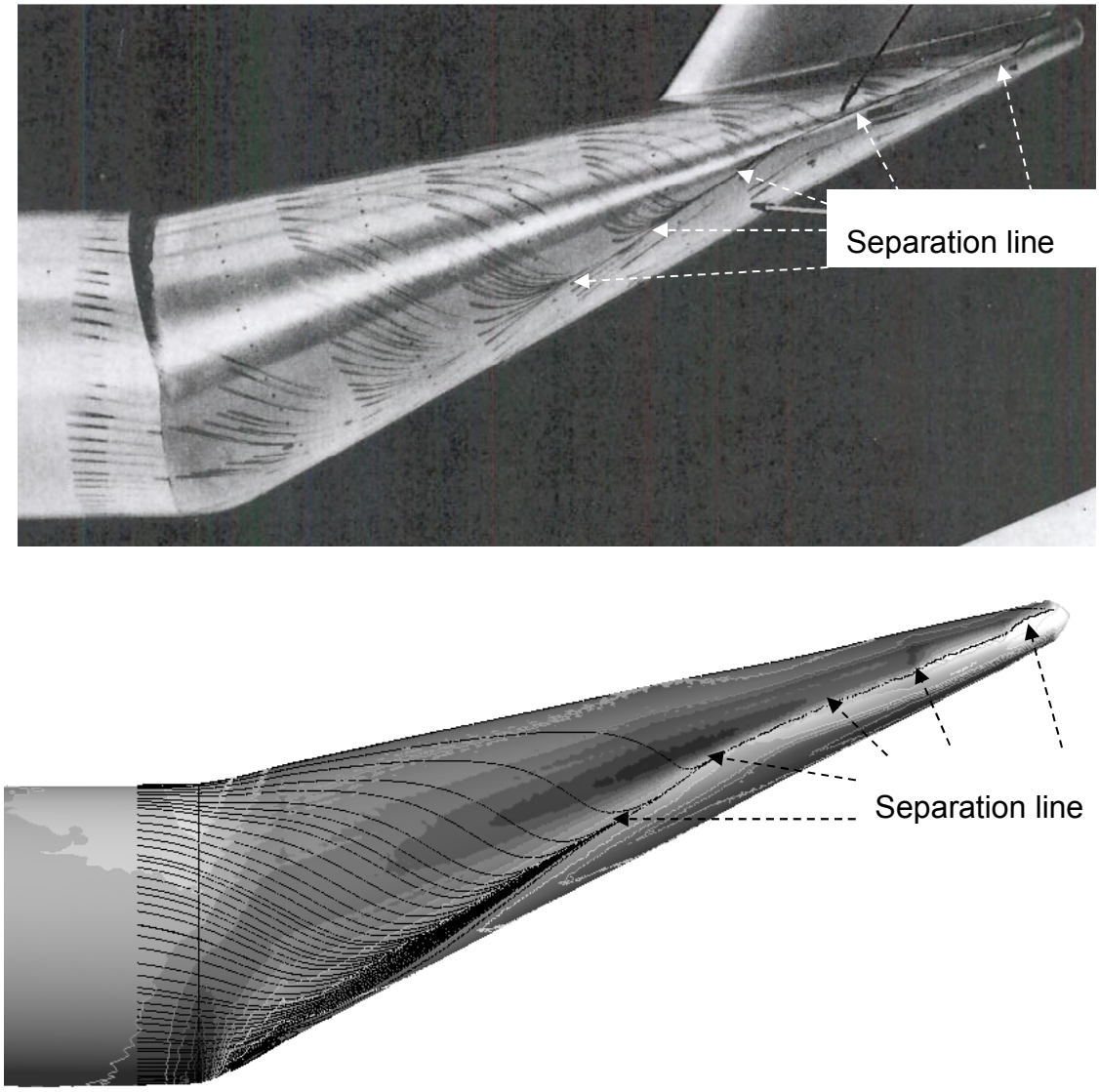

Figure 4-9 a) Oil dot flow visualisation over after body for transport aircraft model TAB [14] 20° upsweep configuration in comparison with b) surface streamlines and shear strain rate contours from CFD simulation with SST turbulence model, which shows reasonable agreement of the separation line position

4.1.6 A330 substitutes transition to full scale

The refuelling simulations for both the DLR-F6 [4] and CRM [5] are conducted under representative refuelling flight conditions which are at full scale. Therefore a geometrical scaling of both aircraft models is required. However, the CFD validation was performed at model scale and wind tunnel operation conditions. The scaling to full scale increases the Reynolds number by the scaling factor, which can introduce Reynolds number effects. For the same geometry at the same operation conditions a change in Reynolds number can result in a change in lift and drag. To exclude a misinterpretation of a possible change in lift and drag at refuelling conditions which are made at full scale and high Reynolds number an intermediate step is considered. As presented in chapter 3.2.2.7 the CFD model is first scaled at a constant Reynolds number, to ensure that the parameters of interest which are lift and drag remain constant with the geometrical scaling. Table 4-11 shows the results of this intermediate step and compares the angle of attack α, lift coefficient Cl and drag coefficient Cd between experiments at model scale and low Reynolds number, CFD at model scale and low Reynolds number, and CFD at full scale and low Reynolds number. It can be observed that for a constant nominal Cl of 0.5 both parameters α and Cd remain the same. Consequently the flow field characteristics should be the same for the model scale and the full scale simulations which is illustrated in Figure 4-10 and 4-11. In both cases similar flow field characteristics can be observed. Hence, the geometrical scaling can be regarded as correct and can be excluded as a cause for any deviation of the parameters of interest for the high Reynolds number simulations.

Parameter	Unit	Model Scale Experiments	Model Scale CFD	Full Scale CFD
AOA	°	2.79	2.1	2.08
Cl	-	0.5	0.5	0.5
Cd	-	0.0248	0.028	0.026

Table 4-11 Parameters of interest in comparison between experiments, model scale CFD and full scale CFD

Rear fuselage angle $\gamma = 13°$

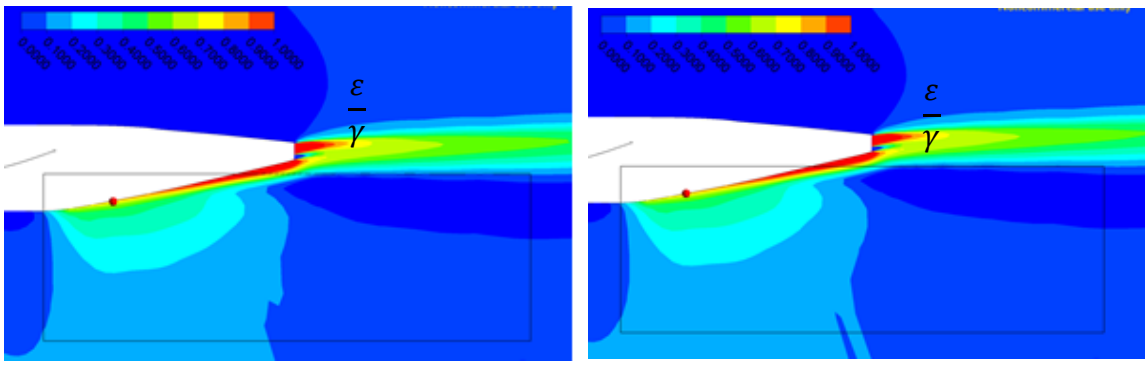

Figure 4-10 Upwash angle ε normalised by the rear fuselage angle γ in comparison on the symmetry plane at model scale left and full scale right for CRM [5] WB configuration

Mach number Ma∞ = 0.85

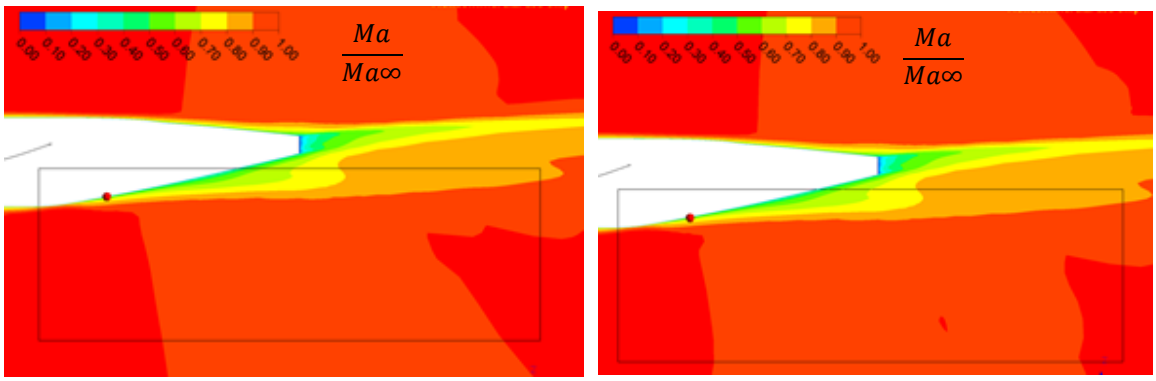

Figure 4-11 Mach number normalised by the free stream Mach number Ma∞ in comparison on the symmetry plane at model scale left and full scale right for CRM [5] WB configuration

4.1.7 Representative flight conditions

The flight conditions provided by Cobham were speed and altitude. The total mass of the aircraft is based on an assumption and corresponds to the mean value of nominal mass (174'000 kg) and maximum mass (212'000 kg) of an A330 [54]. The lift coefficient Cl is determined as follows

$$Cl = \frac{F_{lift}}{P_{dyn} A_{ref}} \qquad \text{Eq. (4-2)}$$

Where

- The lift force F_{lift} is a function of mass and gravity
- The dynamic pressure P_{dyn} is a function of speed and density
- The density is a function of the altitude
- A_{ref} is the reference area

Table 4-12 shows the flight conditions with corresponding lift coefficient (Cl). Conditions 1 to 4 correspond to the flight conditions provided by Cobham, flight condition 5 corresponds to the cruise condition of an A330 [54]. The lift coefficient determination of this flight condition has been taken into account to double check the validity of the mass assumption. The resulting Cl of 0.497 is a reasonable value, which indicates that the assumption is feasible.

Flight Condition	Speed kcas	Speed m/s	Mach -	Altitude feet	Mass kg	$C\,l$ -	Reynolds Number -
1	180	126	0.40	20`000	193`000	0.95	36.5E^6
2	200	140	0.44	20`000	193`000	0.77	40.5E^6
3	250	173	0.55	20`000	193`000	0.5	50.5E^6
4	325	222	0.70	20`000	193`000	0.3	65.0E^6
5	-	-	0.82	36`000	193`000	0.497	-

Table 4-12 Representative refuelling operation flight conditions 1 to 4, defined through speed, altitude and total mass of the aircraft along with required lift coefficient. Flight condition 5 corresponds to cruise condition of an A330

4.1.8 Turbulence model study

A turbulence model study has been conducted at full scale. Comparison parameters are lift coefficient Cl as a function of angle of attack α and vorticity ω. The strength of a vortex can be quantified through Vorticity ω which describes the spinning of the fluid. For an inviscid fluid, vorticity is defines as follows

Eq. (4-3)

$$\vec{\omega} = \nabla \times \vec{V} = \left(\frac{\partial}{\partial x}, \frac{\partial}{\partial y}, \frac{\partial}{\partial z}\right) \times \left(V_x, V_y, V_z\right) = \left(\frac{\partial V_z}{\partial y} - \frac{\partial V_y}{\partial z}, \frac{\partial V_x}{\partial z} - \frac{\partial V_z}{\partial x}, \frac{\partial V_y}{\partial x} - \frac{\partial V_x}{\partial y}\right)$$

Where

- $\vec{\omega}$ is the vorticity
- ∇ is the Nabla operator
- V_x, V_y, V_z are the vectorial velocity components

As can be observed on the right hand side of equation 4-2, where the spatial velocity derivatives are outlined, vorticity is closely related to the shear within the fluid. Turbulence models determine the Reynolds stress terms. Furthermore, a 3D separation typically generates a vortex. The turbulence model plays an important role for the prediction of separation, as it determines the turbulence intensity in the boundary layer. The state of the boundary layer determines whether separation occurs or not. Therefore, if two turbulence models predict separation differently, this will be noted in the strength and scale of the developed vortices at a predefined spatial location. Hence, vorticity is a suitable measure to compare turbulence models. The vorticity is plotted two dimensionally on predefined cross flow planes along the fuselage. Figure 4-12 shows the definition of the cross flow planes 0 to 7.

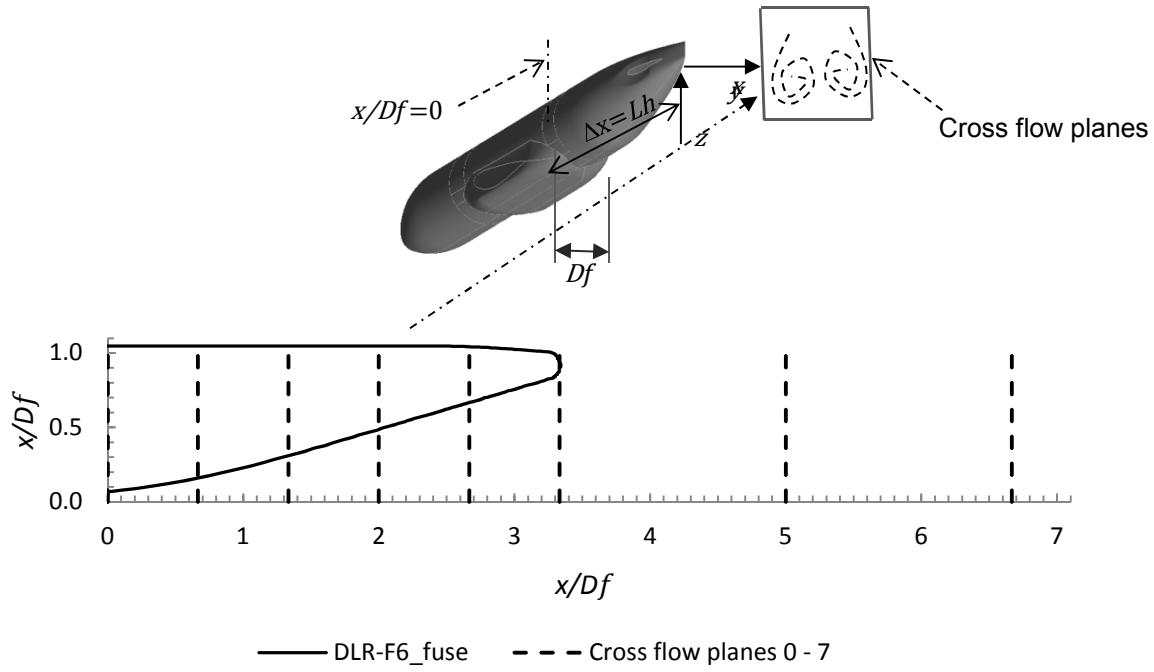

Figure 4-12 Definition of cross flow planes 0 to 7 along and beyond rear part of the fuselage, where position 0 is at 25m rearward the fuselage end and corresponds to the length of a representative refuelling hose length Lh

Figure 4-13 a) shows lift coefficient Cl as a function of angle of attack α in comparison between SST and SA turbulence model. There is no difference between both models. Figure 4-13 b) shows ω/ω_{max} where ω_{max} is the maximum vorticity within the considered flight conditions. The dashed arrows indicate the vortex core and it can be observed, that the SA model predicts a 20% lower maximum vorticity. This is considered low and irrelevant as it not expected to change the overall characteristics of the flow. Hence, the conclusion of the turbulence study is that for the prediction of the expected flow features the choice of the turbulence model is not a determining factor.

a)

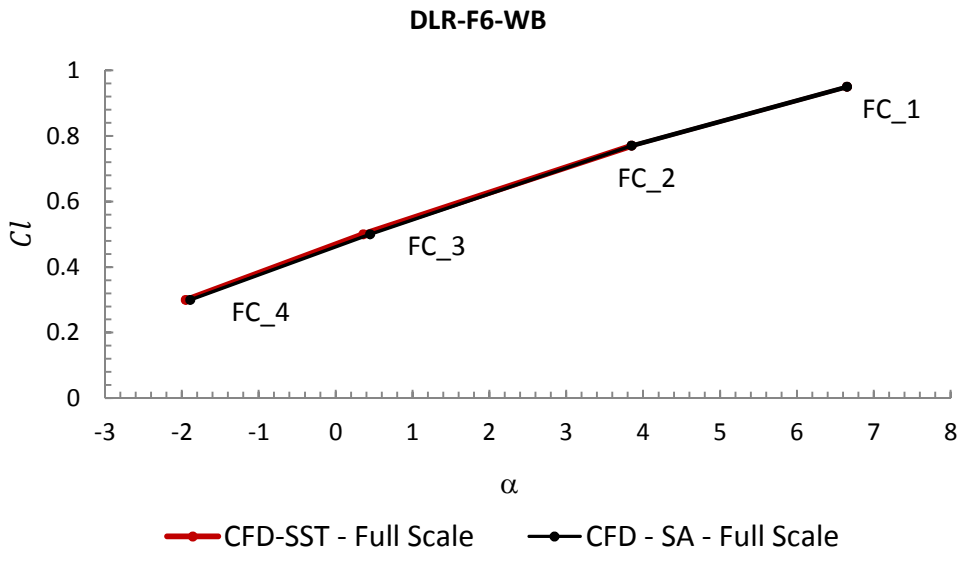

b)

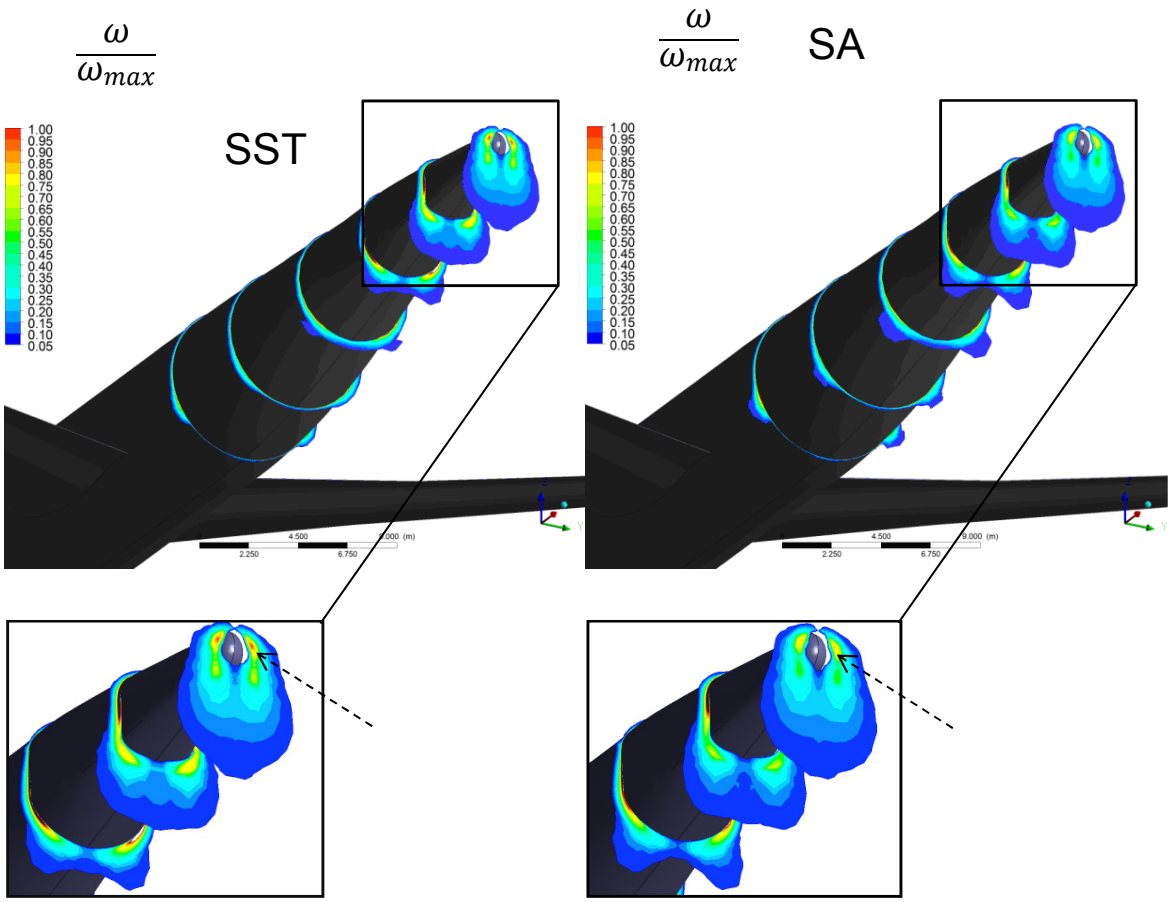

Figure 4-13 a) comparison of Cl as a function of AoA obtained from full scale simulations at flight conditions FC_1 to FC_4, b) vorticity ω normalised by maximum ω of the entire operation range FC_1 to FC_4, where $\boldsymbol{\omega_{max}}$ = 115 1/s

4.1.9 A330 substitute with hose exit fairing

The geometry of the DLR-F6 [4] WBF with hose fairing has been meshed with a medium and a fine mesh as shown in Table 4-13. The fine mesh is shown in Figure 4-14 along with a zoomed representation of the fairing surface mesh. There are no experimental results available for the geometry with fairing. Therefore, these CFD results are compared to those from the full scale DLR-F6 [4] WB configuration, which is successfully validated.

Configuration	Mesh density	Number of nodes (Volume mesh)	Number of nodes (Surface mesh)
DLR – F6 WBF	Medium	5.5 million	150`000
	Fine	8.5 million	300`000

Table 4-13 Meshes for the DLR-F6 [4] WBF configuration which is with hose fairing, and volume as well as surface densities

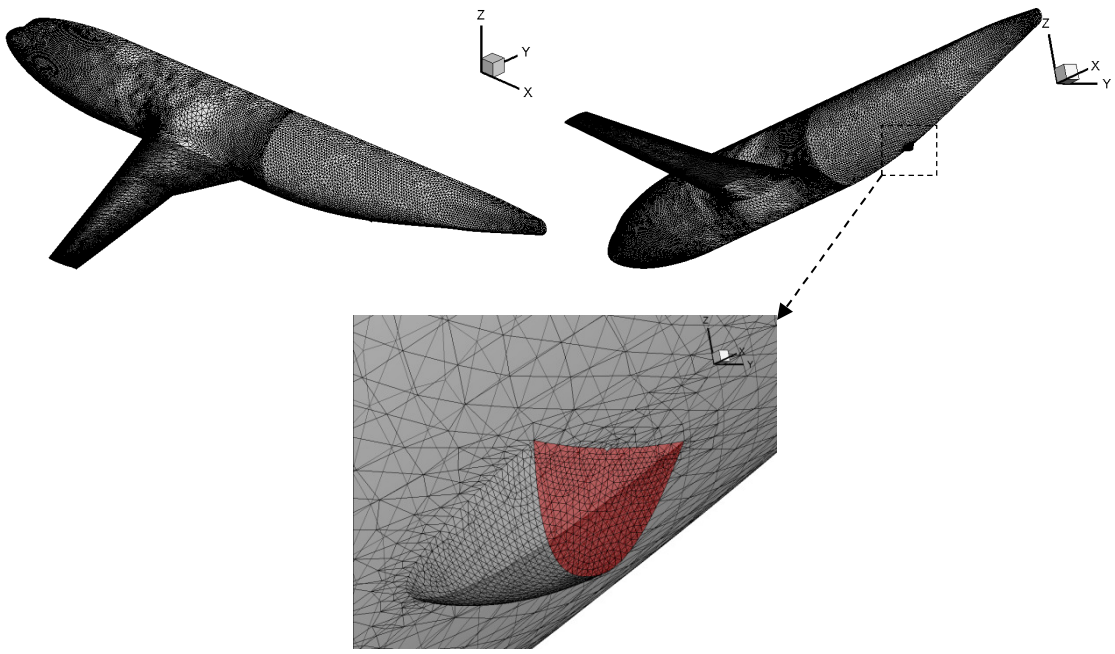

Figure 4-14 Fine surface mesh for the DLR-F6 [4] WBF configuration on top and the zoomed hose fairing mesh on the bottom

The y^+ criterion in Figure 4-15 has at the rear fuselage, which is the main zone of interest, a value not much higher than 1. This is suitable for the Spalart Allmaras turbulence model to resolve the low Reynolds number region near to the wall [70].

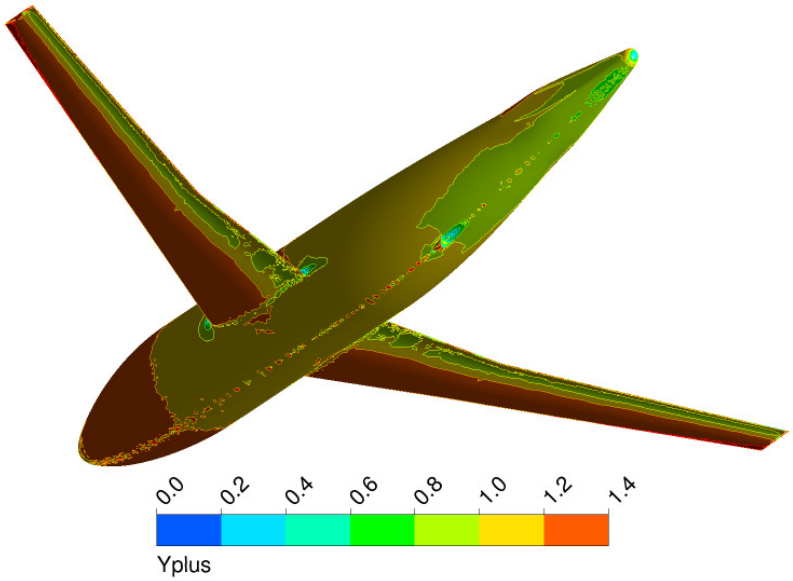

Figure 4-15 DLR-F6 [4] WBF geometry with y^+ contours on the surface and a legend which reaches from 0 to 1.4

The comparison parameters for the DLR-F6 [4] WB configuration are surface streamlines on the rear fuselage as well as drag and lift coefficients Cl – Cd at a representative flight condition in conjunction with the corresponding angle of attack α. The parameters are presented in Table 4-14.

Parameter		DLR-F6 WB	DLR-F6 WBF
α	°	0.38	0.45
Cl	-	0.5	0.52
Cd	-	0.028	0.034

Table 4-14 Lift, drag coefficient Cl, Cd and angle of attack α of DLR-F6 WBF configuration compared to those from DLR-F6 WB configuration at flight condition 3

The results of lift coefficient Cl and drag coefficient Cd for the WB and the WBF configuration are both in the same order. Both parameters are higher for the WBF configuration but this is consistent with the higher angle of attack. Figure 4-16 presents the surface streamlines on the rear fuselage. Both patterns are very similar to each other. No major separation can be observed on any of the rear bodies, which is typically characterised by a separation line.

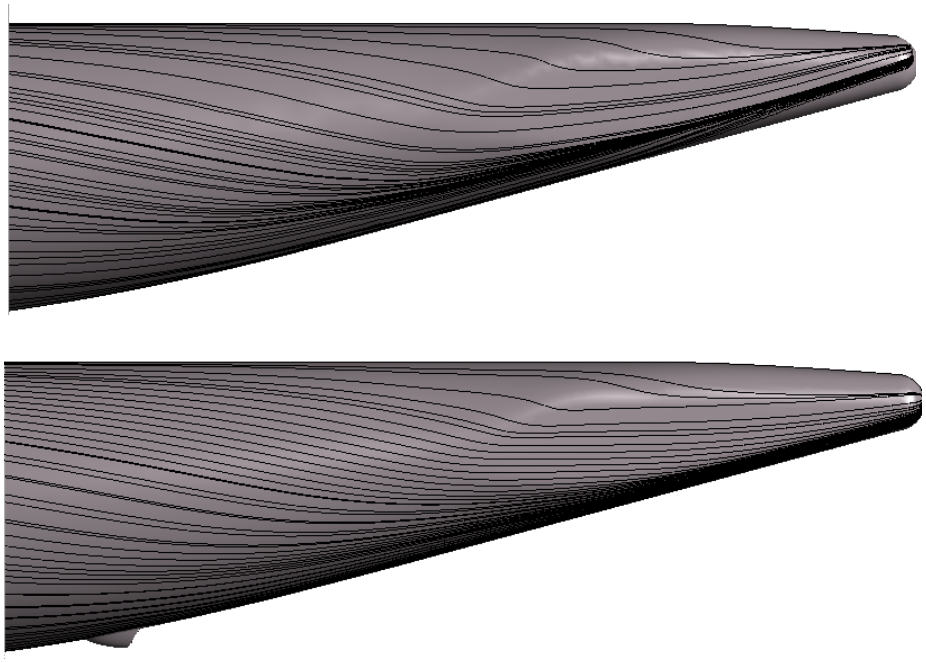

Figure 4-16 Surface streamlines on rear fuselage of the DLR-F6 [4] WB configuration on the top and WBF configuration on the bottom, where the solution is determined on two independently generated meshes

4.2 Full scale inflight refuelling simulations

In this section the results of the inflight refuelling simulations with the A330 [54] full aircraft substitutes DLR-F6 [4] and CRM [5] are presented. Furthermore, a wake analysis is carried out followed by the analysis of the wake-hose interaction and the resulting effect on the hose characteristics. The simulations are all conducted at full scale and for representative flight conditions which are outlined in Table 4-15 including the corresponding angles of attack for the CRM WBT [5] and DLR-F6 [4] WB. The corresponding figures for the DLR-F6 [4] and CRM [5] configurations at different flight conditions are presented Figure 4-17. The presented 2D plots all show the flow field features on the symmetry plane, as the hose is in a first step assumed to be exposed from the centreline of the aircraft. Therefore, circumferential effects on the hose eliminate each other and are not studied. All calculations are conducted steady state.

Flight Condition	Mach -	Altitude feet	Mass kg	Cl -	α CRM WBT	α DLR-F6 WB
1	0.40	20`000	193`000	0.95	8.5°	6.65°
2	0.44	20`000	193`000	0.77	6.2°	3.85°
3	0.55	20`000	193`000	0.5	3.2°	0.45°
4	0.70	20`000	193`000	0.3	1°	-1.9°

Table 4-15 Representative full scale refuelling operation flight conditions 1 to 4 with required lift coefficients and resulting angles of attack for the CRM [5] WBT and DLR-F6 [4] WB configurations

FC_1	FC_2
FC_3	FC_4

Figure 4-17 Figure presentation order for flight conditions 1 to 4

4.2.1 A330 substitutes

The complexity of the wake is studied through an investigation of the vortical structures in the near wake region where the hose is exposed. Figure 4-18 shows the absolute value of vorticity ω normalised by the maximum vorticity value of the flight conditions 1 to 4 ω_{max} at different cross flow planes along the rear fuselage of the CRM [5] WBT configuration. Two pairs of vortices can be observed one of which develops underneath the body indicated through the red dashed arrows and one on top of the body. The upper vortices disappear with decreasing angle of attack α. They originate from a separation on the rear body which occurs as α increases. The lower vortices originate from a separation at the upstream edge of the wing box and persist for all four flight conditions. However, the vortex core path changes (Δy) and separation decreases towards the end of the fuselage with decreasing angle of attack. The vortex structures appear only around the fuselage. For the present grid resolution this indicates non-vortical flow with increasing distance from the rear underneath the rear fuselage where the hose is exposed. This is true for all flight conditions considered.

Maximum vorticity ω_{max} = *115* $\frac{1}{s}$

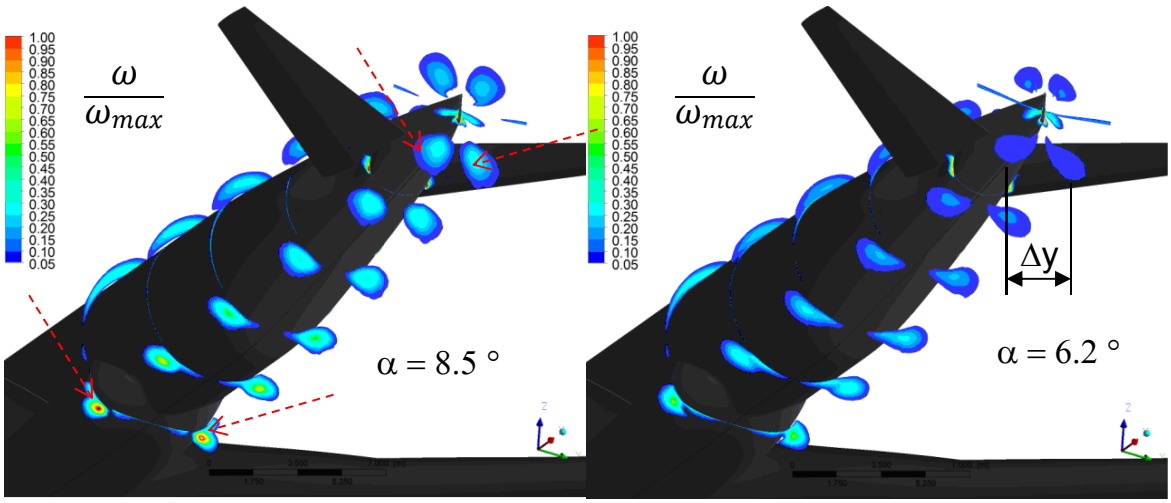

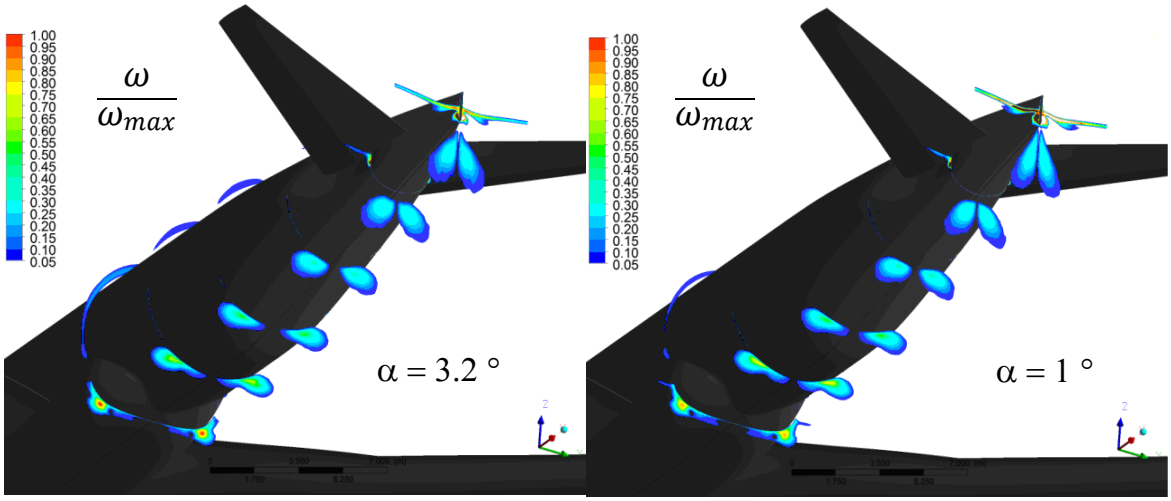

Figure 4-18 Comparison of vorticity around rear fuselage of the CRM [5] WBT configuration, normalised by the maximum vorticity of 115 1/s of entire operating range, for all flight conditions and corresponding angles of attack α FC_1: Mach=0.4, c_l = 0.9, FC_2: Mach=0.44, c_l = 0.77, FC_3: Mach = 0.55, c_l = 0.5, FC_4: Mach = 0.7, c_l = 0.3

In a first step the hose is employed from the centreline of the aircraft. The circumferential position of the fully trailed hose is expected to be in line with the centreline of the aircraft, as the lateral forces are balanced. Hence, the flow characteristics on the symmetry plane predominantly determine the characteristics of the hose. Figure 4-19 shows surface streamlines on the symmetry plane coloured by upwash angle ε normalised by the rear fuselage angle γ. ε is defined as follows:

$$\epsilon = \operatorname{atan}\left(\frac{V_x}{V_z}\right) \qquad \text{Eq. (4-4)}$$

Where

- V_x and V_z are the flow velocity components in X and Z direction, respectively

The nominal hose exit is indicated with a red point (Figure 4-19). Furthermore, the grey rectangular box indicates the area on the symmetry plane where the hose is expected to be exposed.

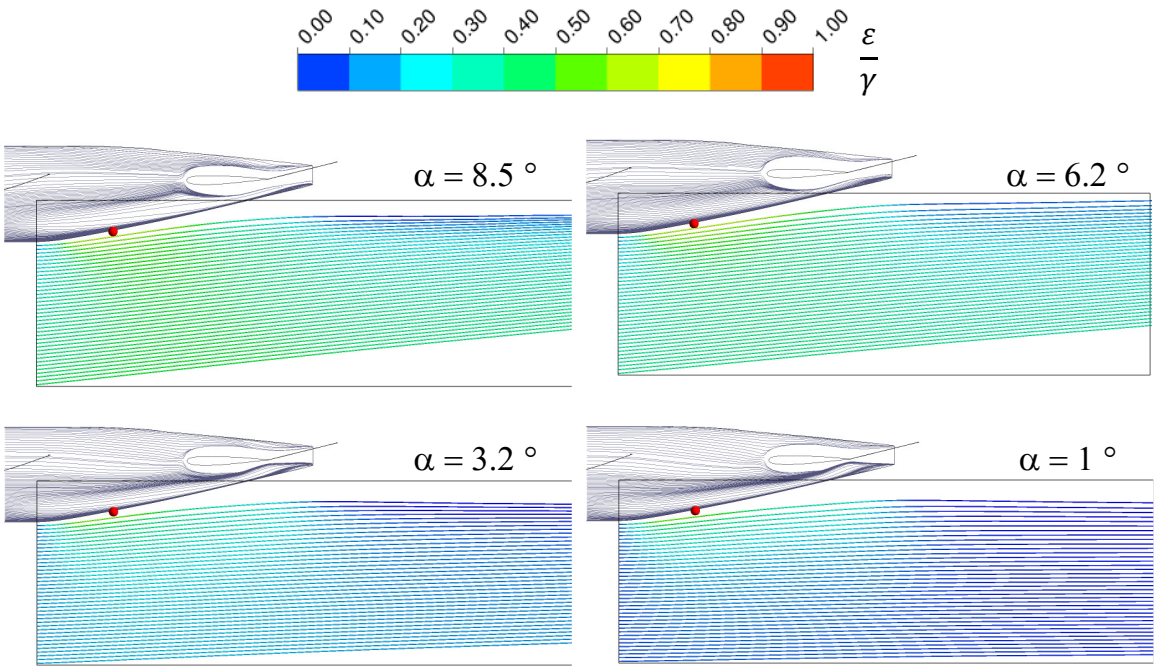

Figure 4-19 Comparison of streamlines on symmetry plane, coloured with upwash angle ε normalised by the rear fuselage angle γ of 13° for all flight conditions and for the CRM [5] WBT configuration, FC_1: Mach=0.4, C_l = 0.95, FC_2: Mach=0.44, C_l = 0.77, FC_3: Mach = 0.55, C_l = 0.5, FC_4: Mach = 0.7, C_l = 0.3

It can be observed that with decreasing angle of attack α the rear body upwash angle within the area of interest decreases as well. The flow direction relative to the hose changes with angle of attack. Hence, the angle of attack is expected to have an impact on the final hose shape and position. Figure 4-20 illustrates a contour plot of the same parameter ε/γ.

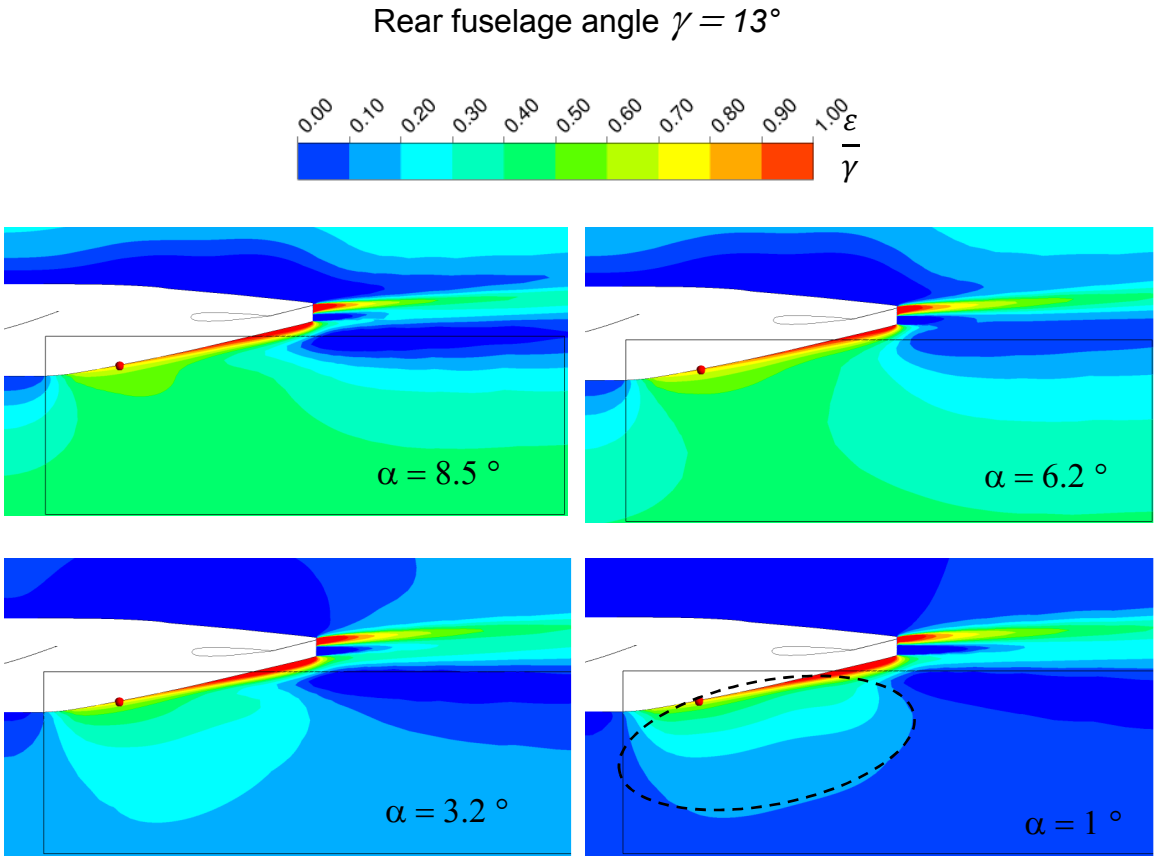

Figure 4-20 Comparison of contour plots on symmetry plane, coloured with upwash angle ε normalised by the rear fuselage angle γ of 13° for all flight conditions and for the CRM [5] WBT configuration FC_1: Mach=0.4, C_l = 0.95, FC_2: Mach=0.44, C_l = 0.77, FC_3: Mach = 0.55, C_l = 0.5, FC_4: Mach = 0.7, C_l = 0.3

The parameter ε/γ considers the flow field direction which is a result of the angle of attack α and the shape of the rear fuselage. It is of interest to know the contribution of the rear fuselage shape to the flow direction as this could have an impact on the hose characteristics. To illustrate the impact of the fuselage shape onto the wake field, α should be as close as possible to zero. This is the case for flight condition 4 as the corresponding angle of attack is 1°. In Figure 4-20 the lower right contour plot shows that the rear upwash angle in close vicinity to the nominal hose exit (red dot – dashed ellipse) assumes, about a third of the rear fuselage angle. This is predominantly the impact of the rear fuselage shape on the flow field because of a low α of 1°. Within this area the relative flow direction onto the hose is for any flight condition, different than that

beyond this area and is therefore expected to have significantly different impact on the hose. A further parameter which plays an important role is the dynamic pressure as it represents the aerodynamic force which acts on the hose. Figure 4-21 shows the local dynamic pressure P_{dyn} normalised by the free stream dynamic pressure $P_{dyn}\infty$ on the symmetry plane for all considered flight conditions.

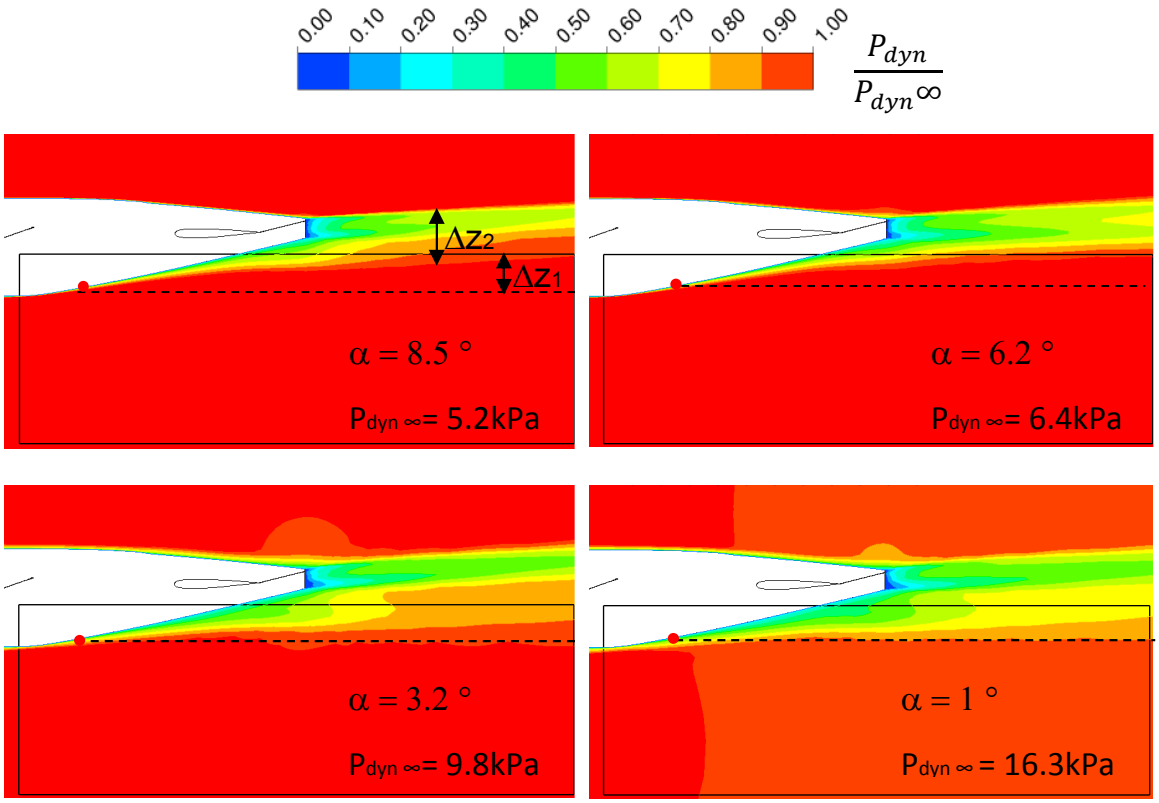

Figure 4-21 Comparison of local dynamic pressure $\boldsymbol{P_{dyn}}\infty$ on the symmetry plane normalised by the free stream dynamic pressure $\boldsymbol{P_{dyn}}\infty$ for all flight conditions and for the CRM [5] WBT configuration, FC_1: Mach=0.4, FC_2: Mach=0.44, FC_3: Mach = 0.55, FC_4: Mach = 0.7

The width of the dynamic pressure deficits is indicated through Δz1 and the distance of the dynamic pressure deficits lower limit to the hose exit vertical position is indicated trough Δz2 and the dashed black line. Both are qualitative parameters and are used to support the text. It can be observed that with decreasing angle of attack Δz1 increases and Δz2 decreases. At an angle of

attack of α=1° Δz2 is in the order of the fuselage diameter. However, underneath the vertical hose exit position where the hose trail is expected to take place almost no flow field changes can be observed. In this region the dynamic pressure ratio remains constant for flight condition 1 to 3 and decreases by approximately 5 – 10 % for flight condition 4 but is evenly distributed for all flight conditions. This leads to the conclusion that the parameter which varies most throughout the considered flight conditions is the rear fuselage upwash angle ε, which is a function of angle of attack α and the rear fuselage angle γ and which determines the direction of the flow onto the hose. The dynamic pressure in turn, which is the measure for the aerodynamic force on the hose, is evenly distributed along most of the hose. This is illustrated in a direct comparison of the upwash angle parameter ε/γ and the local dynamic pressure ratio for flight condition 3 in Figure 4-22. The hose experiences similar dynamic pressure in any position below the dashed line but considerable different relative flow angles in the same region

$\gamma = 13°$ $P_{dyn}\infty$ = 9760 Pa

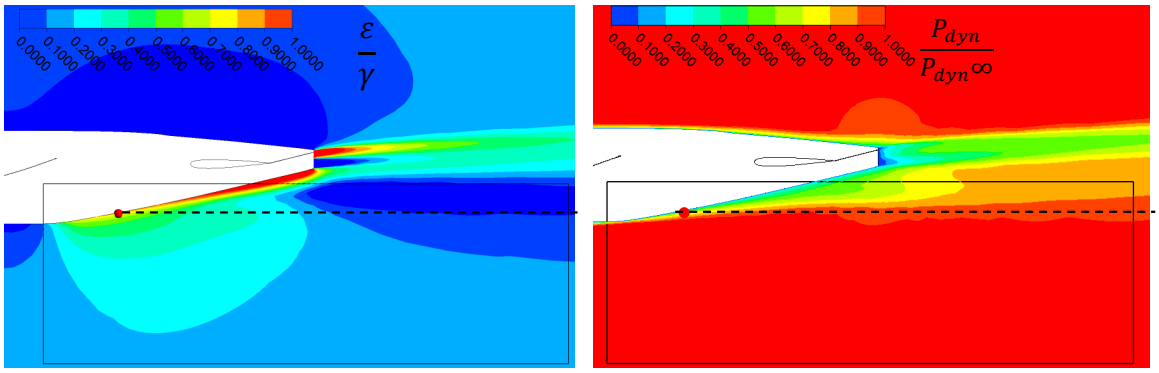

Figure 4-22 Both predominant flow parameter, the rear fuselage upwash angle which is a function of α and ε (left) and the local dynamic pressure (right) within the interrogation area of interest for the CRM [5] WBT configuration, FC_3: Mach = 0.55, $\alpha = 3.2°$

The final impact on the hose is illustrated in Figure 4-23 where it can be observed that the hose is pushed upward within the area where the upwash varies most and this is predominately the effect of the rear fuselage shape. The consequence is an inflection point of the hose which is an unwanted characteristic since it amplifies the unwanted hose whip phenomenon, but it is also typical for the deployment of the hose at the fuselage centreline [74]. The hose inflection point and the final spatial drogue position are the parameters through which the hose characteristics are determined.

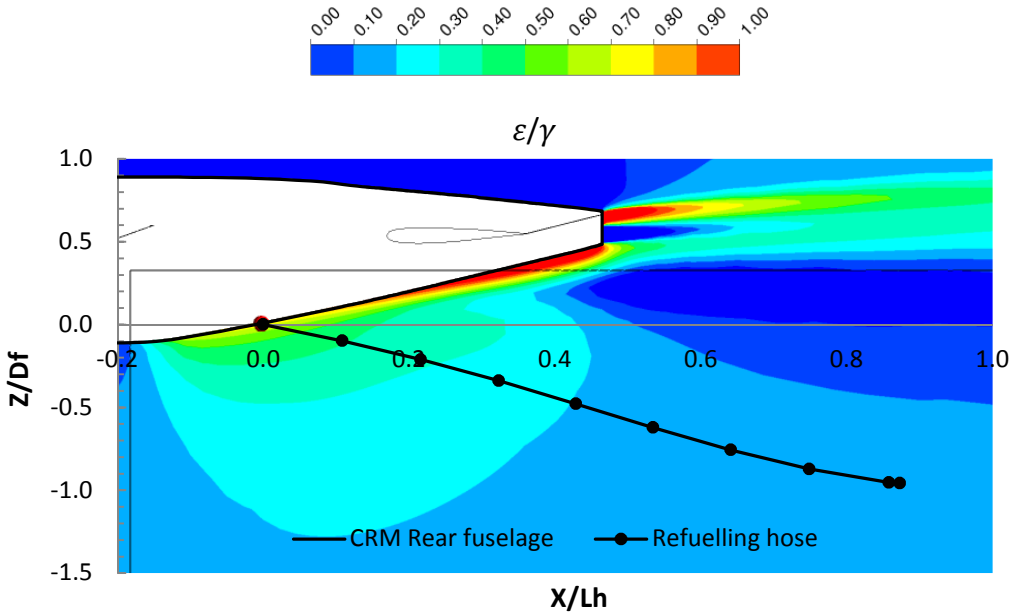

Figure 4-23 Calculated final hose shape coloured with the rear upwash angle in the background for flight condition 3 and for the CRM [5] WBT configuration, FC_3: Mach = 0.55, C_l *= 0.5,* $\alpha = 3.2°$*,*

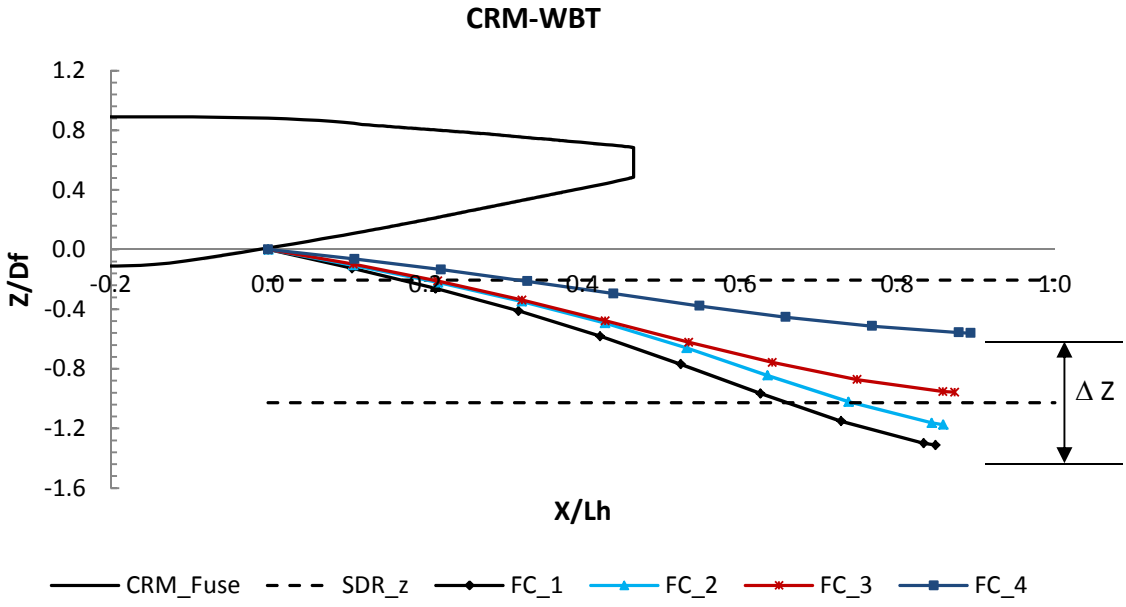

Figure 4-24 Static hose characteristics for flight conditions 1 to 4 with the CRM [5] WBT configuration with required spatial drogue range indicated by the dashed lines, FC_1: Mach=0.4, C_l = 0.95, $\alpha = 8.5°$, FC_2: Mach=0.44, C_l = 0.77, $\alpha = 6.2°$, FC_3: Mach = 0.55, C_l = 0.5, $\alpha = 3.2°$, FC_4: Mach = 0.7, C_l = 0.3, $\alpha = 1°$

Figure 4-24 shows the calculated static hose characteristics for all considered flight conditions with the common research model CRM [5] wing body tail WBT configuration. It can be observed, that the flight condition (FC) has a significant impact on the final drogue position. The vertical variation from FC1 to FC4 is in the order of the required drogue position range which is indicated by the dashed black lines. It also shows that only FC3 and FC4 fulfil the spatial position requirement for the drogue. The hose shapes are characterised through either one or two inflection points as illustrated in Figure 4-25, where the hose for flight condition 1 and 2 shows two inflection points and that for flight condition 3 and 4 one inflection point. Different behaviour can be observed for the calculations with the DLR-F6 [4] in Figure 4-26.

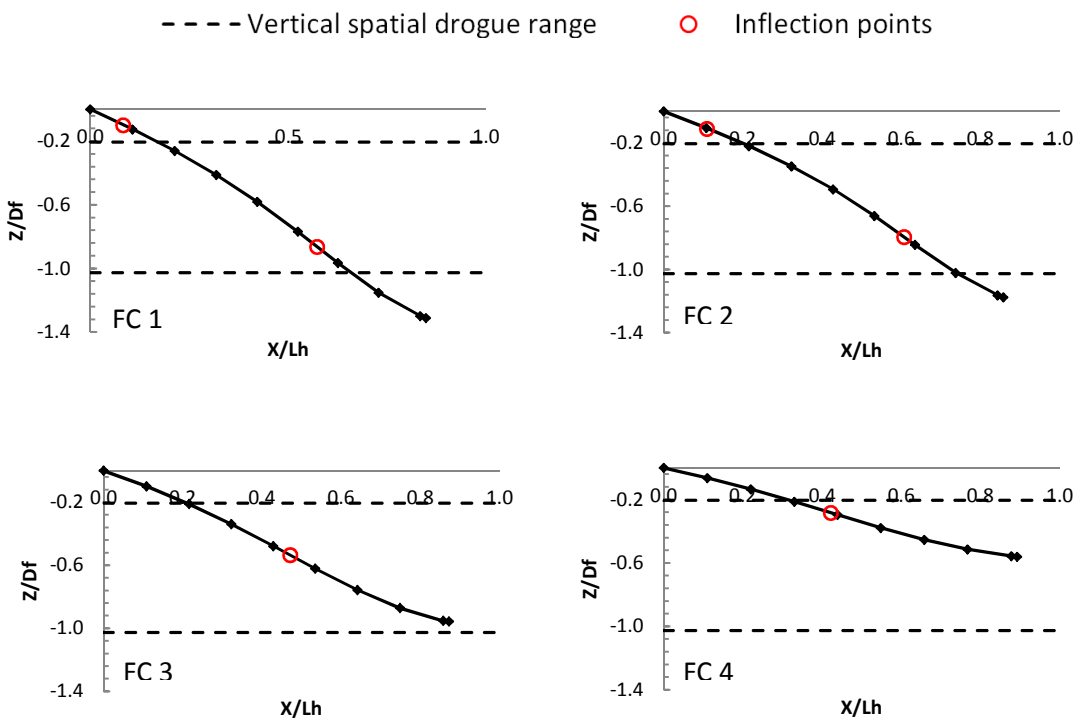

Figure 4-25 Hose characteristics for all flight conditions with inflection points indicated by the red circle and spatial drogue range indicated by dashed lines with CRM [5] WBT, FC_1: Mach=0.4, C_l = 0.95, $\alpha = 8.5°$, FC_2: Mach=0.44, C_l = 0.77, $\alpha = 6.2°$, FC_3: Mach = 0.55, C_l = 0.5, $\alpha = 3.2°$, FC_4: Mach = 0.7, C_l = 0.3, $\alpha = 1°$

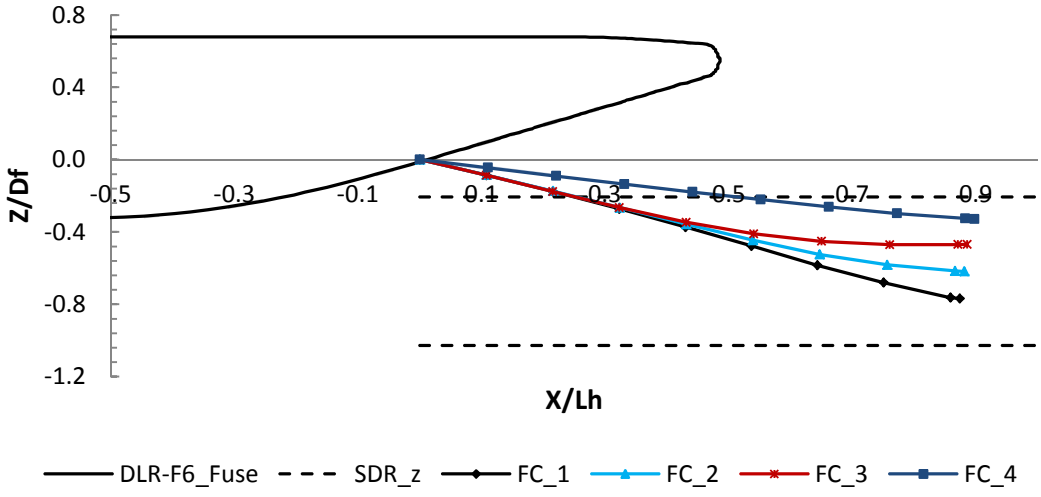

Figure 4-26 Static hose characteristics for flight conditions 1 to 4 with the DLR-F6 WB configuration with required spatial drogue range indicated by the dashed lines, FC_1: Mach=0.4, C_l = 0.95, $\alpha = 6.65°$, FC_2: Mach=0.44, C_l = 0.77, $\alpha = 3.85°$, FC_3: Mach = 0.55, C_l = 0.5, $\alpha = 0.45°$, FC_4: Mach = 0.7, C_l = 0.3, $\alpha = -1.9°$

The drogue position changes also notably with changing flight condition (Figure 4-26). However, the range within which the drogue position changes for the DLR-F6 [4] WB configuration is smaller than for the CRM [5] WBT (Figure 2-24) configuration, and the drogue for all positions is within the required range. As illustrated in Figure 4-27 the behavior of the inflection point formation is also different. The static hose shape for flight condition 1 (FC 1) shows two inflection points, for FC 2 and FC 3 one inflection point, while for FC 4 no inflection point at all and above all it is almost a straight line.

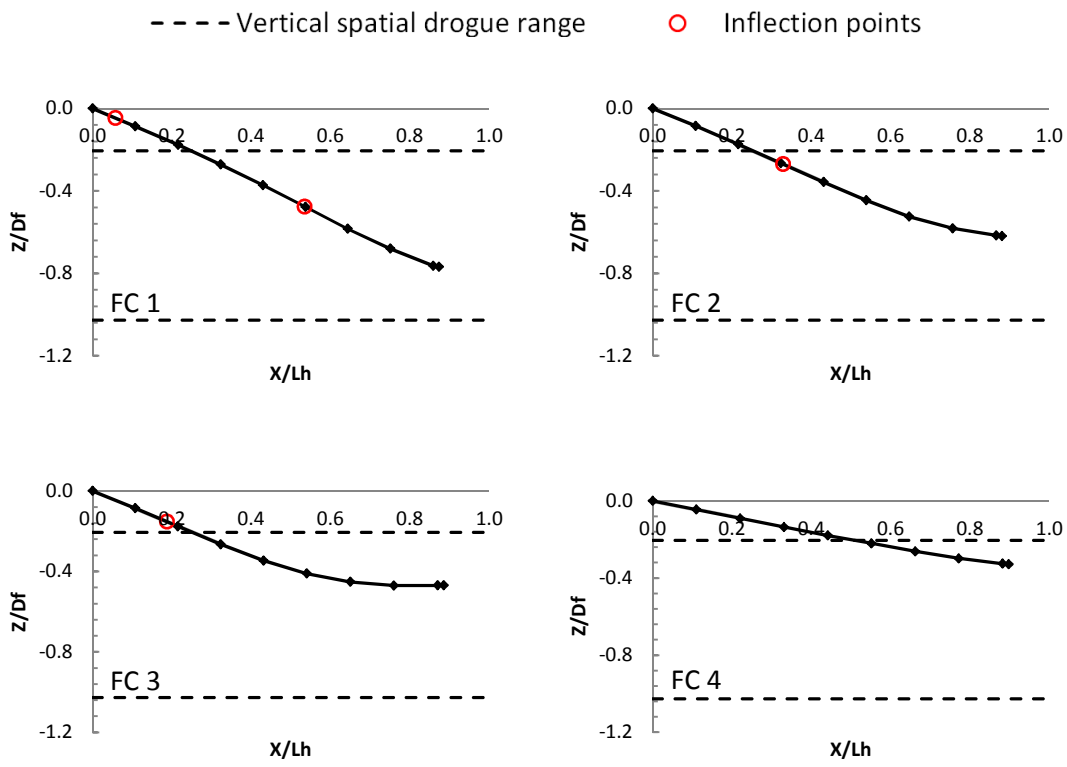

Figure 4-27 Hose characteristics for all flight conditions with inflection points indicated by the red circle and spatial drogue range indicated by dashed lines with DLR-F6 [4] WB, FC_1: Mach=0.4, C_l = 0.95, $\alpha = 8.5°$, FC_2: Mach=0.44, C_l = 0.77, $\alpha = 6.2°$, FC_3: Mach = 0.55, C_l = 0.5, $\alpha = 3.2°$, FC_4: Mach = 0.7, C_l = 0.3, $\alpha = 1°$

The most significant geometrical differences between the DLR-F6 [4] WB and the CRM [5] WBT configurations are the rear fuselage angle γ, which is 13° for the CRM [5] and 15° for the DLR-F6 [4] and the configuration, where a tail is included for the CRM [5] but not for the DLR-F6 [4]. But there is also an operational difference which is the angle of attack as shown in Table 4-16. The whole angular range is shifted towards smaller angles for the DLR-F6 [4] with a negative angle of -1.9° for flight condition 4.

	FC 1	***FC 2***	***FC 3***	***FC 4***
CRM WBT	8.5°	6.2°	3.2°	1°
DLR-F6 WB	6.65°	3.85°	0.45°	-1.9°

Table 4-16 Angle of attack α for all considered flight conditions and the DLR-F6 [4] WB as well as the CRM [5] WBT configuration

As previously stated for the CRM [5] and supported by Figure 4-22, the angle of attack, is along with the rear fuselage shape, one of the parameters for the formation of the rear upwash angle. The rear upwash angle in turn, has along with the dynamic pressure, a significant effect on the hose characteristics. To illustrate the effect of the rear fuselage shape and the angle of attack and to exclude the effect of the tail on the hose characteristics Figure 4-28 compares the static hose shapes for the DLR-F6 WB [4] and CRM [5] WB configurations at flight condition 3. The drogue position changes by $0.18D_f$ which is indicated through Δz and corresponds to approximately 25% of the valid spatial drogue range.

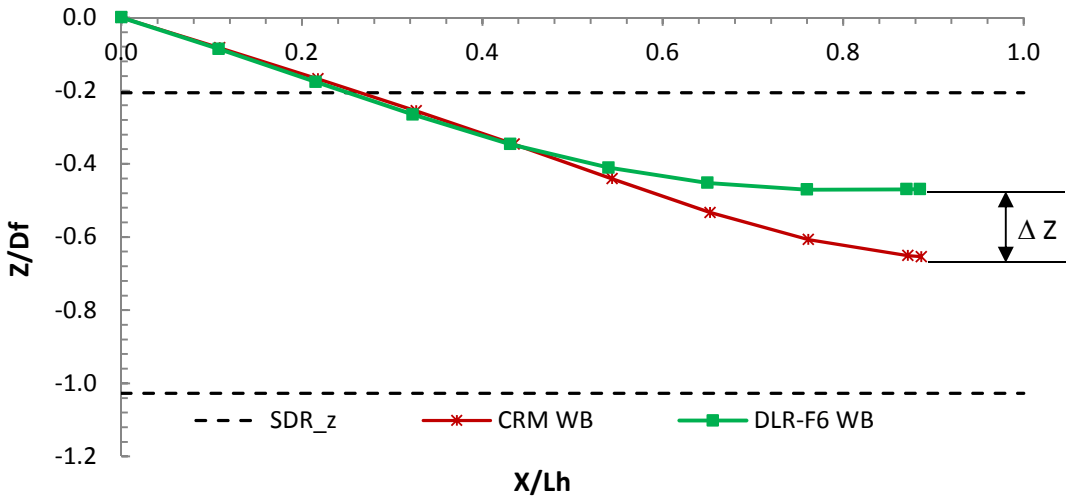

Figure 4-28 Static hose shapes for CRM [5] WB and DLR-F6 [4] WB FC 3: Mach 0.55, c_l = 0.5, α CRM WB = 2.1° α DLR-F6 WB = 0.45°

As illustrated in Figure 4-29 the hose shows two inflection points for the CRM and only one for the DLR-F6 [4]. Furthermore, the inflection point position for the DLR-F6 [4] is located very close to the hose exit which indicates a smaller effect of the upwash on the hose. As shown in Figure 4-21 the dynamic pressure deficits beneath the rear fuselage are a function of the angle of attack α. The smaller α the higher the deficits of P_{dyn}. α is smaller for the DLR-F6 [4] and thus the deficits of P_{dyn} are expected to be higher. Hence, the hose experiences less lift close to hose exit where the deficits of P_{dyn} occur.

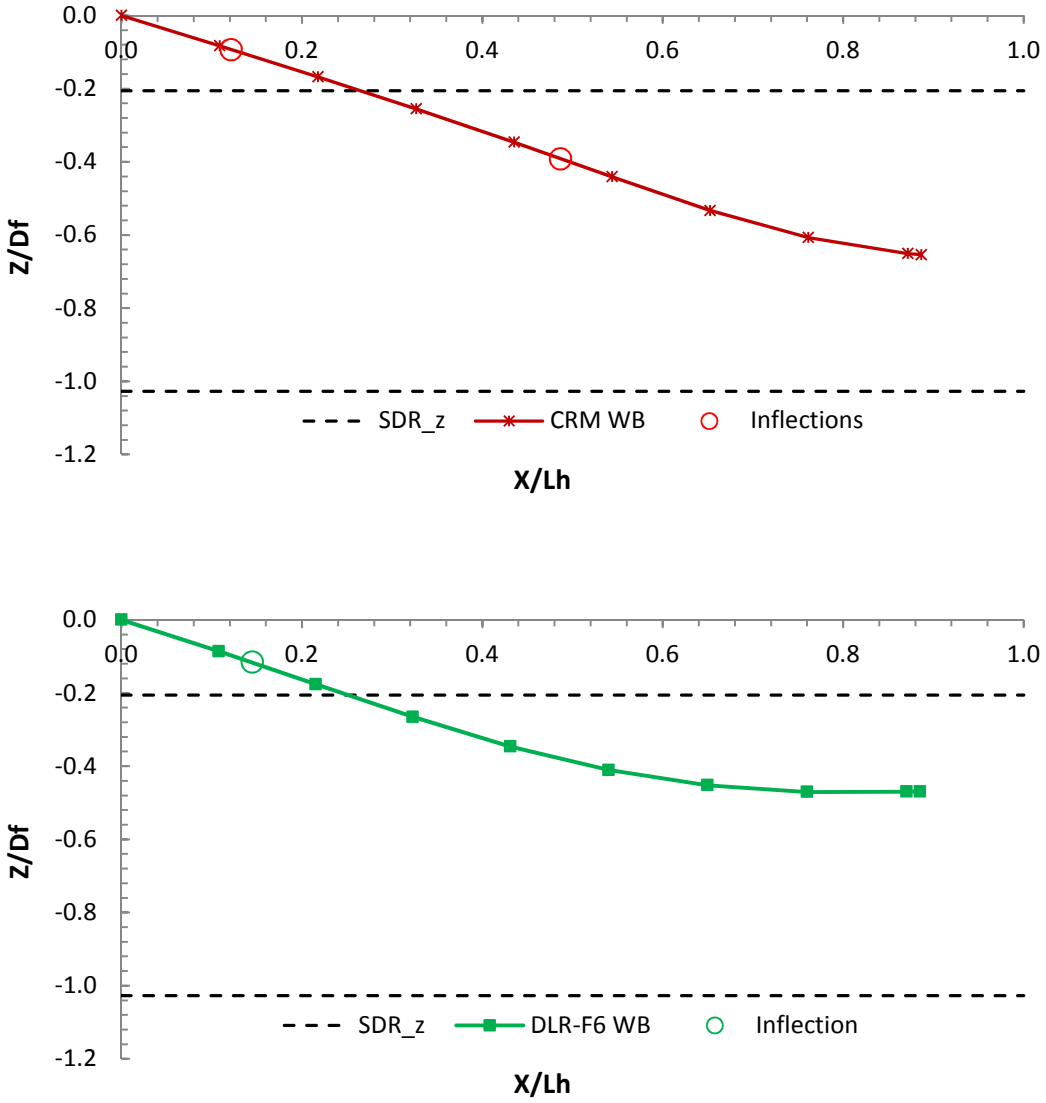

Figure 4-29 Static hose shapes for CRM [5] WB (above) and the DLR-F6 [4] WB (bottom) with indicated inflection points FC 3: Mach 0.55, C_l = 0.5, α CRM WB = 2.1° α DLR-F6 WB = 0.45°

Figure 4-30 shows a comparison between the hose characteristics obtained for the CRM [5] with and without tail at the same flight condition 3, Mach = 0.55, C_l=0.5. However, both models have different angles of attack to maintain the same lift condition. Thus, the effect shown is not exclusively the effect of the tail. Nevertheless, a significant effect on the final drogue position as well as on the characteristic of the hose can be observed, which leads to the conclusion that for a more realisic simulation an aircraft model with a tail should be preferred.

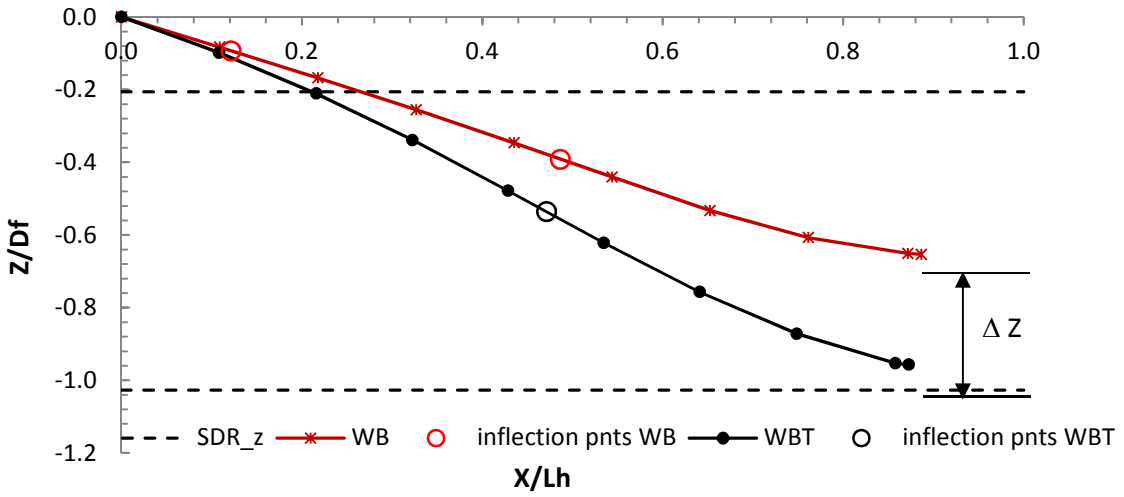

Figure 4-30 Effect of the tail on the hose shape and drogue position for CRM wing body tail configuration FC 3: Mach 0.55, C_l = 0.5, α CRM WB = 2.1° α CRM WBT = 3.2°

4.2.1.1 Summary

The near field wake close to the rear fuselage of an aircraft which is broadly similar to the A330 [54] has a generally benign behaviour (Figure 4-18). The relevant parameters for the hose deployment through which the wake can be characterised are the local dynamic pressure and the rear fuselage upwash angle (Figure 4-22). For fuselage centreline deployed hose the rear fuselage upwash causes the unwanted inflection point (Figure 4-23) as long as the dynamic pressure deficits close to the hose exit are not too high. The flight condition has a significant impact on the final drogue position as well as on the hose shape characteristics. An important criterion for the selection of suitable substitute aircraft geometries is the range for angle of attack as well as the presence of the tail. The range for the angle of attack, within which the substitute geometry operates, should be as similar as possible to the operating range of the original aircraft.

4.2.2 Hose fairing effects

The hose fairing effect is analysed in close vicinity to the fairing as well as on the overall wake. Furthermore, the effect on the hose characteristic is shown.

4.2.2.1 Close vicinity flow pattern

Figure 4-31 shows the left half of the hose fairing sliced through the symmetry plane, with 3D streamlines and surface streamlines on the symmetry plane. A separation bubble can be observed right behind the hose fairing.

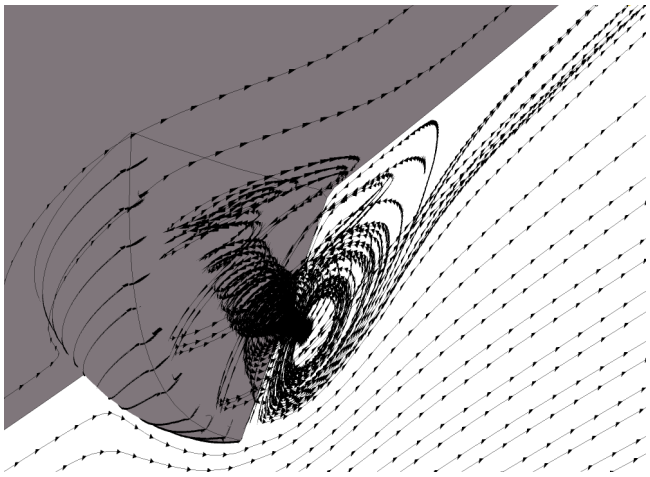

Figure 4-31 Streamlines in recirculation zone behind hose exit fairing

Figure 4-32 shows the hose fairing outline on the symmetry plane with surface streamlines only and the corresponding pressure distribution along the outline. The flow direction is from left to right. In Figure 4-32 b) from x/L_{hf}=-2 to x/L_{hf}=-0.5 a smooth slope the pressure ratio $P/P\infty$ can be observed with a following rapid increase in pressure with culminates at x/L_{hf}=0. This is the point where the dynamic pressure is lowest and the static pressure highest, as the flow is decelerated to low velocity. After this point the flow is re accelerated until it reaches the geometrically sharp edge, which is the well-defined separation point. This is indicated with the red circle and the red dashed line and is characterised by a negative pressure peak, which comes from the inverse pressure gradient. As a consequence the flow now forms a recirculation zone behind the fairing.

a)

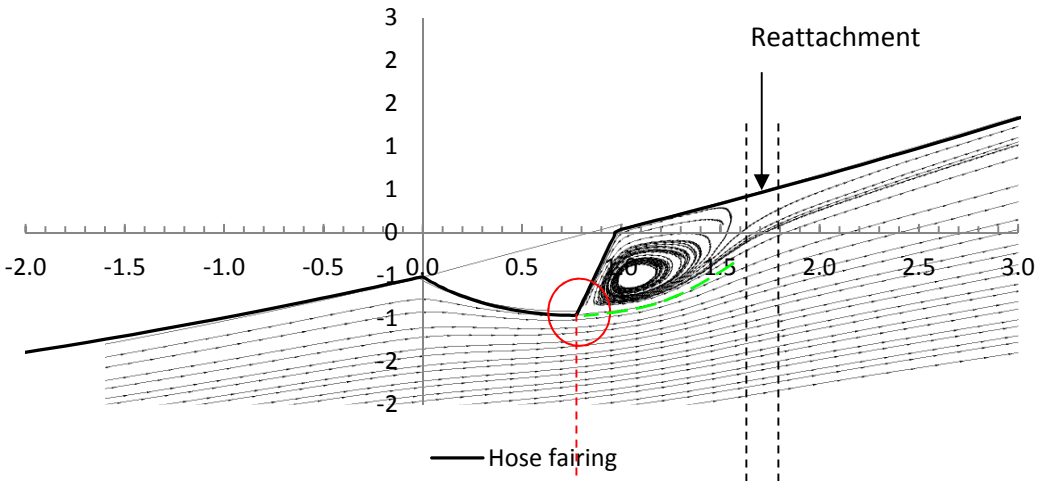

b)

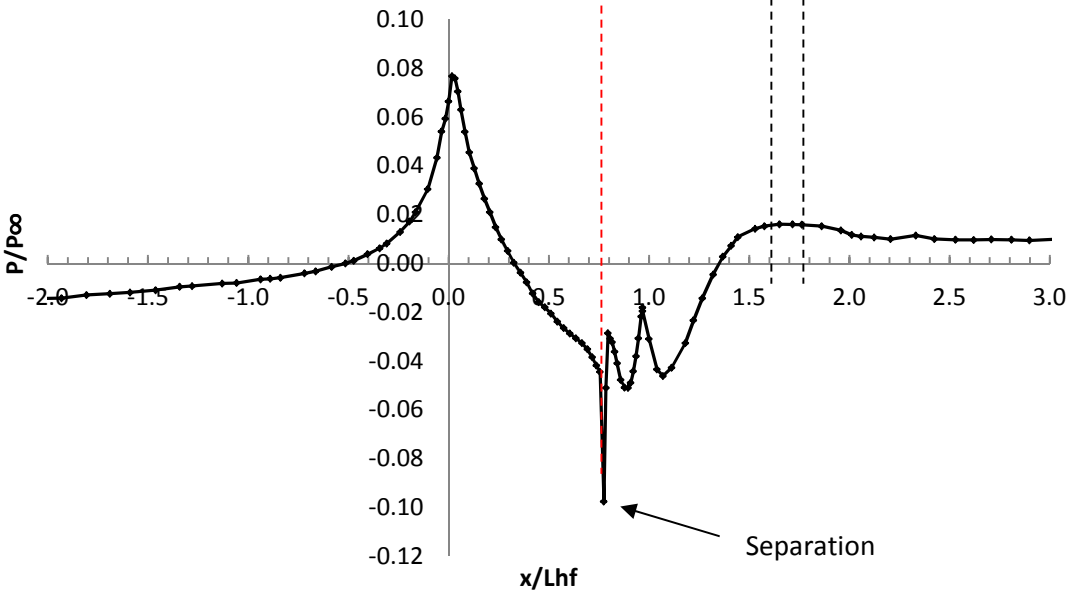

Figure 4-32 a) Hose fairing outline with surface streamlines on the symmetry plane, b) corresponding pressure coefficient P/P∞ distribution - flow direction from left to right

At approximately x/L_{hf}=1.7 the flow reattaches which is characterised through a positive pressure plateau. Observation reveals that the location of the reattachment point is not as well-defined as the location of the separation point. Hence, the dashed lines indicate a range instead of a point. The configuration of a hose exit fairing on a fuselage is very similar to a backward facing step

problem. As the flow is separated in this region, the flow field will be unsteady. These unsteady aspects have not been evaluated in this work. Given the relative diameter, mass and length of the hose, any local unsteady flow aspects are considered as being unlikely to have a notable impact on the hose shape.

4.2.2.2 Overall wake effect

Figure 4-33 shows the rear fuselage outline of the DLR-F6 [4] with hose exit fairing, HEF. The cross flow planes where the wake impact of the fairing is investigated are indicated by the dashed lines. The first cross flow plane is positioned right after the HEF followed by three further cross flow planes downstream. The heights of the cross flow plane follow the rear fuselage shape and reach their maximum at the fuselage end. This is the height which is used for normalisation of the vertical length scales. The distance from the first to the last cross flow plane is in the order of a representative refuelling hose length. The horizontal length scales are normalised by this length. The minimum height is in the order of the vertical drogue position of a fully trailed hose at a representative refuelling condition. The parameters in Figure 4-34 and 4-35 are plotted along the intersection line of the symmetry plane. Hence, the flow pattern on the symmetry plane is shown.

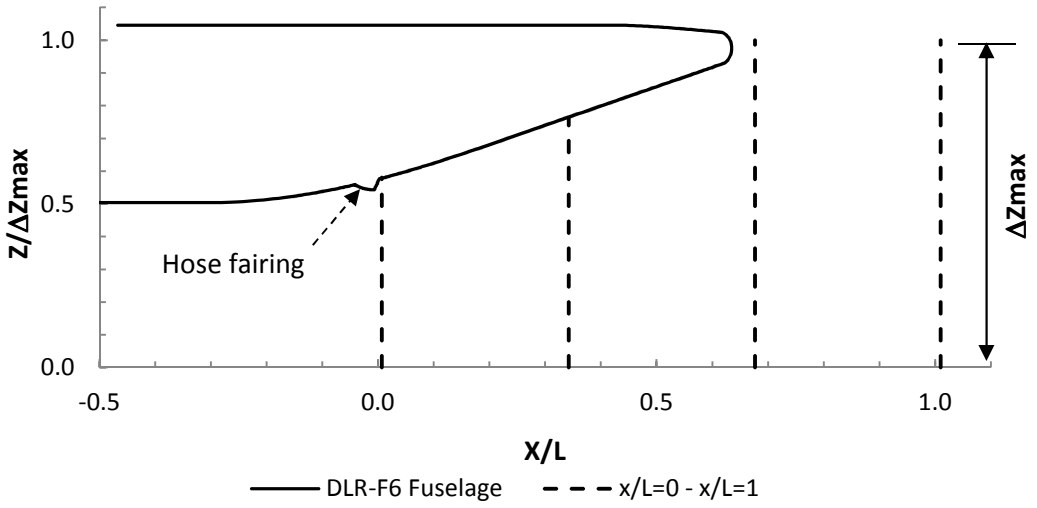

Figure 4-33 Rear fuselage outline with dashed line indicated cross flow planes. Vertical length scales are normalised by the maximum height ΔZmax and horizontal length scales are normalised by the distance of the first to the last cross flow plane

Figure 4-34 shows the total pressure distribution normalised by the free stream total pressure for all cross flow planes plotted along the intersection line of cross flow planes and symmetry plane. There is no significant change on any of the cross flow planes X/L=0 to X/L=1, which means that there are no major losses

due to the fairing which affect the overall wake field, on particular on the symmetry plane where the hose is exposed.

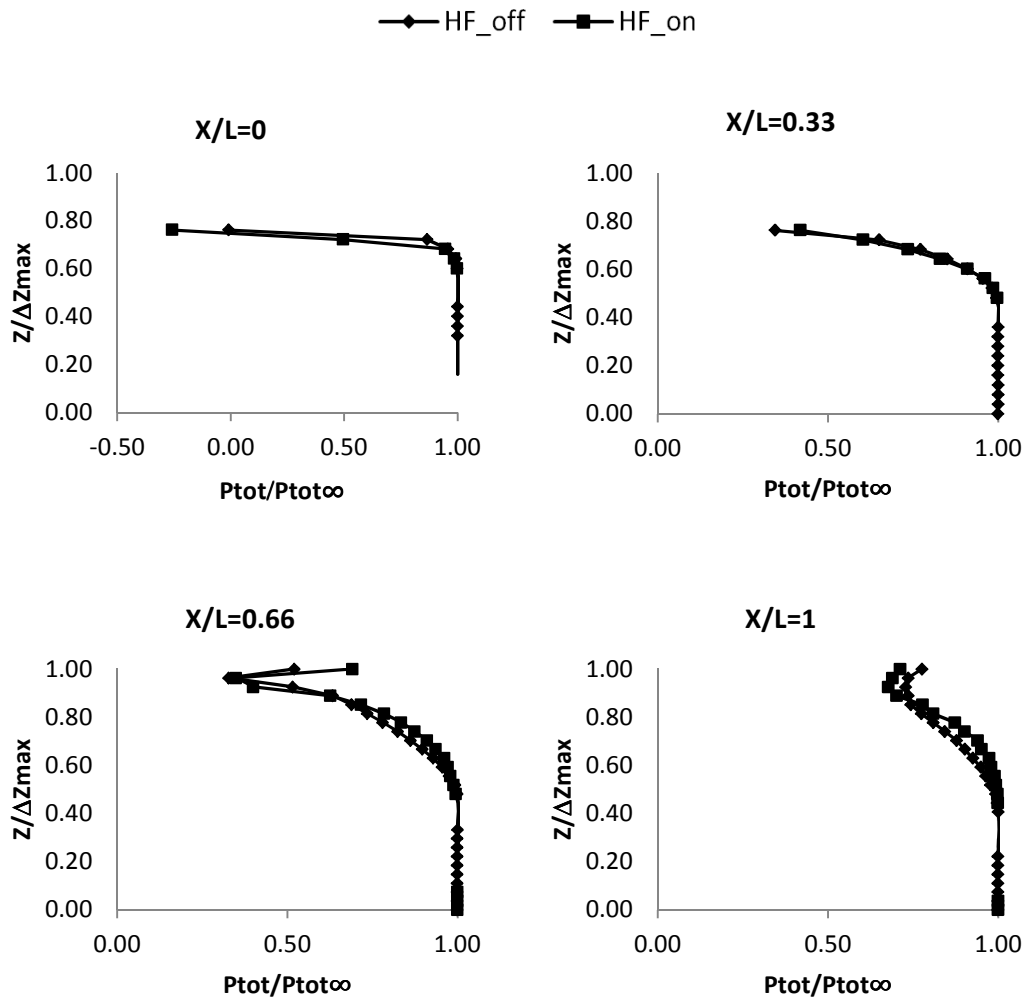

Figure 4-34 Comparison of total pressure Ptot normalised by the rear fuselage Ptot∞ for all cross flow planes plotted along the intersection line of cross flow planes and symmetry plane at flight condition 3 for the DLR-F6 [4] WB, WBF configuration respectively, FC_3: Mach = 0.55, C_l *= 0.5,* $\alpha = 0.52°$

Figure 4-35 shows the upwash angle ε normalised by the rear fuselage angle γ of 15° for all cross flow planes also plotted along the intersection line of cross flow planes and symmetry plane. The normalised upwash angle is a measure

for the redirection of the flow due to the presence of the hose fairing. There is almost no redirection along the first two cross flow planes. At X/L=1 a redirection of *0.14*ε/γ can be observed close to the maximum height Zmax, which corresponds to a redirection of the rear upwash angle of approximately 2° and is indicated through the red dashed arrow. For the wake-hose interaction this region is not of interest, as the fully trailed hose cannot be influenced at this height. Therefore, there is almost no impact of the hose fairing on the hose characteristics, which can be observed in Figure 4-36 for two different flight conditions.

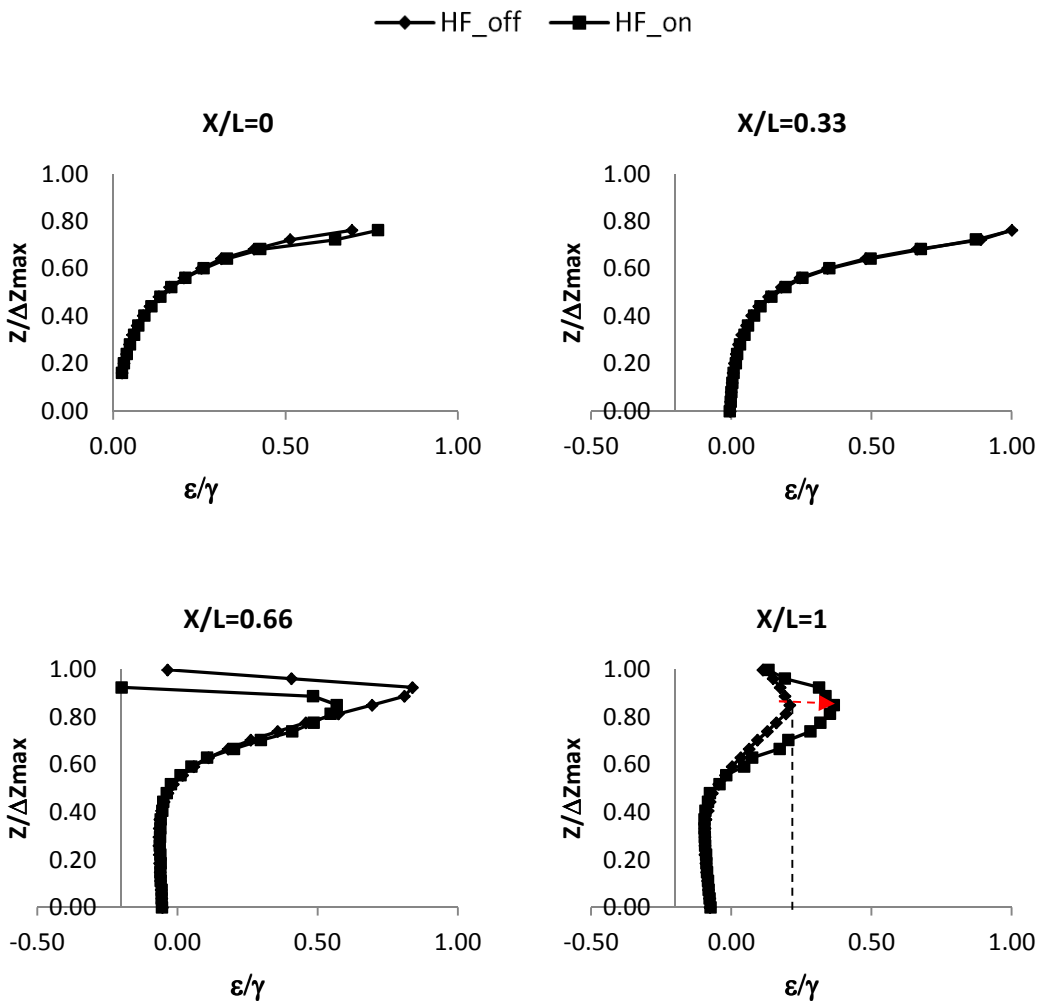

Figure 4-35 Comparison of upwash angle ε *normalised by the rear fuselage angle* γ *of 15° for all cross flow planes plotted along the intersection line of cross flow planes and symmetry plane, at flight condition 3 for the DLR-F6 [4] WB, WBF configuration respectively, FC_3: Mach = 0.55,* C_l *= 0.5,* α *=0.52°*

a)

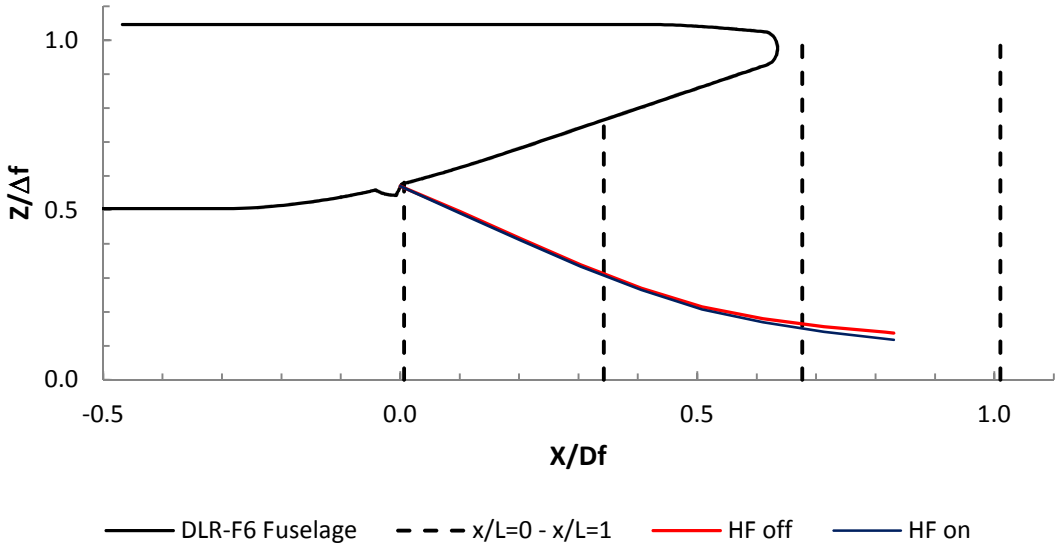

b)

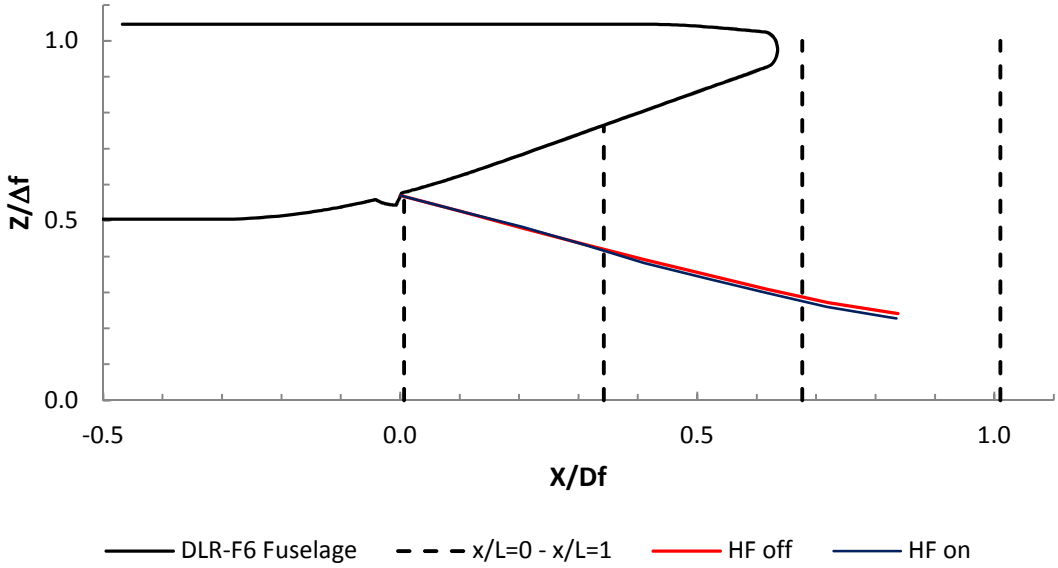

Figure 4-36 Hose characteristics in comparison with (blue line) and without (red line) hose fairing, a) FC_3: Mach = 0.55, C_l = 0.5, α =0.52° and b) FC_4: Mach = 0.7, C_l = 0.3, α =-1.92° DLR-F6 [4] WB, WBF configuration respectively

4.2.3 Hose fairing ventilation

To avoid recirculation behind the hose fairing a ventilated faring has been considered. A naturally ventilated fairing could physically be realised through a perforated, air-permeable fairing surface as schematically shown in Figure 4-37 a). However, artificial ventilation could also be of interest, which could be realised through pressurised air ejection like that shown in Figure 4-37 b) or through the redirection of air around the fuselage as shown in Figure 4-37 c). A speculative study has been conducted to assess these options.

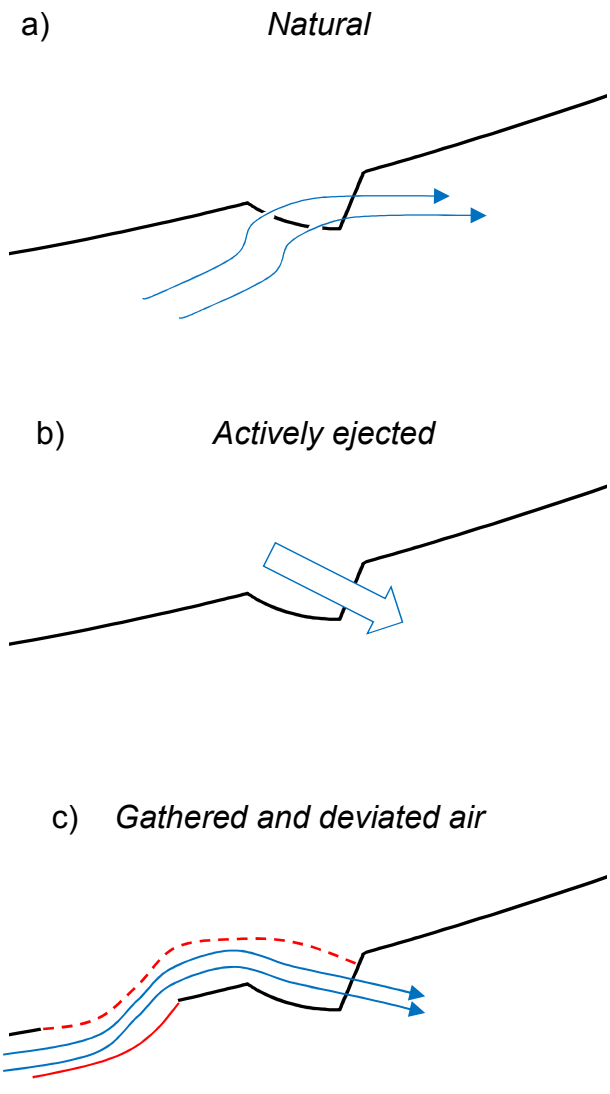

Figure 4-37 a) Air-permeable, b) ejected, c) deviated air hose fairing ventilation

For the CFD calculation the ventilation is modelled as a constant velocity inlet at the front face of the fairing, which is indicated through the red surface in Figure 4-38 a). Density and static temperature correspond to the free stream conditions. Ventilation parameters are air velocity magnitude and direction. The direction is defined as the angle θ between a horizontal line and the velocity vector V as shown in Figure 4-38 b).

a)

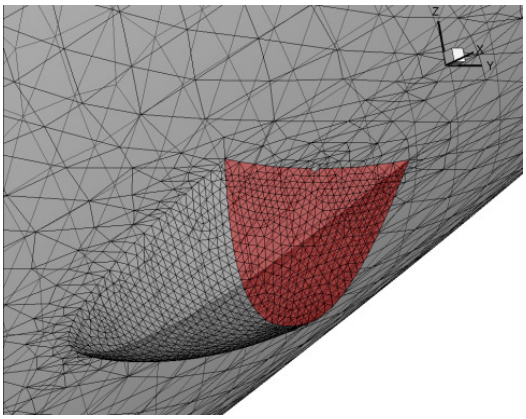

b)

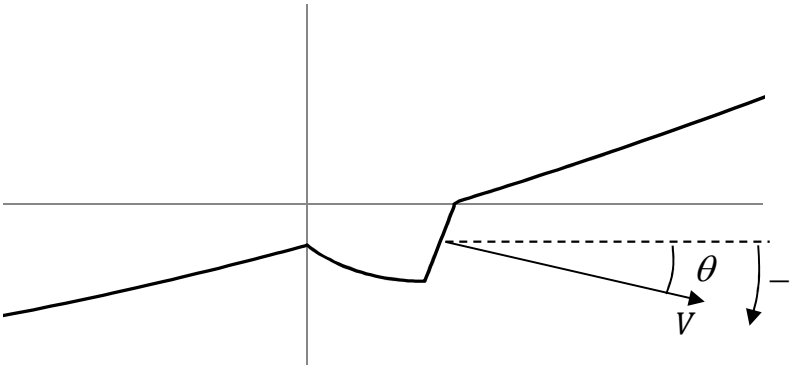

Figure 4-38 a) Hose fairing with red patch used for ventilation boundary condition and b) the ventilation definition with velocity magnitude V and direction angle θ

The calculated cases are listed in Table 4-17. Three different ventilation mass flows and five different ventilation angles θ_1 to θ_5 have been applied. Case V_1 θ_1 corresponds to ideal natural ventilation as θ is equal to the fuselage slope and the pressure drop caused by the perforated surface is not considered in a

first step. The mass flow based on V_1 corresponds approximately to 10% of the mass flow through a representative propulsion engine of an A330 [54] at cruise condition [76].

	$\boldsymbol{V}$	$\dot{\boldsymbol{m}}$	$\boldsymbol{\theta_1}$	$\boldsymbol{\theta_2}$	$\boldsymbol{\theta_3}$	$\boldsymbol{\theta_4}$	$\boldsymbol{\theta_5}$
V_1	$V\infty$	17.2 kg/s	10°	0°	-10°	-20°	-30°
V_2	$0.5V\infty$	8.6 kg/s	-	-	-	-	-30°
V_3	$0.25V\infty$	4.3 kg/s	-	-	-	-	-30°

Table 4-17 Case matrix for all ventilation cases and ventilation angle θ with applied mass flows which are defined through ventilation velocity and free stream density, V∞=172 m/s

4.2.3.1.1 Natural ventilation

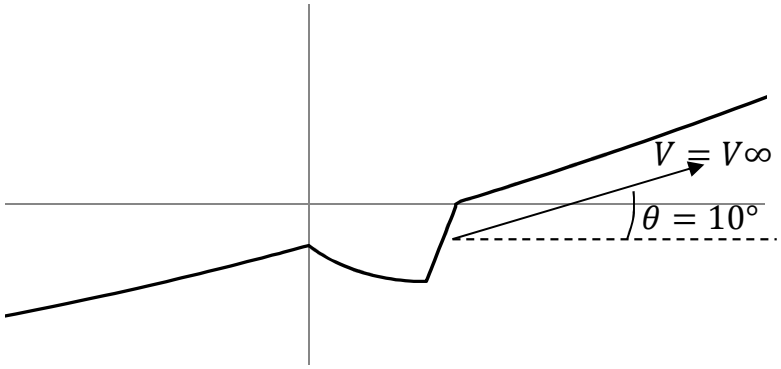

Figure 4-39 Setup for the simulation of ideal natural ventilation with ventilation angle θ parallel to fuselage slope and ventilation velocity V equal to free stream velocity

Natural ventilation is considered as a potential flow control mechanism and avoids recirculation behind the fairing. A schematic sketch is presented in Figure 4-39 and the result can be observed in Figure 4-40 b) where the streamlines are straight and even compared to those from Figure 4-40 a) where a separation bubble is generated.

a)

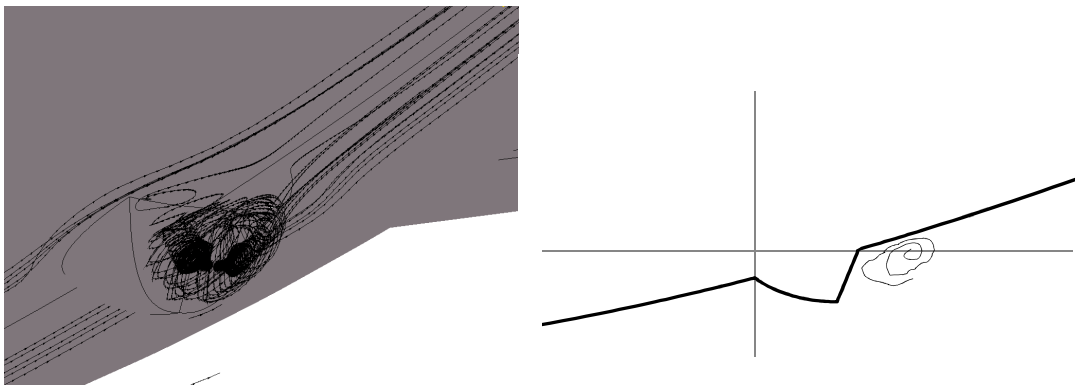

b)

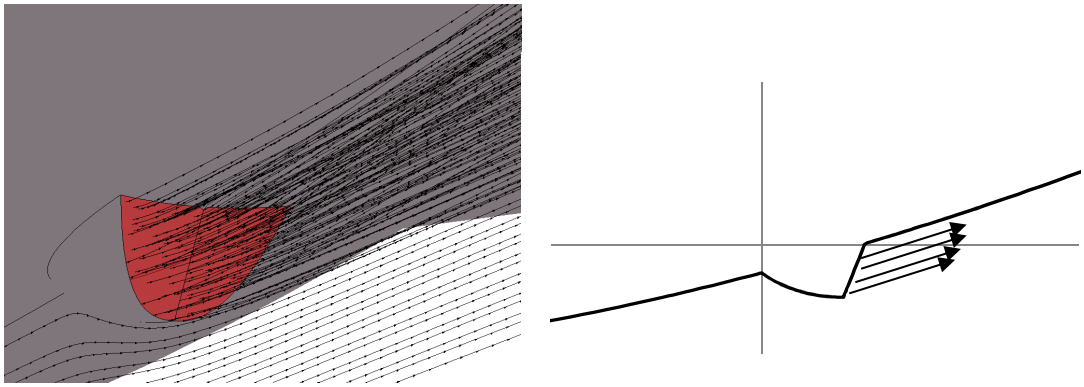

Figure 4-40 a) Recirculation zone behind fairing in comparison with ventilated fairing in Figure b)

4.2.3.1.2 Artificial ventilation

In Section 3.2.1 the sensitivity of the hose characteristic on the wake pattern has been presented. The rear fuselage upwash pushes the hose upward which is the primary cause for the unwanted inflection point in the hose shape. A manipulation of the rear fuselage upwash could therefore be an approach to control the position and shape of the hose and the drogue, where the possible potential is assessed through the application of artificial ventilation. As shown in Figure 4-41 the dynamic pressure deficits are associated to the rear fuselage upwash which in turn is characterised by the rear fuselage shape and the angle of attack. The dynamic pressure deficits increase with decreasing upwash and

with decreasing angle of attack. Therefore, through redirection of the local upwash a control of the hose could be achieved.

$$\gamma = 13°\ P_{dyn}\infty = 9760\ Pa\ Ma\infty = 0.55$$

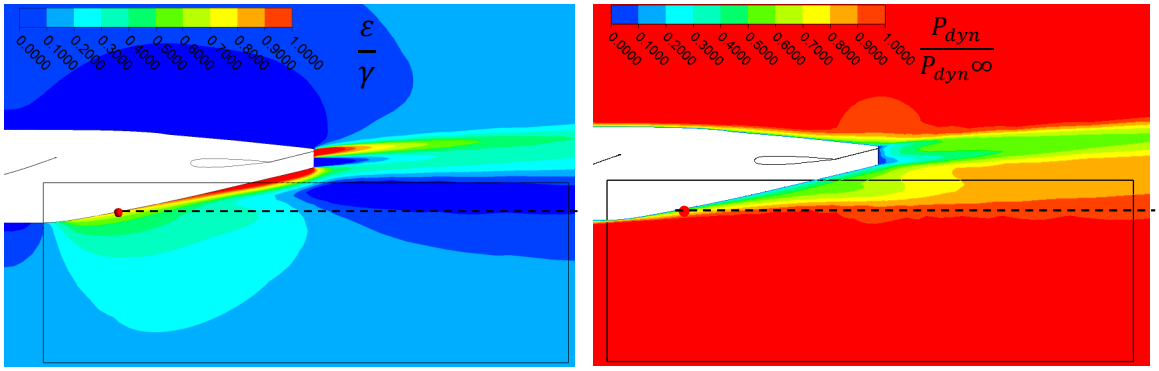

Figure 4-41 Both predominant flow parameter, the rear fuselage upwash angle which is a function of α and ε (left) and the local dynamic pressure (right) within the interrogation area of interest for the CRM [5] WBT configuration, FC_3: Mach = 0.55, c_l = 0.5, $\alpha = 3.2°$

The assessment of this approach has been made through a parametric study, where the ventilation angle θ varies from 10° to -30° in steps of 10° as shown in Table 4-18.

		$\dot{m}_1$	θ_1	θ_2	θ_3	θ_4	θ_5
V_1	$V\infty$	17.2 kg/s	10°	0°	-10°	-20°	-30°

Table 4-18 Case matrix for artificial variation of ventilation angle θ with constant mass flow based on ventilation velocity, free stream density and the hose exit area

The effect of the ventilation angle θ variation at a constant ventilation mass flow of $\dot{m}_1$= 17.2 kg/s is shown in Figure 4-42. The left column presents the local dynamic pressure P_{dyn} normalised to the free stream dynamic pressure $P_{dyn}\infty$, and the right column the total pressure distribution P_{tot} normalised by the free stream P_{tot} ∞. The simulations are made at Mach 0.55 and α=0.52°. With decreasing ventilation angle θ the dynamic pressure deficits increase above the vertical fairing position where the air is ejected. This is indicated with the

dashed line. The ejection of the air introduces air flow of high kinetic energy and creates a barrier between the air above the vertical ejection position and the air beneath. The flow cannot follow the rear fuselage shape anymore and the flow field in close vicinity to the rear fuselage is disrupted. The consequence is higher total pressure loss. This can be observed especially for $\theta = -30°$. However, the overall performance of the aircraft is not affected. For all cases shown in Table 4-16 the drag coefficient remains at a constant value of C_d= 0.034. This is a crucial finding since this is the prerequisite for the approach to be classified as potentially applicable or not – an excessive aerodynamic performance loss would eliminate the approach. The effect on the hose however is notable and can be observed in Figure 4-43.

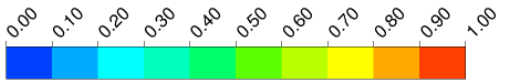

Ma∞ = 0.55, α=0.52°, P_{dyn} = 9.8kPa

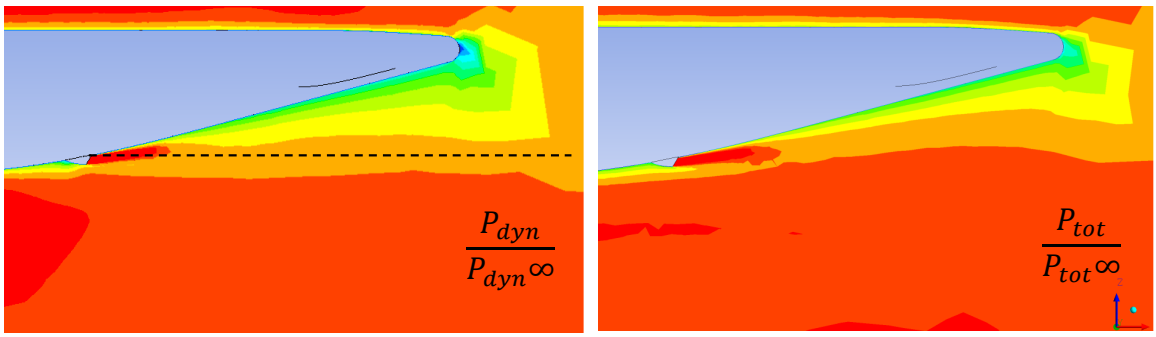

θ =10°

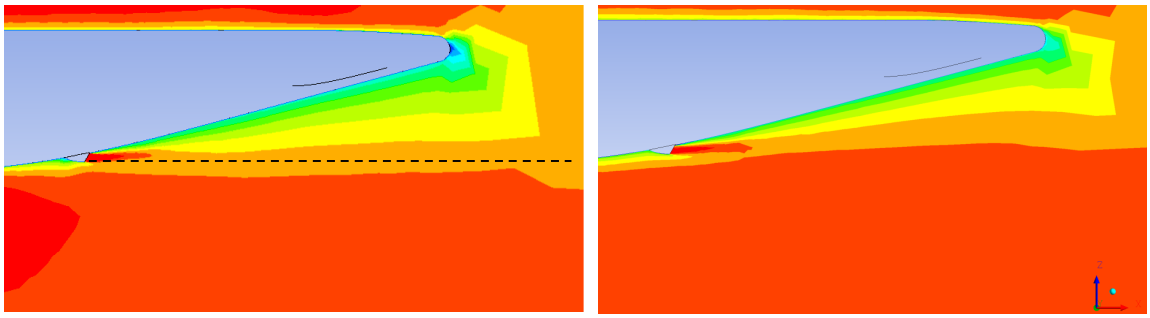

θ =0°

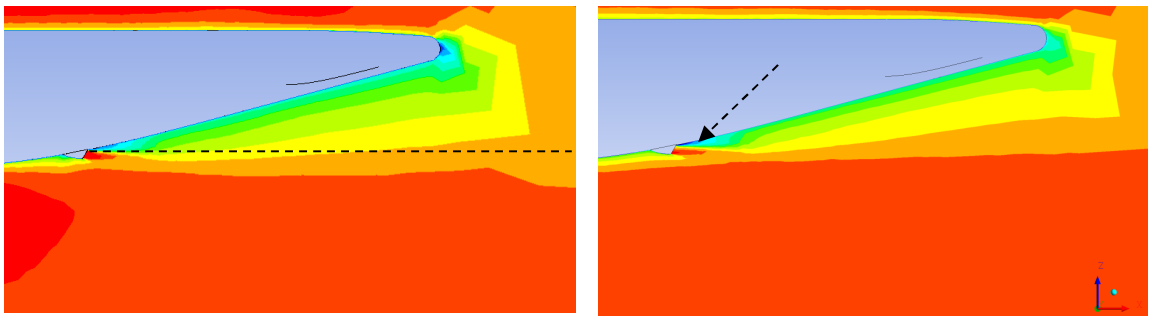

θ =-10°

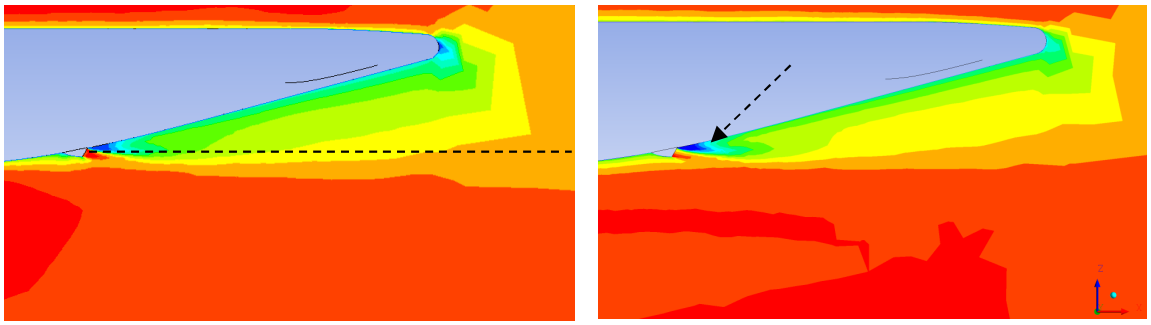

θ =-20°

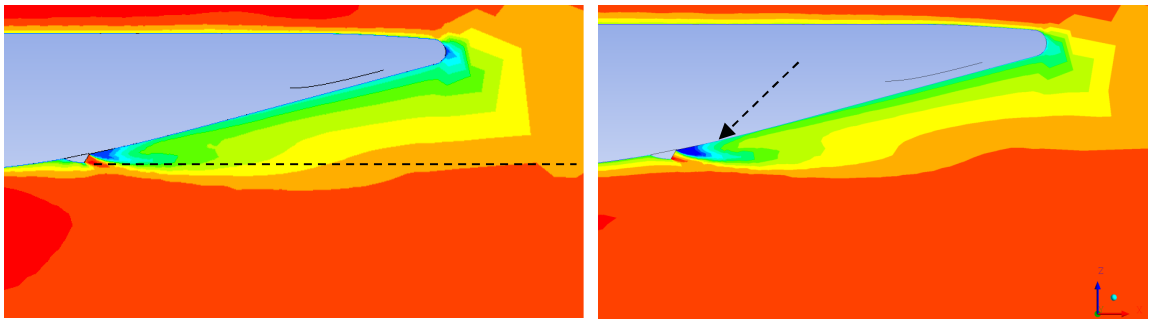

θ =-30°

Figure 4-42 Local dynamic pressure number normalised by the free stream dynamic pressure on the left and total pressure normalised by the free stream total pressure on the right for ventilation angles θ=10° to −30° and the DLR-F6 [4] FC_3: Mach = 0.55, c_l = 0.5, α = 3.2°, the dashed line separates the area of total pressure losses and the area of hose deployment

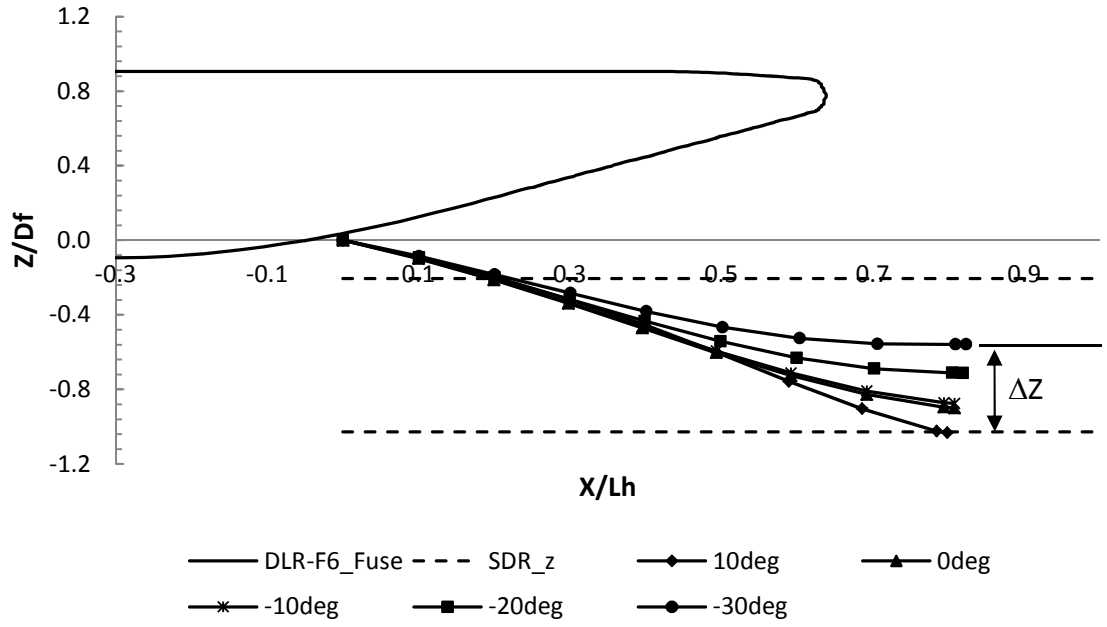

Figure 4-43 Effect of ventilation angle θ on drogue position and hose shape for θ=10° to -30° at a constant mass flow of 17.2 kg/s for the DLR-F6 [4] including the nominal vertical drogue position range SDR_z FC_3: Mach = 0.55, C_l = 0.5, α = 0.45°

The difference of the vertical position between $\theta = 10°$ and between $\theta = -30°$ is more than 50% of the vertical drogue range and final drogue position is moved into the required range (Figure 4-43). Furthermore, through the lift of the drogue for $\theta = -30°$ the number of the unwanted inflection points is reduced from two to one as shown in Figure 4-44.

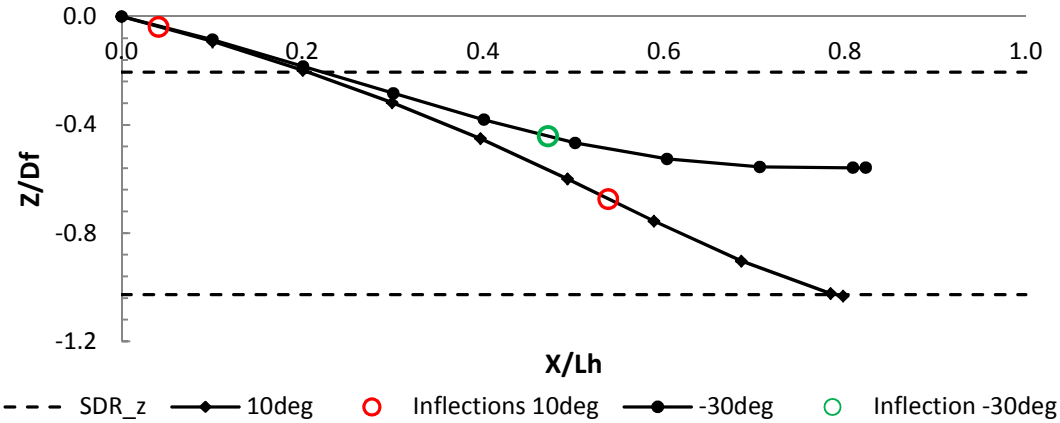

Figure 4-44 Hose characteristics for θ=10° and θ=-30° with inflection points indicated by the circles and spatial drogue range indicated by dashed lines

However, the effectiveness of this approach does not depend predominantly on the kinetic energy of the ejected flow. This is investigated through the variation of the ventilation velocity. The applied parameters V_2, V_3 at constant ventilation angle $\theta = -30°$ are listed in Table 4-19 and the results of the hose characteristics are presented in Figure 4-45. It can be observed that the hose tends to be notably lifted as the ventilation velocity decreases. A possible explanation is presented later in this section.

	V	$\dot{m}_1$	θ_1	θ_2	θ_3	θ_4	θ_5
V_2	$0.5V\infty$	8.6 kg/s	-	-	-	-	-30°
V_3	$0.25V\infty$	4.3 kg/s	-	-	-	-	-30°

Table 4-19 Case matrix for variation of ventilation mass flow at constant angle θ=–30° where the mass flow is based on the free stream density and the velocities V_1, V_2

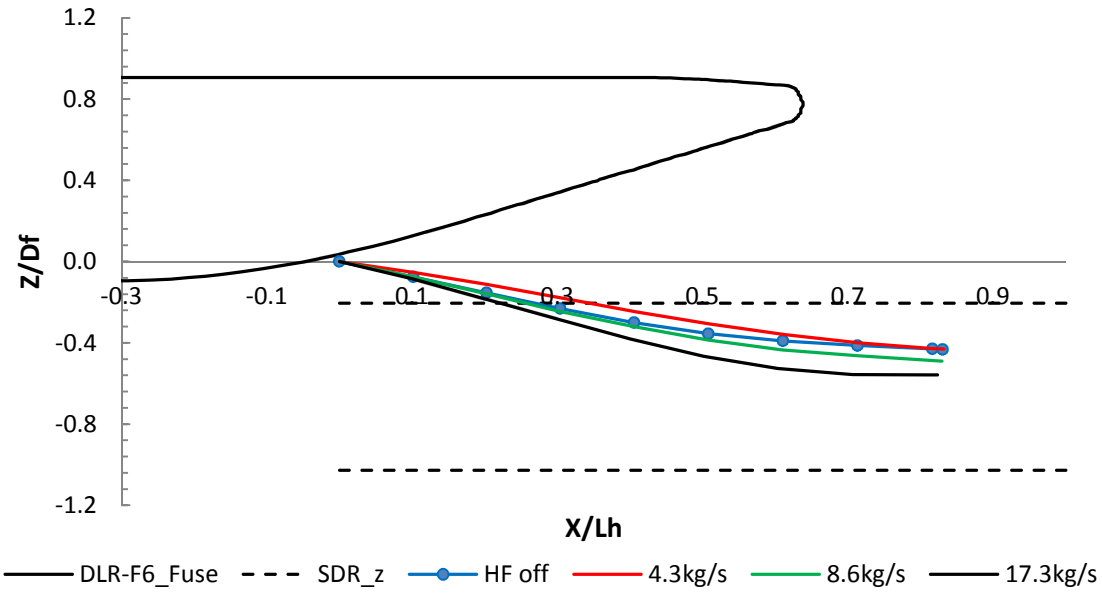

Figure 4-45 Effect of ventilation velocity variation on hose characteristic and position in comparison for 0.25V∞ (red), 0.5V∞(green), V∞(black) and no fairing (blue with dots) for a ventilation angle θ of -30°

The increase in total pressure loss with decreasing ventilation velocity can be explained as follows. The following flow field comparisons from Figure 4-46 are indicative of the cause of total pressure loss.

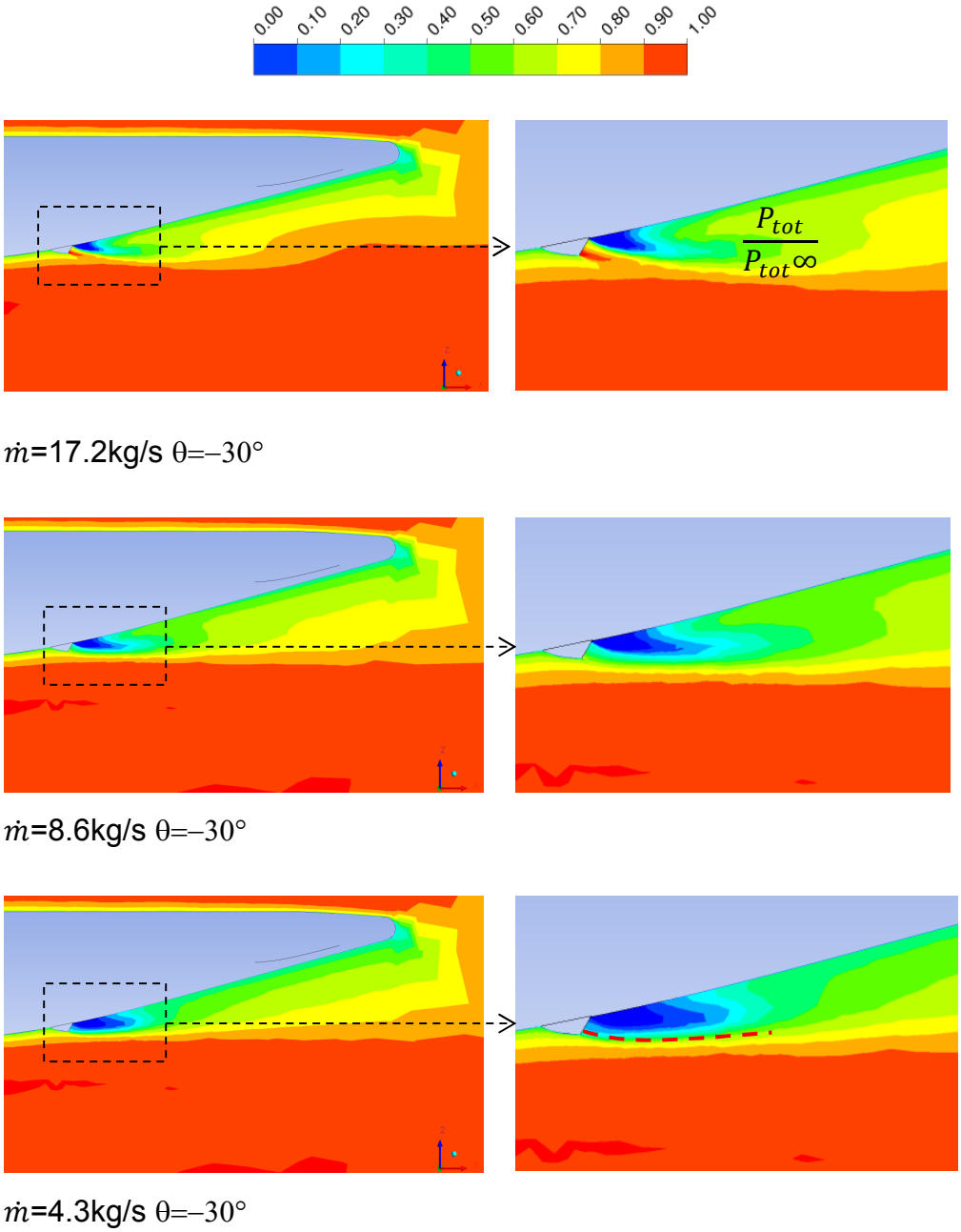

Figure 4-46 Total pressure ratio distributions Ptot/Ptot∞ along the rear fuselage centreline of the DLR-F6 [4] configuration showing the effect of ventilation mass flow for a fixed ejection angle θ= -30° with zoomed separation zone on the right

With decreasing mass flow the separation bubble grows and thus the loss in total pressure increases. The growth of the separation bubble is most probably caused by the velocity difference between the ejection velocity and the surrounding velocity. The higher the difference the bigger the separation bubble becomes. The notable effect on the hose is presented in Figure 4-47 a), where the red line is the hose shape obtained for the case $\dot{m} = 17.2kg/s$ at θ=-30° and the blue line is that for the case $\dot{m} = 4.3kg/s$ at θ=-30°. A clear lifting effect can be observed for the case $\dot{m} = 4.3kg/s$ at θ=-30°. However, for both cases the rear upwash angle as well as the dynamic pressure level within the interrogation area is very similar as illustrated in Figure 4-47 b) and 4-48 b). The cause for the lift is most probably the different boundary layer properties on the hose surface.

a)

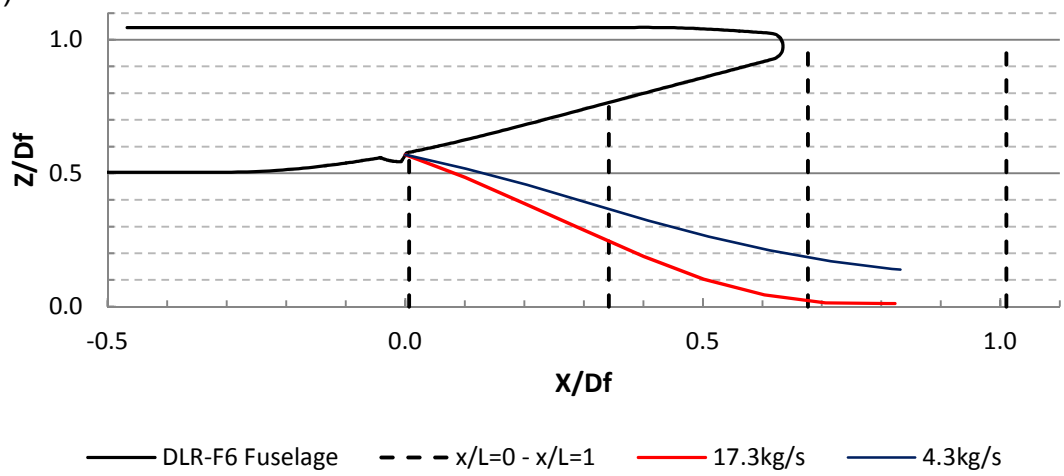

b)

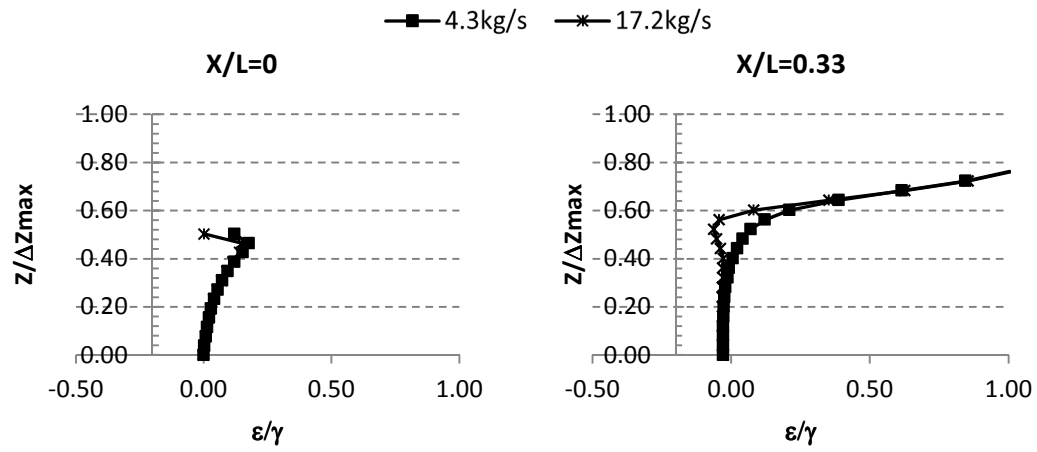

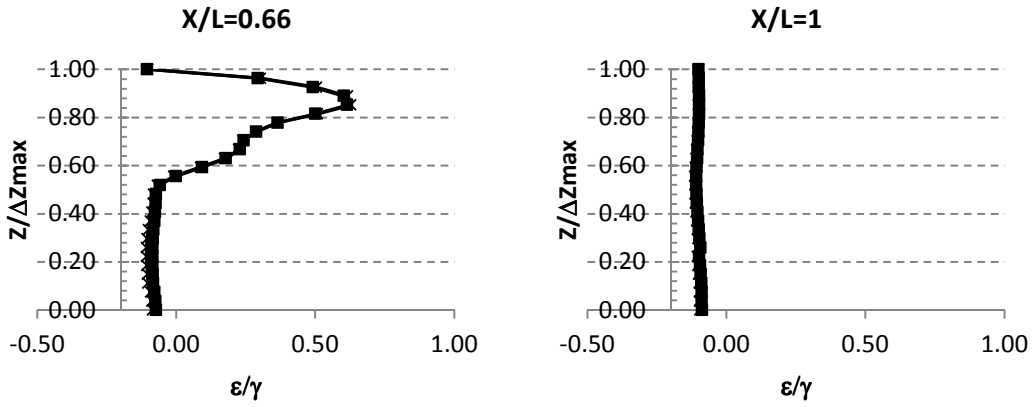

Figure 4-47 a) Hose characteristics in comparison Blue: $\dot{m}$=17.2 kg/s θ=-30°, Red: $\dot{m}$=4.3 kg/s θ=-30, b) Comparison of upwash angle ε normalised by the rear fuselage angle γ of 15°, FC_3: Mach = 0.55, C_l = 0.5, α =0.52

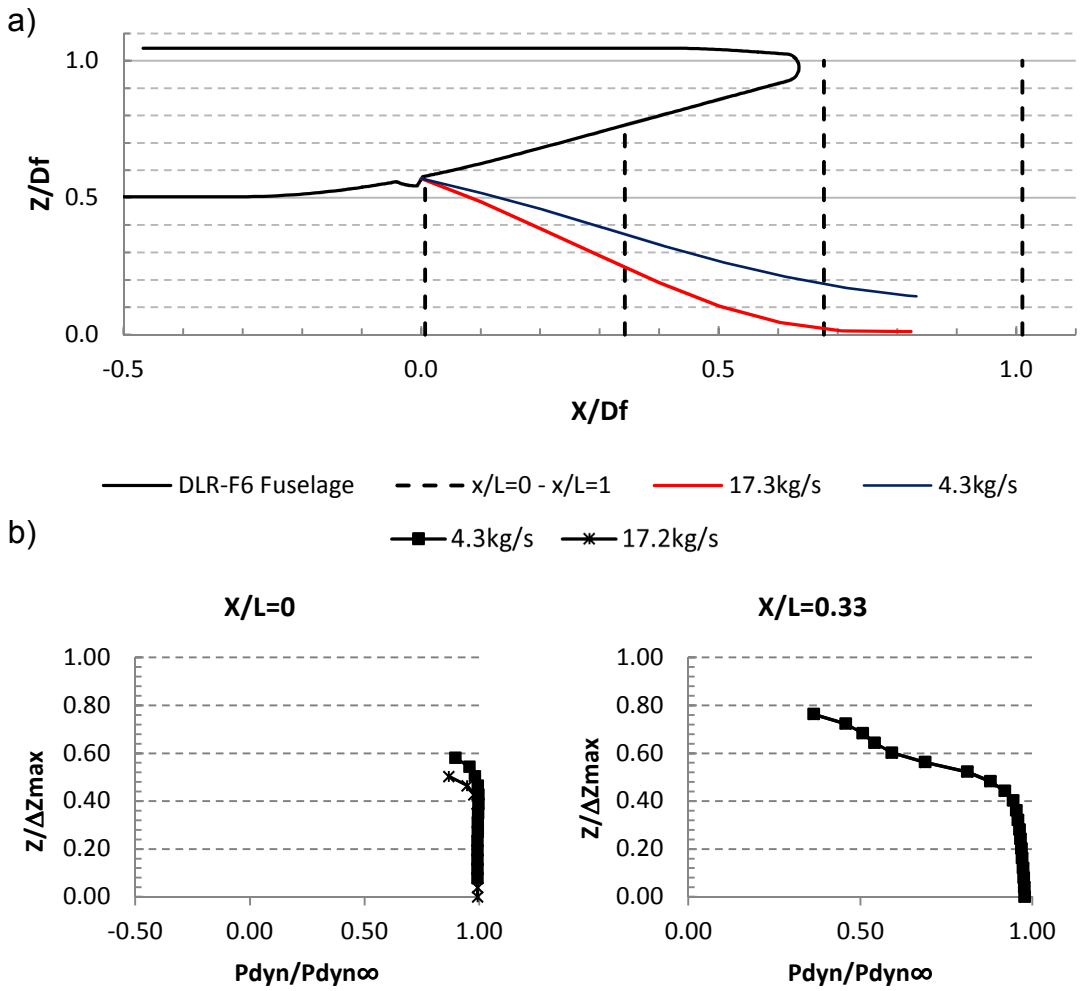

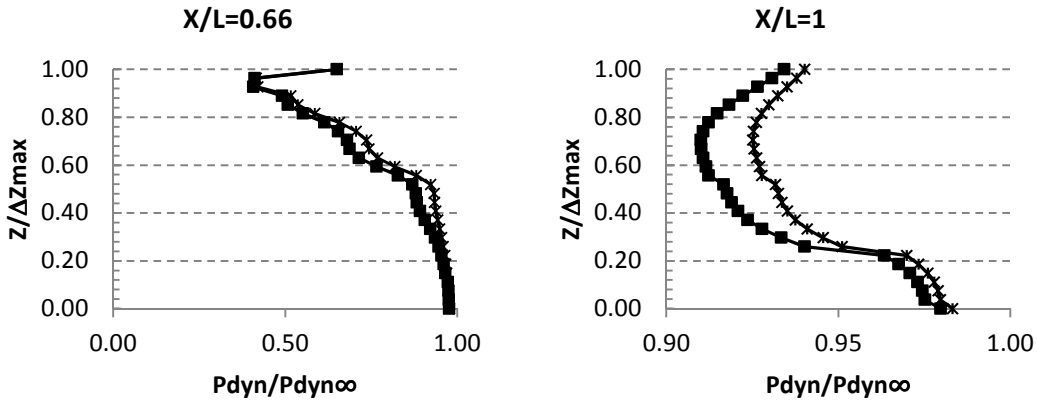

Figure 4-48 a) Hose characteristics in comparison red: $\dot{m}$=17.2 kg/s θ=-30°, blue: $\dot{m}$=4.3 kg/s θ=-30, b) Comparison of dynamic pressure P_{dyn} normalised by the free stream pressure $P_{dyn}\infty$, FC_3: Mach = 0.55, C_l = 0.5, α =0.52

As studied in the literature review in Section 3.3.2 the drag force on the hose strongly depends on the state of the boundary layer. Depending on the critical Reynolds number in close vicinity to the hose, the separation points are located differently – either more downstream or more upstream as illustrated in Figure 4-49 [6].

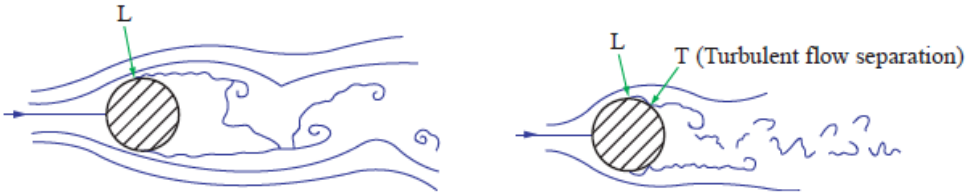

150 < Re_e < 3E^5 *3E^5 < Re_e < 1E^6*

Figure 4-49 2D flow separation point locations on a circular geometry for different Reynolds numbers [6]

Hence, depending on where the separation points are located the drag force varies with the downstream facing area and the associated pressure behind the hose. As shown in Figure 4-50, within the transcritical Reynolds number range, even small differences in Reynolds number between two different flow fields can yield notable differences in shape and position of the hose, due to rapid drop of drag.

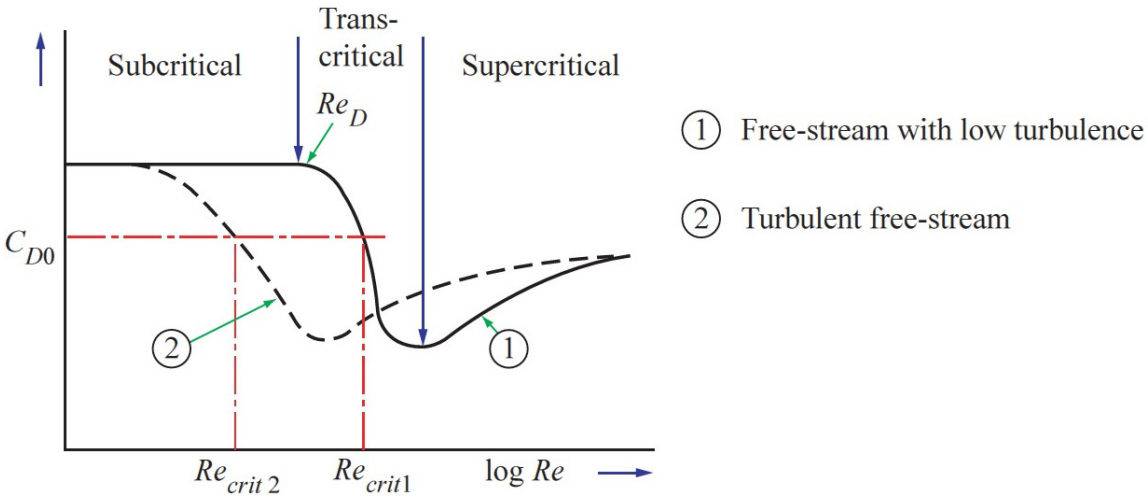

Figure 4-50 Drag coefficient C_{D0} as a function of Reynolds number for a cylinder normal to the flow and the influence of higher turbulence intensity (dashed curve) on C_{D0} [6]

The local Reynolds number distribution on the cross flow planes can be observed in Figure 4-51 b) on the left row and the differences between case $\dot{m} = 17.2kg/s$ at θ=-30° (Figure 4-51 a) red line) and case $\dot{m} = 4.3kg/s$ at θ=-30° (Figure 4-51 a) blue line) in Figure 4-51 b) on the right row. The reference length for the Reynolds number is the hose diameter. The Reynolds number differences between the two cases are along cross flow plane x/L=0 in the order of 10^4, for x/L=0.33 in the order of 6*10^4, for x/L=0.66 in the order of 2*10^4 and for x/L=1 in the order of 4*10^3. If the variation takes place within the transcritical range, these differences can result in notably different hose characteristics. The most direct and precise way to compare the local critical Reynolds number associated to the static hose position is to plot the local Reynolds number along the hose. However, this couldn't be performed due to time constraints.

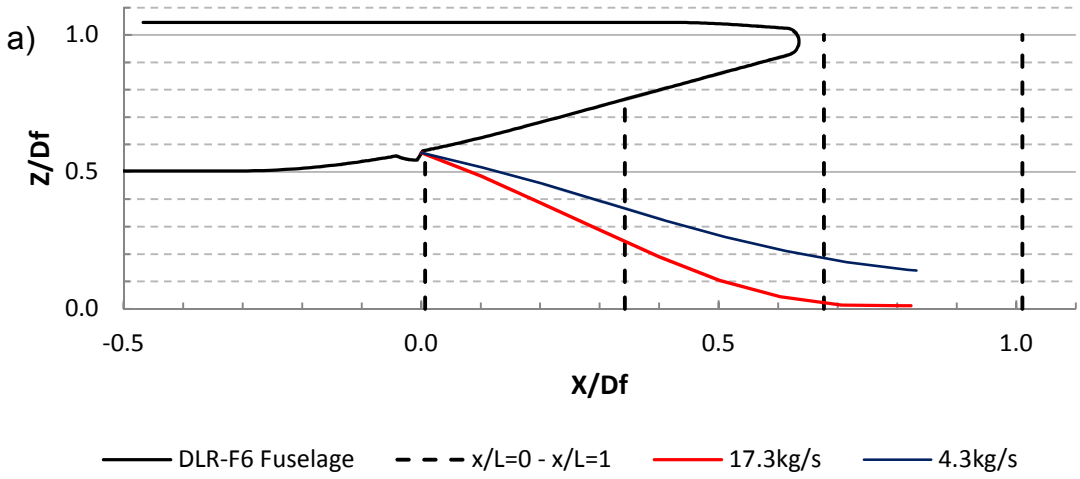
a)
1.0
0.5
0.0
Z/Df
-0.5
0.0
0.5
1.0
X/Df
DLR-F6 Fuselage
x/L=0 - x/L=1
17.3kg/s
4.3kg/s

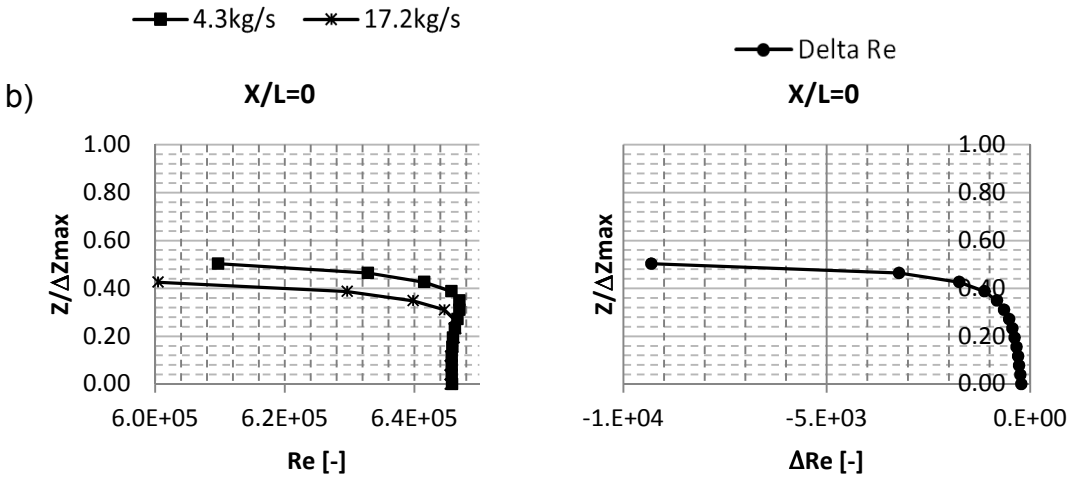
4.3kg/s
17.2kg/s
b)
X/L=0
1.00
0.80
0.60
0.40
0.20
0.00
Z/ΔZmax
6.0E+05
6.2E+05
6.4E+05
Re [-]

Delta Re
X/L=0
1.00
0.80
0.60
0.40
0.20
0.00
Z/ΔZmax
-1.E+04
-5.E+03
0.E+00
ΔRe [-]

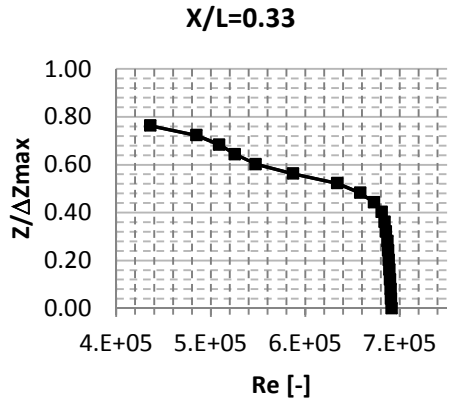
X/L=0.33
1.00
0.80
0.60
0.40
0.20
0.00
Z/ΔZmax
4.E+05
5.E+05
6.E+05
7.E+05
Re [-]

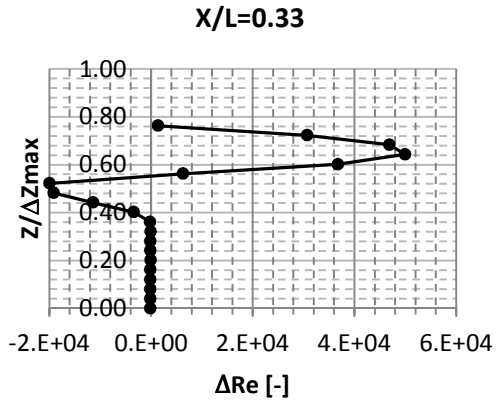
X/L=0.33
1.00
0.80
0.60
0.40
0.20
0.00
Z/ΔZmax
-2.E+04
0.E+00
2.E+04
4.E+04
6.E+04
ΔRe [-]

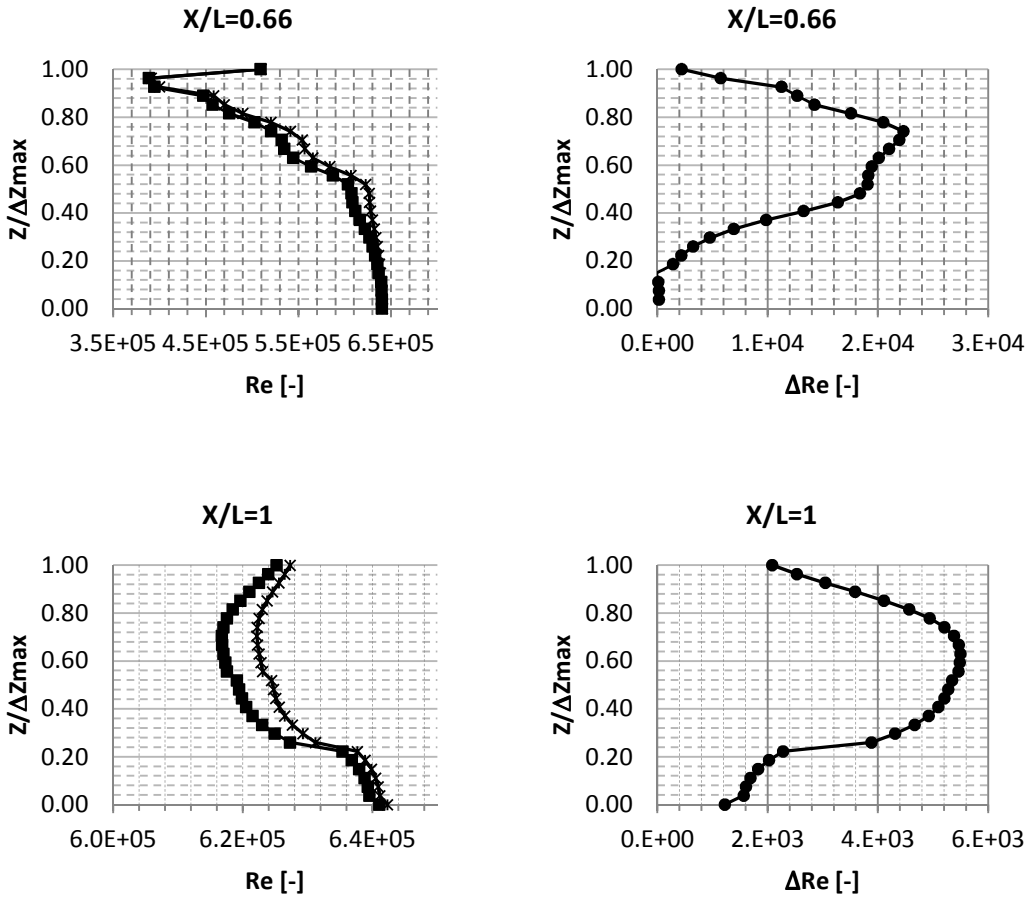

Figure 4-51 a) a) Hose characteristics in comparison red: $\dot{m}$=17.2 kg/s θ=-30°, blue: $\dot{m}$=4.3 kg/s θ=-30,b) Comparison of the local Reynolds number related to the hose diameter (left) and the differences of the local Reynolds number of both flow fields (right) , FC_3: Mach = 0.55, C_l = 0.5, α =0.52

4.2.4 Hose exit position variation

For current conventional hose and drogue systems with hose deployment from the fuselage the hose exit is usually located on the fuselage and at the centreline of the fuselage. This configuration has been considered for all hitherto conducted hose calculations. The analysis of the hose-wake interaction in Section 4.2.1 revealed that the hose shape characteristics are strongly associated with the wake characteristic, with respect to the hose inflection point predominantly by the rear fuselage upwash. The wake analysis in turn revealed a longitudinal and vertical variation of the rear fuselage upwash. In particular, the upwash decreases with increasing vertical distance from the fuselage as well as in longitudinal direction as shown in Figure 4-52 by the white arrows. A shifting of the hose exit towards these directions means a shifting out of the critical upwash zone. The study of different hose exit positions along the fuselage is studied independently and does not refer to any of the previously presented results. Thus, the reference or baseline cases for the hose exit variation study are provided within the study itself.

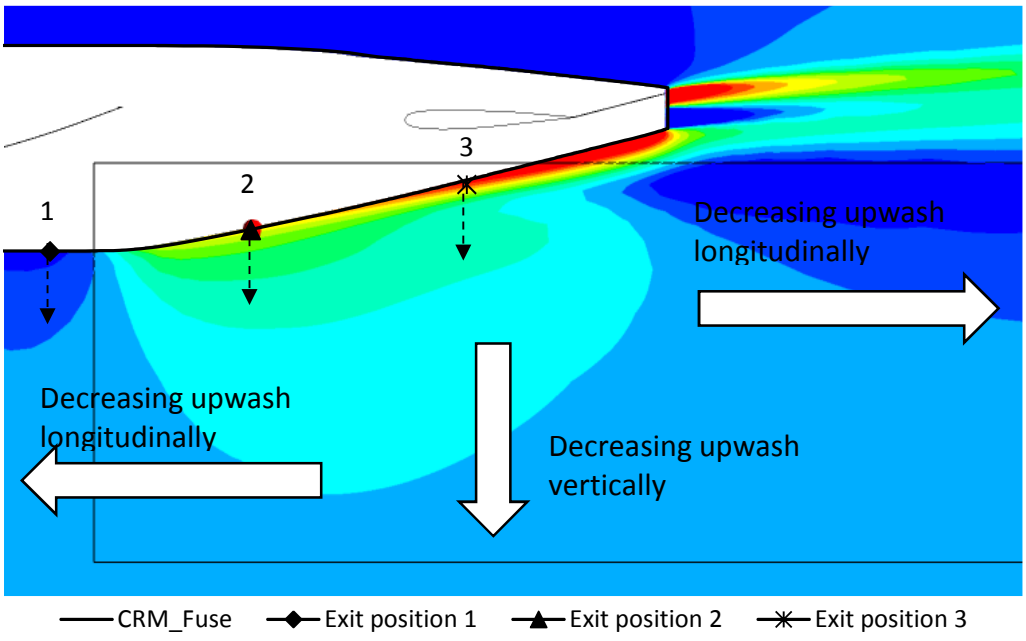

Figure 4-52 Typical near field wake of an aircraft similar to the A330 [54] on symmetry plane with randomly chosen hose exit positions along the fuselage, which shows the potential to take the hose out of the critical upwash areas vertically and longitudinally

In Figure 4-52 the longitudinal shift is indicated through exit position 1, 2, and 3. The vertical shift is indicated through the black dashed arrows, which means an off fuselage deployment. Technically this could be realised through the use of a rigid telescopic device as shown in Figure 4-53, similar to a flying boom.

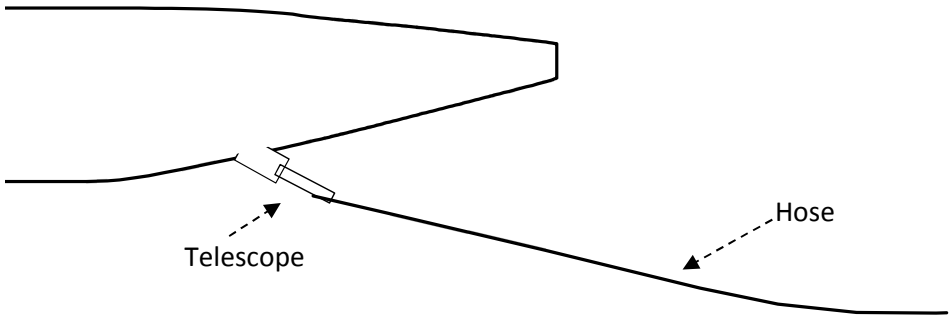

Figure 4-53 Off-fuselage hose deployment with telescopic device

So far both approaches, the longitudinal (x) shift and the vertical (z) shift, are discussed for a deployment on the fuselage centreline. However, an additional circumferential shift on and off fuselage, as shown in 4-54, could also be an approach. The technical solution for a circumferential deployment on the fuselage could simply be a circumferentially shifted hose fairing (red arrow), and for off-fuselage also a telescope like for the centreline deployment shown above in Figure 4-53.

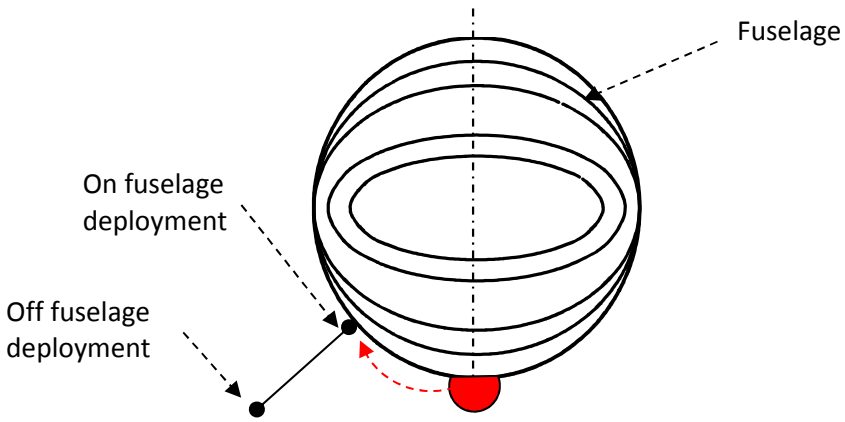

Figure 4-54 Circumferential on and off fuselage hose deployment view from back of fuselage

4.2.4.1 Variation with DLR-F6

To investigate the effect of the hose exit position on the hose characteristics a variation of the hose exit has been conducted both with the DLR-F6 [4] and the CRM WBT [5] geometry. The considered hose exit positions are explained in 2D by means of the DLR-F6 [4] geometry in Figure 4-55.

a)

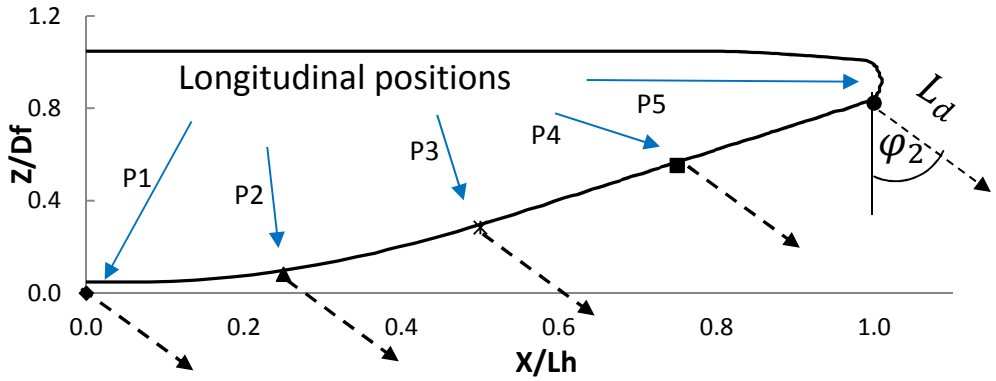

b)

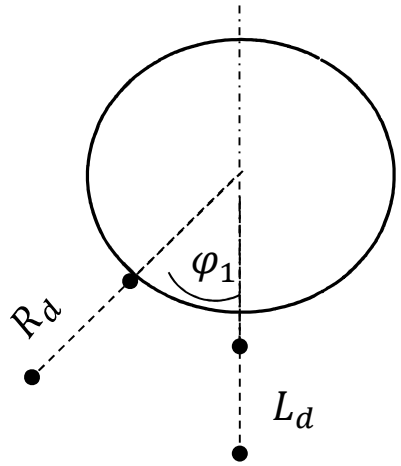

Figure 4-55 a) Schematic side view of the DLR-F6 [4] fuselage with indicated longitudinal hose exit positions, on (blue arrows) and off fuselage (black dashed arrows), including off fuselage displacement $\boldsymbol{L_d}$ *and pivoting angle* $\boldsymbol{\varphi_2}$ *, b) schematic rear view of an arbitrary fuselage, with circumferentially shifted hose exit positions, including off fuselage displacement* $\boldsymbol{L_d}$*, radial off fuselage displacement* $\boldsymbol{R_d}$*, and azimuthal angle* $\boldsymbol{\varphi_1}$

The hose exit variation is conducted longitudinally on and off fuselage and at regular distances (4 longitudinal positions Figure 4-55 a). The separations correspond to fuselage diameter D_f. The longitudinal variation starts with position P_1 at x/Lh=0 which corresponds to the same height as the wing trailing edge of the DLR-F6 [4]. A circumferential variation on and off fuselage is also considered as schematically shown in Figure 4-55 b). Every hose calculation result for any of the positions presented below is supported by similar 2D figures which indicate the position of the hose exit along the fuselage.

The variation has been conducted at flight condition 3 at a Mach number of 0.55 and an angle of attack α=0.45°. The results for the longitudinal variation on the centreline and on the fuselage are presented in Figure 4-56 which shows that for all positions, P_1 to P_5, the hose assumes a shape with one or two inflection points. Furthermore it can be observed, that the hose curvature between the origin and the inflection point increases notably form P_1 to P_2. This is due to stronger upwash at position P_2. The results also reveal that the drogue height relative to the vertical hose exit position decreases as the longitudinal position is placed more downstream.

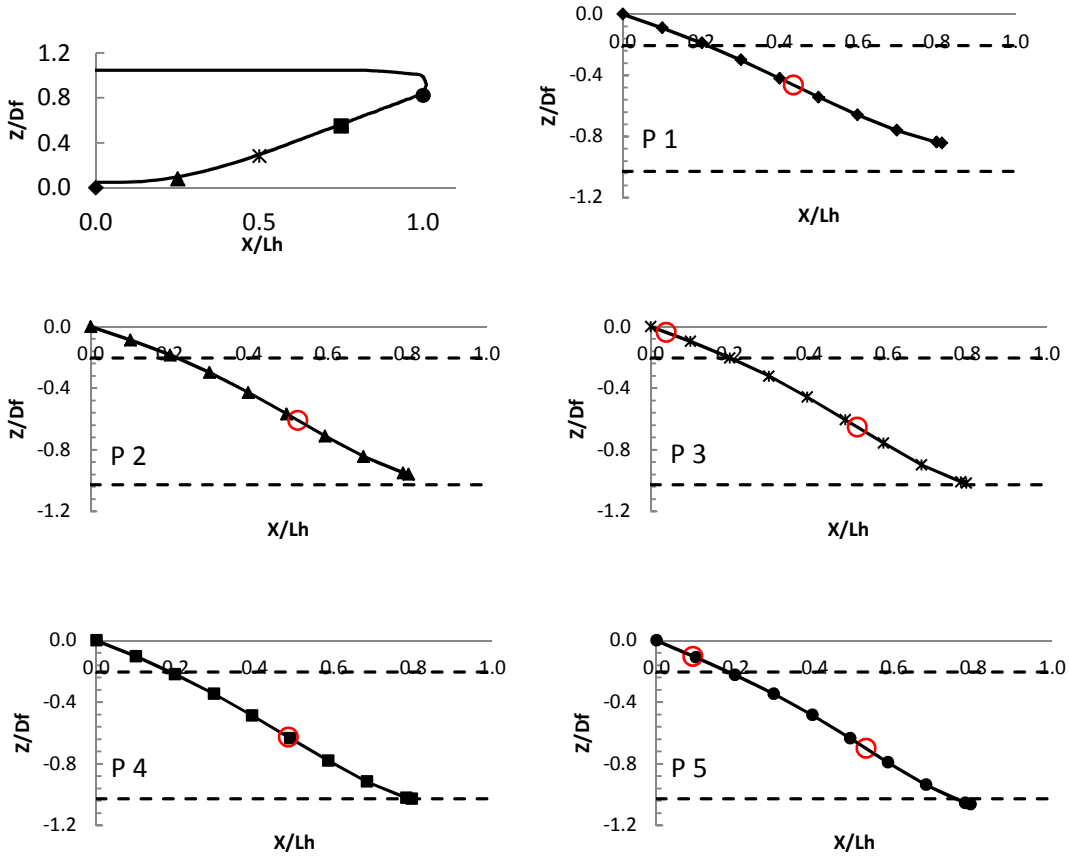

Figure 4-56 Hose shape results for longitudinal exit variation on centreline and on fuselage with inflection point positions indicated by the red circles, for the DLR-F6 [4] FC_3: Mach = 0.55, C_l = 0.5, α =0.45°, hose exit positions are always shifted to X, Z origin 0, 0 for graphical representation

For the configurations in Figure 4-56, this makes the crucial difference on whether the drogue is within the required spatial drogue range or not. A comparison between hose exit position P_1 and P_5 makes this clear. Hence, for a fixed flight condition the position of the hose exit along the centreline and on the fuselage the hose characteristics change notably, and can make a crucial difference in terms of the catenary requirement.

Exactly the same behaviour can be observed for the configurations presented in Figure 4-57 where the hose exit is still on the centreline but off fuselage. There is no improvement regarding the inflection point and the hose curvature between the origin and the inflection point increases notably from position P_1 to P_2. Moreover, the hose exposed form P_1 is within the required vertical drogue range whereas all other drogue positions are either on the lower limit or outside the range. Hence, an off fuselage deployment on the centreline yields no improvement relative to the same longitudinal position on the fuselage. For the next variation the hose exit is shifted circumferentially and therefore off centreline.

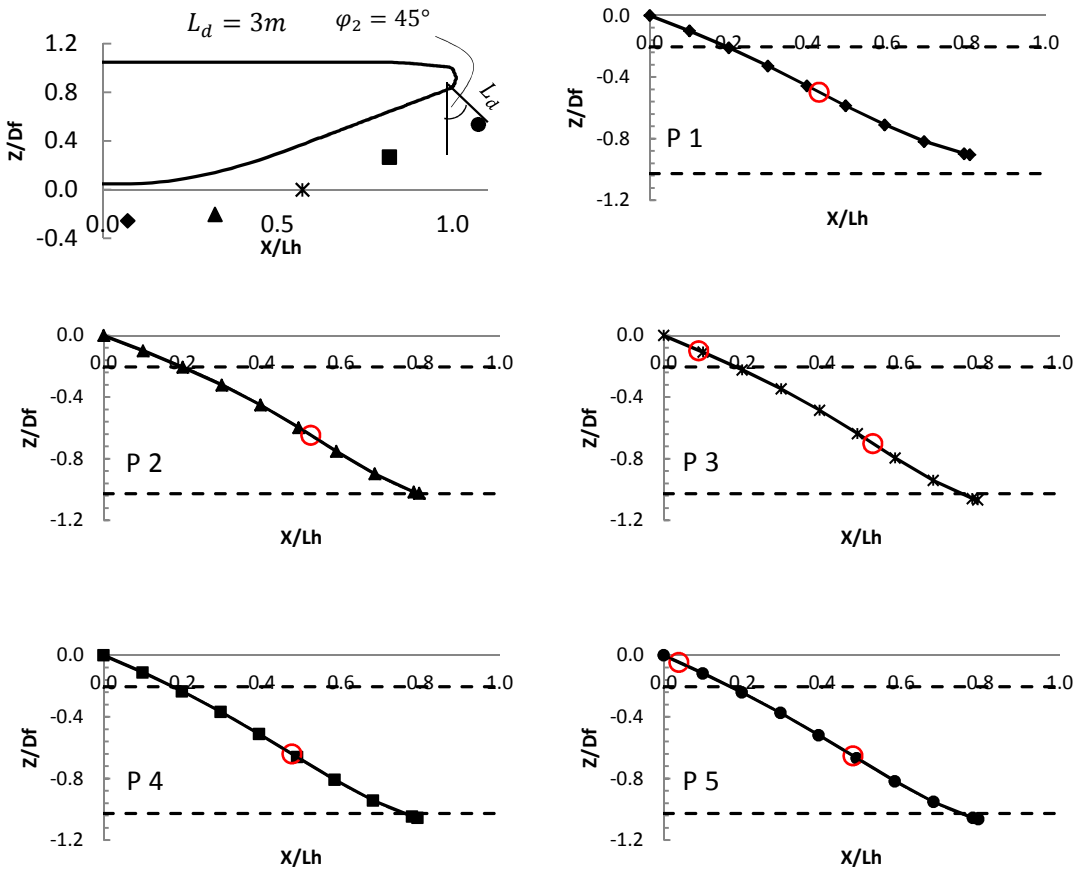

Figure 4-57 Hose shape results for longitudinal exit variation on centreline and off fuselage, with inflection point positions indicated by the red circles, for the DLR-F6 [4] FC_3: Mach = 0.55, C_l = 0.5, α =0.45°, hose exit positions are always shifted to X, Z origin 0, 0 for graphical representation

The hose exit is on the fuselage and varied longitudinally throughout 4 positions which are shown in Figure 4-58 a) at a constant azimuthal angle φ of 45° (Figure 4-58 b)). Figure 4-58 c) illustrates that the vertical drogue position meets the range requirement for all longitudinally varied hose exit positions. However, regarding the inflection point no improvement has been achieved as the hose assumes an inflected shape for all positions

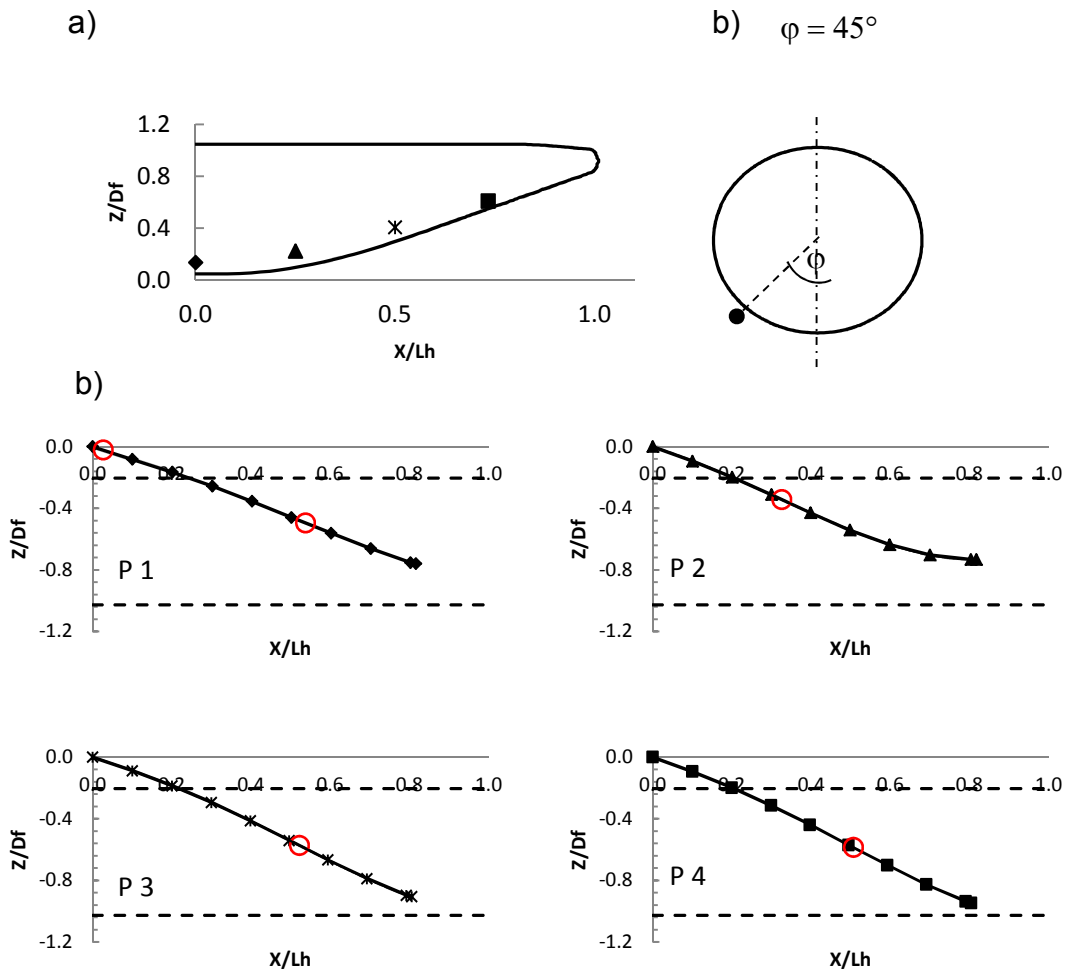

Figure 4-58 a) Longitudinal hose exit positions, b) circumferential hose exit positions, c) hose shape results for longitudinal exit variation off centreline and on fuselage, with inflection point positions indicated by the red circles, for the DLR-F6 [4] FC_3: Mach = 0.55, C_l *= 0.5,* α *=0.45°, hose exit positions are always shifted to X, Z origin 0, 0 for graphical representation*

For the deployment on the centreline it could be assumed that the lateral forces on the hose are balanced. No plots were required to show the lateral hose displacement since the hose is in line with the fuselage centreline. However, with the circumferential displacement of the hose exit the lateral forces on the hose are not balanced anymore. Furthermore, the effect of an inflected hose shape on the dynamic response of the hose has been studied for the case where the inflection point takes place vertically. The effect of a horizontally aligned inflection point has not been studied. Nevertheless, the hose characteristics obtained for the circumferential hose exit positions are investigated for possible inflection points as shown in Figure 4-59 where the response of the hose on the circumferential displacement can be observed.

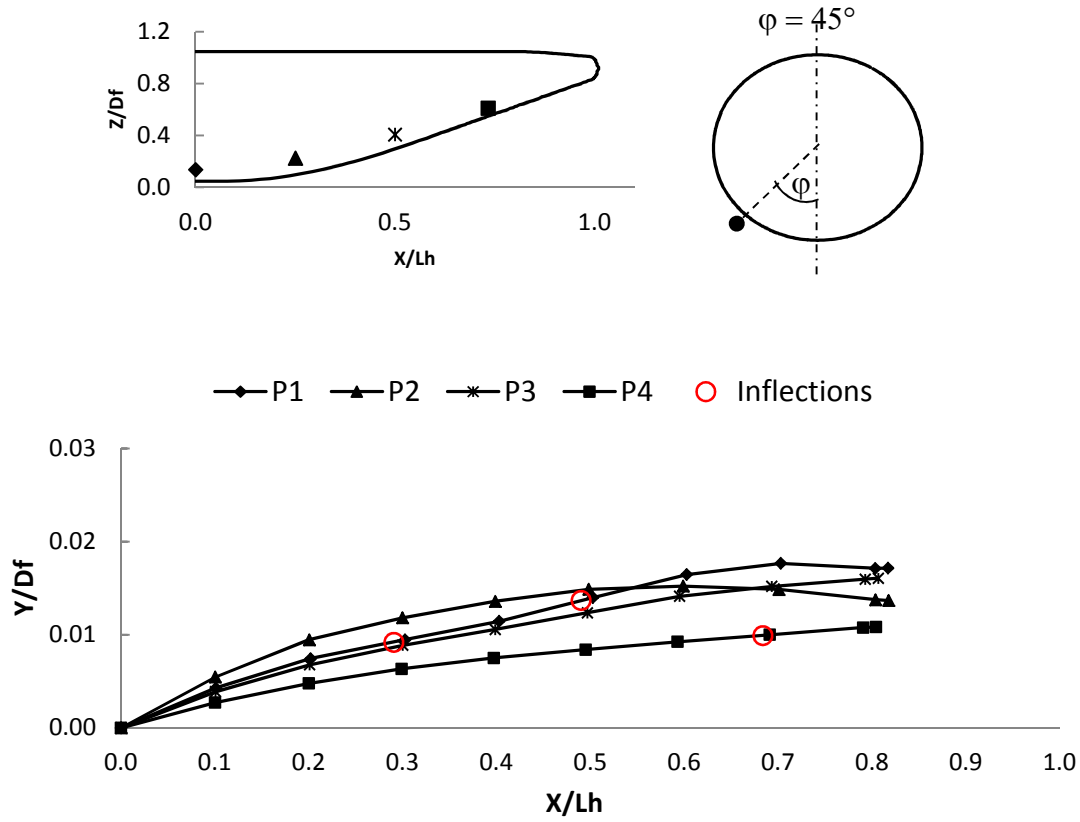

Figure 4-59 Hose shape results for longitudinal exit variation off centreline and on fuselage, view from above, which shows the lateral displacement normalised by the fuselage diameter D_f and the inflection points indicated by the red circles, for the DLR-F6 [4] FC_3: Mach = 0.55, C_l = 0.5, α =0.45°, hose exit positions are always shifted to X, Y origin 0, 0 for graphical representation

The ordinate shows the lateral displacement of the hose normalised by the fuselage diameter D_f. The hose which is deployed from position P_1 shows the highest displacement and two inflection points as indicated by the red circles. The hose deployed from P_4 shows the lowest displacement and only one inflection point. In terms of lateral displacement this makes sense, insofar as downstream of P_4 the hose approaches flow field characteristics with almost symmetrical conditions. The highest displacement is $0.02D_f$ which is a value of 0.148m. This value can be regarded as very low as it is lower than the lateral grid spacing of 0.25m within which the hose shape has been calculated and it is also in the order of the diameter of a representative refuelling hose. The variation within the grid spacing originates form the 3D interpolation, which allows spatial values lower than the grid spacing to be considered. Also, the fact that the maximum displacement is in the order of the refuelling hose diameter, has no practical relevance. All hitherto applied hose exit position variations do not show any significant improvement of the hose characteristics. None of the positions can be regarded to be of direct benefit for a favourable hose shape, since all hose shapes show the unwanted inflection point.

The next and final hose exit position variation is again a longitudinal variation (Figure 4-60 a)) from circumferential positions but off fuselage, at a constant azimuthal angle φ of 45° and two different radial distances of 1m and 3m from the fuselage (Figure 4-60 b) and 4-61 b)). The results are presented in Figure 4-60 c) for a displacement of 1m and 4-61 c) for 3m.

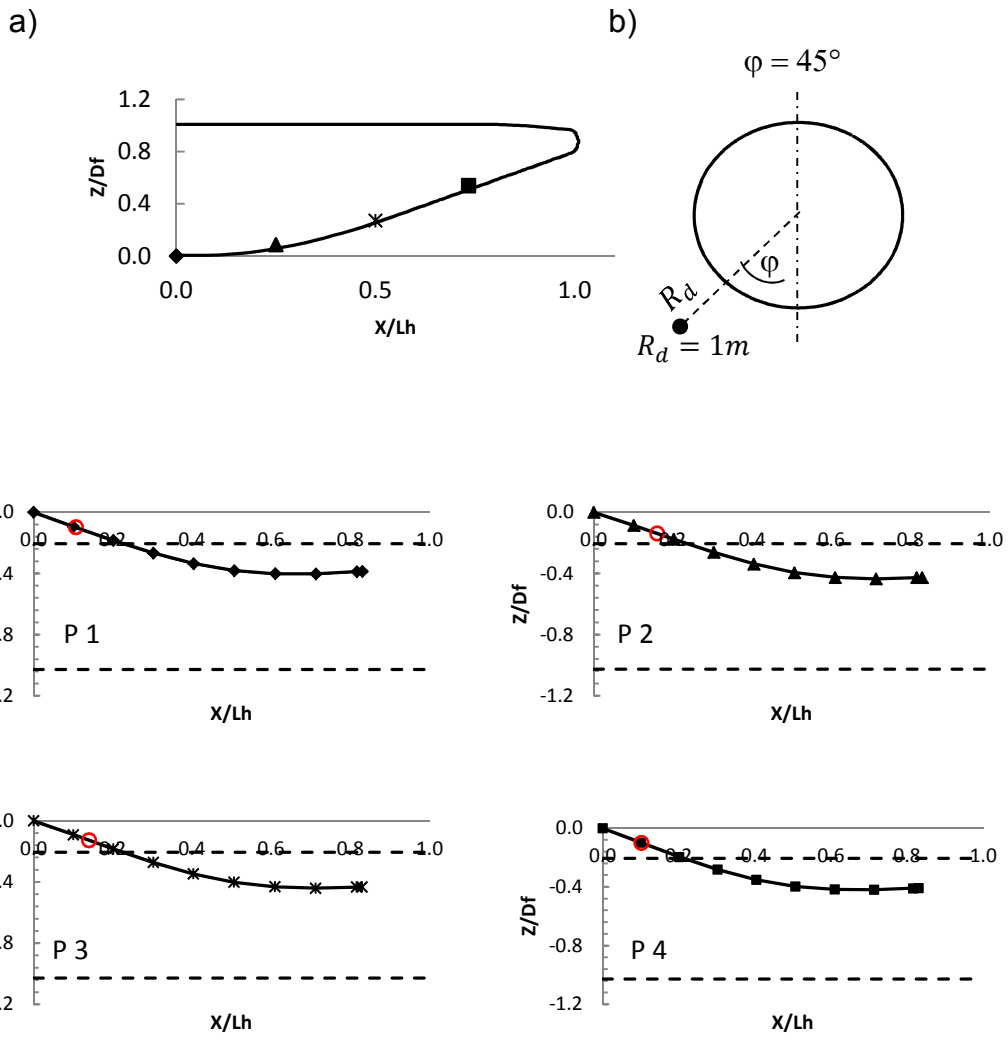

d)

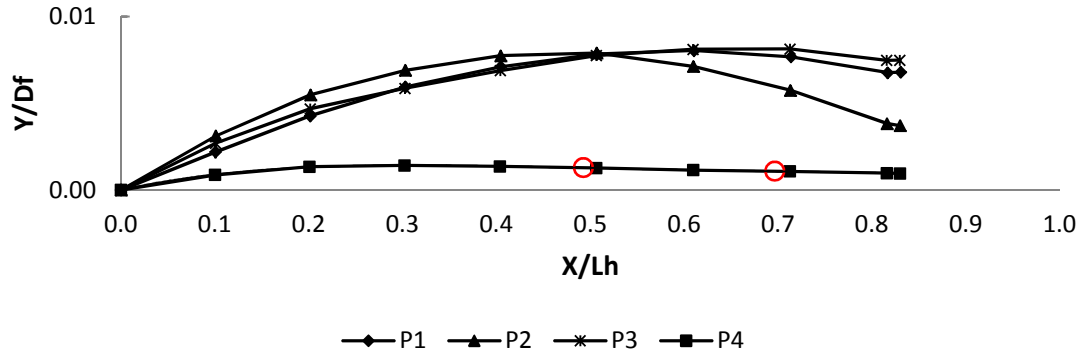

Figure 4-60 a) b) Definition of hose exit positions, c) Hose shape results for longitudinal exit variation off centreline and off fuselage with inflection point positions indicated by the red circles d) lateral hose displacement for all positions, DLR-F6 [4] FC_3: Mach = 0.55, C_l *= 0.5,* α *=0.45°, hose exit positions are always shifted to X, Z origin 0, 0 or X, Y origin 0, 0 respectively for graphical representation*

Figures 4-60 c) and 4-61 c) illustrate that all hoses show an inflection point, but the distinct difference is that the inflection point is very close to the hose exit, which is less than 15% of the hose length. For the dynamic response calculations presented in Section 2.5.3 the inflection point was placed approximately in the middle of the hose length. Most likely, this allows higher amplitudes to be built up and above all to be reflected with a stronger consequent hose whip. The bending moment within the hose has a resetting effect to hose deflections caused by a wave. Generally, the force required to deflect a hose is inversely proportional to the distance of two defined points along the hose, which can be defined as hose exit and inflection point position. Hence, an inflection point close to a hose exit is likely to result in a lower amplitude and thus in a lower amplification through the surrounding flow as the wave travels back downstream. Furthermore, for both cases, 1m and 3m displacement, the drogue is well within the required spatial range which is indicated through the dashed lines. Additionally, from X/Lh=0.7 to X/Lh=0.8 the hose assumes a horizontal position which is favourable for the probe hose engagement as the hose and the probe are similarly aligned. The lateral

displacement shown in Figure 4-60 d) and 4-61 d) is for all configurations below 0.01 D_f as well as lower than the grid spacing of 0.25m within which the hose shape has been calculated. Furthermore, it is in the order of the diameter of a representative refuelling hose. In terms of the inflection point, for the 1m case, only the hose deployed from P_4 assumes an inflected shape, all other are free of inflection points as well as all those in the 3m case.

a)

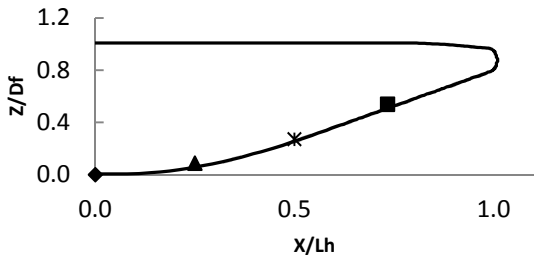

b)

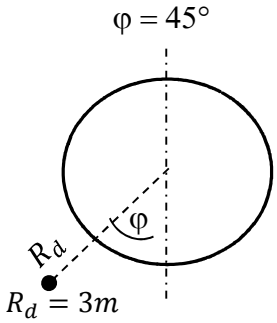

c)

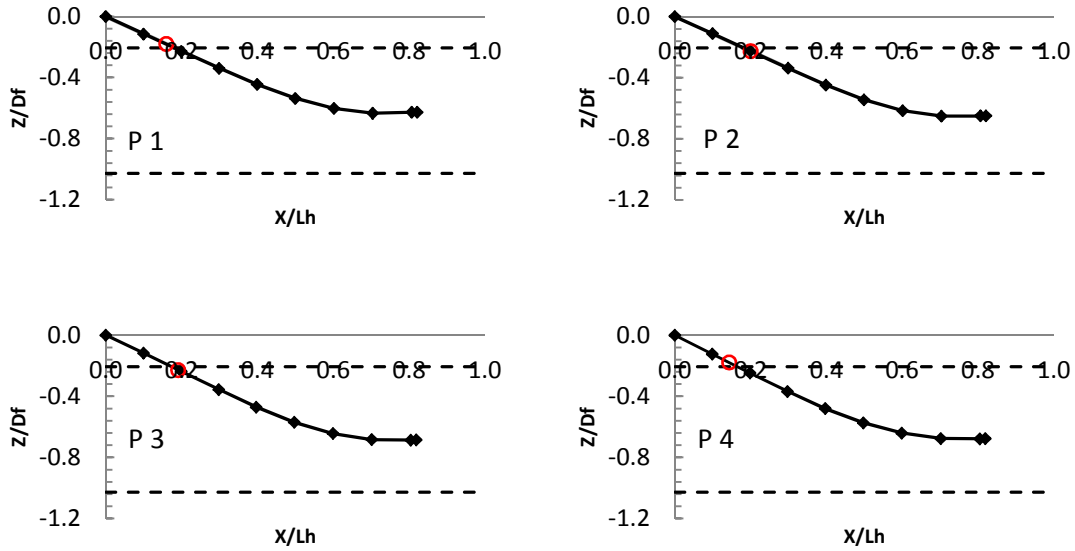

d)

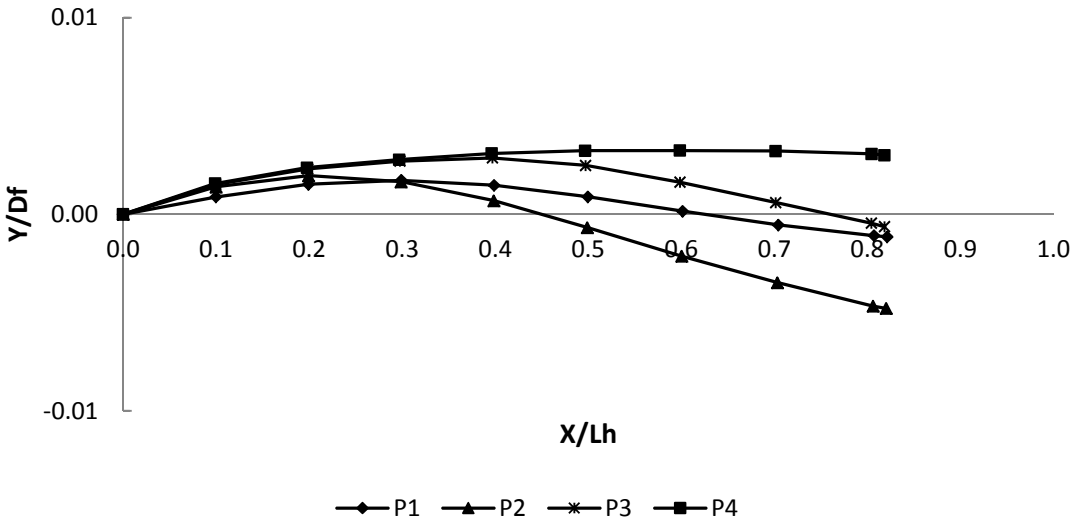

Figure 4-61 a) b) Definition of hose exit positions, c) Hose shape results for longitudinal exit variation off centreline and 3m off fuselage with inflection point positions indicated by the red circles d) lateral hose displacement for all positions, DLR-F6 [4] FC_3: Mach = 0.55, C_l *= 0.5,* α *=0.45°, hose exit positions are always shifted to X, Z origin 0, 0 or X, Y origin 0, 0 respectively for graphical representation*

To show the benefit for a circumferential, off fuselage deployment in Figure 4-62 the resulting hose characteristic is directly compared to the hose characteristic of a centreline on fuselage configuration. The longitudinal position corresponds to positions P_3, since this is approximately the representative position for current inflight refuelling systems.

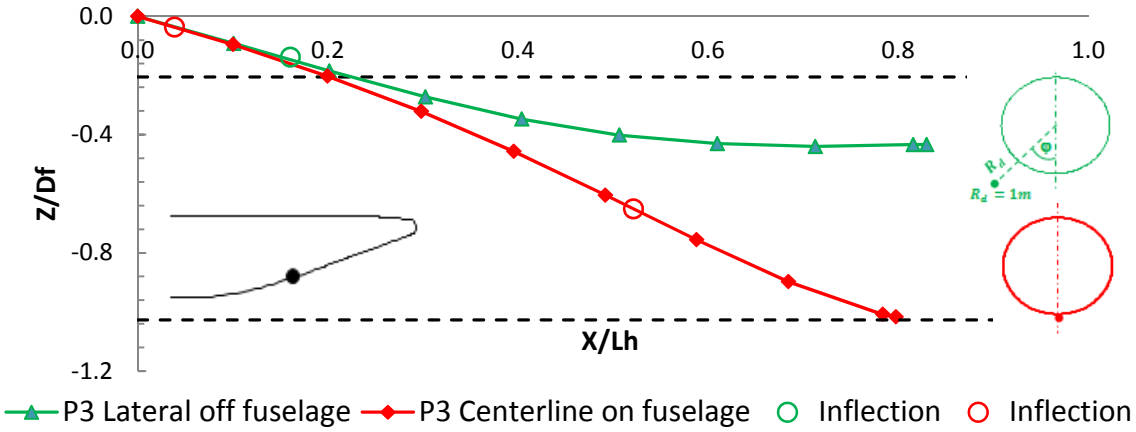

Figure 4-62 Hose charcteristics of a centerline on fuselage (red) and a circumferential off fuselage (green) deployment at longitudinal position P3, DLR-F6 [4] FC_3: Mach = 0.55, c_l = 0.5, α =0.45°, hose exit positions are always shifted to X, Z origin 0, 0 for graphical representation

The hose exit position variation study has predominantly been made with the DLR-F6 [4] geometry, as the rear fuselage shape has more similarity to that of the A330 [54]. This is especially the case with the rear fuselage angle γ, which mainly determines the rear fuselage upwash, which has a value of 15° and is close to that of the A330 [54] with 18°. The common research model (CRM) rear fuselage angle γ is 13° and thus 5° lower than that of the A330 [54]. However, the CRM provides a configuration with a tail section. In Section 4.2.1 the effect of the tail was investigated and illustrated with Figure 4-30 and reveals that there is a difference of the vertical drogue position due to the presence of a tail of approximately 50% of the required spatial drogue range.

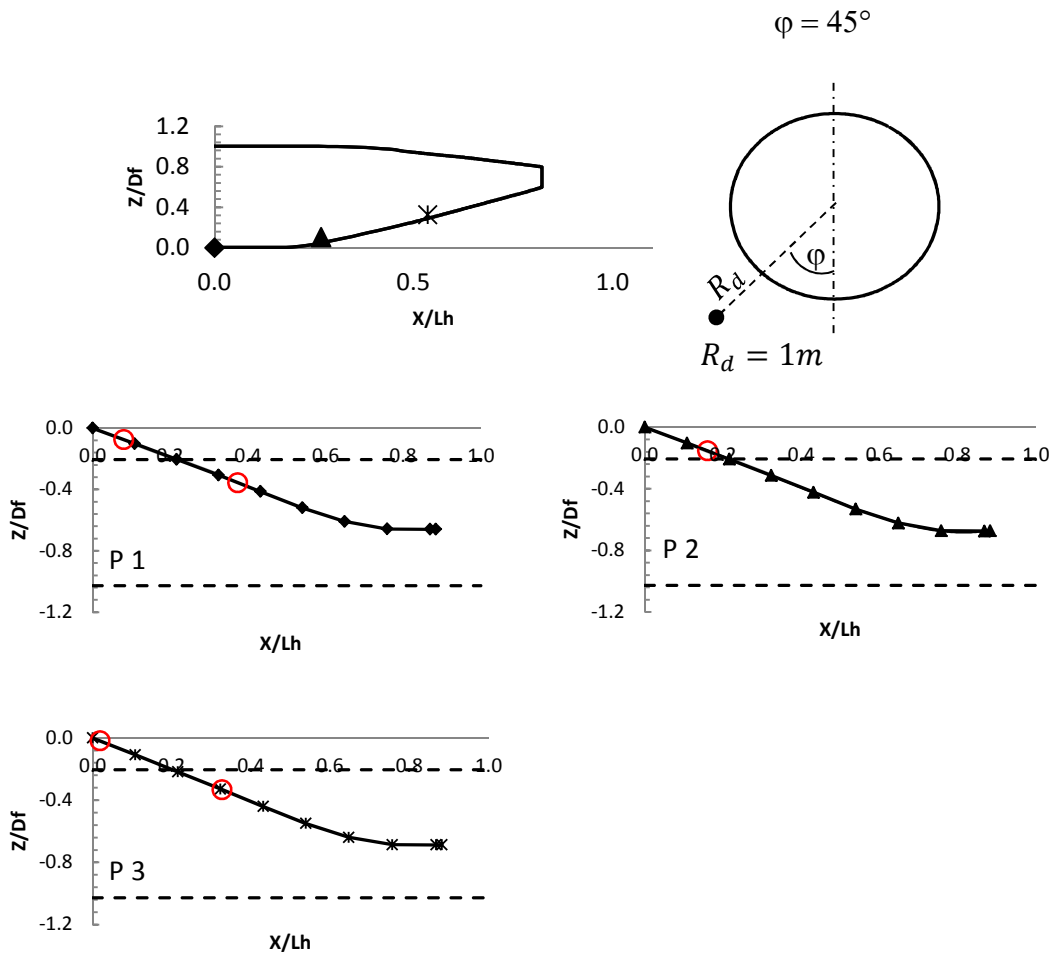

Figure 4-63 Hose shape results for longitudinal exit variation off centreline and off fuselage, with inflection point positions indicated by the red circles, for CRM [5] WBT FC_3: Mach = 0.55, C_l = 0.5, α =3.2°, hose exit positions are always shifted to X, Z origin 0, 0 for graphical representation

Hence, it is of interest to see whether the promising results of a circumferential deployment can be confirmed through the use of aircraft geometry with tail. The results are presented in Figure 4-63, where the hose calculations were conducted with the CRM [5] WBT configuration, and where the hose is positioned circumferentially and off fuselage. It can be observed, that the hose exposed from position P_1 and P_3 assumes a shape with two inflection points where one is close to the hose exit and one approximately at half hose length. The hose started at P_2 instead has one inflection point only and the inflection point is located very close to the hose exit. The inflection point takes place at approximately 15% of the hose length. Furthermore, in Figure 4-64 it can be

observed that there is almost no lateral displacement of the hose, as the maximum value is approximately $0.005D_f$ which is in the order of the hose diameter of a representative refuelling hose.

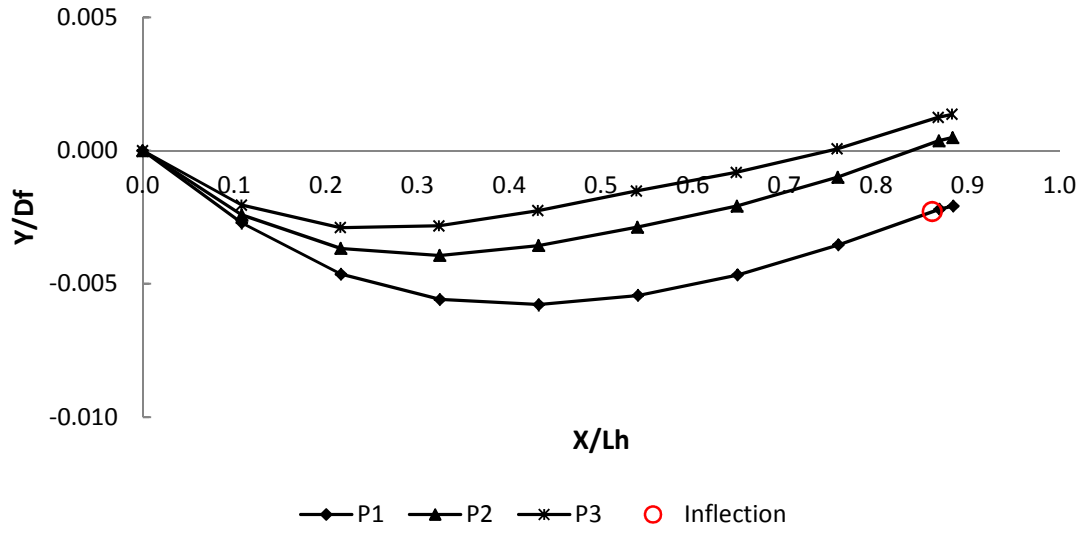

Figure 4-64 Lateral hose displacement for positions P1 to P3, CRM [5] WBT FC_3: Mach = 0.55, C_l = 0.5, α =3.2°, hose exit positions are always shifted to X, Y origin 0, 0 for graphical representation

To show that a circumferential, off fuselage deployment is also beneficial for an aircraft configuration with tail, in Figure 4-65 the resulting hose characteristic is directly compared to the hose characteristic of a centreline on fuselage configuration. The longitudinal position corresponds to positions P_2, and is in the vicinity of a representative position for current inflight refuelling systems. The inflection point of the circumferentially deployed hose (green) is notably shifted towards the hose exit and the drogue is aligned horizontally, whereas the inflection point of the hose deployed on the centreline is almost located in the middle of the hose.

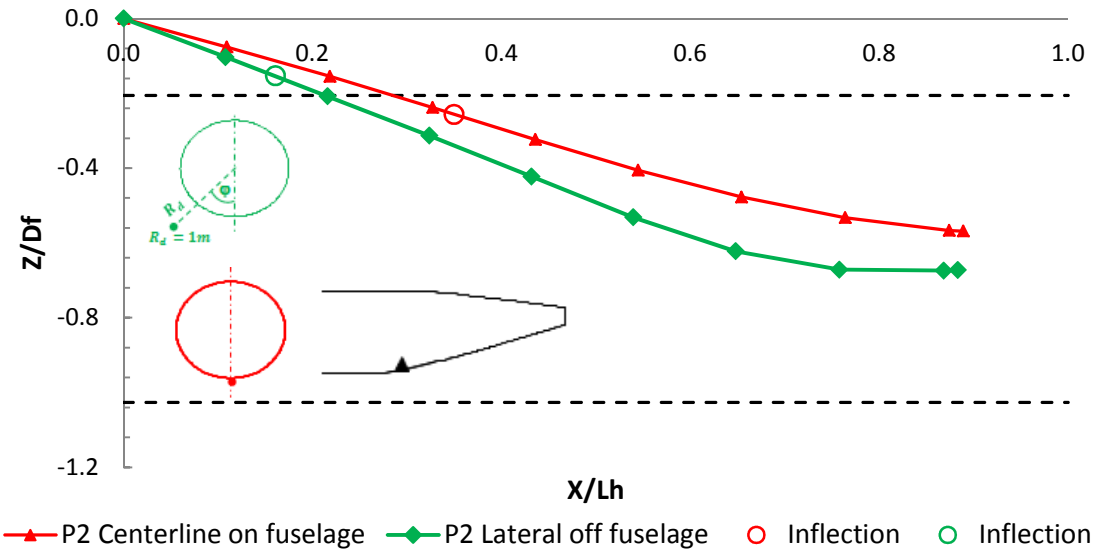

Figure 4-65 Hose charcteristics of a centerline on fuselage (red) and a circumferential off fuselage (green) deployment at longitudinal position P2, CRM[5] WBT FC_3: Mach = 0.55, C_l = 0.5, α =3.2°, hose exit positions are always shifted to X, Z origin 0, 0 for graphical representation

4.2.5 Comparison with Cobham hose model

A comparison of the results obtained from Cobham's hose model has been conducted. The purpose was to evaluate whether the results obtained with the hose model used for this work differ compared to those obtained by the hose model used by Cobham, and to define the differences quantitatively and qualitatively. The results are presented in Figure 4-66 and illustrate that the overall hose position is similar for both models including the vertical drogue position. For the presented case, the vertical position difference of the drogue ΔZ_{drogue} is 7.5% relative to the position obtained with the hose model used by Cobham. The maximum vertical difference ΔZ_{max} is approximately between 14% and 20% relative to the position obtained with the hose model used by Cobham. Moreover, the hose model used in this thesis predicts an inflection point whereas the hose model used by Cobham does not. Given the fact, that the inflected hose is a known phenomenon [74] for tanker aircraft like the A330

[54], it is likely that the hose model used in this thesis may rather better reflect the situation of a real application than the hose model used by Cobham. Nevertheless, since the overall positions are similar, the results obtained within this work may be considered as plausible, in particular regarding the static drogue position.

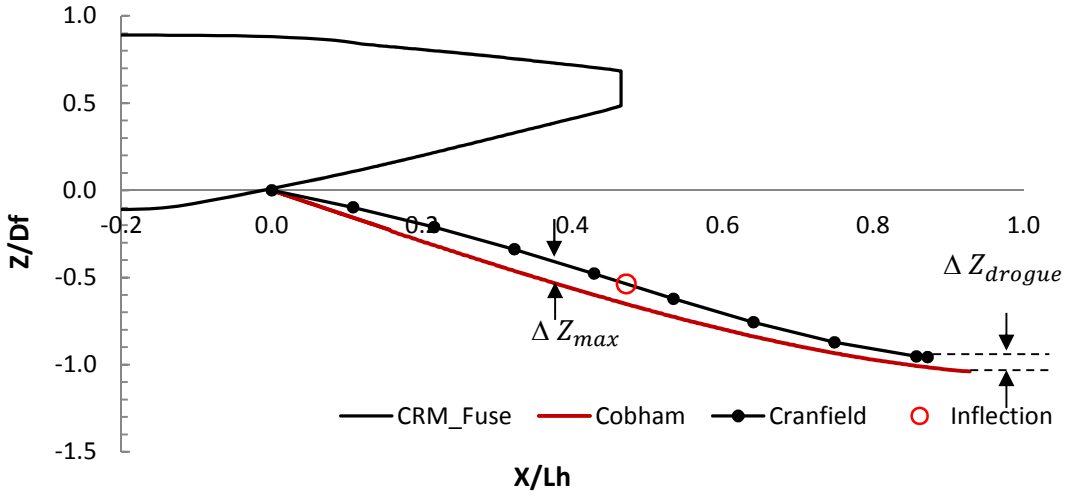

Figure 4-66 Hose characteristic result obtained with hose model from Cobham (red) in comparison with that from hose model used in this thesis (black), hose deployed on the centerline and on fuselage with CRM[5] WBT FC_3: Mach = 0.55, C_l = 0.5, α =3.2°

4.2.6 Summary

The hose fairing effect on the wake field as well as on the hose characteristics has been investigated. The investigation revealed that there is almost no impact both on the overall near field wake (Figure 4-34, 4-35) and on the hose characteristics (Figure 4-36). The size of the recirculation zone behind the fairing is in the order of the hose fairing shape (Figure 4-32). The unsteady aspects of the recirculation have not been evaluated in this work, but are considered as being unlikely to have a notable impact on the hose. Furthermore, a speculative study on the effect of a naturally as well as artificially ventilated hose fairing has been conducted. The purpose for the natural ventilation was primarily to assess a potential flow control mechanism whereas

the artificial ventilation was investigated to assess the potential for a hose control through the manipulation of the near wake field. The investigations show, that the hose responds sensitively on a wake manipulation through the ejection of air (Figure 4-43, 4-44). The aircraft in turn does not show any negative effect in terms of aerodynamic performance since the drag coefficient remains constant for all air ejection configurations. The ejection of air into the near field wake could theoretically be an option to control the hose, in particular the hose position. The potential to control the hose shape in turn is much lower. The maximum applied mass flow of 17.2 kg/s corresponds to approximately 10% of a representative engine flow rate of an A330 [5] engine. Hence, the mass flow of 17.2 kg/s is most probably too high to be delivered by the engines. The applied minimum mass flow of 4.3 kg/s in turn corresponds to 2.5% and might be more realistic to be delivered by the engines. However, this method is complex and needs more thorough investigation. The variation of the hose deployment within the near field wake has been also studied, with the purpose to avoid the negative impact of the rear fuselage upwash onto the hose (Figure 4-52). Hence, the hose exit position has been varied along the rear fuselage. Different configurations along the fuselage centreline and with circumferential displacement have been considered as well on and off fuselage. The study revealed that for all positions along the centreline the hose assumed the unwanted inflected characteristic with either two or one inflection points. The inflection point was mostly located approximately at mid hose length, which is expected to be more critical to the hose dynamic response than an inflection point located close to a hose exit. The inflection point at mid hose length occurred both for on and off fuselage configurations (Figure 4-56, Figure 4-57). The circumferential displacement of the hose exit positions in turn showed high potential for the inflected hose shape to be avoided, or at least to be considerably shifted towards the hose exit. This is particularly likely if the configuration is circumferentially shifted and off fuselage (Figure 4-60, Figure 4-63). A radial distance from the fuselage of R_d=1m shows a better effectiveness than for a distance of 3m, since the inflection points for the 3m configurations are shifted more downstream and therefore further from the hose exit. Hence,

there is a notable sensitivity regarding the radial distance. However, an ideal radial distance to achieve the most positive effect on the hose, which is a non-inflected hose within the spatial drogue range, has not been assessed. Moreover, for this configuration, circumferentially shifted and off fuselage, the longitudinal position plays an important role, especially for the case with tail (CRM [5] WBT configuration). A more desirable hose characteristic with the inflection point close to the hose exit was obtained at one position only (Figure 4-63). However, it was not possible to obtain a shape which was free of inflection points for any of the considered hose exit positions.

4.2.7 Conclusion

The study of the naturally ventilated hose exit fairing revealed that the natural ventilation can be an option for the purpose of flow control. The idea of the artificially ventilated fairing is interesting as it provides a wide spectrum of parameter variation. For example it could be an approach to support the automated engagement of probe and hose, through the specific ejection of air into the wake, through which the position of the drogue could be influenced. However, there are also other techniques available which are simpler to handle, like a controllable drogue [28]. Furthermore, the installation effort and control for this method is likely to be highly complex. Therefore, this approach is considered to be technically realisable, but unreasonable with respect to effort and cost. The highest potential for the inflection point to be avoided or shifted towards the hose exit and for the drogue to be positioned well within the required spatial range has a circumferentially shifted and off fuselage hose exit position configuration. This is also the approach with the smallest constructive complexity compared to the approach with the ejected air. An installation of the trailing mechanism towards the end of the fuselage is difficult. However, it doesn’t look as if this would be necessary, since the best results in terms of hose inflection point were obtained on a longitudinal position similar to the position of current inflight refuelling systems. A circumferential hose exit shift of a current system with additional radial displacement seems reasonable and technically realisable.

4.3 Wake analysis transport aircraft

The wake analysis for the transport aircraft body only geometry TAB [14] is conducted at model scale and at wind tunnel operating conditions which are at a Mach number of 0.73 and a Reynolds number of 3E^6. Furthermore, the wake analysis is made qualitatively and not quantitatively. This means that the analysis focusses on the overall wake characteristics and the wake formation mechanisms rather than on the exact determination of aerodynamic data. The aim of the study is to underline the distinction which was derived in the literature review chapter between the wake of the A330 [54] and the A400M [54]. This is considered as essential since both aircraft are of interest to be equipped with an inflight refuelling system, but probably require different consideration of the near field wake aerodynamics. Moreover, this study can be regarded as an assessment for a suitable test case for further hose calculations.

4.3.1 Introduction to figure notation

The literature review Section 2.4.1 revealed that a transport aircraft wake is typically characterised through two vortices within the wake which originate from the underside of the afterbody [14]. The flow separates at the circumferential edges of the rear body through which the vortices are developed. Hence, the separation is the wake formation mechanism and the following vortex is the phenomenon through which the wake is characterised. To illustrate the flow features, four pertinent plots are shown throughout the wake analysis as introduced in Figure 4-67.

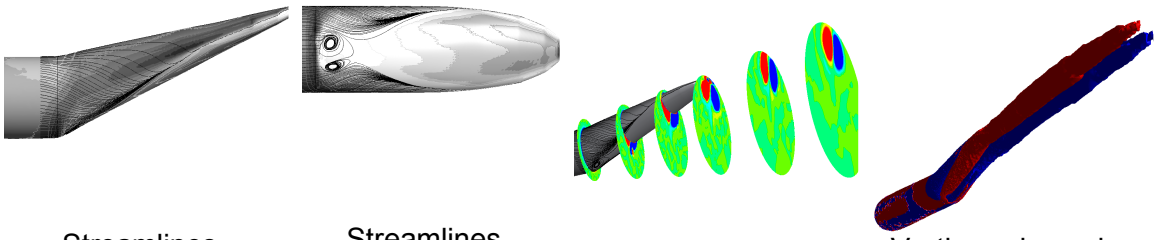

Figure 4-67 Plot types pertinent to expected flow features of transport aircraft near field wake

The 3D separation on the after body is expected to form a separation line, which can be visualised through surface streamlines. Therefore, in Figure 4-67 the first two plots from left to right illustrate surface streamlines and the shear strain rate on the surface, both as side and bottom view. The shear strain rate is useful to identify the areas on the surface where the separation takes place and where the flow on the areas is fully separated. Attached flow produces high strain rates whereas separated flow notably lower rates. The related contours are plotted onto the surface of the rear body. Depending on the size of the separation, the strength and size of the vortices change as well. This is illustrated through plot three and four in Figure 4-67, where the vortices are visualised by means of vorticity onto equally distant cross flow planes, which are introduced in Figure 4-68. Plot four shows the iso- surface of a single vorticity value to illustrate radial and longitudinal growth of the vortex with changing configuration. The spinning convention is as follows:

- clockwise and in flow direction = positive (red)
- counter clockwise and in flow direction = negative (blue)

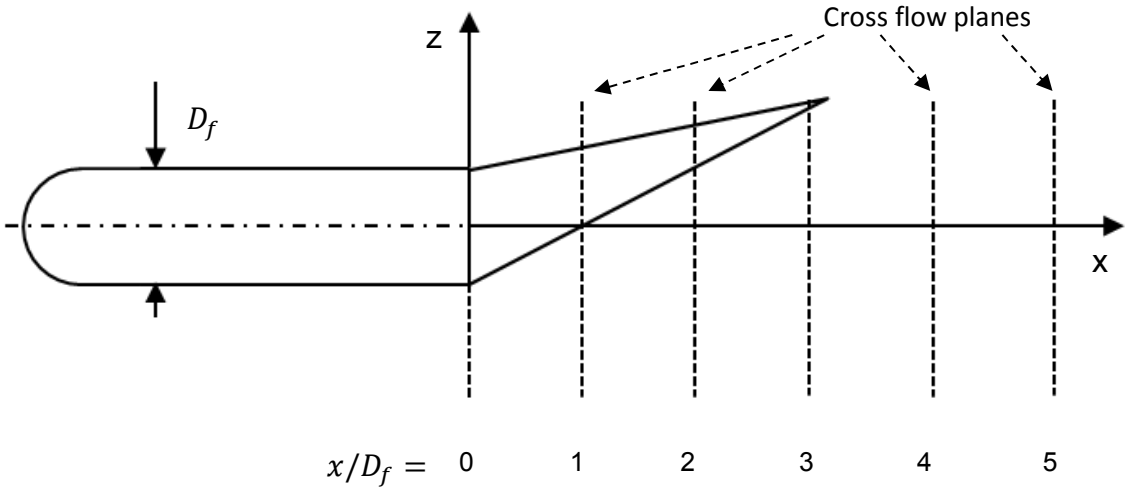

Figure 4-68 Definition of cross flow planes 0 to 5 along and beyond rear part of the transport aircraft fuselage, where x/D_f =0 is at the joint of fore and rear body and the distance between the planes corresponds to fuselage diameter D_f

For upsweep angle $\gamma = 0°$, the body shows smooth aerodynamic behaviour. The flow remains attached over the entire body which can be observed in Figure 4-69 on the top. The streamlines are evenly distributed and no vortices shed into the wake. This can be seen on the cross flow plane plots, where the vorticity value is predominantly around zero.

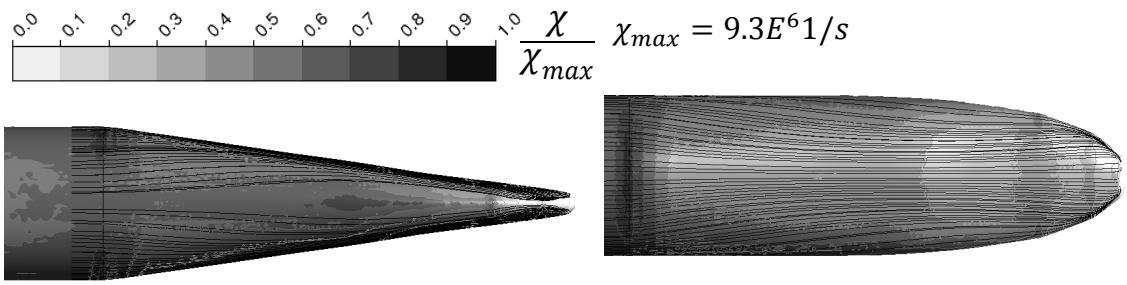

$\beta = 0$ °

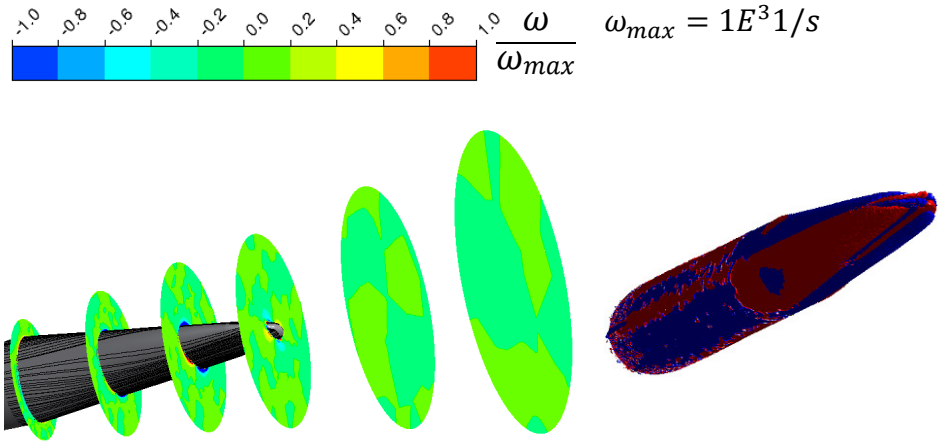

$\beta = 0$ °

Figure 4-69 Surface streamlines on rear body for upsweep angle β=0° (top) with associated wake field (bottom)

The wake assumes a different characteristic as the upsweep angle increases. Figure 4-70 shows the 5° upsweep configuration and illustrates that the flow starts to separate. The wake is now characterised through two counter rotating vortices indicated by the dashed arrows and the plus and minus symbols. However, the overall wake underneath the rear fuselage remains benign. The vortical structures are compared to the fuselage diameter of relatively small size and above all far away from a possible hose trailing zone.

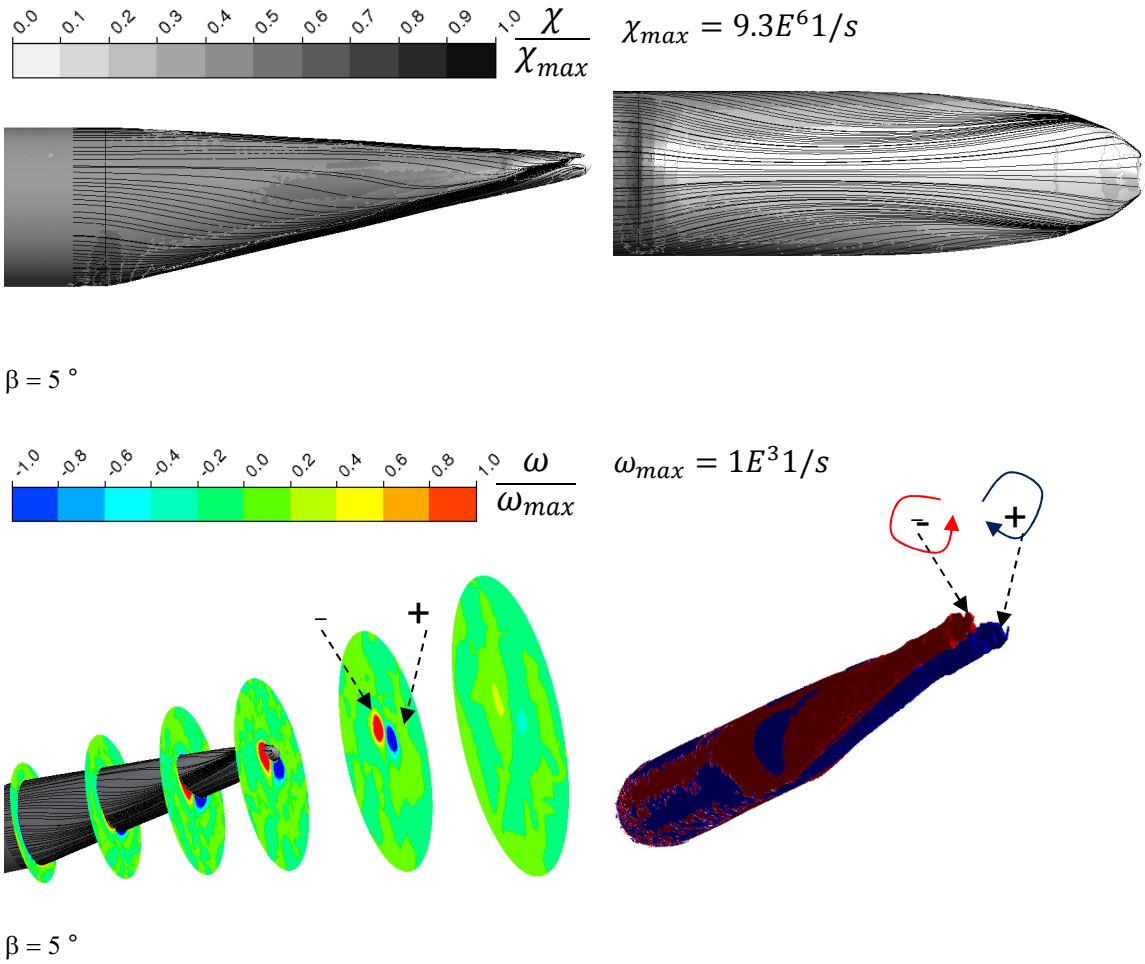

Figure 4-70 Surface streamlines on rear body for upsweep angle β=5° (top) with starting separation and associated counter rotating vortices which shed into the wake field (bottom)

As the upsweep increases, the separation and the vortices increase as well. The vortex diameter grows with increasing upsweep which can be observed in Figure 4-71. Also, through the higher induced rotating energy the vortex dissipates later downstream. However, in reality the vortex would dissipate even more downstream. The mesh is made to see the basic characteristics of the wake. Therefore, the mesh density behind the body where the vortices dissipate is too coarse for a higher resolution of the vortex structures.

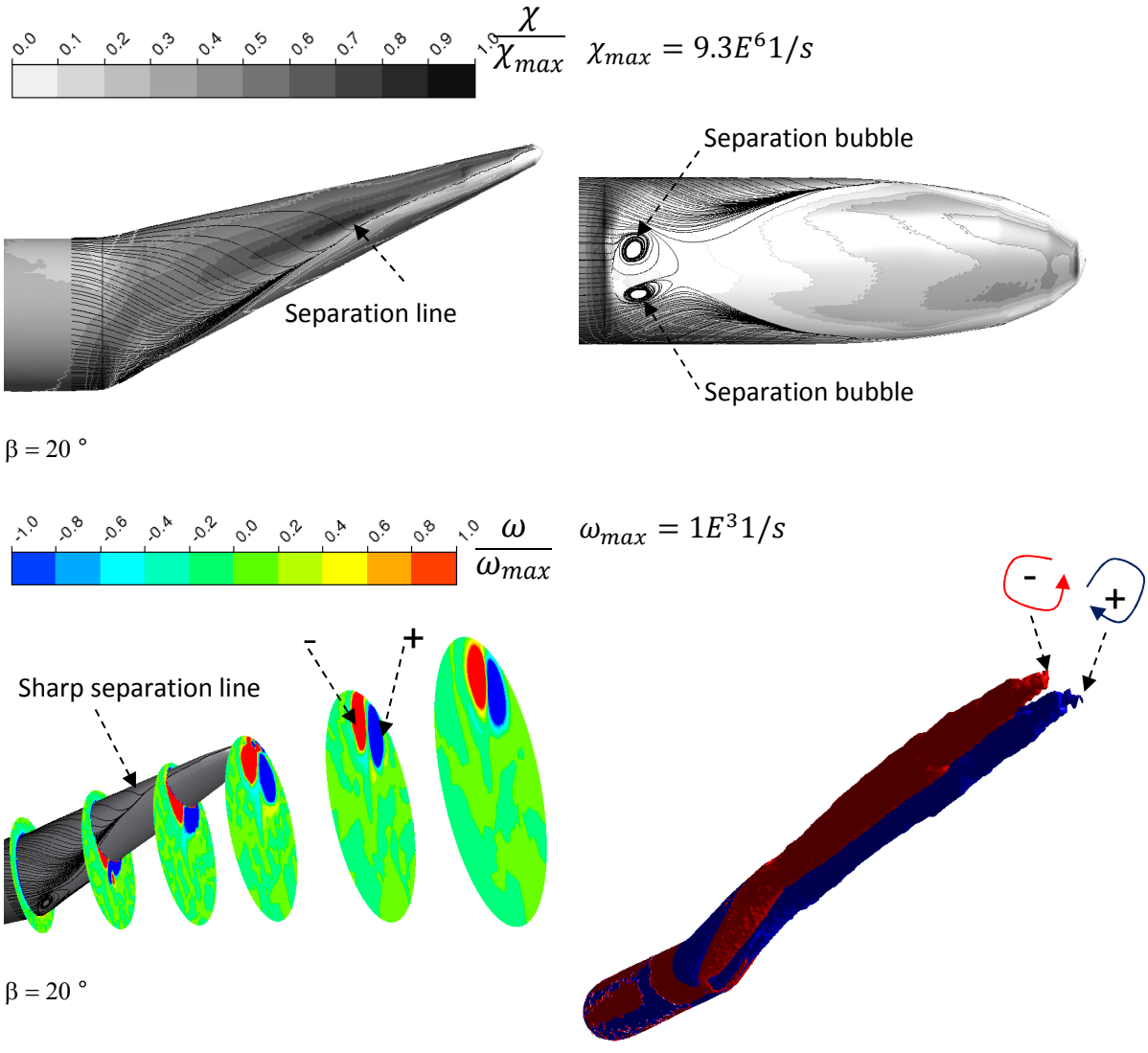

Figure 4-71 Surface streamlines on rear body for upsweep angle β=20° (top) with starting separation and associated counter rotating vortices which shed into the wake field (bottom)

In Figure 4-71 the 20° configuration shows an additional separation on the edge from fore to rear body which forms two asymmetric separation bubbles underneath the fuselage even if there is no yaw applied and therefore symmetrical conditions. The asymmetry can also be observed on the shear strain rate contour plot with view to the underside. However, symmetrical conditions do not necessarily generate symmetrical flow pattern. It can be assumed that the flow field is highly unstable and therefore transient. This steady state solution represents one moment in time. This is why the steady state solution is asymmetric. Beyond the vortices the wake remains benign also for this high upsweep angle of β=20°.

4.3.2 Summary

For the transport aircraft model the flow already separates for relatively low upsweep angles, in the present case at an upsweep angle of 5°. The consequent vortices are of small scale and do not influence the benign overall wake characteristic underneath the rear fuselage, where a possible hose trailing takes place. With growing upsweep angle the separation line moves from underneath the fuselage outwards onto the outer edges of the fuselage. This can be observed in Figure 4-72.

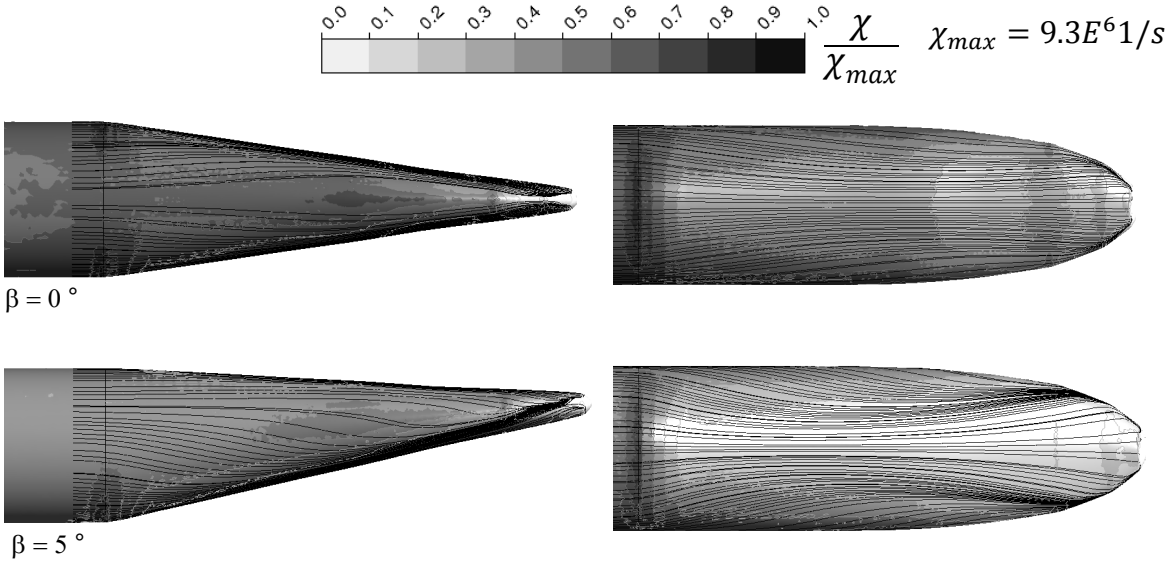

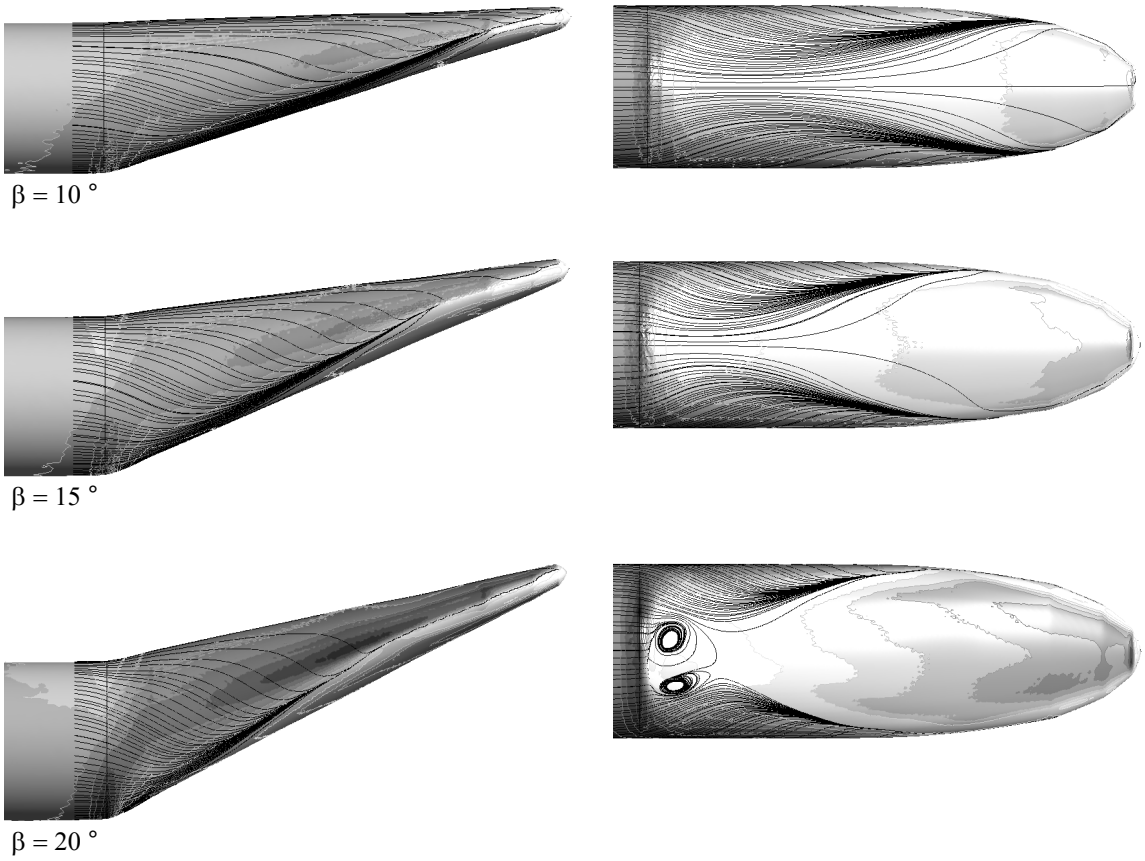

Figure 4-72 Surface streamlines on rear body for upsweep angle β=0° to β=20°, side view in the left column and view under the fuselage in the right column

For an upsweep angle of 10°, which corresponds to that of the A440M [54], the flow separates within the second half of the after body. This is illustrated by Figure 4-73 a). Figure 4-73 b) shows an A400M and a zoomed part of the rear fuselage. A circumferentially mounted strake can be observed in the same region where the separation occurs on the transport aircraft model with 10° upsweep. This can be regarded as an indication that the transport model used for this study is suitable to generically investigate the wake characteristics of the A400M.

a)

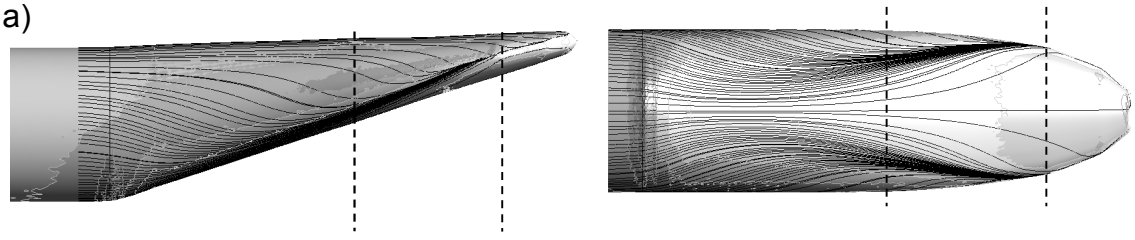

b)

Figure 4-73 a) Separation area on rear fuselage of 10° configuration, b) strake on A400M rear fuselage potentially used to avoid separation [68]

5 DISCUSSION

This chapter comprises a summary of the whole thesis, discusses key results and findings in a generic manner, puts them into a bigger context and derives conclusions and consequences. Furthermore, different palliatives are suggested as well as recommendations for the most suitable approach to tackle one of the main problems, the inflection point of the hose, as well as the reliable positioning of the drogue within the required spatial range. Also discussed are possible research scenarios for the future. This is split into two parts. The first part outlines the potential for further research with the findings and results obtained in this study which can be directly used for further processing. The second part gives an overview about research topics which can be derived from this work. These are parts of the present work related to the suggested palliatives, which need to be investigated more thoroughly if the palliative is

considered to have enough potential to be converted into a real technical solution.

5.1 Summary

The aim of the present work was to develop an understanding of a typical refuelling tanker wake like that of an A330 [54], in particular the near field wake close to the rear fuselage, the wake-hose interaction as well as the resulting hose characteristics. Furthermore, the wake characteristics of a typical transport aircraft like the A400M [54] was required to be analysed and understood, but not in conjunction with resulting hose characteristics. To achieve this, a number of steps were necessary. A literature review on current inflight refuelling systems has been conducted with an emphasis on automated inflight refuelling for unmanned aircraft systems (UAS) and the associated technological challenges. Furthermore, a theoretical understanding about rear fuselage flows in general but with focus on fuselages similar to pertinent tanker aircraft has been developed during the literature review. The acquired knowledge related to both aspects, automated inflight refuelling challenges and rear fuselage flows, could directly be adapted to the present work. In terms of automated inflight refuelling the literature review revealed that one major challenge is the appearance of a hose perturbation associated to the probe-hose engagement [19] [21] [26] [31] [37]. The initial hose shape characteristic plays an important role in this context [72] [74]. The dynamic response to perturbations is a function of the initial hose shape and becomes critical through specific hose shape characteristics. In particular there is one hose shape that needs to be avoided, which is characterised through an inflection point along the hose. This characteristic favours the formation of a wave after a perturbation as it describes a curvature similar to a sine wave [74]. It also favours an amplification of the propagating wave due to the interaction with the rear fuselage upwash because the hose part between hose exit at the tanker and the inflection point tends to move in the amplification direction. The literature review also revealed, that there is a distinct difference between the near field wake of a civil aircraft like the A330 [54] and that of a transport aircraft like the A400M [54]. The

fuselage of a civil aircraft is not critical regarding separation and associated vortex build up [62], whereas the fuselage of a typical transport aircraft shows significant tendency to flow separation and thus to vortex shedding into the near field wake [9] [14]. Either wake characteristics could be reproduced through the use of CFD simulations and confirmed the characteristics obtained from experimental studies which were studied in the literature review. It was expected that the near field wake of the tanker has a major impact on the formation of the hose shape. However, the detailed mechanisms between the wake characteristics and hose shape formation were not clear. The assumption, that the wake has a major impact on the hose shape formation has been confirmed through this work and the mechanisms on how the wake affects the hose are also presented. The results regarding the hose shape formation mechanisms refer all to the wake of a civil aircraft similar to the A330 [54].

5.2 Key conclusions

- The wake underneath the rear fuselage of modern civil aircraft similar to the A330 [54] is, where the refuelling hose is exposed, generally of benign nature.
- The wake underneath the rear fuselage of modern transport aircraft similar to the A400M [54] is also generally benign in nature. However, the wake is characterised by two counter rotating separation vortices, which are strengthened with increasing upsweep angle β. The vortices develop above the hose deployment space and are unlikely to interact with the exposed refuelling hose, as long as the hose is exposed from the aircraft centreline.
- The aerodynamic parameters which predominantly determine the refuelling hose characteristics, shape and position, are

    1. The dynamic pressure P_{dyn} in conjunction with flow direction relative to the hose, where P_{dyn} and flow direction are a function

of altitude, speed, aircraft angle of attack α and rear fuselage shape, in particular the rear fuselage angle γ.

2. The drag over the entire hose length, which is predominantly form drag and a function of the local effective Reynolds number close to the hose, since it determines whether the boundary layer is laminar or turbulent. The effective Reynolds number in turn is a function of the local free stream Reynolds number, approaching turbulence properties and hose surface roughness.

- The undesirable refuelling hose shape, which is characterised through at least one inflection point is formed by the rear fuselage upwash.
- The inflection point tends to be shifted towards hose exit position with decreasing upwash.
- The presence of a tail has a considerable effect on the hose characteristics, which implies, that the vertical tail position is likely to have an effect of the hose characteristics too.
- For the hose deployment it is generally recommended to avoid an interaction between refuelling hose and the rear fuselage upwash, since this favours the formation of an inflected hose shape.

5.3 Palliatives

Two different approaches have been studied as possible palliative against the formation of an undesirable hose shape. One aims at the control of the wake characteristics and one at the avoidance of an upwash-hose interaction. It is recommended avoiding the interaction of the hose with the rear fuselage upwash. This can be achieved through a circumferentially shifted hose exit with additional radial displacement from the fuselage. The results obtained for this configuration revealed a notable shift of the inflection point towards the hose exit (Figure 5-1, Figure 5-2), which is expected to have a beneficial effect on the hose whip phenomenon.

a)

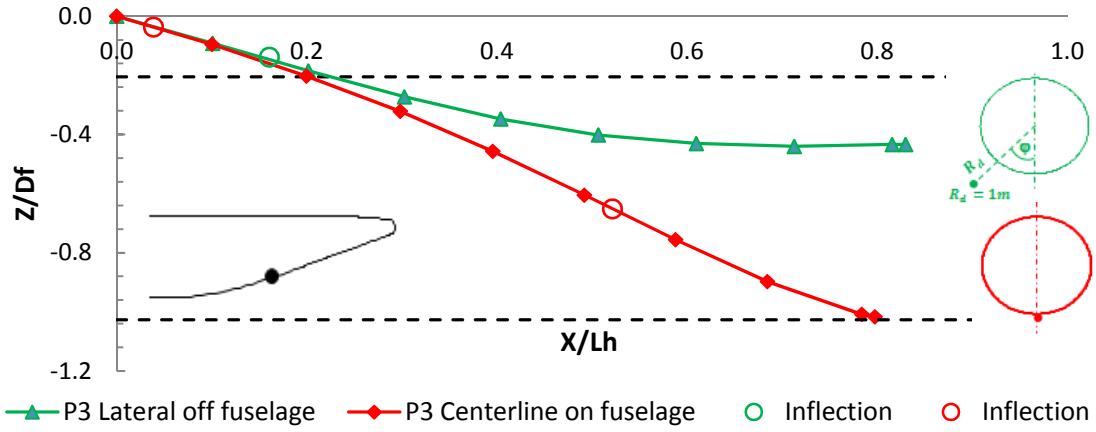

b)

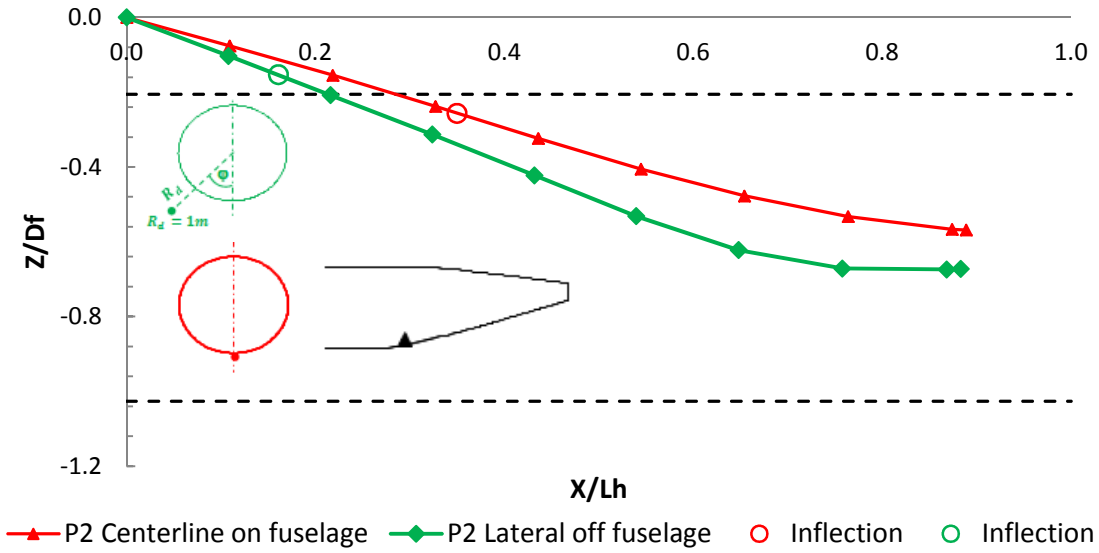

Figure 5-1 Hose charcteristics of a centerline on fuselage (red) and a circumferential off fuselage (green) deployment at longitudinal positions for FC_3: Mach = 0.55, c_l = 0.5 a) DLR-F6 [4], α =0.45°, b) CRM[5] WBT α =3.2°

Technically this could be realised through the use of an incorporated mechanism that can be swivelled from a lateral position of the fuselage, similar to the mechanism of a refuelling probe as illustrated in Figure 5-2.

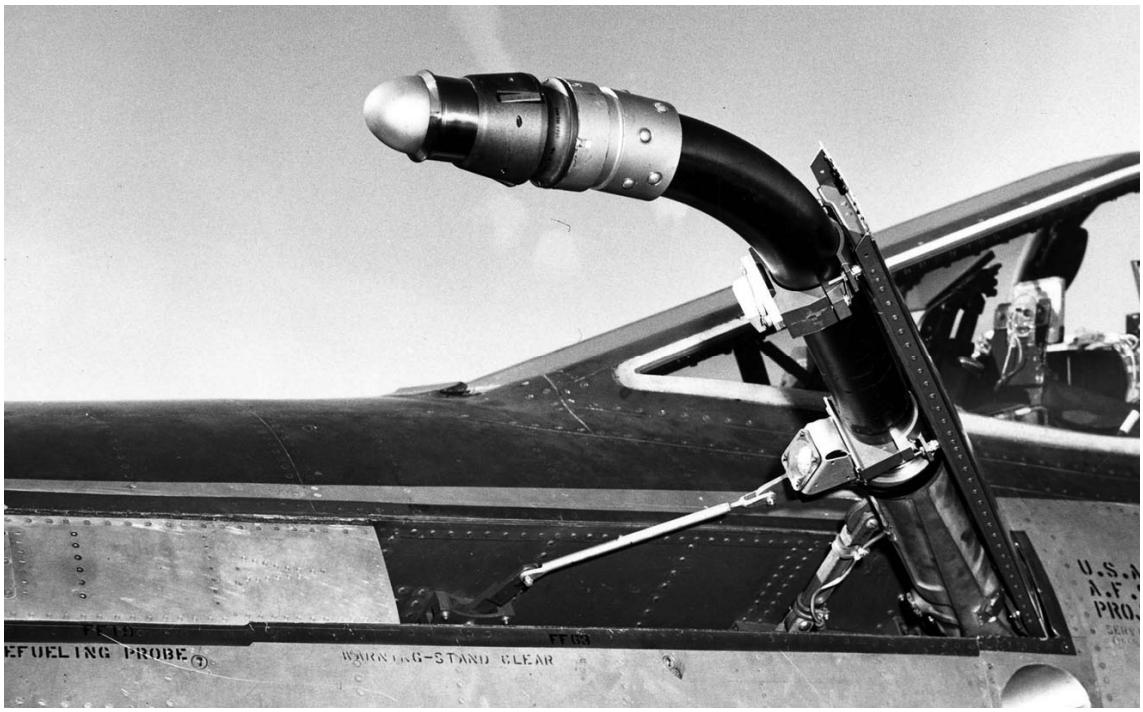

Figure 5-2 Hydraulically activated refuelling probe mechanism [69]

The use of a lateral strake with encapsulated mechanism similar to a hose fairing could also be an approach. This solution doesn't require any swivelling mechanism. The realisation could be possible with minor constructive and economic effort. In particular this solution is interesting for fuselages where separation is expected. This is the case for a transport aircraft like the A400M [54].

5.4 Future work

This chapter suggests a few ideas for further research based on the current work.

5.4.1 Refuelling hose dynamic response

The recommendation for a circumferentially shifted hose deployment is based on the static hose shape, in particular on the fact, that the inflection point is shifted towards the hose exit. This is expected to have a beneficial effect on the hose whip phenomenon, but has not been proved within this work. Further research could investigate the effect on the dynamic response for the recommended configuration. However, the hose characteristic results obtained within this work also represent a data base for general investigations on the dynamic response of a refuelling hose for different positions along a representative tanker aircraft like the A330 [54]

5.4.2 Transport aircraft model

The wake of the transport aircraft model [14] has been studied qualitatively and without hose. Hence, a further research topic could be a quantitative analysis of the transport aircraft rear fuselage wake. The transport aircraft model is a body only configuration. However, within this work the effect of the wings on the static hose shape has not been investigated. The hose calculations have revealed a high sensitivity of the hose characteristics on small changes of the flow. Hence, for a determination of the hose characteristics associated to the wake of the transport aircraft model [14] it is recommended to first study the effect of the wings, or to directly choose a wing body configuration if available.

REFERENCES

[1] The ASTREA II programme, available at

http://www.astraea.aero/

(accessed 17/03/2013)

[2] Aviation accidents, available at:

http://aviation-safety.net/database/record.php?id=19690518-1

(accessed 05/10/2012)

[3] Aerial refuelling, available at:

http://en.wikipedia.org/wiki/Aerial_refuelling

(accessed 06/10/2012)

[4] 2nd AIAA Drag Prediction Workshop, available at:

http://aaac.larc.nasa.gov/tsab/cfdlarc/aiaa-dpw/Workshop2/workshop2.html

(accessed 10/01/2012)

[5] 4nd AIAA Drag Prediction Workshop, available at:

http://aaac.larc.nasa.gov/tsab/cfdlarc/aiaa-dpw/Workshop4/workshop4.html

(accessed 10/01/2012)

[6] ESDU, available at: http://www.ihsesdu.com/ Document number: 80025

(accessed 16/01/2012)

[7] Far Wake Project, available at: http://www.far-wake.org/

(accessed 20/01/2012)

[8] F. Doetter, I. Acisu,P. Aumann, O. Brodersen, A. Ronzheimer“ A400M WAKE FLOW STUDIES BASED ON RANS CFD METHODS ON HYBRID

MESHES" Germany Institute of Aerodynamics and Flow Technology DLR Braunschweig, Germany

[9] R. H. Wickens, 1965 "Observations of the Vortex Wake of a Lifting Fuselage Similar to Those on Rear-Loading Transport Aircraft" National Aeronautical Establishment, Canada

[10] D. Morton, 1974 "The effect of mild rear fuselage upsweep on rear fuselage loads and pressure distributions for a swept wing-body combination at subsonic speeds" Aircraft research association limited, UK

[11] B. G. Loewe, W. J. G. Trebble, 1968 "Low speed wind-tunnel tests and drag analysis on the short SC 5 Belfast with special reference to upswept fuselage drag", Royal Aircraft Establishment

[12] M. Hahn, G. W. Brune, P. E. Rubbert, T. C. Nark, 1974 "Drag measurement of upswept afterbodies and analytical study on axisymmetric separation" USA

[13] S. Faulkner, J. L. Hess, J. P. Giesing 1964 "Comparison of experimental pressure distributions with those calculated by the Douglas Neumann program", US

[14] D.J. Peake 1974 "The flow about upswept rear fuselages of typical transport aircraft", National Aeronautical Establishment

[15] J.R. Hooker 2002 "Aerodynamic development of a refuelling pod for a tanker aircraft", 20th AIAA Applied aerodynamic conference, US

[16] I. H. Abbott, A. E. 1959 von Doenhoff "Theory of wing sections" US

[17] B. W. McCormick, 1994 "Aerodynamics Aeronautics and Flight Mechanics"

[18] Patrick J. Roache, 1998 "Verification and Validation in Computational Science and Engineering"

[19] Zhu, Z. H., and Meguid, S. A., 2006 "Elastodynamic Analysis of Aerial Refuelling Hose Using Curved Beam Element", AIAA Journal, Vol. 44.

[20] Meng DING, Li WEI, Bangfeng WANG, 2011 “Vision-based Estimation of Relative Pose in Autonomous Aerial Refuelling”, Chinese Journal of Aeronautics

[21] Andrey Styuart, Robert Gaston, Hisako Yamashiro, Robert Stirling, Marat Mor, 2011 “Numerical Simulation of Hose Whip Phenomenon in Aerial Refuelling”, AIAA Atmospheric Flight Mechanics Conference

[22] Shahab Shahinfar, 2012 "Revival of Classical Vortex Generators Now for Transition Delay", Physical Review Letters, American Physical Society

[23] “Fluid Mechanics Tutorial Nr. 3, Boundary Layer Theory”, available at:
www.freestudy.co.uk/fluid%20mechanics/t3203.pdf
(accessed 11/10/2012)

[24] C. Breitsamter, 2011 “Wake Vortex Characteristics of Transport Aircraft”, Progress in Aerospace Sciences, available at:

http://www.sciencedirect.com/science/article/pii/S0376042110000576

(accessed 11/10/2012)

[25] “Boundary Layer Theory”, available at:

http://www.grc.nasa.gov/WWW/k12/VirtualAero/BottleRocket/airplane/boundlay.html

(accessed 11/10/2012)

[26] Kapseong Ro, James W. Kamman, 2010 “Modelling and Simulation of Hose- Paradrogue Aerial Refuelling Systems”, Journal of Guidance, Control and Dynamics, Western Michigan University.

[27] NASA Tech Briefs, August 2007, “Automated Aerial Refuelling Hitches a Ride on AFF”, Dryden Flight Research Center, Edwards, California

[28] Walton R. Williamson, Eric Reed, Stephen M. Stecko, Jeffrey Musgrave and John M, 2010 “Controllable Drogue for Automated Aerial Refuelling”, JOURNAL OF AIRCRAFT, Vol. 47, No. 2.

[29] Jennifer L. Hansen, James E. Murray, Norma V. Campos, “A Flight Test Approach to an Aerial Refuelling System”, NASA Dryden Flight Research Center, Edwards, California.

[30] Michael Jacob Vachon, Ronald J. Ray, 2004, “Calculated Drag of an Aerial Refuelling Assembly through Airplane Performance Analysis”, Dryden Flight Research Center, Edwards, California.

[31] John C. Vassberg, David T. Yeh, Andrew J. Blair, and Jacob M. Evert, 2005, “Numerical Simulations of KC-10 In-Flight Refuelling Hose-Drogue Dynamics with an Approaching F/A-18D Receiver Aircraft”, 23rd AIAA Applied Aerodynamics Conference.

[32] William Ellet, 2008, “The case study handbook”, Harvard Business School Press.

[33] G. Thomas, 2011, “A typology for the case study in social science following a review of definition, discourse and structure”.

[34] Robert K. Yin, 2002, “Case Study Research: Design and Methods”

[35] Robert E. Stake, 1995, “The Art of Case Study Research”

[36] Z.H. Zhu, S.A. Meguid, 2007 “Modelling and simulation of aerial refuelling by finite element method” International Journal of Solids and Structures

[37] William H. Phillips, 1949 “Theoretical analysis of oscillations of a towed cable” Langley Aeronautical Laboratory

[38] Examining Spatial (Mesh) Convergence, available at:

http://www.grc.nasa.gov/WWW/wind/valid/tutorial/spatconv.html

(accessed 18/10/2012)

[39] Airbus A330 geometry sketch, available at:

http://commons.wikimedia.org/wiki/File:A330-200v1.0.png?uselang=fr?uselang=fr

(accessed 22/10/2012)

[40] Spalart, P. R., and Allmaras, 1991 S. R., “A One-Equation Turbulence Model for Aerodynamic Flows," AIAA 92–0439.

[41] Menter, F.R., 1993 “Zonal two-equation k-w turbulence model for aerodynamic flows”. AIAA Paper 1993-2906.

[42] Ansys CFX [42] description, available at:

http://en.wikipedia.org/wiki/CFX [42]

(accessed 22/10/2012)

[43] T. Louagie, L. Georges, P. Geuzaine, 2008 “Comparison of Wind Tunnel Measurements on the TAK Model with RANS and RANS-LES Simulations” FAR-Wake Workshop Marseille

[44] Thomas Gerza, Frank Holzapfel, Denis Darracq, 2002, “Commercial aircraft wake vortices”, Progress in Aerospace Sciences 38

[45] Grégoire Winckelmans, Roger Cocle, Louis Dufresne, Raphaël Capart, 2005, “Vortex methods and their application to trailing wake vortex simulations” Université catholique de Louvain (UCL)

[46] J.D. Crouch & M.J. Czech, 2009 “Near Near--field evolution of trailing vortices far and initialization of far-field models” WakeNet3 Workshop

[47] Thomas LEWEKE, 2009 “Fundamental Research on Aircraft Wake Phenomena” WakeNet3-Europe Workshop

[48] Michael Czech, Gregory Miller, Jeffrey Crouch, Michail Strelets, 2005 “Predicting the near-field evolution of airplane trailing vortices”

[49] Alexander Allen, Christian Breitsamter, 2008 “Experimental investigation of counter-rotating four vortex aircraft wake” Lehrstuhl für Aerodynamik, Technische Universität München

[50] A330 drawing, available at:

http://i636.photobucket.com/albums/uu87/jephryc/a0e1c1e7.jpg

(accessed 25/10/2012)

[51] A400M sketch, available at:

http://upload.wikimedia.org/wikipedia/commons/thumb/4/45/Airbus_A400M_%28Sketch%29.svg/2000px-Airbus_A400M_%28Sketch%29.svg.png

(accessed 25/10/2012)

[52] Wake picture, available at:

http://talkaviation.com/images/Books/phak/chapter-13/vortex%20generation.jpg

(accessed 26/10/2012)

[53] Hose exit fairing A330 example available at:

http://en.wikipedia.org/wiki/File:Royal_Air_Force_Airbus_A330MRTT_Bidini.jpg

(accessed 27/10/2012)

[54] Airbus Military, available at:

http://www.airbusmilitary.com/

(accessed 27/10/2012)

[55] Drogue and probe system schematic 1, available at:

http://www.flightglobal.com/blogs/graham-warwick/Boeing%20refuel%20patent.jpg

(accessed 28/10/2012)

[56] Drogue and probe system schematic 2, available at:

http://www.freepatentsonline.com/6926049-0-large.jpg

(accessed 28/10/2012)

[57] Flying boom schematic, available at:

http://www.strutpatent.com/patent/07309047/systems-and-methods-for-controlling-flexible-communication-links-used-for-aircraft-refuelling#!prettyPhoto[patent_figures]/0/

(accessed 28/10/2012)

[58] Flying boom and fighter photograph, available at:

http://files.air-attack.com/MIL/kc30/kc30_f16_20071210.jpg

(accessed 28/10/2012)

[59] Approaching receiver aircraft, available at:

http://www.airtanker.co.uk/wp-content/uploads/2010/12/FSTA-1st-dry-contact-FRU.jpg

(accessed 28/10/2012)

[60] Drones during in-flight refuelling, available at:

http://www.aviationweek.com/Portals/AWeek/Ares/KQ-X%20formate%201.jpg

(accessed 28/10/2012)

[61] Stephen B. Pope, 2000 “Turbulent Flows”, Cambridge University Press

[62] T. Louagie, L. Georges, P. Geuzaine, S. Melber-Wilkending, A. Allen, C. Breitsamter, 2008, “Wake Vortices generated by an Aircraft Fuselage: Comparison of Wind Tunnel Measurements” FAR-Wake Workshop

[63] Modal available at:

http://en.wikipedia.org/w/index.php?title=File:Harmonic_partials_on_strings.svg&page=1

(accessed 28/10/2012)

[64] A330 in-flight refuelling with A400M available at:

http://www.airbus.com/typo3temp/pics/2c9ca5f66c.jpg

(accessed 28/10/2012)

[65] Ismail B. Celik, Urmila Ghia, Patrick J. Roache, Christopher J. Freitas, Hugh Coleman, Peter E. Raad, 2008 “Procedure for Estimation and Reporting of Uncertainty Due to Discretization in CFD Applications” ASME

(accessed 28/10/2012)

[66] “Glossary of Verification and Validation Terms” available at:

http://www.grc.nasa.gov/WWW/wind/valid/tutorial/glossary.html

(accessed 19/11/2012)

[67] Matlab the Language of technical computing available at:

http://www.mathworks.co.uk/products/matlab/

(accessed 19/11/2012)

[68] A400M with strakes available at:

http://media.defenseindustrydaily.com/images/AIR_A400M_Test_Rear_lg.jpg

(accessed 26/11/2012)

[69] Probe mechanism available at:

http://airrefuelingarchive.files.wordpress.com/2011/01/060901-f-1234s-0061.jpg

(accessed 28/11/2012)

[70] Y+ Spalart Allmaras available at:

http://jullio.pe.kr/fluent6.1/help/html/ug/node456.htm

(accessed 29/11/2012)

[71] Young-Tai, Choi and Norman, M. Wereley, “Semi-Active Magnetorheological Refueling Probe Systems for Aerial Refueling Events“University of Maryland USA

[72] Kapseong Ro, Taeseung Kuk, James W. Kamman, 2011 “Dynamics and Control of Hose–Drogue Refueling Systems During Coupling“, Western Michigan University USA

[73] Roshawn Elisabeth Bowers, 2005 “ESTIMATION ALGORITHM FOR AUTONOMOUS AERIAL REFUELING USING A VISION BASED RELATIVE NAVIGATION SYSTEM“ University of Texas USA

[74] John C. Vassberg, David T. Yeh, Andrew J. Blair, Jacob M. Evert, 2004 “Numerical Simulations of KC-10 Centerline Aerial Refueling Hose-Drogue Dynamics With A Reel Take-Up System” AIAA 2004-4719

[75] Tom Rendall, Private communication via E-Mail, 04/05/2012

[76] Representative thrust for A330 [54] and resulting mass flow available at:

http://en.wikipedia.org/wiki/Airbus_A330

(accessed 07/12/2012)

[77] Tecplot available at:

http://www.tecplot.com/

(accessed 10/12/2012)

APPENDICES

Appendix A Literature Review

A.1 Research philosophies

A case study typically simulates and models a real life situation [32] aiming at the identification and solution of problems. According to Thomas [33] case studies are analyses of [...] or other systems that are studied holistically by one or more methods. The case that is the *subject* of the inquiry will be an instance of a class of phenomena that provides an analytical frame — an *object* — within which the study is conducted and which the case illuminates and explicates.

The present work fulfills all points of Thomas' definition of a case study. The case focus and thus the object is the wake-hose interaction. The subject of the inquiry is a refuelling situation with a representative aircraft at representative flight conditions. This provides the analytical frame within which the study is conducted and through which the object can be illuminated and explicated. Furthermore Yin [34] states, that a case study design should be considered when: (a) the focus of the study is to answer "how" and "why" questions, (b) you cannot manipulate the behaviour of those involved in the study, (c) you want to cover contextual conditions because you believe they are relevant to the phenomenon under study or (d) the boundaries are not clear between the phenomenon and context. According to Yin [34] there is a justification for a case study if any of these points apply. For the present work at least three points apply: (a) one focus of the study aims at "how" the tanker wake influences the hose characteristics, (b) it involved an aircraft and a refuelling hose – the behavior of the hose cannot be manipulated due to the underlying physics, (c) the contextual conditions are the different refuelling conditions and are believed to be relevant to the wake-hose interaction. Thus, the present work can and is embedded into the structure of a case study.

A.2 Case study types

One suggestion for the definition of different case study types was made by Yin [34]. Six different types are outlined in Table 5-1.

Type of Structure	**Purpose of Case Study**		
	Exploratory	Descriptive	Explanatory
Linear Analysis	✗	✗	✗
Comparative	✗	✗	✗
Chronological	✗	✗	✗
Theory-building	✗		✗
Suspense			
Un-sequenced		✗	

Table 5-1 Different case study types with their typical features and purposes [34]

The current study is a blend of linear and comparative analysis. The linear analysis is typical for scientific research and is suggested to be organized in the IMRAD style. It consists of Introduction, Methods, Results and Discussion. The present structure is the same, but with an additional chapter termed literature review. A comparative study investigates the same object from different points of view. There are two objects in the current study, the wake-hose interaction and the specific wake of rear fuselage flows. Both objects are studied from different points of view, involving the comparison of different hose configurations and different fuselage types under different conditions. Both types are exploratory, descriptive and explanatory. There is also a distinction between an analytical approach and problem oriented approach. The analytical approach aims at the understanding and the reason of an event. No solution to a problem is required. The problem oriented approach aims at the identification of problems and at the suggestion of solutions to the problems. The present work is clearly a problem oriented case study.

Appendix B Wind tunnel experiments

B.1 TAB geometry

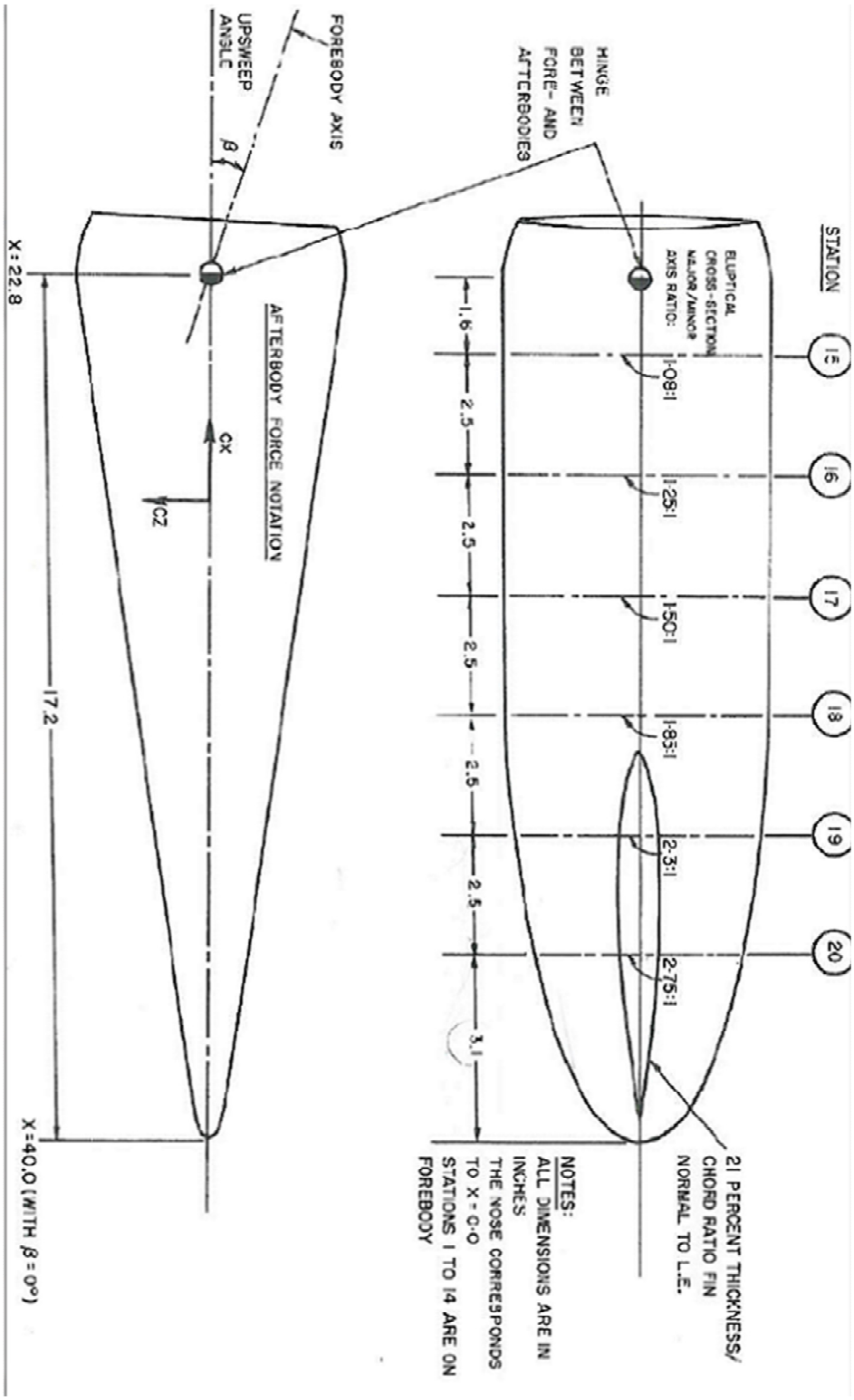

Figure 5-3 Afterbody geometry of transport aircraft model

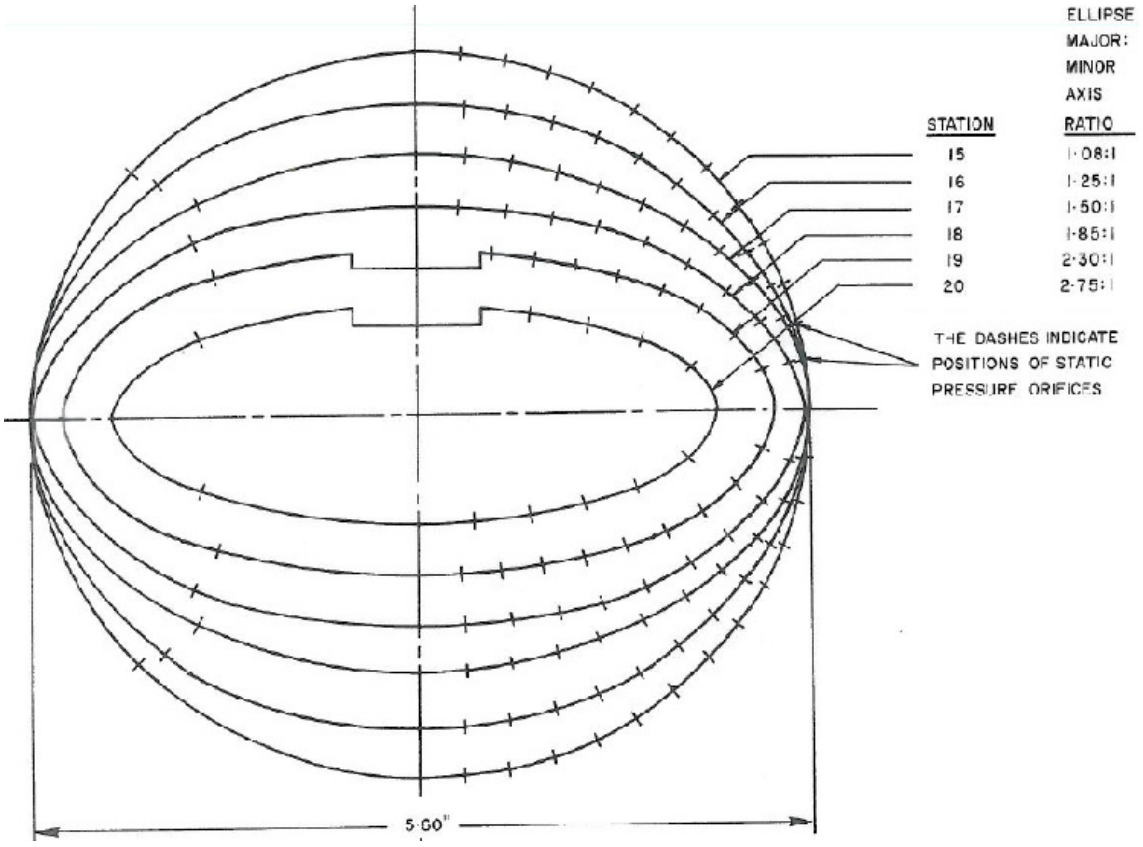

Figure 5-4 Afterbody cross sections of transport aircraft model